LANCASTER UNIVERSITY

Earth's Outer Electron Radiation Belt: Sources, Losses and Predictions

by

David Paul Hartley

A thesis submitted in partial fulfillment for the
degree of Doctor of Philosophy

in the
Space Plasma Environment And Radio Science Group
Physics Department
Faculty of Science and Technology
Lancaster University
UK

February 2015

Declaration of Authorship

I, David Paul Hartley, declare that this thesis titled, 'Earth's Outer Electron Radiation Belt: Sources, Losses and Predictions' and the work presented in it are my own. I confirm that:

- This work was done wholly or mainly while in candidature for a research degree at this University.
- Where any part of this thesis has previously been submitted for a degree or any other qualification at this University or any other institution, this has been clearly stated.
- Where I have consulted the published work of others, this is always clearly attributed.
- Where I have quoted from the work of others, the source is always given. With the exception of such quotations, this thesis is entirely my own work.
- I have acknowledged all main sources of help.
- Where the thesis is based on work done by myself jointly with others, I have made clear exactly what was done by others and what I have contributed myself.

Signed:

Date:

"Physics is like sex: sure, it may give some practical results,

but that's not why we do it."

Richard P. Feynman

Abstract

The outer electron radiation belt is highly dynamic in space and time. Understanding the mechanisms that drive these variations is of high interest to the scientific community because of the negative effects that the radiation belt can have on satellite instrumentation. Evidence in support of a wide range of processes has been uncovered, yet a complete understanding of the relative contribution of each processes, and how these contributions vary over time, is yet to be fully determined.

The first body of research (Chapter 4) follows the evolution of the electron radiation belt at geosynchronous orbit through three high-speed solar wind stream induced dropouts. Electron flux, magnetic field, and phase space density results from GOES-13 indicate that outwards adiabatic transport plays a key role in causing radiation belt flux dropouts at GEO. This leads to enhanced magnetopause losses and subsequent outwards radial diffusion. Other loss processes may also play a role.

In the second body of research (Chapter 5), the partial moments (electron number density, temperature and energy density) from GOES-13 are compared to different solar wind parameters, both instantaneous and time delayed, in order to develop a coarse predictive capability. Using these partial moments allows for changes in the number of electrons and the temperature of the electrons to be distinguished, which is not possible with the particle flux output from individual instrument channels. It is found that using solely the solar wind velocity as a driver results in predicted values that accurately follow the general trend of the observed moments. Given that electron number density and temperature are the fundamental physical parameters of a plasma, the result is a testable model that addresses elementary plasma properties. Hence, for a Maxwellian

plasma, it is possible to infer the flux at any energy, not just energy channels tied to a particular instrument.

In the final research study (Chapter 6), the validity of using the cold plasma dispersion relation to infer the magnetic field wave power from the measured wave electric field is tested using Van Allen Probes EMFISIS observations in the chorus wave band (0.1-0.9 f_{ce}). Results from this study indicate that for observed wave intensities $>10^{-3}$ nT^2, using the cold plasma dispersion relation results in an underestimate of the wave intensity by a factor of 2 or greater, 56% of the time over the full chorus wave band, 60% of the time for lower band chorus, and 59% of the time for upper band chorus. Hence during active periods, empirical wave models that are reliant on the cold plasma dispersion relation will underestimate chorus wave intensities to a significant degree, thus causing questionable calculation of wave-particle resonance effects on MeV electrons.

Acknowledgements

I would firstly like to thank Mick Denton for the guidance, support and advice he has given me throughout the duration of my Ph.D. I would also like to thank all members of the Space Plasma Environment And Radio Science Group, past and present; in particular, Nathan Case, Carl Bryers, and Patrick Cannon who have all helped to make this Ph.D. an enjoyable experience. I would like to express my thanks to Juan Rodriguez for providing a number of IDL routines and invaluable assistance with analysis of GOES satellite data. Additionally, I would like to thank Yue Chen for providing me with the opportunity and funding to attend the Los Alamos Space Weather Summer School 2013. Also, I am grateful for the assistance provided by all other collaborators; Janet Green, Craig Kletzing, Bill Kurth, Terry Onsager, and Howard Singer. I would also like to thank the Royal Astronomical Society Conference Travel Fund, the Institute of Physics Research Student Conference Fund, the C R Barber Trust, and Lancaster University Faculty of Science and Technology for their kind financial support. Finally I would like to give special thanks to my (soon-to-be) wife, Jade, in addition to my parents and the rest of my family, for their patience, unwavering support and encouragement.

Contents

Declaration of Authorship **i**

Abstract **iii**

Acknowledgements **v**

List of Figures **x**

List of Tables **xvi**

1 Introduction **1**
1.1 Basic Plasma Physics . . . 2
1.1.1 Debye Shielding and Debye Length . . . 3
1.1.2 Plasma Parameter . . . 5
1.1.3 Plasma Frequency . . . 7
1.2 Single Charged Particle Motion . . . 10
1.2.1 Gyromotion . . . 11
1.2.2 Bounce Motion . . . 13
1.2.3 Drift Motion . . . 15
1.2.3.1 $\mathbf{E} \times \mathbf{B}$ Drift . . . 15
1.2.3.2 Gradient Drift . . . 17
1.2.3.3 Curvature Drift . . . 19
1.2.4 Adiabatic Invariants . . . 21
1.2.4.1 First Adiabatic Invariant . . . 21
1.2.4.2 Second Adiabatic Invariant . . . 24
1.2.4.3 Third Adiabatic Invariant . . . 27
1.2.5 Frozen-in Theorem . . . 29
1.3 The Sun-Earth System . . . 32
1.3.1 Solar Wind . . . 32
1.3.2 Magnetosphere . . . 34
1.3.2.1 Magnetic Reconnection and Convection . . . 36

1.3.2.2 Geomagnetic Storms . . . 40
1.3.2.3 Substorms . . . 42
1.3.2.4 Radiation Belts . . . 43
1.3.2.5 Ring Current . . . 45
1.3.2.6 Plasma Sheet . . . 46
1.3.2.7 Plasmasphere . . . 47
1.3.2.8 Ionosphere . . . 48
1.4 Outer Electron Radiation Belt Dynamics . . . 49
1.4.1 Adiabatic Variations . . . 51
1.4.2 Magnetopause Shadowing . . . 52
1.4.3 Diffusion . . . 55
1.4.4 Waves . . . 56
1.4.4.1 Ultra Low Frequency (ULF) Waves . . . 57
1.4.4.2 Chorus Waves (0.1 f_{ce} to 0.9 f_{ce}) . . . 58
1.4.4.3 Plasmaspheric Hiss (100 Hz to ($\sim$ 2) kHz) . . . 59
1.4.4.4 Electromagnetic Ion Cyclotron (EMIC) Waves (<1-2 Hz) 60
1.4.4.5 Magnetosonic Equatorial Noise . . . 60

2 Instrumentation 62
2.1 Particle Detectors . . . 62
2.1.1 Electrostatic Analysers . . . 65
2.1.2 Solid State Detectors . . . 67
2.2 Magnetometers . . . 67
2.2.1 Fluxgate Magnetometer . . . 68
2.2.2 Search-Coil Magnetometer . . . 69
2.3 OMNIweb . . . 71
2.3.1 Dst Index . . . 72
2.3.2 SYM-H . . . 72
2.3.3 Kp Index . . . 73
2.3.4 AE Index . . . 73
2.4 GOES . . . 74
2.4.1 Space Environment Monitor . . . 74
2.4.1.1 MAGED . . . 75
2.4.1.2 Magnetometer . . . 79
2.5 Van Allen Probes . . . 79
2.5.1 Mission Objectives . . . 80
2.5.2 Overview of Instrument Suites . . . 82
2.5.3 EMFISIS . . . 83
2.5.3.1 Waves Instrument and the Magnetic Search Coil (MSC) . 83
2.5.3.2 Magnetometer (MAG) . . . 86

3 Solving the Radiation Belt Riddle: A Guide to Phase Space Density 87
3.1 Abstract . . . 88
3.2 Introduction . . . 89

3.3 Methodology 92
3.4 Sources and Losses 97
3.5 Summary 99

4 Case Studies of the Impact of High-Speed Solar Wind Streams on the Electron Radiation Belt at Geosynchronous Orbit: Flux, Magnetic Field and Phase Space Density 101
4.1 Abstract 102
4.2 Introduction 103
4.3 Analysis Method and Instrumentation 105
4.4 Quiet Time Variation 108
4.5 Event 1: January 6, 2011 114
4.5.1 Solar Wind and Geomagnetic Conditions 114
4.5.2 Flux 114
4.5.3 Pitch Angle Distribution 116
4.5.4 Magnetic Field 117
4.5.5 Phase Space Density 118
4.5.6 Discussion 119
4.6 Event 2: February 4, 2011 121
4.6.1 Solar Wind and Geomagnetic Conditions 121
4.6.2 Electron Flux 123
4.6.3 Pitch Angle Distribution 124
4.6.4 Magnetic Field 124
4.6.5 Phase Space Density 125
4.6.6 Discussion 126
4.7 Event 3: April 11, 2011 127
4.7.1 Solar Wind and Geomagnetic Conditions 129
4.7.2 Electron Flux 129
4.7.3 Pitch Angle Distribution 130
4.7.4 Magnetic Field 131
4.7.5 Phase Space Density 132
4.7.6 Discussion 132
4.8 Summary and Conclusions 135

5 Electron number density, temperature and energy density at GEO and links to the solar wind: A simple predictive capability 139
5.1 Abstract 140
5.2 Introduction 141
5.3 Instrumentation 144
5.4 Analysis and Results 146
5.4.1 Determining the primary driver 147
5.4.2 Distribution of partial moments with varying primary solar wind driver 151
5.4.3 Calculating prediction functions 154
5.4.4 Testing the prediction 160

5.5 Discussion and Conclusions 166

6 Applying the cold plasma dispersion relation to whistler mode chorus waves: EMFISIS wave measurements from the Van Allen Probes 170
6.1 Abstract 171
6.2 Introduction 172
6.3 Motivation and Methodology 173
6.4 Results 176
6.5 Discussion 185
6.6 Conclusions 187

7 Summary and Further Research 188
7.1 Case Studies of the Impact of High-Speed Solar Wind Streams on the Electron Radiation Belt at Geosynchronous Orbit: Flux, Magnetic Field and Phase Space Density 190
7.2 Electron number density, temperature and energy density at GEO and links to the solar wind: A simple predictive capability 191
7.3 Applying the cold plasma dispersion relation to whistler-mode chorus waves: EMFISIS wave measurements from the Van Allen Probes 192
7.4 Further Research 193
7.4.1 Testing the validity of the cold plasma dispersion relation for different wave modes 194
7.4.2 Evidence of acceleration by whistler-mode chorus waves at geosynchronous orbit 194
7.4.3 Predictive model using Van Allen Probes data 195

A Pitch-Angle Distribution Retrievals from GOES 13-15 Magnetospheric Electron Detector (MAGED) Observations 197

B Further examples of testing the prediction functions calculated in Chapter 5 203

C The Cold Plasma Dispersion Relation ($k \parallel B_0$) 206

Bibliography 209

List of Figures

1.1 Due to a temporary external force (caused by a temporary external electric field in this case), the electrons (blue) are displaced from the ions (red). When the temporary electric field is no longer present, the charge separation induces a restoring electric field. Because of the electron momentum and the electric field induced by charge separation, simple harmonic motion occurs. Adapted from *Knipp* [2011]. 8

1.2 A schematic representation showing the effect of gradient drift on a proton and an electron in a magnetic field [*Somov*, 2013]. 20

1.3 Schematic representation of a particle drifting in the (distorted) geomagnetic field. If the magnetic field is static (or the variations are slow in comparison to the characteristic timescales of each type of particle motion), the particle will reflect at the same B_m and as the particle drifts, for each longitude the particle will bounce on the field line on which its motion between the mirror points conserves the second adiabatic invariant. From *Walt* [1994]. 27

1.4 A schematic showing how plasma elements initially positioned on a magnetic field line at time t_0, remain situated on that field line at a later time, t_1. That is, for the one-dimensional line element shown, the magnetic flux passing through, remains constant. Adapted from *Haigh et al.* [2006]. . . 30

1.5 A schematic representation of how solar rotation causes the solar wind to form the Parker spiral. From *Kivelson and Russell* [1995]. 33

1.6 A schematic diagram showing the structure of a high-speed solar wind stream in the ecliptic plane. From *Pizzo* [1978]. 35

1.7 The magnetic field configuration in GSM coordinates when (left) isolated from the solar wind, analogous to a simple dipole, and (right) distorted by the solar wind. From *Knipp* [2011]. 36

1.8 A schematic representation of the magnetosphere showing the location of different plasma regimes. From *Kivelson and Russell* [1995]. 37

1.9 A diagram showing the evolution of reconnecting antiparallel magnetic field lines. From *Baumjohann and Treumann* [1997]. 38

1.10 A schematic diagram of the reconnection process in the magnetosphere. From *Dungey* [1961]. 39

1.11 A schematic diagram of the electric field equipotential contours in the equatorial plane. From *Baumjohann and Treumann* [1997]. 40

1.12 Schematic representation of how a geomagnetic storm might appear in the measured magnetic field at the Earth's surface with the initial phase, main phase, and recovery phase highlighted. 42
1.13 The intensity structure of the radiation belts from true count rates measured by Geiger tubes carried by Explorer IV and Pioneer III. Also shown are the outbound and inbound trajectories of Pioneer III. Both the inner and outer radiation belts are visible. From *Van Allen* [1959]. 44
1.14 The top graph shows the intensity of 2.5 MeV electrons as measured by NASAs twin Van Allen Probes satellites. The second graph shows the intensity of 2.5 MeV electrons at a fixed radial distance of 4.2 Earth radii (L = 4.2). The bottom three graphs show solar wind velocity (V_{sw}), the IMF north-south component (*IMF* B_z), and the Dst index. The geomagnetic activity on October 8-9 produces an intense and rapid enhancement of the electron radiation belt. From *Reeves et al.* [2013a] 51
1.15 Contours of constant equatorial magnetic field strength within the magnetosphere under average conditions. a indicates the magnetopause boundary and γ is used to denote nanotesla. After *Fairfield* [1968]. 52
1.16 The impact of the diffusion process on a initial distribution function, $f(x,t)$. From *Walt* [1994]. 56
1.17 A schematic illustration of the spatial distribution of waves in the magnetosphere in relation to the plasmasphere, the drift paths of ring current ions and electrons, and the drift path of relativistic electrons. From *Thorne* [2010]. 57
1.18 A sample spectrogram from the CRRES satellite highlighting the different waves that occur in the magnetosphere. From *Kletzing et al.* [2013]. . . . 61

2.1 A schematic representation of how an electrostatic analyser measures electrons with a specified energy, E_d. This energy may be altered by varying the voltage, and therefore the electric field, applied across the curved plate walls of the instrument. 66
2.2 A schematic representation of a hysteresis loop (magnetism, M as a function of applied magnetic field, H) for the core material of a fluxgate magnetometer in the absence of an external magnetic field. 68
2.3 A diagram showing the voltage in the sensory coil of a fluxgate magnetometer both in the absence of an external magnetic field (top) and in the presence of an external magnetic field (bottom). Adapted from *Fiorillo* [2004]. 70
2.4 The orbit of both Van Allen Probes A and Van Allen Probes B on October 1, 2012 between 08:00 and 14:00 UT in GSE coordinates. 81
2.5 The Van Allen Probes instrument suite layout. EMFISIS MSC and MAG sensors are nominally aligned with the EFW wire booms which define the UVW coordinate system (spinning coordinates) which is implemented for science data. Also shown is the spacecraft XYZ coordinate system. From *Kletzing et al.* [2013]. 85

3.1 A representation of the Van Allen radiation belts with two spacecraft, representing the Van Allen Probes, and their orbit through the heart of the radiation belts. Credit: JHU/APL, NASA 90

3.2 A schematic representation of the phase space density calculation. Initially, a value of μ and K are selected to remain constant throughout the calculation. Panel (a) shows schematically the relationship between the second adiabatic invariant, K, and pitch angle, α, for one instance of time, calculated by Eqn. 1 from the Figure. The dashed red line indicates the selected value of K, and the dashed blue line indicates the pitch angle that corresponds to the selected K, α_K. Panel (b) is a schematic representation of the relationship between μ and E, (as calculated by Eqn. 2 from the Figure) for the pitch angle obtained in panel (a), α_K. The dashed red line indicates the selected value of μ and the dashed orange line indicates the energy that corresponds to the selected value of μ, E_μ. Panel (c) represents the electron flux pitch-angle distribution for three instrument energy channels. The dashed blue line indicates the pitch angle that corresponds to the selected K, α_K, from panel (a). From these pitch-angle distributions, it is possible to 'read off' the electron flux values at the pitch angle α_K to obtain a set of flux values that vary with instrument energy channels. These flux values are then converted to PSD using Eqn. 3 from the Figure. Panel (d) displays these phase space density values as a function of the instrument energy channels. By fitting a function to these values of the form shown on panel (d), and substituting in the energy corresponding to the selected value of μ, E_μ, from panel (b), it is possible to obtain the phase space density corresponding to selected values of μ and K, $f(E_\mu, \alpha_K)$. Using α_K and the spacecraft position $\mathbf{x}$, the IRBEM library is used to calculate L^*. The electron PSD has now been calculated in adiabatic invariant coordinates for one instance of time. This process can be repeated for the required number of time intervals. 94

3.3 Schematic diagram showing how internal and external acceleration may appear in the PSD vs. L^* profile (adapted from *Green and Kivelson* [2004]). Panel (a) shows a PSD increase caused by radial diffusion from an external source mechanism, whereas panel (b) indicates a PSD increase caused by a local internal acceleration mechanism. The red lines indicate the PSD vs. L^* profile prior to acceleration (time = t_1) with the blue line showing the effect of the acceleration event (time = t_2). 98

3.4 A schematic diagram showing how the PSD vs. L^* profile might evolve during a period of elevated solar wind pressure (adapted from *Turner et al.* [2012]). Panel (a) shows an initial peaked PSD vs. L^* profile. Panel (b) depicts the magnetopause location moving inwards, due to the increased solar wind pressure, resulting in losses to the magnetopause (magnetopause shadowing). In panel (c), the solar wind pressure relaxes, resulting in the magnetopause location moving back to larger L^*. The PSD vs. L^* profile contains a steep radial gradient at the magnetopause location from panel (b), resulting in enhanced radial diffusion (blue arrows). Outwards radial transport may result in further losses to the magnetopause. 100

4.1 (a) Schematic representation of how an error in the calculation of the inverse of the third adiabatic invariant, L^*, will affect the predicted phase space density. (b) Schematic representation of how an error in the calculation of the second adiabatic invariant, K, will affect the predicted phase space density (after *Green and Kivelson* [2004]). 110
4.2 Quiet time variation: 0 UT January 30 to 0 UT January 31. (a) Solar wind speed (black) and solar wind flow pressure (red) from OMNI2. (b) Geomagnetic indices Dst, Dst* (calculated using methodology of *Borovsky and Denton* [2010a]), SYM-H and Kp indices. (c) The magnetic field magnitude from the T96 magnetic field model and as measured in situ by GOES-13. (d) The magnetic field stretching angle from T96 and as measured by GOES-13 (centred dipole coordinates). An indicator of the 'goodness' of the model fit to the observed magnetic field is displayed in colour at the top of the panel; green indicates that the model is within ±15% of the measured magnetic field, yellow indicates ±30%, orange ±45% and red ± > 45%. (e) Omnidirectional flux measurements for three energy channels from GOES-13 where colour coding is electron anisotropy (warm colours indicating parallel orientation and cold colours indicating perpendicular orientation). (f) The phase space density as a function of time and L^* with fixed values of μ and K (μ=200 MeV/G and K=2500 $G^{1/2}$km or K∼ 0.4 $G^{1/2}R_E$). In panels (c) through (f) vertical dashed orange and black lines indicate local noon and midnight respectively. . . . 112
4.3 Event 1: 16 UT January 6 to 10 UT January 7. Displays the same parameters as described in Figure 4.2. 115
4.4 Event 2: 12 UT February 4 to 6 UT February 5. Displays the same parameters as described in Figure 4.2. 122
4.5 Event 3: 12 UT April 11 to 12 UT April 12. Displays the same parameters as described in Figure 4.2. 128
4.6 Pitch angle distributions for the quiet event and the three HSS events. Unfilled white areas indicate either bad/missing data or where the fit of the pitch angle distribution to the data produces unrealistically low flux values. These pitch angle distributions are used to calculate the pitch-angle anisotropy indicated in panel (e) of Figures 4.2, 4.3, 4.4 and 4.5. . . 133

5.1 Variability of partial moments (electron number density and temperature) measured at GEO by GOES-13 with solar wind velocity (a) and density (b) for a 24 hour time delay in the noon sector. 148
5.2 Density plots displaying the partial moments (electron number density, temperature and energy density) from GOES-13 at GEO for varying solar wind conditions with a time delay of 24 hours applied; solar wind velocity (a), (c) and (e), and solar wind density (b), (d) and (f). 150

5.3 Density plots of solar wind velocity against electron number density at GEO in the noon sector for increasing time delay. (a) negative 12 hour delay, (b)instantaneous, (c) 12 hour delay, (d) 24 hour delay, (e) 36 hour delay and (f) 48 hour delay. The pink line indicates the median number density for each solar wind velocity bin whilst the straight black lines indicate a linear fit of the mean ± two standard deviations for each solar wind velocity bin (lower and upper bounds). Equations describing these upper and lower bounds, as well as the predicted quantity, are listed on the Equation 5.6 with coefficients listed in Table 5.1. 153

5.4 Density plots of solar wind velocity against electron temperature at GEO in the noon sector for increasing time delay. (a) negative 12 hour delay, (b)instantaneous, (c) 12 hour delay, (d) 24 hour delay, (e) 36 hour delay and (f) 48 hour delay. The pink line indicates the median temperature for each solar wind velocity bin whilst the straight black lines indicate a linear fit of the mean ± two standard deviations for each solar wind velocity bin (lower and upper bounds). Equations describing these upper and lower bounds, as well as the predicted quantity, are listed on the Equation 5.7 with coefficients listed in Table 5.2. 155

5.5 Density plots of solar wind velocity against electron energy density at GEO in the noon sector for increasing time delay. (a) negative 12 hour delay, (b)instantaneous, (c) 12 hour delay, (d) 24 hour delay, (e) 36 hour delay and (f) 48 hour delay. The pink line indicates the median energy density for each solar wind velocity bin whilst the straight black lines indicate a linear fit of the mean ± two standard deviations for each solar wind velocity bin (lower and upper bounds). Equations describing these upper and lower bounds, as well as the predicted quantity, are listed on the Equation 5.8 with coefficients listed in Table 5.3. 156

5.6 (a) The solar wind velocity during May 2012, (b) the electron number density at geosynchronous orbit measured by GOES-13 (red), the prediction as calculated 24 hours in advance (dark blue) and the upper and lower bounds to 90% confidence limits (blue shading), (c) the electron temperature at geosynchronous orbit measured by GOES-13 (red), the prediction as calculated 24 hours in advance (dark blue) and the upper and lower bounds to ∼ 90% confidence limits (blue shading), and (d) the electron energy density at geosynchronous orbit measured by GOES-13 (red), the prediction as calculated 24 hours in advance (dark blue) and the upper and lower bounds to ∼ 90% confidence limits (blue shading). 164

5.7 Figure showing the percentage error (magnitude of the residual divided by the observed quantity) for the same time period and delay shown in Figure 5.6 (May 2012, 24hr delay). The figure also contains a colour indicator at the bottom of each panel in order to show the magnitude of the percentage error; less than 10% (green), between 10% and 25% (yellow), between 25% and 50% (orange) and greater than 50% (red). Also listed on the figure is the percentage of the time period whereby the percentage error falls in the bounds defined above. 166

6.1 A survey plot of the electric, S_E, (top) and magnetic, S_B, (bottom) wave spectral intensity observed by Van Allen Probe A during an 8-hour period on December 16, 2012. The dashed pink lines indicate 0.1 and 0.9 f_{ce} and the dashed red line indicates 0.5 f_{ce} as calculated from the onboard magnetometer measurements. Whistler mode chorus waves and plasmaspheric hiss are highlighted in the spectrogram. 177

6.2 The magnetic field power spectral density in the chorus wave frequency band (between 0.1 and 0.9 f_{ce}) as measured by EMFISIS on-board Van Allen Probe A (blue) and as calculated using the cold plasma dispersion relation (red) at 12:01:41 (a), 11:21:47 (b) and 12:00:11 (c) on November 20, 2012. The normalized root-mean-square errors (NRMSE) are also listed. 179

6.3 (a) Plot showing how the observed wave intensity from Van Allen Probe A compares with that calculated using the cold plasma dispersion relation in the 0.1 to 0.9 f_{ce} range for the 20 day sample period used in this study. The color indicates the number of occurrences in each bin, normalized to the number of occurrences in each observed wave intensity column. The line plot above each panel indicates the number of occurrences in each observed wave intensity column, in addition to listing the total number of occurrences (ΣN) and the number of occurrences with high observed wave intensity (ΣN ($B_w^2 > 10^{-3} nT^2$)). (b and c) The same quantities calculated separately for lower band (0.1 to 0.5 f_{ce}) and upper band (0.5 to 0.9 f_{ce}) chorus frequencies. 181

6.4 The probability distributions of the logarithm of the wave intensity ratio (observed/calculated) in the full chorus wave frequency band for low ($B_w^2 < 10^{-3} nT^2$, (a)) and elevated ($B_w^2 > 10^{-3} nT^2$, (b)) observed wave intensities. Also shown are the percentages of data that occur in discreet ratio bins parametrized as; Ratio < 0.2, $0.2 <$ Ratio < 0.5, $0.5 <$ Ratio < 2.0, $2.0 <$ Ratio < 5.0, and Ratio > 5.0. (c) and (d) show the same parameters for lower band chorus and (e) and (f) show the same parameters for upper band chorus. 184

A.1 Examples of PADs (peaked and butterfly) obtained using the retrieval code as described in the appendix for energy channels; 40 keV, 150 keV and 475 keV. The blue line indicates the retrieved PAD with red stars indicating the measurements from GOES-13. 202

B.1 The same parameters as shown in Figure 5.6 for January 2012. 204

B.2 The same parameters as shown in Figure 5.6 for August 2012. 205

C.1 The geometry used for waves propagating parallel to the background magnetic field, $k \parallel B_0$. Both the background magnetic field and wave vector are oriented in the z direction, $\mathbf{B}_0 = B_0 \hat{z}$ and $\mathbf{k} = k\hat{z}$. 207

List of Tables

1.1 Approximate periods of motion for a 1keV and a 1MeV electron in the geomagnetic field at a radial distance of $6.6R_E$ (calculated using equations presented in *Knipp* [2011]; *Fitzpatrick* [2014]). 22
1.2 Typical solar wind values observed at a distance of 1 AU. From *Baumjohann and Treumann* [1997] and OMNIweb [*King and Papitashvili*, 2005]. 34
1.3 Typical classification of ULF waves. From *Jacobs et al.* [1964] 58

2.1 The energy thresholds of the MAGED voltage level detectors and the conditions that need to be met in order for a particle to be considered in the defined energy channels. From *Hanser* [2011]. 77
2.2 Description of the orientation of the nine MAGED telescope detectors. Orientations may be used in Equation 2.8 to determine the central pitch angle of each detector telescope. From *Rodriguez* [2014] 78

4.1 Solar wind and geophysical parameters for the events in this study; maximum/minimum solar wind velocity, maximum solar wind pressure, maximum/minimum flux observed by GOES-13 in the 475 keV electron channel, maximum/minimum Dst index and maximum Kp index. 109

5.1 A table showing the parameters to be used in equation 5.6 to calculate the predicted value, the lower bound and the upper bound of the electron number density at GEO for five different time delays (0 hr, 12 hr, 24 hr, 36 hr, 48 hr) for four local time sectors at GEO. 160
5.2 A table showing the parameters to be used in equation 5.7 to calculate the predicted value, the lower bound and the upper bound of the electron temperature at GEO for five different time delays (0 hr, 12 hr, 24 hr, 36 hr, 48 hr) for four local time sectors at GEO. 161
5.3 A table showing the parameters to be used in equation 5.8 to calculate the predicted value, the lower bound and the upper bound of the electron energy density at GEO for five different time delays (0 hr, 12 hr, 24 hr, 36 hr, 48 hr) for four local time sectors at GEO. 162

Chapter 1

Introduction

Earth's outer electron radiation belt is highly dynamic in space and time. It is the processes that fuel the outer belt's variability that are of high interest and are, as yet, not fully understood. There exists a lack of quantitative detail as to how different source mechanisms (that increase radiation belt populations) and loss processes (that reduce particle populations) wax and wane between different events. In order to obtain a complete and accurate physical understanding, the relative contribution of each mechanism requires investigation. With a high number of satellites operating in this region, and the fact that relativistic electrons pose a significant risk to orbital hardware, the dynamics of the radiation belt are of paramount interest to the scientific community. This is highlighted by the launch of the high-profile NASA Van Allen Probes mission in 2012, more than 50 years since the discovery of the Van Allen radiation belts.

The research presented in this thesis aims to address the complex physics of radiation belt dynamics. Initially, the basic principles of plasmas are introduced. These are

subsequently expanded upon to provide the underlying physics required to describe the complex region of Earth's outer electron radiation belt. More specifically; the different loss mechanisms that drive rapid reductions in the number of radiation belt particles over short timescales, the acceleration of electrons to relativistic energies within the outer radiation belt region, and how these competing processes can be resolved to obtain a predictive capability are discussed in Chapters 4, 5 and 6.

1.1 Basic Plasma Physics

The launch of the Sputnik satellite in 1957 signalled the dawn of the space age. With the near-Earth space environment becoming accessible, a broadening of geophysical interests was sparked. Many satellite missions followed, with instrumentation measuring the different characteristics of this previously inaccessible region. In-situ observations of the near-Earth environment showed matter in this region to enjoy a significant degree of ionisation, very different to the types of matter observed on, or close to, the planets surface. This ionised state of matter is called a plasma. A plasma is defined as an ionised fluid that contains approximately equal numbers of positively and negatively charged particles [*Baumjohann and Treumann*, 1997]. The random distributions of both positive and negative charge carriers means that the net charge in any volume element of a plasma is close to zero (positive and negative charges cancel) and a plasma is therefore considered to be *quasineutral*. That is, charge imbalance may exist over small length scales however, over larger volume elements the density of positive and negative charge carriers is equal (zero net charge). Particles in a plasma are unbound, meaning that the random kinetic energy of a particle is dominant over the electric potential energy of its

neighbours. Since the particles, and therefore the charges, are unbound, plasmas are able to conduct electric currents. Also, plasmas typically respond to external forces (such as those created by external magnetic or electric fields) in a collective manner. In order for a medium to be classified as a plasma, three requirements need to be fulfilled [*Baumjohann and Treumann*, 1997]. These criteria are discussed in the following sections.

1.1.1 Debye Shielding and Debye Length

The electric field, $\mathbf{E}$, associated with an isolated point charge, q, at distance, r, is defined by Coulombs Law:

$$\mathbf{E} = \frac{q}{4\pi\epsilon_0}\frac{\hat{\mathbf{r}}}{r^2} \tag{1.1}$$

where ϵ_0 is the permittivity of free space and $\hat{\mathbf{r}}$ is the unit vector in the direction of distance, r. Since $\nabla \times \mathbf{E} = \mathbf{0}$ for an electrostatic field, the electric field is determined by the divergence of the electrostatic potential, ϕ.

$$\mathbf{E} = -\nabla\phi \tag{1.2}$$

Using Coulombs Law, the electrostatic potential of an isolated point charge at distance r is:

$$\phi = \frac{1}{4\pi\epsilon_0}\frac{q}{r} \tag{1.3}$$

The potential of a negatively charged particle results in the attraction of positively charged particles and the repulsion of negatively charged particles. Similarly, the potential of a positively charged particle results in the attraction of negatively charged particles and the repulsion of positively charged particles. Since the particles of a plasma are unbound, this results in positive ions attracting electrons and therefore shielding the electrostatic field of the ion from the rest of the plasma. Conversely, negatively charged electrons attract ions and therefore shield the electrostatic field of the electron from the rest of the plasma. That is, the surrounding plasma adjusts so that fewer electrons, and more ions, surround a negative charge and that more electrons, and fewer ions, surround a positive charge. The result is that the distance over which a single charge can influence is reduced. This is known as Debye shielding (named after the Dutch Nobel Laureate in Chemistry, Peter Debye). In other words, the electrostatic field of particles in a plasma must cancel out over small length scales in order to maintain charge neutrality on the larger scale.

Equation 1.3 is for a point charge in isolation. When other point charges are present, such as in a plasma, the electrostatic potential is dampened with increasing radial distance by Debye shielding. Therefore the electrostatic potential of a charged particle in a plasma, the Debye potential ϕ_D, becomes:

$$\phi_D = \frac{q}{4\pi\epsilon_0}\frac{1}{r}\,e^{-r/\lambda_D} \tag{1.4}$$

where λ_D is the Debye length defined as:

$$\lambda_D = \sqrt{\frac{k_B\, T_e\, \epsilon_0}{n\, e^2}} \tag{1.5}$$

where k_B is the Boltzmann constant, T_e is the electron temperature (assumed equal to the ion temperature), n is the plasma density (assumed $n_e = n_i$), and e is the elementary charge.

Equation 1.4 shows us that for $r \ll \lambda_D$, the potential is simply the Coulomb potential shown in Equation 1.1. However for $r \gg \lambda_D$, the potential around a point charge is almost fully shielded and becomes negligible. Therefore, in order to maintain quasineutrality, the characteristic length scale of a plasma, L, must satisfy the condition:

$$\lambda_D \ll L \tag{1.6}$$

This requirement is the first criterion of a plasma.

1.1.2 Plasma Parameter

In order for the description of Debye shielding to be meaningful, it is required that there are a large enough number of particles to apply statistical concepts. The number of particles contained in a Debye sphere (a sphere with a radius equal to the Debye length) is:

$$N_D = \frac{4\pi n {\lambda_D}^3}{3} \tag{1.7}$$

This quantity is dictated by the plasma parameter $\Lambda = n\,\lambda_D^3$. The second criterion of a plasma is:

$$\Lambda = n\,{\lambda_D}^3 \gg 1 \tag{1.8}$$

This criterion quantifies what is meant by an unbound particle (random kinetic energy of a particle is dominant over the electric potential energy of its neighbours). Substituting in the Debye length from Equation 1.5 yields:

$$\left(\frac{k_B\,T_e\,\epsilon_0}{n^{1/3}\,e^2}\right)^{3/2} \gg 1 \tag{1.9}$$

Neglecting the constants, this can be rewritten as:

$$k_B\,T_e \gg n^{1/3} \tag{1.10}$$

Since the electric potential energy of a particle due to its neighbours is determined by the inverse of the distance between the particles, and r is proportional to $n^{1/3}$, the second plasma criterion states that this electric potential energy be much less than the particles kinetic energy, $k_B\,T_e$. That is, the particles of a plasma are free particles [*Baumjohann and Treumann*, 1997].

1.1.3 Plasma Frequency

If a plasma is perturbed by an external force (e.g. by a temporary electric field) that disturbs the quasineutral state of the plasma, the 'lighter' electrons are displaced whereas the 'heavier' ions positions remain relatively unchanged. This sets up a small electric field between the electron-ion pair that acts to reduce charge separation and thus accelerates electrons towards the ions in an attempt to restore quasineutrality. Due to momentum, the electrons are carried past their equilibrium position, thus inducing an oppositely directed electric field. This process continues, resulting in a simple harmonic oscillation. This process is shown schematically in Figure 1.1 (adapted from *Knipp* [2011]).

The equation of motion for an electron in this case is:

$$m_e \frac{d^2 \Delta x}{dt^2} = eE \tag{1.11}$$

where Δx is the electron displacement and m_e is the electron mass. By treating the electrons of the plasma as a thin slab, displaced from a thin slab of ions of equal density by small distance, Δx, the induced electric field between the two regions is:

$$E = -\frac{\Delta x n e}{\epsilon_0} \tag{1.12}$$

Substituting Equation 1.12 into Equation 1.11 yields:

$$m_e \frac{d^2 \Delta x}{dt^2} = \frac{\Delta x n e^2}{\epsilon_0} \tag{1.13}$$

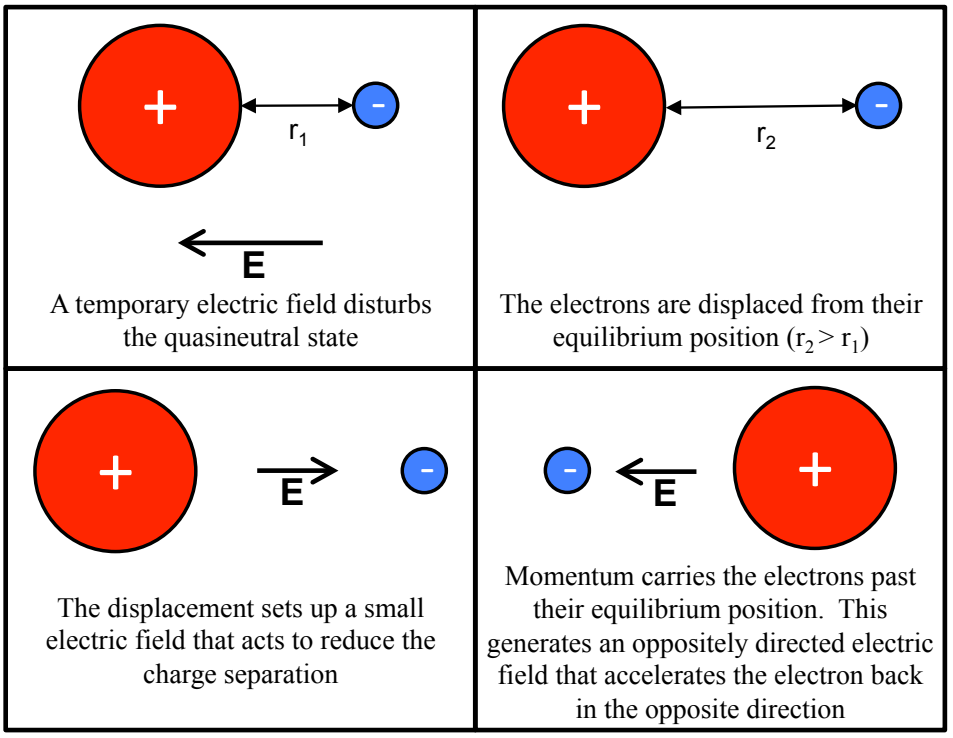

FIGURE 1.1: Due to a temporary external force (caused by a temporary external electric field in this case), the electrons (blue) are displaced from the ions (red). When the temporary electric field is no longer present, the charge separation induces a restoring electric field. Because of the electron momentum and the electric field induced by charge separation, simple harmonic motion occurs. Adapted from *Knipp* [2011].

The equation for a simple harmonic oscillator is:

$$F = ma = m\frac{d^2\Delta x}{dt^2} = -k\Delta x \tag{1.14}$$

Relating this to Equation 1.13 yields:

$$k = \frac{ne^2}{\epsilon_0} \tag{1.15}$$

Since $\omega = \sqrt{\frac{k}{m}}$ in general, the angular plasma frequency of electrons, ω_{pe} is defined as:

$$\omega_{pe} = \sqrt{\frac{ne^2}{\epsilon_0 m_e}} \tag{1.16}$$

The ions also oscillate at the angular ion plasma frequency, ω_{pi}, with the angular plasma frequency defined as $\omega_p^2 = \omega_{pe}^2 + \omega_{pi}^2$. However, since the mass term is in the denominator, and the mass of ions is significantly greater than that of electrons, the angular plasma frequency is dominated by the electron plasma frequency term and thus $\omega_p \approx \omega_{pe}$.

Since angular frequency is related to linear frequency through the expression $\omega = 2\pi f$, the linear plasma frequency may be defined as:

$$f_{pe} = \frac{\omega_{pe}}{2\pi} = \frac{1}{2\pi}\sqrt{\frac{ne^2}{\epsilon_0 m_e}} \tag{1.17}$$

The plasma frequency, $f_{pe}(Hz)$ is also related to the electron density, $n_e(cm^{-3})$, through the expression:

$$f_{pe} = 8980\sqrt{n_e} \tag{1.18}$$

Some plasmas contain a significant number of neutral particles and are therefore not fully ionised. If collisions between the charged particles and the neutral atoms occur frequently, the medium becomes less like a plasma and more like a neutral gas. It is therefore required that electrons are not affected by collisions with neutrals if the medium is to continue to behave as a plasma. In order for this to be the case, the

average time between electron-neutral collisions, τ_n, must be significantly greater than the inverse of the angular plasma frequency, ω_{pe} [*Baumjohann and Treumann*, 1997].

$$\tau_n \gg \frac{1}{\omega_{pe}} \tag{1.19}$$

This is the third criterion for a plasma.

1.2 Single Charged Particle Motion

The forces experienced by a particle with charge, q, moving with velocity, $\mathbf{v}$, through a magnetic field, $\mathbf{B}$, and electric field, $\mathbf{E}$, are the Coulomb force, F_C, and the Lorentz force, F_L. These are defined as:

$$\mathbf{F}_C = q\mathbf{E} \tag{1.20}$$

$$\mathbf{F}_L = q\left(\mathbf{v} \times \mathbf{B}\right) \tag{1.21}$$

The equation of motion for such a particle can therefore be expressed as the addition of Equations 1.20 and 1.21. This is known as the Lorentz equation [*Walt*, 1994].

$$\mathbf{F}_{total} = m\frac{d\mathbf{v}}{dt} = q\left(\mathbf{E} + \mathbf{v} \times \mathbf{B}\right) + \mathbf{F}_{other} \tag{1.22}$$

where $\mathbf{F}_{other}$ is the sum of additional forces that are not electromagnetic in origin (e.g. gravitational forces).

Considering purely an electric field, ($\mathbf{B} = 0$), it is apparent that any acceleration experienced by the particle will be in the direction parallel to the electric field. If purely a magnetic field is considered ($\mathbf{E} = 0$), any acceleration will occur perpendicular to both the magnetic field direction, $\mathbf{B}$, and the velocity of the particle, $\mathbf{v}$.

1.2.1 Gyromotion

Taking the equation of motion for a charged particle and assuming $\mathbf{E} = 0$, the magnetic field, $\mathbf{B}$, is uniform and constant, and there are no additional forces present $\mathbf{F}_{other} = 0$ yields:

$$m\frac{d\mathbf{v}}{dt} = q\left(\mathbf{v} \times \mathbf{B}\right) \tag{1.23}$$

Splitting this into velocity components that are parallel and perpendicular to $\mathbf{B}$ gives:

$$\left(m\frac{d\mathbf{v}}{dt}\right)_{\parallel} = q\left(\mathbf{v}_{\parallel} \times \mathbf{B}\right) = 0 \tag{1.24}$$

$$\left(m\frac{d\mathbf{v}}{dt}\right)_{\perp} = q\left(\mathbf{v}_{\perp} \times \mathbf{B}\right) \tag{1.25}$$

Integrating the parallel component shown in Equation 1.24 yields:

$$m\mathbf{v}_{\parallel} = constant \tag{1.26}$$

This implies that a magnetic field does not accelerate particles in the parallel direction, that is, the particle moves parallel to $\mathbf{B}$ at constant velocity, $\mathbf{v}_{\parallel}$.

Considering Equation 1.25, the velocity change is perpendicular to both the uniform field, $\mathbf{B}$, and $\mathbf{v}_{\perp}$. Through the conservation of momentum, it follows that $|\mathbf{v}_{\perp}|$ is constant. This means that the particle travels in a circular path with radius, r, in the plane perpendicular to the magnetic field [*Walt*, 1994]. Therefore the force exerted on the particle by the Lorentz force, must be balanced by the centripetal force, thus giving:

$$qv_{\perp}B = \frac{mv_{\perp}^2}{r} \tag{1.27}$$

The radius of this circular motion about the magnetic field (gyromotion) is called the gyroradius, or cyclotron radius, r_c and, by rearranging Equation 1.27, may be defined as:

$$r_c = \frac{mv_{\perp}}{|q|B} \tag{1.28}$$

The angular frequency of this motion, the angular gyrofrequency or cyclotron frequency, ω_c, is therefore:

$$\omega_c = \frac{|q|B}{m} \tag{1.29}$$

Note that the direction of a particle's acceleration is dependent on the charge of the particle, q, (see Equation 1.25). Therefore, electrons and ions gyrate in opposite directions about the magnetic field, electrons anticlockwise and ions clockwise.

The centre of this orbit about the magnetic field line is called the *guiding centre*. In addition to circular motion about the magnetic field, a particle may also have a constant velocity parallel to the uniform, constant magnetic field (see Equation 1.26). The sum of these velocity vectors implies that a particle travels with a helical trajectory along and around the magnetic field. The angle between the velocity vector of a particle, $\mathbf{v}$, and the magnetic field vector, $\mathbf{B}$, is called the pitch angle. The pitch angle, α, of a helix is defined as:

$$\alpha = arctan\left(\frac{v_{\perp}}{v_{\parallel}}\right) \tag{1.30}$$

1.2.2 Bounce Motion

In a converging magnetic field, the magnetic field magnitude varies with position. However, a static magnetic field does no work on a particle [*Baumjohann and Treumann*, 1997]. Therefore, the magnetic flux, ϕ_m, enclosed by a circle with radius equal to a particles' gyroradius, r_c, is a constant and is given by:

$$\phi_m = B\pi r_c^2 \tag{1.31}$$

Substituting in the definition of the gyroradius from Equation 1.28 yields:

$$\phi_m = \frac{\pi m^2 v_\perp^2}{Bq^2} \tag{1.32}$$

Since π, q and m are all constants for a single particle, it follows that:

$$\frac{v_\perp^2}{B} = constant \tag{1.33}$$

Expressing this in terms of a particle's pitch angle, as defined in Eqution 1.30, gives:

$$\frac{v^2 sin^2\alpha}{B} = constant \tag{1.34}$$

Therefore, for a particle moving from a region with lower magnetic field strength, B_1, to a region with greater magnetic field strength, B_2, it can be stated that:

$$\frac{sin^2\alpha_1}{B_1} = \frac{sin^2\alpha_2}{B_2} \tag{1.35}$$

As the magnetic field magnitude increases, it is required that $sin\,\alpha$ also increases. However, $sin\,\alpha$ can only increase to unity. At this point, the magnetic field strength would be such that a particle's velocity would be completely in the plane perpendicular to the magnetic field, $v = v_\perp$. This point, where all motion parallel to the magnetic field ceases, is called the mirror point. The converging magnetic field causes the particle's velocity parallel to the magnetic field, $v_\parallel$, to increase in the direction towards the region of the weaker magnetic field (magnetic mirror force). Thus, the particle 'bounces back' from the region of larger magnetic field strength in a process called *magnetic mirroring*.

1.2.3 Drift Motion

1.2.3.1 $\mathbf{E} \times \mathbf{B}$ Drift

If an external electrostatic field is present, this modifies the motion of a particle gyrating around the uniform magnetic field. In order to describe these changes, we first consider the equation of motion for a charged particle in both an electric and magnetic field, as shown in Equation 1.22, with no additional forces present. An electric field parallel to the magnetic field accelerates electrons and ions in opposite directions along the magnetic field. This creates a charge displacement which, in turn, produces an additional electric field that acts to cancel out the original electric field. For this reason, most parallel electric fields can not be sustained.

In this case, we assume the electric field to be perpendicular to the magnetic field, $\mathbf{E} = E_x$ and $\mathbf{B} = B_z$. Thus, the equation of motion for a charged particle becomes:

$$m\frac{d\mathbf{v}}{dt} = q\left(E_x + \mathbf{v} \times B_z\right) \tag{1.36}$$

Taking the time derivatives yields:

x-component

$$\frac{dv_x}{dt} = \frac{qE_x}{m} + \frac{qB_z}{m}v_y = \omega_c\left(v_y + \frac{E_x}{B_z}\right) \tag{1.37}$$

y-component

$$\frac{dv_y}{dt} = -\frac{qB_z}{m}v_x = -\omega_c v_x \tag{1.38}$$

z-component

$$\frac{dv_z}{dt} = 0 \tag{1.39}$$

Taking the second time derivatives gives:

x-component

$$\frac{d^2v_x}{dt^2} = \frac{qB_z}{m}\frac{dv_y}{dt} = -\left(\frac{qB_z}{m}\right)^2 v_x = -\omega_c^2 v_x \tag{1.40}$$

y-component

$$\frac{d^2v_y}{dt^2} = -\frac{qB_z}{m}\frac{dv_x}{dt} = -\frac{qB_z}{m}\left[\omega_c\left(v_y + \frac{E_x}{B_z}\right)\right] = -\omega_c^2\left(\frac{E_x}{B_z} + v_y\right) \tag{1.41}$$

z-component

$$\frac{d^2v_z}{dt^2} = 0 \tag{1.42}$$

The x-component, Equation 1.40, describes a harmonic oscillator with a frequency equal to the gyrofrequency. Using the simple substitution of ${v_y}' = v_y + E_x/B$, the y-component also describes a harmonic oscillator with a frequency equal to the gryofrequency. Therefore, the addition of an electrostatic field has modified the gyromotion of the particle to include an additional component of velocity in the negative y-direction of magnitude E_x/B. This velocity is a drift of the guiding centre called $\mathbf{E} \times \mathbf{B}$ *drift*. In vector form, this drift velocity, $\mathbf{v}_E$, is parametrised as:

$$\mathbf{v}_E = \frac{\mathbf{E} \times \mathbf{B}}{B^2} \tag{1.43}$$

It should be noted that the $\mathbf{E} \times \mathbf{B}$ drift is independent of the sign of the charge of a particle and therefore electrons and ions drift in the same direction.

By substituting in the Coulomb force from Equation 1.20 ($\mathbf{E} = \mathbf{F}/q$), the equation can be generalised to include drifts due to any external force perpendicular to the magnetic field and not simply limited to the Coulomb force.

$$\mathbf{v}_F = \frac{\mathbf{F} \times \mathbf{B}}{qB^2} = \frac{1}{\omega_c}\left(\frac{\mathbf{F} \times \mathbf{B}}{mB}\right) \tag{1.44}$$

1.2.3.2 Gradient Drift

If the magnetic field in which a charged particle travels is weakly inhomogeneous, the particle's motion is further modified. Consider a weak gradient in the magnetic field, ∇B, exists in the y direction perpendicular to the magnetic field vector, $\mathbf{B}$, which is in the z direction ($\mathbf{B} = B_z$). It follows that the magnetic field experienced by a gyrating charged particle will vary in magnitude during a single gyration period. This in turn affects the particle gyroradius (as defined in Equation 1.28). The effect of this is shown in Figure 1.2. At position 1, the magnetic field magnitude is weaker and therefore the gyroradius is larger. Conversely, at position 2, the magnetic field magnitude is stronger and thus the gyroradius is smaller. The impact of this on the motion of a particle is a net displacement of the guiding centre in the direction perpendicular to both the magnetic field vector, $\mathbf{B}$, and the magnetic gradient, ∇B.

This description leads to no net motion in the y direction, and therefore no net force in the y direction. Taking the integral of this force, F_y, over one gyration, and the Lorentz force from Equation 1.21 yields:

$$\int F_y dt = 0 = \int q \frac{dx}{dt} B(y)\, dt \tag{1.45}$$

If it is assumed that the length scale of the gradient in the magnetic field is large in comparison to the particle gyroradius, the magnetic field, $B(y)$, may be approximated by a first order Taylor expansion.

$$B(y) = B_0 + y \frac{\partial B}{\partial y} \tag{1.46}$$

where B_0 is the magnetic field at the start and end points of the particle gyration and $\partial B/\partial y$ is a constant. Substituting Equation 1.46 into Equation 1.45 yields:

$$\int q \frac{dx}{dt} B_0 dt + \int q \frac{dx}{dt} y \frac{\partial B}{\partial y} dt = 0 \tag{1.47}$$

Therefore,

$$\int dx = \frac{1}{B_0} \frac{\partial B}{\partial y} \int y\, dx \tag{1.48}$$

$\int y\, dx$ is the area enclosed by the particles trajectory. If it is assumed that the velocity due to gradient drift is small in comparison to the velocity of gyration, this area may

be approximated as πr_c^2. Therefore, the distance travelled in the x direction during one particle gyration is:

$$\Delta x = \frac{1}{B_0}\frac{\partial B}{\partial y}\pi r_c^2 \tag{1.49}$$

The velocity due to a gradient in the magnetic field is $\Delta x/\Delta t$, where Δt is the time taken for one particle gyration ($2\pi r_c/v_\perp$). Using the definition of the gyroradius from Equation 1.28, the velocity due to *gradient drift* is:

$$\mathbf{v}_\nabla = \frac{\Delta x}{\Delta t} = \frac{m v_\perp^2}{2qB^3}(\mathbf{B} \times \nabla B) \tag{1.50}$$

It should be noted that the gradient drift is charge dependent and therefore electrons and ions drift in opposite directions. This is shown schematically for a proton and an electron in Figure 1.2.

1.2.3.3 Curvature Drift

The drift due to a magnetic field gradient is not the only drift motion to occur in an inhomogeneous magnetic field. If the magnetic field lines are curved, this introduces an additional drift velocity called the *curvature drift*. Consider a charged particle with a velocity component parallel to the magnetic field, $v_\parallel$. If the magnetic field line is curved, the particle experiences a centripetal force, $\mathbf{F}_{curve}$ defined as:

$$\mathbf{F}_{curve} = m v_\parallel^2 \frac{\mathbf{R}_c}{R_c^2} \tag{1.51}$$

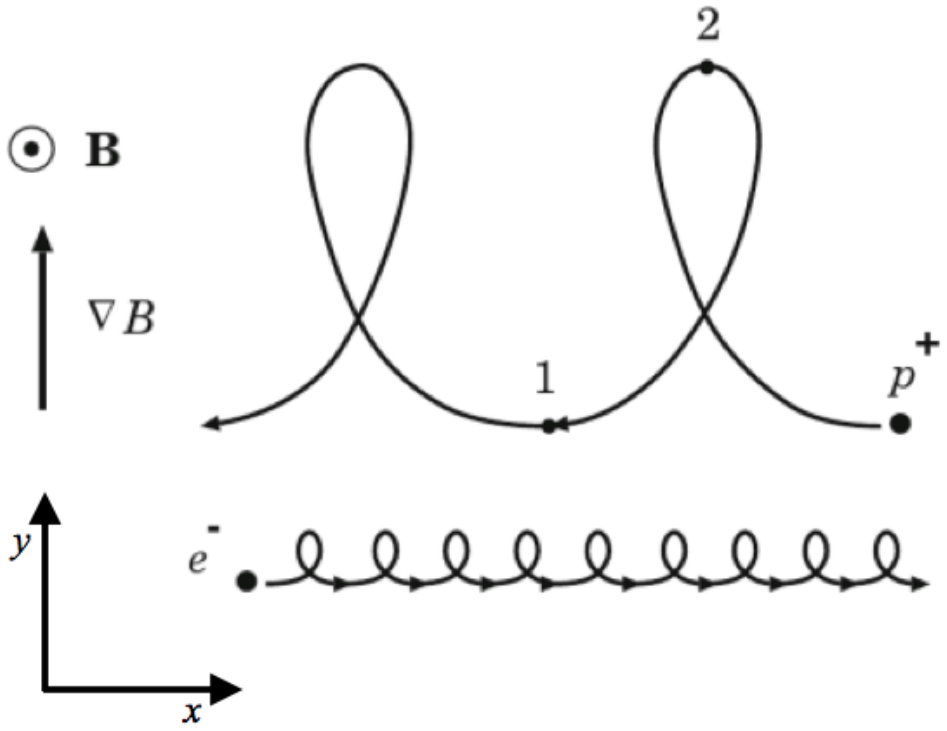

FIGURE 1.2: A schematic representation showing the effect of gradient drift on a proton and an electron in a magnetic field [*Somov*, 2013].

where $\mathbf{R}_c$ is the local radius of curvature.

Substituting this into the equation for general force drift (Equation 1.44), yields:

$$\mathbf{v}_{curve} = \frac{mv_{\parallel}^2}{q} \frac{\mathbf{R}_c \times \mathbf{B}}{R_c^2 B^2} \tag{1.52}$$

Again, it should be noted that curvature drift is charge dependent and therefore electrons and ions drift in opposite directions.

The drift velocity due to a combination of gradient and curvature in the magnetic field is the addition of the gradient drift velocity, v_{∇} and the curvature drift velocity, v_{curve}.

1.2.4 Adiabatic Invariants

For each of the three types of motion introduced in the preceding sections (gyration, bounce, drift), a characteristic constant exists called an *adiabatic invariant*. In comparison to other characteristic constants, such as total energy or momentum, adiabatic invariants are not indefinitely conserved. Each adiabatic invariant may temporally evolve, however the rate of change is generally very slow in comparison to the periodicity of the associated motion. That is, if the magnetic field changes infinitely slowly in comparison to the period of motion, the adiabatic invariant associated with that type of motion remains constant (typical periods for each type of motion are shown for a 1 keV and 1 MeV electron at a radial distance of 6.6 R_E in the geomagnetic field in Table 1.1).

The general definition of an adiabatic invariant is:

$$J = \oint [\mathbf{p} + q\mathbf{A}] \cdot d\mathbf{l} \tag{1.53}$$

where J is the adiabatic invariant, $\mathbf{p}$ is the particle momentum, q is the particle charge, $\mathbf{A}$ is the vector potential of the magnetic field and $d\mathbf{l}$ is the element of particle path associated with the type of motion [*Walt*, 1994].

1.2.4.1 First Adiabatic Invariant

The first adiabatic invariant, μ, is associated with the gyromotion of a particle about a magnetic field line. Applying the general adiabatic invariant integral to a single particle gyration yields:

Approximate Period of Motion (seconds)		
Type of Motion	1 keV	1 MeV
Gyration	$\sim 1 \times 10^{-4} s$	$\sim 1 \times 10^{-4} s$
Bounce	$\sim 10 s$	$\sim 0.1 s$
Drift	$\sim 5 \times 10^{5} s$	$\sim 500 s$

TABLE 1.1: Approximate periods of motion for a 1keV and a 1MeV electron in the geomagnetic field at a radial distance of $6.6 R_E$ (calculated using equations presented in *Knipp* [2011]; *Fitzpatrick* [2014]).

$$J_1 = \oint [\mathbf{p} + q\mathbf{A}] \cdot d\mathbf{l} = 2\pi r_c \, p_\perp + q \oint \mathbf{A} \cdot d\mathbf{l} \tag{1.54}$$

where $\mathbf{p}$ is the particle momentum, q is the particle charge, $\mathbf{A}$ is the vector potential of the magnetic field, $d\mathbf{l}$ is a line element of the particle gyration, $p_\perp$ is the particle momentum perpendicular to the magnetic field and r_c is the particle gyroradius.

Using Stokes' Theorem, $\oint \mathbf{A} \cdot d\mathbf{l} = \oint \nabla \times \mathbf{A} \cdot d\mathbf{S}$, where $d\mathbf{S}$ is an element of area enclosed by the particle path, and substituting in the gyroradius as defined in Equation 1.28 yields:

$$J_1 = \frac{2\pi p_\perp^2}{Bq} + q \oint \nabla \times \mathbf{A} \cdot d\mathbf{S} \tag{1.55}$$

Since the curl of the vector potential is equal to the magnetic field ($\nabla \times \mathbf{A} = \mathbf{B}$), the second term in the equation, integrated over one gyration where the $d\mathbf{S}$ unit vector points in the opposite direction to $\mathbf{B}$, becomes:

$$q \oint \mathbf{B} \cdot d\mathbf{S} = -qB\pi r_c^2 = -\frac{\pi p_\perp^2}{qB} \tag{1.56}$$

Therefore, J_1 becomes:

$$J_1 = \frac{2\pi p_\perp^2}{Bq} - \frac{\pi p_\perp^2}{qB} = \frac{\pi p_\perp^2}{qB} \tag{1.57}$$

The first adiabatic invariant is often discussed in terms of the magnetic moment of a particle, μ, a quantity that determines the torque experienced in an external magnetic field. This is defined as:

$$\mu = \frac{p_\perp^2}{2m_0 B} \tag{1.58}$$

which, except for constant factors, is equivalent to J_1. In this case, $p_\perp$ is the relativistic momentum in the direction perpendicular to the magnetic field, m_0 is the rest mass of the particle and B is the magnitude of the magnetic field [*Walt*, 1994]. The relativistic momentum, p, is defined as:

$$p^2 = \frac{E^2 + 2m_0 c^2 E}{c^2} \tag{1.59}$$

where E is the kinetic energy of the particle and c is the speed of light. Therefore the equation for the first adiabatic invariant, μ, becomes:

$$\mu = \frac{\left(E^2 + 2m_0c^2E\right) sin^2\alpha}{2m_0c^2B} \tag{1.60}$$

The quantity, $v_\perp^2/B$ is shown to be constant for a static magnetic field in Equation 1.33, thus the quantity $p_\perp^2/B$ is also constant. Thus, in a slowly varying magnetic field (changes occur on timescales much slower than the time of a single particle gyration) the first adiabatic invariant, μ, is conserved.

1.2.4.2 Second Adiabatic Invariant

The second adiabatic invariant is related to the bounce motion of a particle along a magnetic field line and is defined as:

$$J_2 = \oint \left[\mathbf{p} + q\mathbf{A}\right] \cdot d\mathbf{s} \tag{1.61}$$

where $d\mathbf{s}$ is an element of length along a magnetic field line. Considering only the second term and using Stokes' Theorem yields:

$$\oint q\mathbf{A} \cdot d\mathbf{s} = q \int \nabla \times \mathbf{A} \cdot d\mathbf{S} = q \int \mathbf{B} \cdot d\mathbf{S} \tag{1.62}$$

where $\mathbf{S}$ is the surface enclosed by the bounce motion along a magnetic field line. Since this integration path encloses a negligible area and no magnetic flux, $q \int \mathbf{B} \cdot d\mathbf{S} = 0$. Therefore the second adiabatic invariant becomes:

$$J_2 = \oint \mathbf{p} \cdot d\mathbf{s} = \oint p_{\|} \cdot ds = \oint p \; cos\,\alpha \cdot ds \tag{1.63}$$

where α is the pitch angle of the particle. At a position s on a magnetic field line, using Equation 1.35 and setting B_2 to be the particle mirror point, and therefore $sin^2\alpha_2 = 1$, gives:

$$cos\,\alpha = \left[1 - \frac{B\,(s)}{B_m}\right]^{1/2} \tag{1.64}$$

Therefore the second invariant becomes:

$$J_2 = \oint p \left[1 - \frac{B\,(s)}{B_m}\right]^{1/2} ds \tag{1.65}$$

The second invariant is usually discussed solely in terms of magnetic field geometry. In order to do this, it is required to remove the momentum term from the equation [*Walt*, 1994]. This yields related quantity, I, which is defined as:

$$I = \frac{J_2}{2p} = \frac{1}{2} \oint \left[1 - \frac{B\,(s)}{B_m}\right]^{1/2} ds = \int_{s_m}^{s'_m} \left[1 - \frac{B\,(s)}{B_m}\right]^{1/2} ds \tag{1.66}$$

Where s_m and s'_m are the locations of the particle mirror points on a magnetic field line. During the research presented here, the second adiabatic invariant is discussed in terms of K, which is defined as:

$$K = I\sqrt{B_m} = \int_{s_m}^{s'_m} \left[B_m - B\left(s\right)\right]^{1/2} ds \tag{1.67}$$

This invariant implies that particles will move in such a way that the total length of the particle bounce path is conserved. This invariant has implications on the drift shell of a particle, that is, the surface mapped out by the bounce and drift motion of a particle. In an undistorted dipole magnetic field the drift path of a particle mapped to the equatorial plane would be circular since the magnetic field is cylindrically symmetric. In the case of a distorted magnetic field (such as that of the Earth) the magnetic field geometry varies along the drift orbit and hence the drift path is not circular when mapped to the equatorial plane. Figure 1.3 shows this effect in the case of the geomagnetic field. Consider a particle on field line 1 bouncing between mirror points, B_m. As the particle drifts due to the curvature and gradient of the magnetic field, it will also bounce between the mirror points. During the azimuthal drift, due to the distortion of the magnetic field, the particle will encounter magnetic field lines of varying geometry. Additionally, at any given longitude, there is only one magnetic field line that a particle can exist on that will allow for the second adiabatic invariant, K, to be conserved. As such, for K to be conserved in a distorted magnetic field, a particle that was initially on magnetic field line 1, may move to magnetic field line 2 at a different azimuthal position in its drift orbit. If the second adiabatic invariant remains conserved, the particle will return to the initial position on magnetic field line 1 once it has completed a full drift orbit about the magnetic axis. Particles on the same field line but with a different initial pitch angle (and therefore a different value of K) will return to the same position after a complete drift orbit, however the shell that their drift motion maps out will be different. This

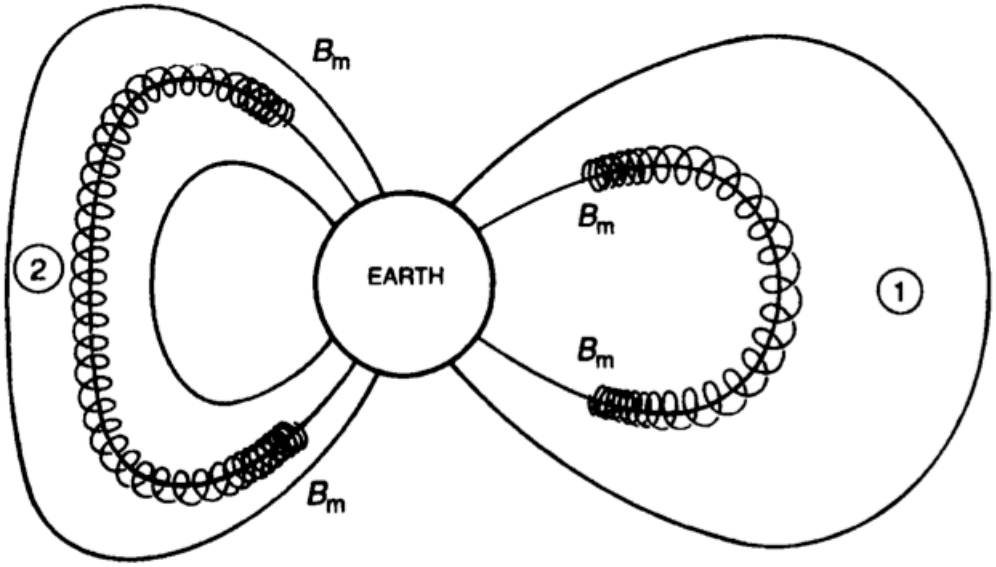

FIGURE 1.3: Schematic representation of a particle drifting in the (distorted) geomagnetic field. If the magnetic field is static (or the variations are slow in comparison to the characteristic timescales of each type of particle motion), the particle will reflect at the same B_m and as the particle drifts, for each longitude the particle will bounce on the field line on which its motion between the mirror points conserves the second adiabatic invariant. From *Walt* [1994].

effect is called *drift shell splitting*.

1.2.4.3 Third Adiabatic Invariant

The third adiabatic invariant relates to the longitudinal drift motion of a particle and is defined as:

$$J_3 = \oint [\mathbf{p} + q\mathbf{A}] \cdot d\mathbf{l} \tag{1.68}$$

where $d\mathbf{l}$ is an element of the particle drift path. In the geomagnetic field, the drift velocity of a particle is usually orders of magnitude smaller than the total particle velocity and thus the momentum in the direction of $d\mathbf{l}$ is negligible ($\oint \mathbf{p} \cdot d\mathbf{l} = 0$). Using Stokes'

Theorem where $d\mathbf{S}$ is the surface element enclosed by the particle drift path, the third invariant becomes:

$$J_3 = q \oint [\nabla \times \mathbf{A}] \cdot d\mathbf{S} \tag{1.69}$$

Since the curl of the vector potential is equal to the magnetic field ($\nabla \times \mathbf{A} = \mathbf{B}$), the third invariant can be defined as:

$$J_3 = q \oint \mathbf{B} \cdot d\mathbf{S} \tag{1.70}$$

The third adiabatic invariant is usually denoted as the magnetic flux enclosed by the drift shell, ϕ, and thus the charge term is usually neglected [*Walt*, 1994]. This yields:

$$\phi = \oint \mathbf{B} \cdot d\mathbf{S} \tag{1.71}$$

The conservation of this invariant implies that drifting particles always enclose the same amount of magnetic flux in their orbit. For a dipole field, this would require the drift orbit to be circular. The L^* parameter is a convenient way of describing the third invariant in the case of particles drifting around the Earth. L^* is defined as the radial distance to a location in the equatorial plane where a charged particle would reside if all external forces were removed leaving only the internal magnetic field.

$$L^* = \frac{2\pi M}{\phi R_E} \tag{1.72}$$

where M is the magnetic moment of the Earth's magnetic field.

1.2.5 Frozen-in Theorem

In 1942, Hannes Alfvén identified the analogy between the dynamics of magnetic fields in infinitely conducting plasmas and vorticity in the theory of non-viscous fluids [*Alfvén*, 1942]. It has been established that a magnetic field can govern the motion of charged particles, however, the charged particles and the magnetic field form a closely coupled system. The Lorentz force, as defined in Equation 1.21, results in gyromotion of charged particles around magnetic field lines. For an infinitely conducting, collisionless plasma, the magnetic field encircled by a closed loop (gyrating particles) remains unchanged even if each point on the closed loop moves with a different local velocity [*Baumjohann and Treumann*, 1997]. Therefore, the field lines are effectively frozen to the plasma. Hannes Alfvén used the term *frozen in magnetic flux* to describe this concept [*Alfvén*, 1942]. The frozen-in condition states that the magnetic flux through a surface that moves with the plasma be conserved. That is, any plasma element that is initially positioned on a magnetic field line, must remain there. This is shown in Figure 1.4. The plasma elements that initially reside on a magnetic field line at time t_0 (left), remain positioned on the same field line at later time, t_1 (right). The magnetic flux passing through a surface, or in this case a one-dimensional line element, remains constant. Motion parallel to the magnetic field is unchanged.

In order to distinguish between conditions where the plasma particles drag the magnetic field with them in their motion, and conditions where the magnetic field determines the

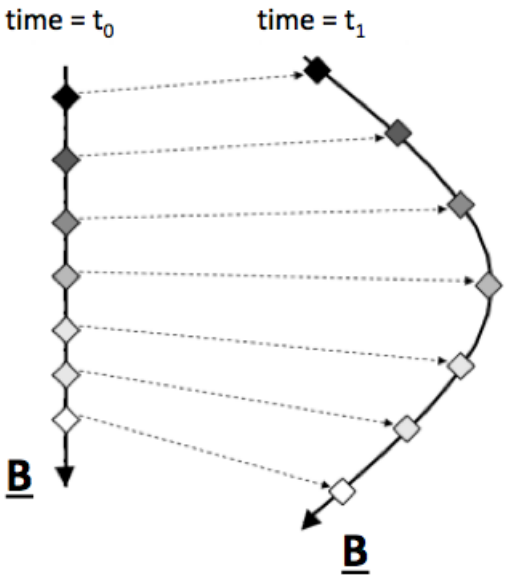

FIGURE 1.4: A schematic showing how plasma elements initially positioned on a magnetic field line at time t_0, remain situated on that field line at a later time, t_1. That is, for the one-dimensional line element shown, the magnetic flux passing through, remains constant. Adapted from *Haigh et al.* [2006].

plasmas motion, the *plasma beta*, β, may be considered [*Knipp*, 2011]. The plasma beta is defined as:

$$\beta = \frac{nk_BT}{(B^2/2\mu_0)} \tag{1.73}$$

where n is the plasma number density (assuming $n_e = n_i = n$), k_B is the Boltzmann constant, T is the plasma temperature, B is the magnetic field magnitude and μ_0 is the permeability of free space. The plasma beta is the ratio between the thermal energy density of the plasma and the magnetic field energy density. If the magnetic field energy density is much greater than the thermal energy density of the plasma ($\beta \ll 1$), the magnetic field determines the plasma motion. If the thermal energy density of the

plasma is much greater than the magnetic field energy density ($\beta \gg 1$), the plasma carries the magnetic field with it in its motion.

In order to determine if the frozen-in condition is applicable, the *magnetic Reynolds Number* may be considered. The magnetic Reynolds Number, R_M, consists of two terms, a term describing the diffusion of magnetic field through the plasma and a term describing the convective motion of the magnetic field with the plasma [*Knipp*, 2011]. This is defined as:

$$R_M = \frac{convection\ term}{diffusion\ term} = \frac{v\,B\,/\,L}{B\,/\,L^2\,\mu_0\,\sigma} = \mu_0\,\sigma\,v\,L \tag{1.74}$$

where μ_0 is the permeability of free space, σ is the electrical conductivity of the plasma, v is the velocity vector of the plasma and L is the characteristic length over which magnetic field variations occur. When the term describing the convective motion of the magnetic field with the plasma is dominant, $R_M \gg 1$, the magnetic field will be frozen-in to the plasma. However, when the term describing the diffusion of the magnetic field through the plasma dominates, $R_M \ll 1$, the motion of the fluid does not significantly affect the magnetic field and the frozen-in condition is not applicable [*Baumjohann and Treumann*, 1997].

1.3 The Sun-Earth System

1.3.1 Solar Wind

The Sun ejects plasma into interplanetary space at supersonic speeds [*Baumjohann and Treumann*, 1997]. Due to the high conductivity of the plasma, the solar magnetic field is 'frozen in' and carried outwards by the flow. This outwards flow of plasma from the Sun is called the *solar wind* and primarily consists of protons and electrons. The magnetic field transported outwards with the plasma is called the interplanetary magnetic field (IMF). The solar wind is ejected from the Sun in an approximately radial direction, however the Sun is rotating with a period of around 25 days at the equator ($\sim$ 27 days when observed from Earth) [*Schrijver and Zwaan*, 2000]. This results in the solar wind producing a spiral shape as it travels away from the Sun and into interplanetary space, an idea first proposed by Eugene Parker in 1958 [*Parker*, 1958]. As such, this spiral may often be referred to as the *Parker spiral*, as shown in Figure 1.5. The formation of the Parker spiral may be visualised by considering the Sun emitting packets of plasma and magnetic field from the surface as shown in Figure 1.5. At a single position on the solar surface at time, t_1, the Sun emits a packet of solar wind, #1. At a later time, t_2, the same position on the solar surface emits a second packet of solar wind, #2. Since the Sun has rotated between time, t_1, and time, t_2, packet #2 does not follow the same path as packet #1. Over several time intervals, t_3, t_4, t_5..., with the Sun emitting packets of solar wind, #3, #4, #5... the result is a spiral of plasma and magnetic field emanating from the Sun. Table 1.2 shows typical solar wind parameters observed at a distance of 1 AU.

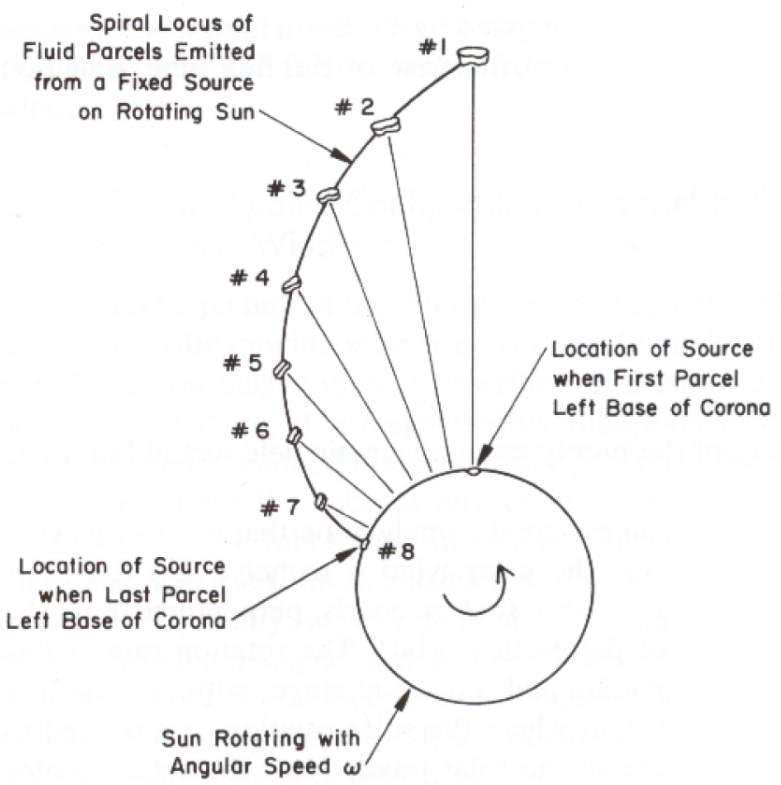

FIGURE 1.5: A schematic representation of how solar rotation causes the solar wind to form the Parker spiral. From *Kivelson and Russell* [1995].

The speed at which material is ejected from the Sun is not uniform, with some regions emitting faster solar wind than others, thus faster solar wind may 'catch up' with slower solar wind. If this occurs, the result is a stream interface with a compression of magnetic field lines and an elevated density. An example of where this may occur is on the leading edge of the fast solar wind that originates from coronal holes on the solar surface. These coronal holes are regions of open magnetic field lines that extend outwards into space allowing for high-speed solar wind to escape. Consider a coronal hole emitting fast solar wind (surrounded by regions producing slower solar wind) rotating on the solar surface as shown in Figure 1.6. The resulting structure is called a *corotating interaction region (CIR)* or *high-speed stream (HSS)* and has a characteristic structure when observed passing a fixed position (e.g. *Tsurutani et al.* [2006]). They typically exhibit; 1) a clear

Typical Solar Wind Parameters at 1 AU	
Flow Speed (v_{sw})	350 km s^{-1}
Proton Density (N_{sw})	5 cm^{-3}
Flow Pressure	1 nPa
Magnetic Field ($\|B\|$)	5 nT
Proton Temperature (T_p)	5×10^4 K
Electron Temperature (T_e)	1×10^5 K

TABLE 1.2: Typical solar wind values observed at a distance of 1 AU. From *Baumjohann and Treumann* [1997] and OMNIweb [*King and Papitashvili*, 2005].

increase in solar wind velocity, 2) a density pulse straddling the boundary between slow and fast solar wind and 3) shear flow as the two regimes of different velocities interact. Coronal holes can be relatively stable and therefore be observed over several periods of solar rotation. Thus, their associated CIR may also be periodically observable.

1.3.2 Magnetosphere

Due to its fluid outer core the Earth produces a magnetic field that, in the absence of the solar wind, can be considered analogous to a tilted dipole field as shown in Figure 1.7 (left). However, this magnetic field is distorted by the interaction with plasma and magnetic field flowing outwards from the Sun. As solar wind plasma impacts the Earth's geomagnetic field, it slows from supersonic to subsonic speeds. Thus, part of the kinetic energy of the solar particles is converted to thermal energy and a *bow shock* is formed. This interaction compresses the geomagnetic field on the dayside and elongates

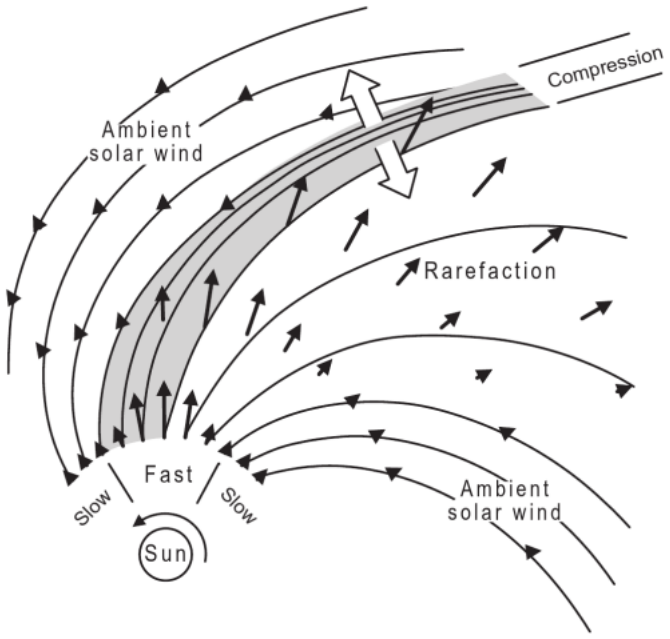

FIGURE 1.6: A schematic diagram showing the structure of a high-speed solar wind stream in the ecliptic plane. From *Pizzo* [1978].

the magnetic field on the nightside as shown in Figure 1.7 (right). The interaction of the geomagnetic field with the IMF is a driver for variability of the different plasma populations within the magnetosphere (as discussed in the following sections). Figure 1.8 is a schematic representation of the magnetosphere, highlighting the regions where these different plasma regimes exist. Since the magnetic axis of the Earth is tilted by $\sim 11^{\circ}$, it is common to use Geocentric Solar Magnetospheric (GSM) coordinates when discussing the magnetosphere. GSM coordinates are a right-handed cartesian coordinate system defined by selecting the x-axis to point towards the Sun along the Sun-Earth line, the z-axis to be perpendicular to the x-axis and parallel to the projection of the magnetic axis in a plane perpendicular to the x-axis (pointing northwards), the y-axis completing the right-handed coordinate system (pointing eastwards or towards dusk). Unless otherwise stated, this coordinate system is used hereafter. The magnetosphere is defined as the

region surrounding the Earth where the geomagnetic field is dominant. The size and shape of the magnetosphere is variable, depending on the solar wind conditions. The boundary between the region where the IMF is dominant and the geomagnetic field is dominant is called the *magnetopause*.

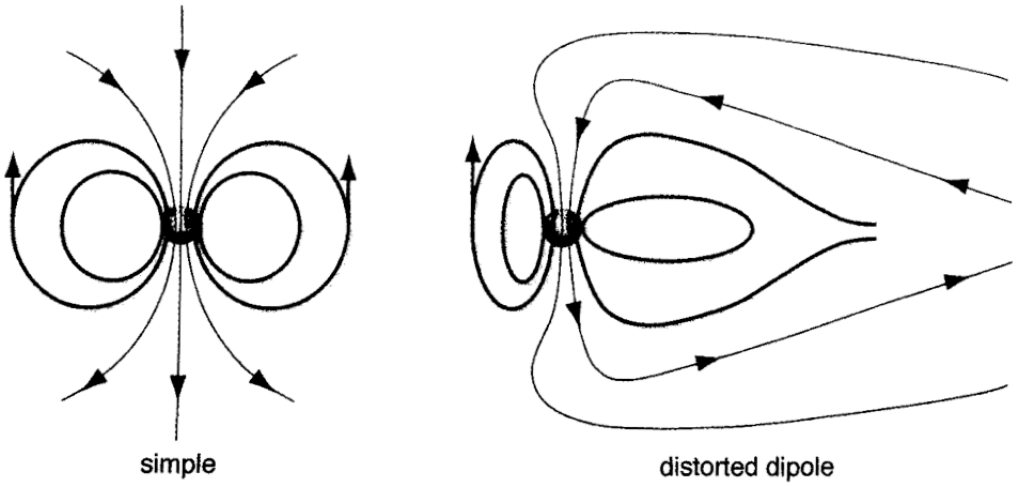

FIGURE 1.7: The magnetic field configuration in GSM coordinates when (left) isolated from the solar wind, analogous to a simple dipole, and (right) distorted by the solar wind. From *Knipp* [2011].

1.3.2.1 Magnetic Reconnection and Convection

A consequence of the frozen-in theorem is that plasma frozen to magnetic field lines that are connected to the Sun remains frozen to those field lines. Conversely, plasma frozen to the magnetic field lines of the geomagnetic field remains frozen to those field lines. If the frozen-in condition is applicable then the two plasma regimes do not mix. However, in the magnetopause transition region, the characteristic length over which magnetic field variations occur, L, is small and therefore the term describing the diffusion of the magnetic field through the plasma is dominant over the term describing the convection

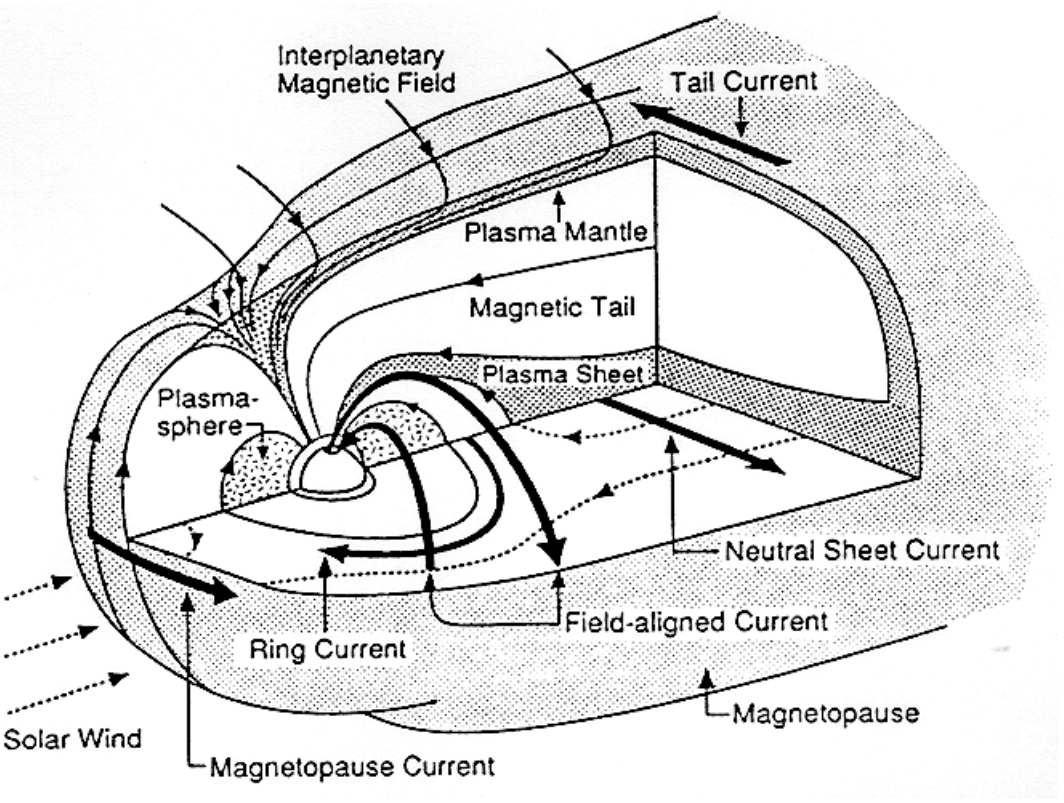

FIGURE 1.8: A schematic representation of the magnetosphere showing the location of different plasma regimes. From *Kivelson and Russell* [1995].

of the magnetic field with the plasma (see Equation 1.74). Thus the frozen-in condition is not applicable.

Consider the magnetic field configuration at the magnetopause boundary with the IMF and geomagnetic field being antiparallel (Southward IMF B_z). The antiparallel magnetic field lines are convected into the region where the frozen-in condition breaks down and diffusion dominates (magnetic field decouples from the plasma). The field lines can then *'reconnect'* with field lines from the opposite side of the boundary before freezing back into the plasma in the reconnection outflow [*Birn and Priest*, 2007]. A simplified, two-dimensional diagram of this process is shown in Figure 1.9. For $t < 0$ (left) the two, antiparallel magnetic fields are convected towards each other. For $t = 0$ (middle), the

frozen-in condition breaks down and at a point where two antiparallel magnetic field lines intersect, the net magnetic field is zero. Such a location is called a magnetic neutral point or X-point. For $t > 0$ (right), the magnetic field lines have reconnected at the X-point, before exiting the diffusion region (as indicated by upwards or downwards motion) and freezing back into the plasma. In the three-dimensional case, the X-point translates to an X-line in the direction in/out of the two dimensional diagram.

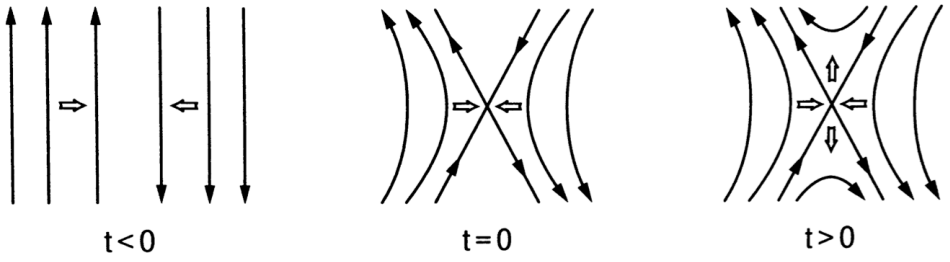

FIGURE 1.9: A diagram showing the evolution of reconnecting antiparallel magnetic field lines. From *Baumjohann and Treumann* [1997].

Reconnection may occur on the dayside magnetosphere, thus allowing for the previously separated plasma regimes of the solar wind and the magnetosphere to interact. The geometry of reconnection between southwards oriented IMF and the geomagnetic field is shown in Figure 1.10, a process first envisaged by James Dungey in 1961 [*Dungey*, 1961]. Firstly, the southward oriented IMF and geomagnetic field are separated by the magnetopause boundary. They are able to reconnect on the X-line of the dayside magnetosphere and are dragged over the polar caps by the solar wind. On the nightside, in the stretched tail of the magnetosphere, antiparallel magnetic field lines are again in close proximity. In the same physical process as on the dayside magnetosphere, the magnetic field lines reconnect at the nightside X-line. The reconnected magnetic field lines then exit the diffusion region with the reconnected geomagnetic magnetic field lines travelling Earthwards, around the flanks, and returning to the dayside magentosphere where the

process may be repeated. The arrows shown on Figure 1.10 indicate the direction of convection. This convection process from the dayside magnetosphere, across the polar caps to the magnetotail and back around the flanks to the dayside may sometimes be referred to as the *Dungey cycle*.

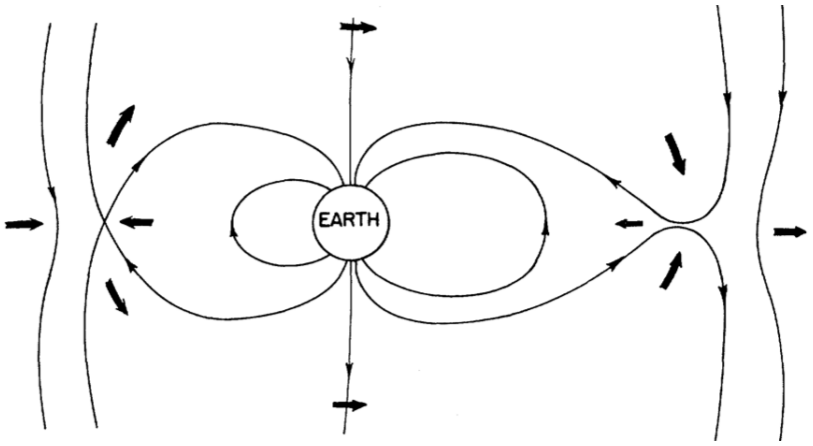

FIGURE 1.10: A schematic diagram of the reconnection process in the magnetosphere. From *Dungey* [1961].

The convection of the magnetic field and plasma produces a convection electric field in the rest frame through the Lorentz transformation ($\mathbf{E} = -\mathbf{v}\times\mathbf{B}$). In the equatorial plane, the convection electric field is directed from dawn-to-dusk (since the geomagnetic field is directed northwards and the velocity is directed sunwards as the magnetic field lines reconnect in the magnetotail and convect back around to the dayside magnetosphere). This dawn-to-dusk electric field may be considered homogeneous to the first approximation and therefore the convection electric potential may be defined as, $\mathbf{E}_c = -\nabla\phi_c$, where $\mathbf{E}_c$ is the convection electric field, and ϕ_c is the associated electric potential. However, the convection field is not the only electric field present in the magnetosphere. As the Earth rotates on its axis, the magnetic field lines corotate with it, thus producing a corotational electric field. The corotating electric field can also be described by the

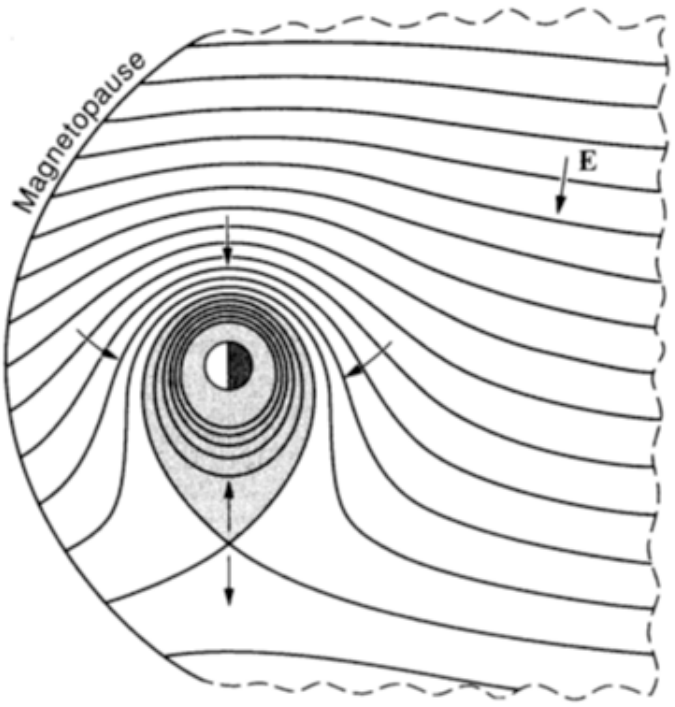

FIGURE 1.11: A schematic diagram of the electric field equipotential contours in the equatorial plane. From *Baumjohann and Treumann* [1997].

Lorentz transformation by using the angular velocity of the Earth's rotation. The result is that the potential of the electric field decreases with increasing radial distance. The total electric field is the superposition of both the convection and corotational electric fields as shown in Figure 1.11. Close to the Earth's surface the electric potential is dominated by the corotating electric field, whereas at larger distances the electric potential is dominated by the convection electric field.

1.3.2.2 Geomagnetic Storms

In contrast to the steady state convection described in Section 1.3.2.1, there are periods when the reconnection process may become enhanced due to structures in the solar wind (e.g. HSSs). The enhanced convection may be driven by a strong southward component

of the IMF and an elevated solar wind velocity which increases the number of magnetic field lines available for reconnection on the dayside magnetosphere. These conditions allow for the solar wind to transfer a greater level of energy into the magnetosphere than occurs during steady magnetospheric convection. Such events are called *geomagnetic storms*. Figure 1.12 is a schematic representation of how a geomagnetic storm might appear in the horizontal component of the magnetic field measured near the equator at the Earth's surface. Geomagnetic storms have three distinct phases that are observable in this measured disturbance. During the initial phase, the magnetic disturbance is positive. This is usually caused by a compression of the magnetosphere by the solar wind, thus increasing the magnetic field strength. This is followed by the main phase of the storm where the ring current (as described in Section 1.3.2.5) becomes enhanced and produces a magnetic field that opposes the direction of the Earth's magnetic field. Finally, the storm enters the recovery phase where the depression in the geomagnetic field subsides.

The depression signature in the geomagnetic field may be location dependent, thus an index is calculated in order to quantify the globally averaged disturbance field near the equator. This calculated index is called the *Dst index*. The Dst index is calculated from the horizontal component, H, of the geomagnetic field recorded at four low-latitude observatories located between 20° and 30° away from the magnetic equator [*Sugiura*, 1964]. The quiet time variation is subtracted from the data before taking the average across each of the four stations, applying a correction factor for the latitude variation. The Dst index is frequently used as a proxy for the ring current intensity (see Section 1.3.2.5), as well as for parametrising the strength of geomagnetic storms.

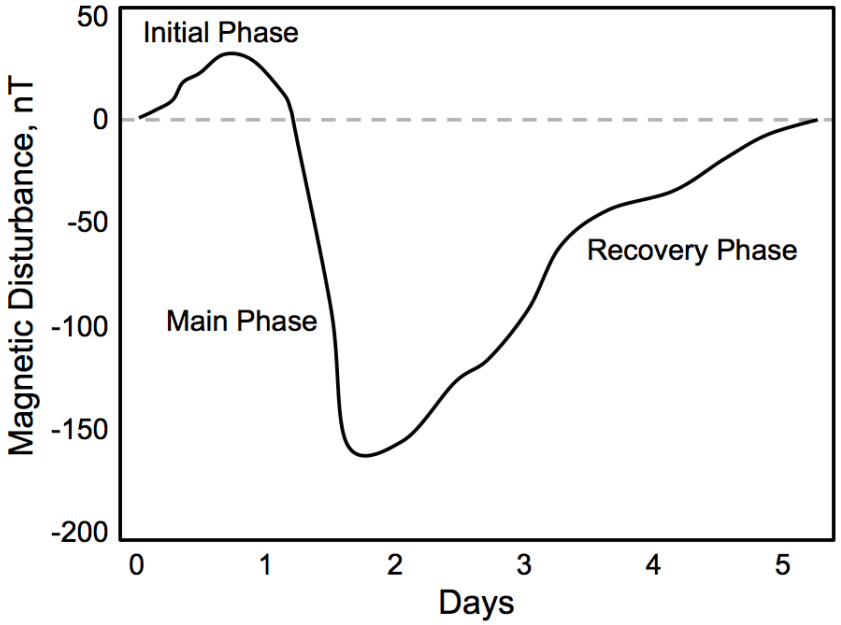

FIGURE 1.12: Schematic representation of how a geomagnetic storm might appear in the measured magnetic field at the Earth's surface with the initial phase, main phase, and recovery phase highlighted.

1.3.2.3 Substorms

In Section 1.3.2.1, magnetospheric convection is treated as a steady process (dayside and nightside reconnection in equilibrium). However if the rate of dayside reconnection is greater than that occurring in the magnetotail, the process changes. A greater number of geomagnetic field lines reconnect with the IMF, are dragged over the poles and into the magnetotail region. This causes thinning of the plasma sheet (see Section 1.3.2.6) and stretching of the magnetic field lines in the tail [*Baumjohann and Treumann*, 1997]. This period of enhanced convection and loading of the magnetotail with magnetic field lines is called the substorm growth phase. In order to reduce the magnetic tension in the magnetotail, the magnetic field lines may reconnect closer to the Earth and trigger the start of the substorm expansion phase. This allows material on the newly reconnected magnetic field lines to convect earthwards, as well as sending a plasma bubble, called

a plasmoid, downstream in the solar wind. This process may also cause particles with small pitch angels to be accelerated along the magnetic field lines and deposit their energy into the upper atmosphere, causing the aurora. The process of the stretched magnetotail reconnecting closer to the Earth may also be called a dipolarisation event. The magnetosphere may then return to a more quiet state in the substorm recovery phase.

1.3.2.4 Radiation Belts

The radiation belts are regions containing highly energetic particles that encompass the Earth. They were first discovered when the Geiger counter onboard the Explorer I spacecraft became unexpectedly saturated. The Geiger tube was sensitive to electrons with energies above 3 MeV and protons with energies above 30 MeV. Subsequent spacecraft missions mapped out the region where these highly energetic particles are confined within the magnetosphere, discovering two toroidal shaped regions with a slot region between them (as shown in Figure 1.13). The innermost of these regions, the inner radiation belt, is dominated by highly energetic protons that are produced by the interaction of cosmic rays with the upper atmosphere. While the inner radiation belt also contains an approximately equal number of protons and electrons, the protons posses the majority of the energy. The inner radiation belt is relatively stable with proton lifetimes of days to years, and typically extends from ~ 1.2 out to ~ 3 Earth radii (R_E) in the equatorial plane. Proton energies in the inner belt range between 1 MeV and 500 MeV.

Beyond the inner radiation belt lies the slot region where the particle density is comparatively low. The slot region is left almost devoid of particle density due to the efficient

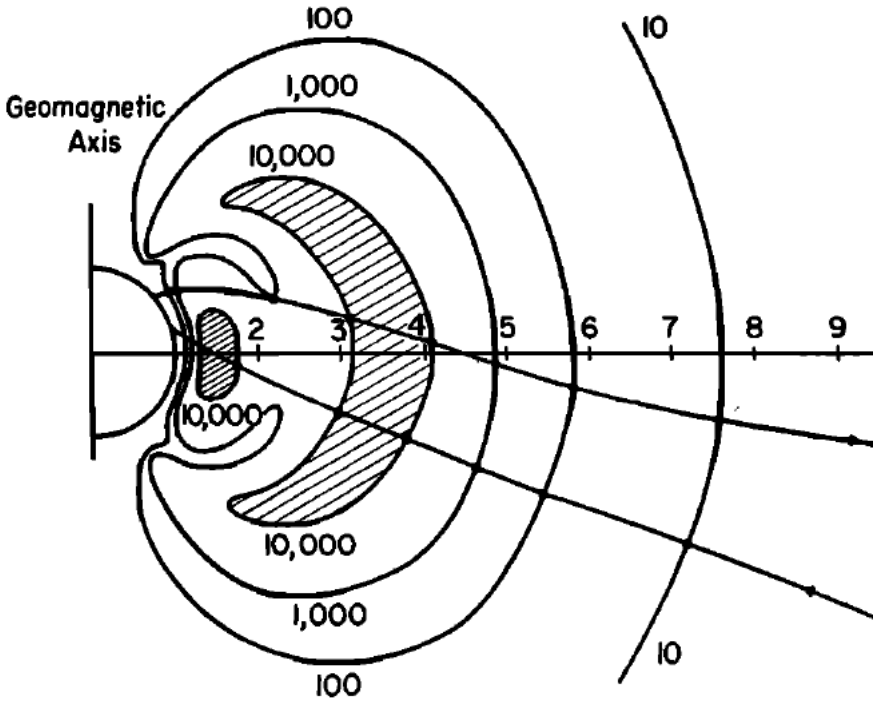

FIGURE 1.13: The intensity structure of the radiation belts from true count rates measured by Geiger tubes carried by Explorer IV and Pioneer III. Also shown are the outbound and inbound trajectories of Pioneer III. Both the inner and outer radiation belts are visible. From *Van Allen* [1959].

process of losses via interactions with very low frequency (VLF) waves. Interactions with VLF waves can scatter the pitch angle of particles and thus enhance losses to the atmosphere. If the pitch angle of a particle is such that it is lost to the atmosphere, the particle is said to be in the *bounce loss cone*. Wave-particle interactions are discussed further in Section 1.4.4.

Beyond the slot region lies the outer radiation belt. Whilst containing approximately equal numbers of protons and electrons, the electrons are dominant in terms of energy. In comparison to the inner radiation belt, the outer radiation belt is highly dynamic in space and time. Since the geomagnetic field is weaker in the outer belt region compared to the inner belt region, the outer belt is more susceptible to the variations of the solar

wind. The outer belt extends from $\sim 3R_E$ out to $\sim 10R_E$ with electron energies ranging between 1 keV and 10 MeV, although are typically of the order of 0.1 MeV [*Knipp*, 2011]. The high degree of variability of the outer belt is an area of active research. Many different source and loss processes have been identified (and are discussed in Section 1.4), however the importance of each mechanism and the variability in processes under different conditions means that a complete predictive capability is difficult to achieve. Due to the high number of satellites that operate in the radiation belt region, and the fact that enhancements of the radiation belt pose a significant risk to orbital hardware, radiation belt dynamics are currently of high interest to the scientific community.

1.3.2.5 Ring Current

As discussed in Section 1.2.3, both curvature and gradient drift are charge dependant [*Baumjohann and Treumann*, 1997]. The result is that electrons and ions drift azimuthally in opposite directions around the Earth. In the magnetosphere this results in a westwards longitudinal drift current called the *ring current* (as shown in Figure 1.8). The ring current exists between a radial distance of 2 and 9 R_E [*Lui et al.*, 1992]. Particle sources for the ring current are the plasma sheet (as described in Section 1.3.2.6) and the ionosphere (as described in Section 1.3.2.8) [*Daglis et al.*, 1999]. When reconnection occurs in the magnetotail, material from the plasma sheet is convected inwards to the inner magnetosphere. As the plasma is convected inwards, the magnetic field strength increases causing the particles to be adiabatically heated. This process allows for the 1-10 keV plasma sheet particles to be heated, and therefore be a source population of

the 10-100 keV ring current particles [*Baumjohann and Treumann*, 1997]. During periods when the number of particles injected from the magnetotail into the ring current is enhanced, the ring current may become intensified (as is the case during geomagnetic storms). This results in a greater induced magnetic field acting to oppose the geomagnetic field, with the net decrease in magnetic field strength measurable near the equator on the Earth's surface. An additional source of ring current particles is via ionospheric upwelling. Particles in the ionosphere may be heated through a variety of processes (i.e. particle precipitation, wave interactions). If ionospheric particles are heated such that their energy exceeds the gravitational binding energy, they are permitted to flow up the magnetic field lines and out into the inner magnetosphere where they may undergo longitudinal drift motion and thus contribute to the ring current.

1.3.2.6 Plasma Sheet

On the nightside of the magnetosphere, in the magnetotail, exists a region of plasma with a thickness of several Earth radii called the *plasma sheet* (see Figure 1.8). The plasma sheet contains both electrons and ions with energies of the order of a few keV. Plasma sheet material originates from both the solar wind (via reconnection in the magnetotail) and the ionosphere (via ionospheric upwelling). Reconnection between the geomagnetic field and the IMF in the magnetotail is the primary dictator of the behaviour of plasma sheet particles [*Knipp*, 2011]. With the plasma sheet connecting the inner and outer magnetosphere, it provides an important means for the redistribution of energy. When reconnection occurs in the magnetotail, plasma sheet particles may convect inwards to the inner magnetosphere. As the plasma is convected earthwards, the particles are

heated adiabatically by the increasing magnitude of the geomagnetic field, thus allowing for the plasma sheet to be considered a source of the ring current particles (as discussed in Section 1.3.2.5). Additionally, the plasma sheet has also been considered to be a seed population for the radiation belt with convection into the inner magnetosphere occurring following substorm activity, followed by in-situ acceleration to radiation belt energies via wave-particle interactions [*Baker et al.*, 1998; *Boyd et al.*, 2014]. The plasma sheet also plays an important role in the aurora. Disturbances in the plasma sheet that occur during substorms cause accelerated particles with small pitch angles to travel along the magnetic field lines and collide with the upper atmosphere [*Knipp*, 2011]. These penetrating particles collide with the atoms in the neutral atmosphere at latitudes around 70°, causing their electrons to become excited. As the excited electrons return to their ground state they emit light in the visible wavelength range which may be observed on the ground as the aurora.

1.3.2.7 Plasmasphere

As indicated in Figure 1.11, there is a region close to the Earth where the equipotential contours are closed (indicated by grey shading [*Baumjohann and Treumann*, 1997]). That is, the magnetic field and plasma are corotating with the Earth. This region, known as the *plasmasphere*, is characterised by a plasma density that is relatively high. The plasmasphere is the upwards extension of the ionosphere (see Section 1.3.2.8) and, in comparison with other magnetospheric plasmas, is considered 'cold' with energies of the order of 1 eV [*Mozer*, 1973]. Outside this region, the electric potential is dominated by the convection electric field and the equipotential contours are open. This means that the

plasma is not in corotation, but is instead convected sunwards and will, at some point, encounter the dayside magnetopause boundary and be lost from the system. Therefore in this region, the plasma density is comparatively low. The boundary region, where a steep transition can be observed from high density to low density with increasing radial distance, is called the *plasmapause*. During active periods (such as geomagnetic storms) the plasmasphere may shed some of its mass to the magnetosphere and ultimately to the dayside magnetopause boundary in long lived structures known as *drainage plumes*. If magnetospheric convection becomes enhanced, the superposition of the corotational and convection electric field changes. That is, the region of closed equipotential contours becomes smaller and some plasmaspheric material is eroded away and convected sunwards towards the magnetopause [*Knipp*, 2011]. As enhanced magnetospheric convection resides, the region of closed equipotential contours grows and the plasmasphere can refill with material from the ionosphere.

1.3.2.8 Ionosphere

Close to the Earth's surface lies the ionosphere, the transition region between fully ionised magnetospheric plasma, and the neutral atmosphere. The density of the ionosphere is dependent on altitude, latitude and time of day. The energy required for ionisation may come from either, incident solar ultraviolet radiation (photoionisation) or particle precipitation from the magnetosphere. For photoionisation to occur, incident solar photons are required to exceed the ionisation energy, which corresponds to the ultraviolet range of the spectrum. Given the variation of incident solar radiation, the photoionisation process is strongly dependent on latitude, local time, and season. Ionisation through

collisions with precipitating particles is also dependent upon local time and latitude. On the dayside at low latitudes, the dominant process is photoionisation. At higher latitudes, collisions between the neutral atmosphere and precipitating particles will be the dominant source of ionospheric plasma. These precipitating particles may also cause the electrons of neutral atmospheric atoms to become excited. When the excited electrons return to their ground state, they emit light in the visible wavelength range which can be seen on the Earth's surface as green (557.7 nm) and red (630.0 nm) aurora [*Baumjohann and Treumann*, 1997]. As mentioned in Sections 1.3.2.5 and 1.3.2.6, ionospheric plasma is a source of ring current particles, as well as for the plasma sheet, through a process known as ionospheric upwelling. If ionospheric plasma is heated such that particles posses energy in excess of the gravitational binding energy, it may flow up the magnetic field lines and out into the magnetosphere thus becoming a source of other magnetospheric plasma populations.

1.4 Outer Electron Radiation Belt Dynamics

The outer electron radiation belt is highly dynamic in space and time, with geomagnetic activity the primary cause of these variations. Figure 1.14 (taken from *Reeves et al.* [2013a]) shows the variation of the electron radiation belt during a 5-day period from 0 UT on October 7, 2012 to 0 UT on October 12, 2012. The top panel shows the intensity of the electron radiation belt as a function of L (where $L = r/R_E$) and universal time. The second panel shows the intensity of the electron radiation belt at L = 4.2 during the same period. The bottom three panels show the geomagnetic conditions during this period (solar wind velocity (V_{sw}), IMF north-south component ($IMF\ B_z$), and Dst index). The

geomagnetic storm (as shown in the Dst index (bottom)) causes an intense and rapid enhancement of the electron radiation belt in this case. However, geomagnetic storms are not always associated with enhancements of the radiation belt. *Reeves et al.* [2003a] found that about half of geomagnetic storms increased the intensity of the radiation belt, about one in five storms resulted in a depleted radiation belt, and the remaining storms produced changes that were less than a factor of two either up or down. Before recovering to either enhanced, depleted or approximately equal intensities, geomagnetic storms may be associated with a rapid decrease in the intensity of the electron radiation belt. Such events are known as radiation belt dropouts (see Chapter 4).

Figure 1.14 shows the variability in intensity of electrons at a specific energy (2.5 MeV), however the number of radiation belt particles, as well as their energy spectra and spatial distribution are all variable factors. With *in situ* observations from spacecraft typically measuring the number of electrons in a specific energy range at a single location, it can be problematic to characterise the nature of variations with certainty. Some variations may be reversible, that is, the distribution of radiation belt particles is temporarily changed before returning back to its initial state. This may appear as a 'loss' in the number of particles in a specific energy range as measured by a spacecraft at a single location, when in reality the spacecraft is simply measuring a different part of the radiation belt distribution with no real loss of particles from the system. Other variations may be caused by processes that drive 'real' losses from the system, i.e. irreversible changes to the energy or spatial distribution of the electrons.

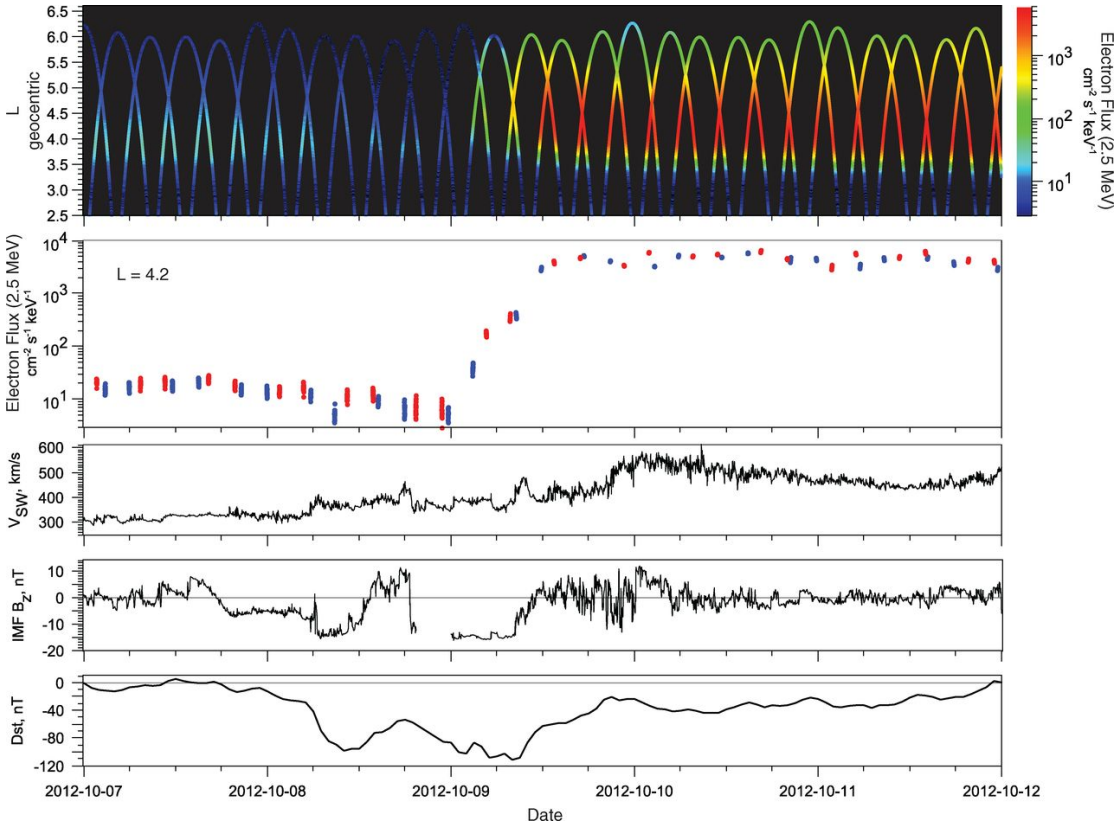

FIGURE 1.14: The top graph shows the intensity of 2.5 MeV electrons as measured by NASAs twin Van Allen Probes satellites. The second graph shows the intensity of 2.5 MeV electrons at a fixed radial distance of 4.2 Earth radii (L = 4.2). The bottom three graphs show solar wind velocity (V_{sw}), the IMF north-south component ($IMF\ B_z$), and the Dst index. The geomagnetic activity on October 8-9 produces an intense and rapid enhancement of the electron radiation belt. From *Reeves et al.* [2013a]

1.4.1 Adiabatic Variations

During a geomagnetic storm, radiation belt electrons exhibit adiabatic variations. These are changes that are reversible should the system return to its initial state. During the main phase of a geomagnetic storm, the ring current becomes enhanced and the geomagnetic field strength decreases. Radiation belt electrons respond to the weaker magnetic field by attempting to conserve the third adiabatic invariant. This results in the expansion of the drift shells in a process called outwards adiabatic transport. As particles on their associated drift shells move to a larger radial distance from the Earth,

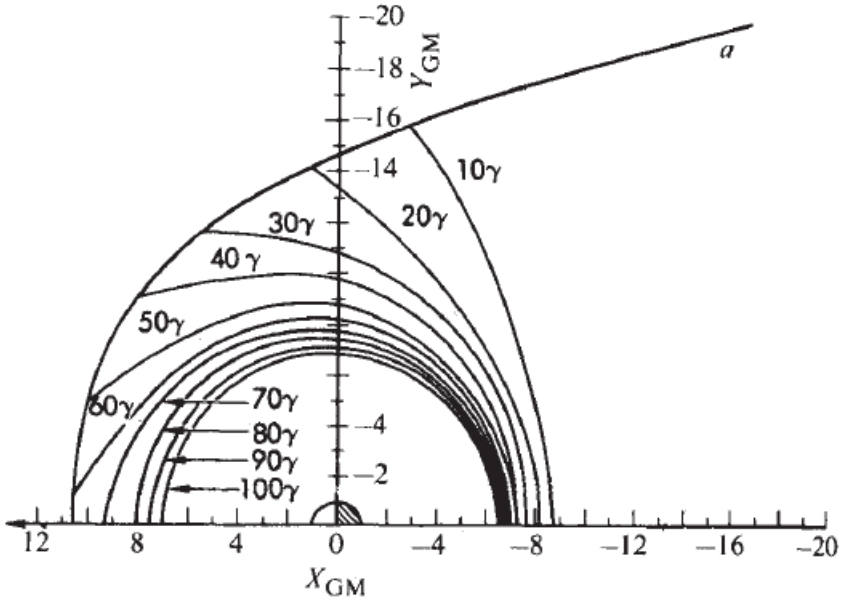

FIGURE 1.15: Contours of constant equatorial magnetic field strength within the magnetosphere under average conditions. a indicates the magnetopause boundary and γ is used to denote nanotesla. After *Fairfield* [1968].

they decrease in energy in order to conserve the first adiabatic invariant. In general, the number of radiation belt particles decreases exponentially with increasing energy, therefore for a spacecraft measuring electrons within a fixed energy range (see Section 2.1), the number of particles detected would significantly decrease during the main phase of a geomagnetic storm. During the recovery phase of a geomagnetic storm, the ring current returns to an initial quiet-time state and the expanded drift shells contract, returning inwards to their initial position. To conserve the first adiabatic invariant, the energy of the particles increases and the system returns to the initial, pre-storm state.

1.4.2 Magnetopause Shadowing

The concept of drift shell splitting (as introduced in Section 1.2.4.2) can play an important role in radiation belt dynamics via a process called *magnetopause shadowing*. Due

to the pitch-angle dependence of a particle's drift path, particles with different initial pitch angles will have different probabilities of encountering the dayside magnetopause on their orbits about the Earth. Consider two radiation belt electrons located on a geomagnetic field line around midnight, one with an equatorial pitch angle of 85° and one with an equatorial pitch angle of 15°. As the two particles travel longitudinally about the Earth, they trace out different drift shells. By the time they reach noon, the particle with an initial pitch angle of 85° is located at a larger radial distance (L^*) than the particle with an initial pitch angle of 15°. Once the two electrons complete their drift shell orbits, they will return back to the same initial location at which they started at midnight. In order to explain why this process occurs, it is necessary to examine the first and second adiabatic invariants. For the particle mirroring close to the equator, the second adiabatic invariant is $\sim$ zero (since the magnetic field at the mirror point is approximately equal to the magnetic field at the location of the particle). The first invariant is defined as the perpendicular energy of the particle divided by the geomagnetic field strength, and as such, the drift path of particles follow contours of constant magnetic field strength. Figure 1.15 shows the contours of constant **B** in the equatorial plane for the magnetosphere under average conditions. In this case, a is the magnetopause boundary and γ is used to denote units of nanotesla. It can be seen that particles that mirror on the magnetic equator have drift shells that are at a greater radial distance on the dayside than on the nightside. It is also evident that some contours that are closed on the nightside are open on the dayside as they intersect with the dayside magnetopause. If this occurs, the particles are said to be on open drift shells and lost from the system via the magnetopause boundary. For the second particle with an initial pitch angle of 15° on a magnetic field line at midnight, the second adiabatic invariant

is approximately equivalent to the length of the magnetic field line. This assumption can be made since the magnetic field at the mirror point is much larger than the local magnetic field, that is B/B_m is small. In comparison to the particle with an initial pitch angle of 85°, the particle with an initial pitch angle of 15° may counteract the increase in magnetic field magnitude encountered on its drift shell by changing pitch angle in order to conserve the first adiabatic invariant (become less parallel oriented). This, in conjunction with conservation of the second adiabatic invariant, K, (length of magnetic field line between mirror points), means that from the same initial position on the nightside, a particle with an initial pitch angle of 85° will be at a greater radial distance than a particle with an initial pitch angle of 15°, once they have azimuthally drifted around to the dayside. Therefore in general, from the same location on the nightside, an electron with a more perpendicular initial pitch angle will drift such that it will be at a greater radial distance than an electron with a more parallel initial pitch angle by the time they reach noon. The two particles will then complete their drift orbits, assuming they do not intersect with the magnetopause, and return to the same location around midnight. When spacecraft measure the particle pitch-angle distribution close to local midnight, it is common to observe a local minima in the number of particles centred around 90° due to the perpendicular population drifting further out on the dayside and therefore increasing the possibility of being lost from the system via the magnetopause. This is the typical signature of magnetopause shadowing, a process that may become enhanced during periods with elevated solar wind pressure, such as during the passing of CIRs.

1.4.3 Diffusion

Particle diffusion is an important process in the context of radiation belt dynamics. For the simple one-dimensional case, consider the distribution function $f(x,t)$ at time t (as shown in Figure 1.16) where $f(x,t)$ is the number of particles contained in element dx. In the context of the radiation belts, the function may be the radial distribution of particles, the energy distribution or the pitch-angle distribution, with diffusion in all three parameters playing a role in radiation belt dynamics. At positions x_1 and x_2 the distribution function vanishes since particles are lost from the system at these boundaries. The net current due to the diffusion of particles in the x-direction is proportional to the negative of the gradient of $f(x,t)$, and is given by Fick's law:

$$Net\ Current = -D\,\frac{\partial f}{\partial x} \tag{1.75}$$

where D is the diffusion coefficient that contains all information on the mechanisms that drive the diffusion process. The diffusion coefficient is always positive and may also be a function of x [*Walt*, 1994]. The direction of charged particle motion, and thus the net currents, are shown for the initial distribution function $f(x,t)$ in Figure 1.16. The process of diffusion acts to smooth the distribution by increasing the distribution function at local minima and decreasing the distribution function at local maxima.

In the case presented in Figure 1.16, the distribution function considered, $f(x,t)$, relates to the number of particles in element dx. In order to remove the periodic motion of radiation belt particles and solely focus on the motion due to diffusion, the distribution function is usually expressed in adiabatic invariant coordinates.

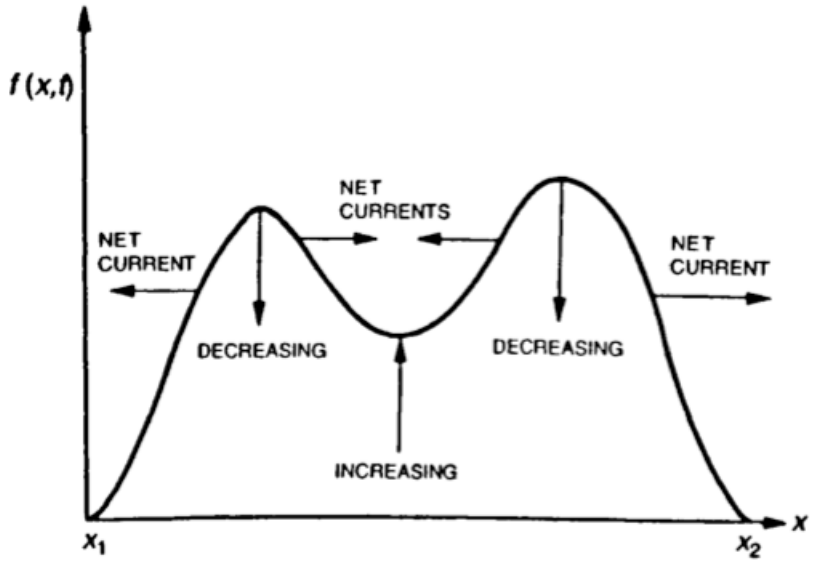

FIGURE 1.16: The impact of the diffusion process on a initial distribution function, $f(x,t)$. From *Walt* [1994].

1.4.4 Waves

Radiation belt dynamics may also be driven by particle interactions with a variety of different wave modes. Figure 1.17 shows the typical distribution of waves in the magnetosphere. Wave-particle interactions may lead to violation of one, or more, of the adiabatic invariants associated with particle motion [*Schulz and Lanzerotti*, 1974] and thus drive diffusion processes. During magnetically active periods, the intensity of plasma waves in the magnetosphere may become enhanced and drive enhanced radial, energy and pitch-angle diffusion. These non-adiabatic processes may lead to losses from the system and are therefore an important factor to consider in the study of radiation belt dynamics. The following sections discuss the roles that specific waves play in the driving of radiation belt dynamics.

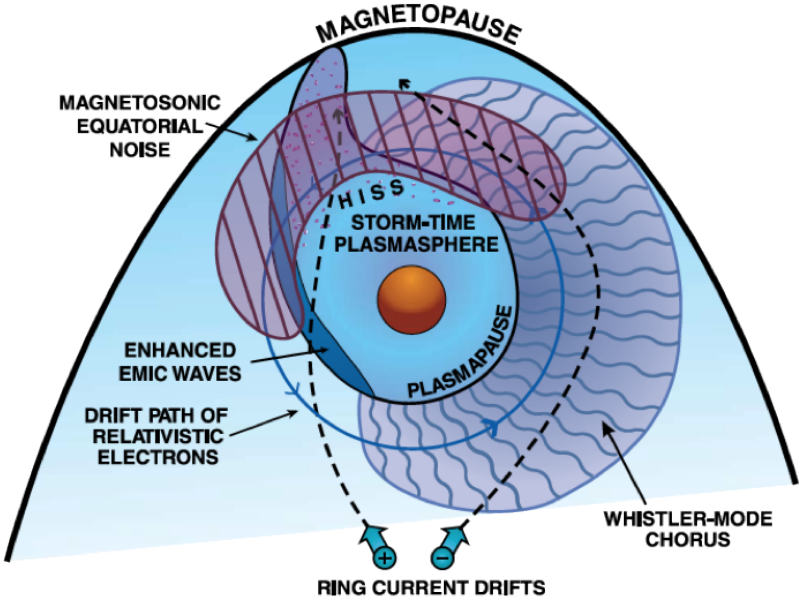

FIGURE 1.17: A schematic illustration of the spatial distribution of waves in the magnetosphere in relation to the plasmasphere, the drift paths of ring current ions and electrons, and the drift path of relativistic electrons. From *Thorne* [2010].

1.4.4.1 Ultra Low Frequency (ULF) Waves

ULF waves typically have frequencies of the order of mHz. Solar wind velocity shear and pressure fluctuations at the magnetopause boundary are known to excite ULF waves [*Ukhorskiy et al.*, 2006; *Claudepierre et al.*, 2008]. The variability and distribution of these ULF waves can be measured by ground-based and space-based instrumentation. Due to the frequency of this type of wave, resonant interactions with the drift periods of radiation belt electrons may occur, thus causing violation of the third adiabatic invariant. The first and second adiabatic invariants usually remain conserved during this process since the timescales of their associated motion are much shorter. Interactions with ULF waves and violation of the third adiabatic invariant causes radiation belt particles to drift inwards or outwards, away from their usual drift shell, in a process know as *radial*

ULF Wave Classification		Frequency	Period (s)
Continuous	Pc 1	0.2-5 Hz	0.2-5
	Pc 2	0.1-0.2 Hz	5-10
	Pc 3	22-100 mHz	10-45
	Pc 4	7-22 mHz	45-150
	Pc 5	2-7 mHz	150-600
Irregular	Pi 1	25-1000 mHz	1-40
	Pi 2	2-25 mHz	40-150

TABLE 1.3: Typical classification of ULF waves. From *Jacobs et al.* [1964]

diffusion. Since an increase in L-shell results in energy loss, and a decrease in L-shell results in particle acceleration, radial diffusion is thought to be an important process for driving both sources and losses of radiation belt particles. ULF waves may be classified by type (c, meaning continuous or i, meaning irregular) and frequency (period). Table 1.3 shows the typical classification categories for ULF waves [*Jacobs et al.*, 1964].

1.4.4.2 Chorus Waves (0.1 f_{ce} to 0.9 f_{ce})

Chorus waves are very low frequency (VLF) waves that occur in the $\sim$ 100 Hz$-$10s of kHz frequency range and primarily occur in the low-density region outside of the plasmasphere. Chorus waves are highlighted in the sample spectrogram from the Combined Release and Radiation Effects Satellite (CRRES) shown in Figure 1.18. Typically occurring in the dawn sector (from around midnight to the early afternoon sector), the

local time distribution of chorus waves is shown in Figure 1.17. The frequency of chorus waves scales with the local electron gyrofrequency, f_{ce}, with emissions usually in the $0.1 - 0.9 f_{ce}$ range. A banded structure is commonly observed with two distinct frequency ranges of elevated wave intensity called the lower band, $0.1 - 0.5 f_{ce}$, and the upper band, $0.5 - 0.9 f_{ce}$, with a local minima between them at around $0.5 f_{ce}$. Waves that are right-hand circularly polarised and with a frequency less than the local electron gyrofrequency are known as whistler-mode waves, hence chorus waves may also be referred to as whistler-mode chorus. It is widely considered that chorus waves are generated through cyclotron resonance with anisotropic electrons injected from the plasma sheet with energies from a few keV up to 10s of keV (e.g. *Hwang et al.* [2007]; *Li et al.* [2009b, 2011] and references therein). Chorus waves play an important role in radiation belt dynamics since they are thought to drive both the acceleration and loss of radiation belt particles [*Bortnik and Thorne*, 2007]. The local acceleration of radiation belt particles through gyro-resonant interactions with whistler-mode chorus waves is currently a topic of intense research and modelling efforts.

1.4.4.3 Plasmaspheric Hiss (100 Hz to ($\sim$ 2) kHz)

Plasmaspheric hiss is an incoherent, structureless wave emission that occurs primarily inside the dense plasmasphere. With typical frequencies between $\sim$ 200 Hz to $\sim$ 2 kHz, hiss was named due to its resemblance to audible hiss or 'white noise'. The slot region between the inner and outer radiation belts is caused by particle interactions with plasmaspheric hiss leading to pitch-angle diffusion and ultimate losses to the atmosphere [*Lyons and Thorne*, 1973; *Meredith et al.*, 2006a]. Hiss is also thought to contribute

towards the quiet time decay of electrons in the outer radiation belt [*Meredith et al.*, 2006b; *Borovsky and Denton*, 2009a]. Plasmaspheric hiss is highlighted in the sample spectrogram from the CRRES shown in Figure 1.18.

1.4.4.4 Electromagnetic Ion Cyclotron (EMIC) Waves (<1-2 Hz)

EMIC waves are left-hand circularly polarised waves that occur in distinct frequency bands separated in multiples of the ion gyrofrequency. EMIC waves are excited through interaction with anisotropic ring current ions, a process that tends to become enhanced during geomagnetic storms. Resonance of EMIC waves with moderately energetic electrons is not possible due to their opposite polarisations. However, relativistic electrons are thought to 'overtake' EMIC waves and thus, in the frame of reference of the electron, the wave polarisation is reversed to be right-handed and therefore gyro-resonance can occur. The minimum resonance energy of electrons is usually >2 MeV, although it may become lower in localised regions of low magnetic field strength or high plasma density [*Meredith et al.*, 2003c]. This resonance with highly energetic electrons is considered a highly efficient mechanism for pitch-angle scattering and ultimate loss to the atmosphere [*Miyoshi et al.*, 2008].

1.4.4.5 Magnetosonic Equatorial Noise

Magnetosonic equatorial noise (as highlighted in Figure 1.18) is an electromagnetic emission that occurs at frequencies between the proton gyrofrequency and the lower hybrid frequency near the Earth's magnetic equator [*Santolík et al.*, 2004]. Magnetosonic equatorial noise may be observed both inside, and outside, the plasmasphere [*Kasahara et al.*,

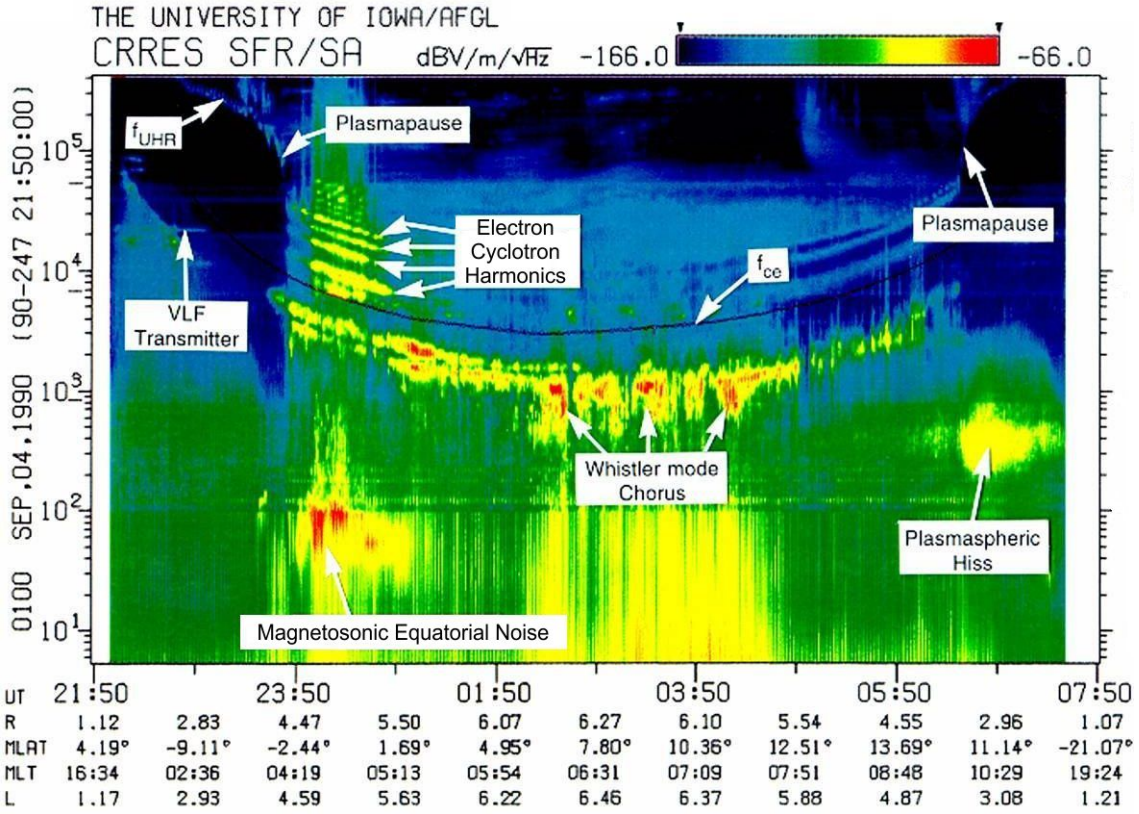

FIGURE 1.18: A sample spectrogram from the CRRES satellite highlighting the different waves that occur in the magnetosphere. From *Kletzing et al.* [2013].

1994; *Horne et al.*, 2000] and is considered to be an important factor for energy and pitch-angle diffusion in the radiation belts. *Horne et al.* [2007] showed that magnetosonic waves can cause pitch-angle and energy diffusion of electrons at rates comparable to those for chorus waves. Pitch-angle diffusion by magnetosonic waves does not extend into the loss cone [*Horne et al.*, 2007] and as such, these waves are not considered an important factor in driving losses to the atmosphere.

Chapter 2

Instrumentation

The research presented in subsequent chapters utilises data from two satellite missions - GOES-13 (NOAA/NASA) [GOES N Databook Revision C, CDRL PM-1-1-03] and the Van Allen Probes (NASA) [*Fox and Burch*, 2014]. Data from the multi-spacecraft database OMNIweb (NASA) [*King and Papitashvili*, 2005] are also used in these studies. This chapter consists of an introduction to the different types of instrumentation usually installed on orbital spacecraft, in addition to a more specific description of the instruments that provide the data implemented in the research chapters that follow.

2.1 Particle Detectors

Particle flux, j, is determined by the number of particles collected by a detector (counts) as well as the detector area (A), the sampling time (t), the viewing solid-angle of the detector (Ω), and the energy that the detector is designed to measure, (E). The relation between counts and particle flux is:

$$counts = \iiiint j \; dA \, dE \, d\Omega \, dt \tag{2.1}$$

Since detector efficiency typically varies with angle and energy, this efficiency must also be considered when converting measured counts to particle flux. Differential, directional particle flux at a given location, direction and energy range may be defined as the number of particles at energy, E, within energy range, dE, which cross unit area, dA, (which is perpendicular to the direction specified) within a unit solid angle, $d\Omega$, in one-second [*Walt*, 1994]. Therefore, the customary units of differential, directional flux are $cm^{-2}s^{-1}sr^{-1}keV^{-1}$. Within the magnetosphere, the specified direction is typically that of the geomagnetic field vector. The differential, directional flux may be written as:

$$differential\, directional\, flux = j\,(E, \alpha) \; dA \; dE \; d\Omega \tag{2.2}$$

This directional flux, $j\,(E, \alpha)$, may be integrated over the full solid angle to give the omnidirectional flux. This omnidirectional flux is:

$$omnidirecitonal\, flux = j\,(E) = \int_{\Omega} j\,(E, \alpha) \; d\Omega = 2\pi \int_{0}^{\pi} j\,(E, \alpha) \; sin\alpha \; d\alpha \tag{2.3}$$

Some detectors are designed to only measure particles above a particular energy threshold. This threshold energy is usually determined by either the magnitude of an applied electric field, or by the shielding provided by the material surrounding the detector. The particle flux above an energy threshold, E_0, is called the integral particle flux and may be defined as:

$$integral\,flux = j\left(E > E_0,\ \alpha\right) = \int_{E_0}^{\infty} j\left(E, \alpha\right)\, dE \tag{2.4}$$

It is also possible to calculate the integral, omnidirectional flux by combining Equation 2.3 and 2.4.

Another method of describing the particle distributions is in terms of phase space density. Phase space density is defined as the number of particles per unit volume of six-dimensional phase space [*Walt*, 1994] (which includes the three orthogonal spatial dimensions and their three conjugate momenta dimensions). Phase space density utilises adiabatic invariant coordinates that directly relate to the paths that radiation belt particles follow. This allows for adiabatic fluctuations caused by the time varying geomagnetic field to be considered in parallel to variations in the measured particle flux. It is common to assume a Maxwellian velocity distribution function (which will be assumed the case hereafter) of the form shown in Equation 2.5.

$$f\left(v\right) = n\left(\frac{m}{2\pi k_B T}\right)^{3/2} e^{-mv^2/2k_B T} \tag{2.5}$$

where $f\left(v\right)$ is the distribution function, n is number density, m is mass, k_B is the Boltzmann constant, T is temperature and v is velocity [*Baumjohann and Treumann*, 1997]. The conversion of measured particle flux to phase space density is discussed in Section 3.

2.1.1 Electrostatic Analysers

Electrostatic analysers are a specific type of detector that are typically used for measuring lower energy particles (< 100s of keV) [*Schrijver and Siscoe*, 2010]. The method of detection works by guiding only the desired species and energy of particles on to the detector, whilst disregarding particles of other energies and species [*Bryant*, 1999]. An electrostatic analyser usually consists of two circularly-curved parallel plates with a voltage applied across them (as shown in Figure 2.1), which in turn generates an electric field. As particles with charge, q, interact with this electric field, E, they experience the Lorentz force, $F = qE$. This force acts to accelerate particles perpendicular to the charged plates, with the direction depending upon the generated electric field and the charge of the particle. Since the direction of the force acting upon the particle is charge dependent, and since the acceleration of the particle by this force is dependent on the particle mass, electrostatic analysers are able to distinguish between 'heavier' and 'lighter' particles, as well as between particles of opposite charge. The circular track that particles follow depends solely upon the total energy of the incident particles (assuming a constant bias is applied to the plates).

Figure 2.1 is a schematic diagram showing the process of electrostatic analysis in the case of detecting electrons with energy, E_d. For electron detection, the top plate should be negatively biased while the bottom plate should be positively biased, thus creating an electric field in the radially outwards direction. Consider three incident electrons, one with energy $E > E_d$ (red), one with energy $E < E_d$ (blue), and one with energy $E = E_d$ (green). The electron with energy $E > E_d$, travels along a trajectory such that the particle intersects with the top boundary and therefore, does not reach the detector. The

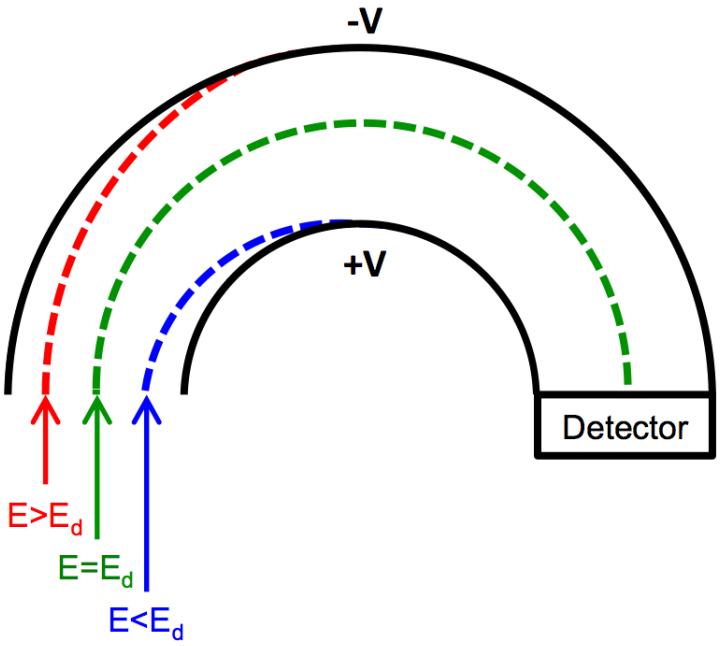

FIGURE 2.1: A schematic representation of how an electrostatic analyser measures electrons with a specified energy, E_d. This energy may be altered by varying the voltage, and therefore the electric field, applied across the curved plate walls of the instrument.

electron with energy $E < E_d$, travels along a trajectory such that the particle intersects with the bottom boundary and again, does not reach the detector. The electron with energy $E = E_d$, travels along a circular trajectory such that the generated electric field guides the particle on to the detector. Positively charged particles will be accelerated in the opposite direction and therefore intersect with the top boundary and not be detected. Therefore, an electrostatic analyser may be configured to measure particles of specific charge, mass and energy (velocity) [*Bryant*, 1999]. Due to the different trajectories a particle can take through the detector, electrostatic analysers usually measure particles within a given energy range [*Schrijver and Siscoe*, 2010]. It is common to vary the voltage bias between the plates and thus 'sweep through' different energy ranges over time in order to measure particles of different energies.

2.1.2 Solid State Detectors

Solid state detectors may be used for measuring particles with energies from $\sim$ 10s eV to well into the MeV range [*Bryant*, 1999]. In contrast to electrostatic analysers, solid state detectors may differentiate between particle energy and species by the amplitude variations of a generated voltage pulse as the particles pass through one, or more, detectors. The detector entrance aperture may be shielded by a thin material in order to place a lower bound on the energy of particles that enter. As charged particles enter the detector, they produce an electrical pulse, the amplitude of which is dictated by the amount of energy a particle deposits in the detector [GOES N Databook Revision C, CDRL PM-1-1-03]. These pulses are then analysed in order to determine the fluxes in different energy ranges. The field of view is defined as the cone angle within which particles may enter the detector and be measured.

2.2 Magnetometers

As described in Section 1, particle dynamics in the magnetosphere are largely driven by the geomagnetic field. Therefore, as well as measuring particle fluxes, it is useful for orbital spacecraft to measure the magnetic field. Fluxgate magnetometers, which are typicality used for measuring the DC magnetic field, as well as search-coil magnetometers, which are typically used for measuring the short timescale variations of the AC magnetic field, are discussed in the sections that follow.

2.2.1 Fluxgate Magnetometer

A fluxgate magnetometer consists of two electrically conductive coils, an inner drive coil, surrounded by an outer sensory coil. The drive coil is wound around a magnetically permeable, ring-shaped core with the sensory coil wound around both the core and the drive coil [*Dyer*, 2001]. An alternating current is passed through the drive coil which, in turn, induces a magnetic field in the core. The magnitude of the applied alternating current is such that it drives the core through cycles of magnetic saturation. If the driving current were turned off once the core had become magnetically saturated, the core would retain some magnetism in a process known as hysteresis. In the absence of an external magnetic field, tracing out the magnetism, M, of the core material as a function of the applied magnetic field, H (which is proportional to the applied AC current in the drive coil), produces a hysteresis loop as shown in Figure 2.2 [*Wilson*, 2005].

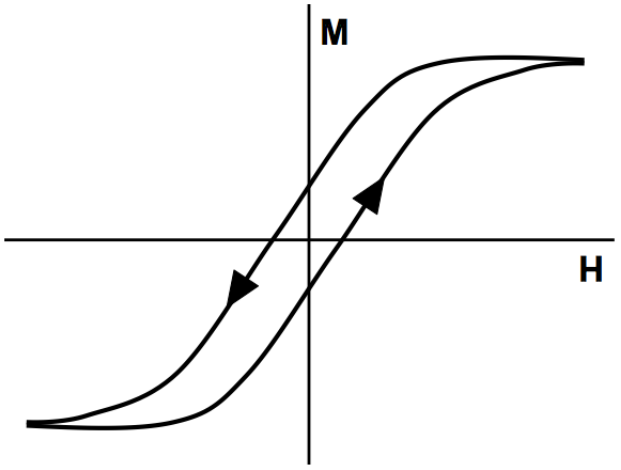

FIGURE 2.2: A schematic representation of a hysteresis loop (magnetism, M as a function of applied magnetic field, H) for the core material of a fluxgate magnetometer in the absence of an external magnetic field.

When there exists an external magnetic field, the hysteresis loop becomes shifted in the

x-direction due to a residual magnetic field even when the applied current is zero. That is, the core will become more easily saturated by a current in the direction of the external field than by a current opposing the external field [*Kivelson and Russell*, 1995]. This effect produces a phase difference between the input current in the drive coil and the output current detected by the sensory coil. Figure 2.3 is a schematic representation of the voltage observed in the sensory coil in the absence of an external magnetic field (top) and in the presence of an external magnetic field (bottom). In the absence of an external magnetic field ($B_{ext} = 0$), the output voltage in the sensory coil is in step with the input AC current applied to the drive coil (even time spacing between voltage minima and maxima). In the presence of an external magnetic field ($B_{ext} \neq 0$), the output voltage in the sensory coil becomes out of step with the input AC current (uneven time spacing between voltage minima and maxima) [*Fiorillo*, 2004].

The difference in both amplitude and phase of the voltage in the sensory coil (in comparison to the drive coil) is used to determine the direction and magnitude of the external DC magnetic field in one dimension. Spacecraft typically use three orthogonal fluxgate magnetometers in order to provide magnetic field observations in three dimensions (tri-axial fluxgate magnetometer).

2.2.2 Search-Coil Magnetometer

Search-coil magnetometers (also known as induction magnetometers) measure variations in the magnetic field and usually consist of a long, electrically-conductive coil wound through multiple turns [*Dyer*, 2001]. The principle behind induction magnetometers is Faraday's law of induction:

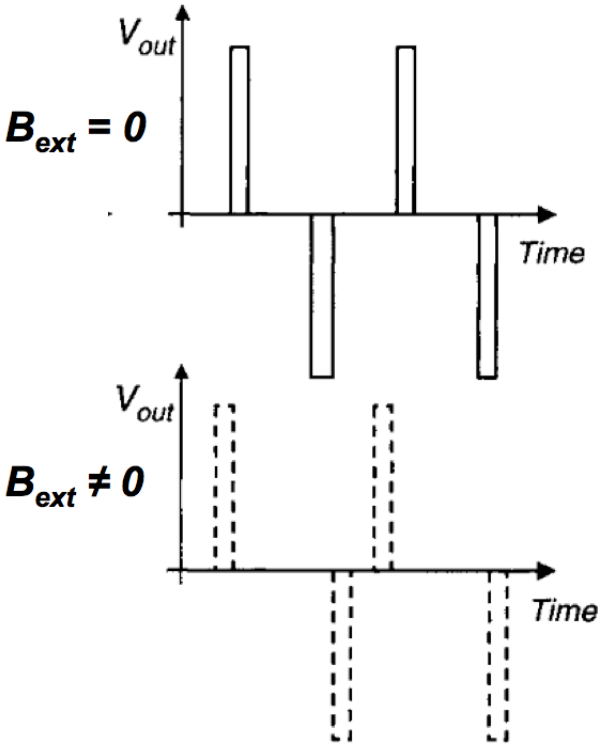

FIGURE 2.3: A diagram showing the voltage in the sensory coil of a fluxgate magnetometer both in the absence of an external magnetic field (top) and in the presence of an external magnetic field (bottom). Adapted from *Fiorillo* [2004].

$$\epsilon = -\frac{d\Phi_B}{dt} \tag{2.6}$$

where Φ_B is the magnetic flux through a coil of surface S and ϵ is the induced voltage. For multiple coils, a multiplication factor of N is introduced, where N is the number of coils. Assuming the magnetic field is homogeneous over the area S, and therefore $\Phi_B = B \times S$, equation 2.6 becomes:

$$\epsilon = -N \times S \, \frac{dB}{dt} \tag{2.7}$$

In order to increase the sensitivity of the magnetometer, and thus amplify the induced voltage, the coil may be wound around a highly magnetically permeable core [*Gubbins and Herrero-Bervera*, 2007]. This core acts to concentrate the magnetic field and thus increases the magnetometers' sensitivity. Search-coil magnetometers are vector sensors, providing measurements of the magnetic field variations in the direction parallel to the rotational axis of the coil. As with fluxgate magnetometers, three orthogonal induction magnetometers are typically used to provide AC magnetic field observations in three dimensions.

2.3 OMNIweb

OMNIweb is a multi-spacecraft (e.g. ACE, Wind, IMP 8, Geotail) database of near-Earth magnetic field and plasma observations [*King and Papitashvili*, 2005]. Data are available in Low Resolution OMNI (LRO) at 1-hour, 1-day and 27-day cadence from 1963 to the near-present day whereas High Resolution OMNI (HRO) data are available at 1-minute and 5-minute resolution between 1981 and the near-present day. The Lagrange L1 point is the location between the Earth and Sun where the gravitational forces balance the centripetal force of the orbital motion. Observations of solar wind parameters from satellites that orbit around L1 are time-lagged to the Earth's bow shock [*Weimer et al.*, 2002]. The time shift is based on the assumption that solar wind parameters observed by upstream spacecraft at a given time lie on a planar surface that convects with the solar wind. Therefore, it is assumed that the same values will be observed at a later time at some greater radial distance as the planar surface continues downstream. Data are time lagged prior to calculating temporal averages. Data products available from OMNIweb

include magnetic field parameters; 3-vector IMF, in addition to plasma parameters; velocity (3-dimensions), proton density, proton temperature, flow pressure, as well as geomagnetic activity indices; Dst (1-hour cadence), Kp (3-hour cadence), AE (1-minute cadence). Descriptions of the geomagnetic indices utilised in Chapters 3, 4, 5 and 6 are given below.

2.3.1 Dst Index

The Dst index (developed by *Sugiura* [1964]) is calculated from the horizontal component, H, of the geomagnetic field recorded at four observatories (Hermanus, Kakioka, Honolulu, and San Juan) located between 20° and 30° in latitude from the magnetic equator. The quiet time baseline is subtracted from data from each observatory before the average over all four stations is taken, applying a correction factor for the variation in latitude. The Dst index is frequently used as a proxy of the ring current intensity, as well as for parametrising the magnitude of geomagnetic storms.

2.3.2 SYM-H

SYM-H is similar to the Dst index in that it is calculated using the symmetric disturbance of the horizontal, H, component of the geomagnetic field. However, whilst Dst is a 1-hour index, SYM-H is available at 1-minute resolution and implements data from a different set of magnetometer stations.

2.3.3 Kp Index

The 3-hour Kp index [*Bartels et al.*, 1939] is derived using observations from mid-latitude ground-based magnetometer stations located in Sitka, Alaska; Meanook, Canada; Ottawa, Canada; Fredericksburg, Virginia; Hartland, UK; Wingst, Germany; Niemegk, Germany; and Canberra, Australia. The maximum fluctuations in the horizontal, H, component of the geomagnetic field from each magnetometer station in a given 3-hour period are averaged together to determine the Kp index on a 9-point logarithmic scale. The Kp index is widely considered as a proxy for magnetospheric convection (e.g. *Thomsen* [2004] and references therein).

2.3.4 AE Index

The AE (Auroral Electrojet) index [*Davis and Sugiura*, 1966] is obtained at 1-minute resolution using data from 12 observatories situated along the auroral zone in the northern hemisphere. The name, auroral electrojet, refers to the ionospheric currents in the auroral zone that become enhanced due to increased conductivity during auroral activity. These currents cause a deviation in the geomagnetic field that can be observed by ground based instrumentation in the auroral zone. Following a baseline subtraction at each station, the largest (AU) and smallest (AL) deviations in the horizontal component of the geomagnetic field at each time interval are selected, with the difference, AU - AL, being defined as the AE index.

2.4 GOES

The Geostationary Operational Environmental Satellite (GOES) spacecraft operate as a two-satellite constellation in geosynchronous orbit, GEO, (meaning that their orbital period is one day, the same as the rotational period of the Earth). The GOES series' primary purpose is to monitor weather and to provide the data and imagery used for daily weather forecasting. Measuring the Earth's atmosphere, surface, cloud cover in addition to the solar and geosynchronous orbit space environments makes the GOES satellites useful for a multitude of purposes. For the studies conducted here, the GOES spacecraft are used for the purpose of measuring energetic particle variations in the magnetosphere.

GOES-13 was launched from Kennedy Space Center on August 1, 2008 aboard a Delta IV rocket and was the first of a new generation of GOES satellites (GOES-N series). This new series of GOES satellites housed improved instrumentation specifically designed to measure variations in magnetospheric particle populations. In GOES spacecraft coordinates, the positive x-direction is equatorial and westward, the positive y-direction is polar and northward, and the positive z-direction is radial and earthwards.

2.4.1 Space Environment Monitor

The Space Environment Monitor (SEM) onboard the current series of GOES satellites consists of multiple instruments that measure a range of parameters in near-Earth space; in-situ magnetic field and energetic particle data, as well as solar radiation. These data are then provided in real-time to the National Oceanic and Atmospheric Administration

(NOAA) Space Weather Prediction Center (SWPC) and are used in conjunction with other data from the solar terrestrial environment to issue reports, alerts, and forecasts for events such as geomagnetic storms and solar flares.

The SEMs X-ray and extreme ultraviolet sensors observe solar output (X-ray flux in two wavelength bands, 0.05-0.3 nm and 0.1-0.8 nm, and extreme ultraviolet flux in three wavelength bands centred at 10, 30 and 126 nm). The Energetic Particle Sensor (EPS) and High Energy Proton and Alpha Detector (HEPAD) instruments measure the flux of protons in the 0.74-900 MeV energy range, alpha particles in the 3.8-500 MeV energy range, and electrons in three energy ranges, >0.6, >2, and >4 MeV. HEPAD also measures protons with energies greater than 330 MeV and alpha particles with energies greater than 2.56 GeV. The Magnetospheric Proton Detector (MAGPD) measures lower energy protons in five energy channels between 80 and 800 keV. The Magnetospheric Electron Detector (MAGED) measures lower energy electrons in five energy channels between 30 and 600 keV. Due to their configuration, both MAGPD and MAGED are able to provide particle measurements at nine different pitch-angles. The SEM suite also includes two tri-axial magnetometers mounted on a 8.5 m boom [GOES N Databook Revision C, CDRL PM-1-1-03]. For the work conducted here, data are used from the MAGED and the onboard magnetometers.

2.4.1.1 MAGED

The Magnetospheric Electron Detector (MAGED) provides electron flux measurements in the 30 keV to 600 keV energy range [GOES N Databook Revision C, CDRL PM-1-1-03]. Located on the zenith-facing (away from the Earth) side of the GOES spacecraft,

MAGED measures electrons at 0°, ±35°, and ±70° from the anti-Earthward direction in both the equatorial and the azimuthal plane. Each GOES telescope measures electrons using a solid state detector. When a charged particle hits the detector, a charge proportional to the particle's energy is converted to a voltage pulse by the charge sensitive pre-amplifier. Shaping amplifiers then distinguish between signal and noise. The amplitude of the voltage output by the shaping amplifiers directly relates to the energy of the incident particle. This output voltage is passed to a set of six voltage comparators which determine the energy range of the incident electron [*Hanser*, 2011]. The energy thresholds of the voltage level detectors are listed in Table 2.1. Based on the channel conditions shown in Table 2.1, the energy level of the particle is determined. If, for example, a particle produces a voltage that meets threshold level one but not threshold level two $(1 \cdot \bar{2})$, an event is counted in the 30 - 50 keV channel. If threshold level six is present, the energy level of the particle is beyond the measurable range of MAGED and no count is produced.

The central pitch angle of each MAGED detector is defined by the orientation of the magnetic field vector at each instance of time. Equation 2.8 shows how the central pitch angle of each telescope number, k, is determined using the telescope orientations (ϕ, l_x, l_y) shown in Table 2.2 and the magnetic field 3-vector in spacecraft coordinates (B_x, B_y, B_z).

$$\alpha_k = arccos\left(\frac{l_x\, B_x\, sin\phi + l_y\, B_y\, sin\phi + B_z\, cos\phi}{\sqrt{B_x^2 + B_y^2 + B_z^2}}\right) \tag{2.8}$$

Thus, MAGED provides pitch-angle-resolved electron flux measurements in the 30 to 600

Threshold Values		Energy Channel Conditions and Ranges		
Threshold Level	Threshold Value (keV)	Channel Name	Channel Condition	Energy Range (keV)
1	25.6	ME1	$1 \cdot \bar{2}$	30 - 50
2	47.0	ME2	$1 \cdot 2 \cdot \bar{3}$	50 - 100
3	98.0	ME3	$1 \cdot 3 \cdot \bar{4}$	100 - 200
4	199.0	ME4	$1 \cdot 4 \cdot \bar{5}$	200 - 350
5	349.0	ME5	$1 \cdot 5 \cdot \bar{6}$	350 - 600
6	599.0			
		$1 \cdot \bar{2}$ is read as level 1 but not level 2		

TABLE 2.1: The energy thresholds of the MAGED voltage level detectors and the conditions that need to be met in order for a particle to be considered in the defined energy channels. From *Hanser* [2011].

Telescope Number	Orientation to -Z axis, ϕ	Orientation to -X Direction, l_x	Orientation to -Y Direction, l_y
1	0°	0	0
2	35°	-	0
3	70°	+	0
4	35°	+	0
5	70°	-	0
6	35°	0	-
7	70°	0	+
8	35°	0	+
9	70°	0	-

TABLE 2.2: Description of the orientation of the nine MAGED telescope detectors. Orientations may be used in Equation 2.8 to determine the central pitch angle of each detector telescope. From *Rodriguez* [2014]

keV energy range in five energy channels (30-50, 50-100, 100-200, 200-350, and 350-600 keV). These fluxes are dead time and proton-contamination corrected [*Hanser*, 2011]. Dead time refers to the time a channel is not available for collecting data due to the processing of previously collected data. Data from the magnetospheric proton detector (MAGPD) are used to determine the extent of proton contamination in the MAGED.

2.4.1.2 Magnetometer

The GOES fluxgate magnetometers measure the three orthogonal components of the magnetic field within a range of ±512 nT and are accurate to ± a few nT [GOES N Databook Revision C, CDRL PM-1-1-03]. Both magnetometers are mounted on a 8.5 metre boom in order to reduce the magnetic effects from the satellite body. One magnetometer is located at the end of the boom, with the second magnetometer located 0.8 metres closer to the spacecraft on the same boom [GOES N Databook Revision C, CDRL PM-1-1-03].

2.5 Van Allen Probes

The Van Allen Probes, formerly Radiation Belt Storm Probes (RBSP), mission is part of NASAs Living With a Star (LWS) program to explore the fundamental processes of the Sun-Earth system that directly affect life and society. The Van Allen Probes mission consists of two identical spacecraft in near-identical, highly eccentric orbits that cut through the heart of the radiation belts (see Figure 2.4). The benefit of having two spacecraft in close proximity is that this provides the capability to distinguish between

the spatial and temporal variations of the radiation belts. The mission is designed to measure the charged particles that make up the terrestrial radiation belts, the plasma waves that interact with them, the large-scale electric fields that transport them, and the magnetic field that constrains them [*Fox and Burch*, 2014].

The orbit of the Van Allen Probes, as shown in Figure 2.4, precesses around the Earth at a rate of about 210° per year. Apogee is located on the dawnside on the date shown (October 1, 2012), approximately one year later, apogee is located on the duskside. This means that the Van Allen Probes will provide full local time and radial coverage of the radiation belts over the nominal 2-year mission lifetime [*Fox and Burch*, 2014].

2.5.1 Mission Objectives

The science objectives of the Van Allen Probes [*Fox and Burch*, 2014] are to:

1. Discover which processes, singly or in combination, accelerate and transport radiation belt electrons and ions and under what conditions.

2. Understand and quantify the loss of radiation belt electrons and determine the balance between competing acceleration and loss processes.

3. Understand how the radiation belts change in the context of geomagnetic storms.

The instrumentation onboard the two identical Van Allen Probes spacecraft is specifically designed to provide the data necessary to achieve these science goals. An overview of the onboard instrumentation is given below.

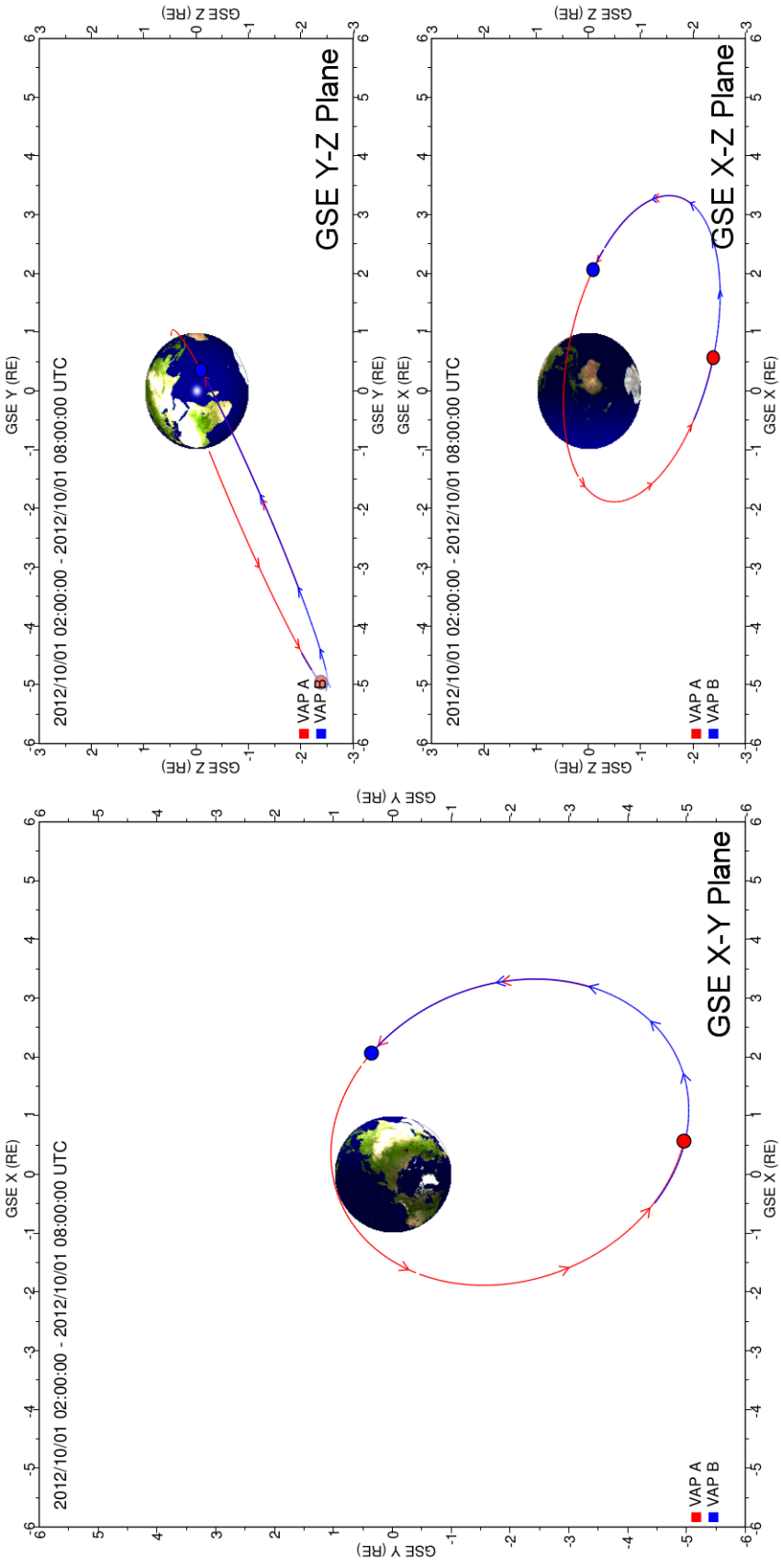

FIGURE 2.4: The orbit of both Van Allen Probes A and Van Allen Probes B on October 1, 2012 between 08:00 and 14:00 UT in GSE coordinates.

2.5.2 Overview of Instrument Suites

The energetic particle, composition, and thermal plasma suite (ECT) [*Spence et al.*, 2013] was designed with the aim of providing the data required to understand the physical processes that control the acceleration, global distribution, and variability of radiation belt electrons and ions. Consisting of three instruments; the Magnetic Electron Ion Spectrometer (MagEIS), the Helium Oxygen Proton Electron (HOPE), and the Relativistic Electron Proton Telescope (REPT), ECT comprehensively covers the electron and ion spectra from 1 eV up to 10s of MeV with resolution in energy, pitch-angle and ion composition [*Spence et al.*, 2013]. All three instrument suites are based on previous measurement techniques that are proven to operate in the harsh environment of the radiation belts whilst still providing unambiguous separation and clean responses to electrons and ions. The electric field and waves suite (EFW) [*Wygant et al.*, 2013] is designed to measure the electric fields that are known to be associated with radiation belt acceleration, scattering and transport mechanisms. Additionally, EFW will provide the data required for further research into the role that the large-scale convection electric field plays in modifying the structure of the inner magnetosphere. The Van Allen Probes ion composition experiment (RBSPICE) [*Mitchell et al.*, 2013] measures the 'storm-time ring current' with the goal of providing the data required to determine how the ring current contributes towards both the enhancement and depletion of the radiation belts. RBSPICE measures the energy spectrum of the ring current, as well as its ion composition (H, He, O). The relativistic proton spectrometer (RPS) [*Mazur et al.*, 2013] measures the protons of the inner radiation belt between energies of 50 MeV and 2 GeV, extending the upper energy range of previous satellite observations. With

existing models thought to underestimate the intensity of protons above ∼150 MeV, this instrumentation will assist in the development of a new standard radiation model for spacecraft design to withstand these hazards. The goal of the electric and magnetic field instrument suite and integrated science (EMFISIS) [*Kletzing et al.*, 2013] is to characterise the magnetic field and plasma waves that drive variations of the radiation belt through acceleration, loss and transport mechanisms. The work conducted in Chapter 6 utilises data from the Van Allen Probes EMFISIS instrumentation, of which a more detailed description is given in Section 2.5.3.

2.5.3 EMFISIS

The EMFISIS project [*Kletzing et al.*, 2013] provides measurements of both the wave and DC magnetic fields. EMFISIS consists of a tri-axial fluxgate magnetometer and a tri-axial search coil magnetometer that provide the DC vector and AC wave components of the magnetic field respectively. In conjunction with the electric field observations from the EFW instrument, and the particle measurements from other Van Allen Probes instrument suites, EMFISIS provides the data required to identify the origins of the plasma waves that play a crucial role in driving radiation belt dynamics.

2.5.3.1 Waves Instrument and the Magnetic Search Coil (MSC)

The EMFISIS waves instrument measures all three components of the electric field and all three components of the magnetic field for waves with frequencies between ~ 10 Hz and 12 kHz [*Kletzing et al.*, 2013]. The data consists of a set of spectral matrices including auto- and cross-correlations between the measured components of both sensors. This allows for

the spectral densities and wave propagation characteristics to be determined. Measuring both the electric and magnetic wave fields allows electromagnetic and electrostatic waves to be distinguished. EMFISIS uses the UVW coordinate system shown in Figure 2.5. The W axis is aligned with the sunward-facing spin axis of the satellite, with the U and V axes orthogonal to the spin axis in the plane of rotation. All electric and magnetic sensors are aligned with this coordinate system.

The electric wave field is provided by the EFW instrument which uses double probe spherical sensors located at the end of long booms to reduce spacecraft effects. In the spin plane, wire booms are used to give a 100 metre tip-to-tip separation between the two probes of the instrument. Along the spin axis, rigid booms are used to give a tip-to-tip separation of between 12 and 14 m [*Wygant et al.*, 2013]. The potential difference between the two spherical probes in each orthogonal axis is used to determine the electric field. The three orthogonal search coil magnetometers of EMFISIS are aligned with the three pairs of electric field probes from EFW in order to allow comparisons between them.

The magnetic search coil (MSC) consists of three orthogonal sensors, each approximately 40 cm in length and wound with 10,000 coil turns. These instruments measure the wave magnetic field in three dimensions from less than 10 Hz up to 12 kHz [*Kletzing et al.*, 2013]. The power spectral density is output as a function of frequency in each dimension. Outputs from this instrument provide the information necessary for determining the effectiveness of waves in accelerating, heating, and pitch-angle scattering of particles in the radiation belts. Additionally, a high frequency receiver (HFR) provides spectral densities of the wave electric field from 10 kHz up to 500 kHz. In conjunction with the

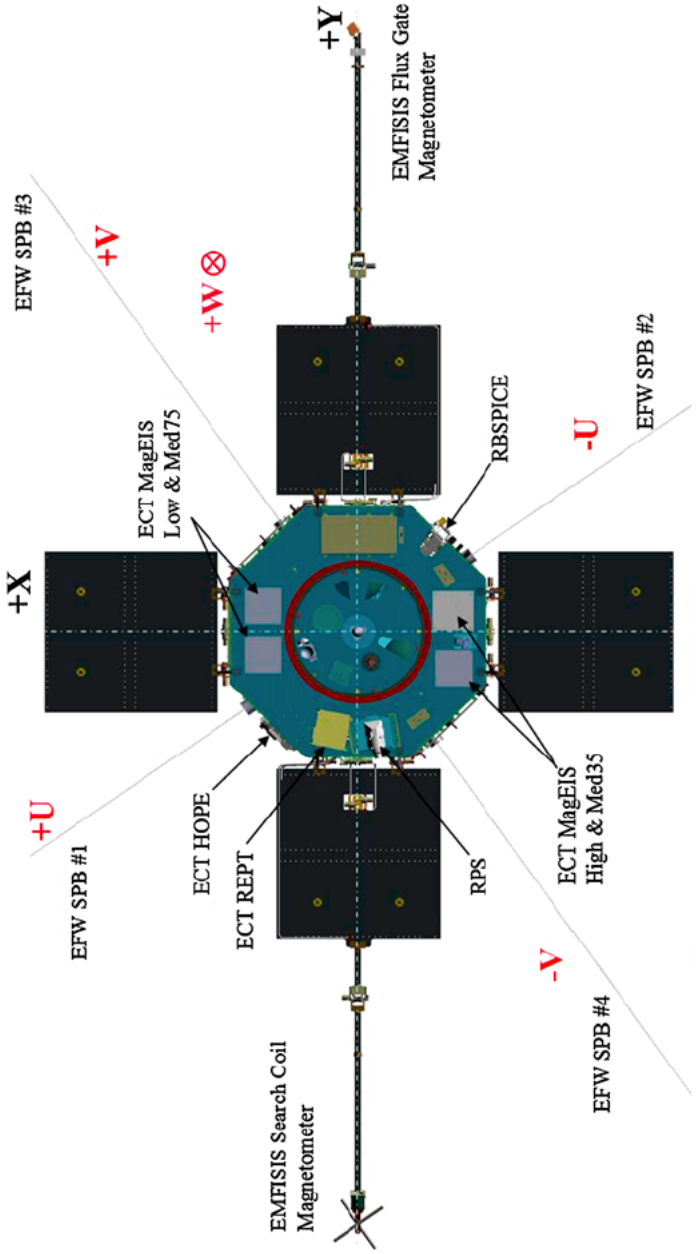

FIGURE 2.5: The Van Allen Probes instrument suite layout. EMFISIS MSC and MAG sensors are nominally aligned with the EFW wire booms which define the UVW coordinate system (spinning coordinates) which is implemented for science data. Also shown is the spacecraft XYZ coordinate system. From *Kletzing et al.* [2013].

electron gyrofrequency calculated using the onboard magnetometer, this data allows for the calculation of the electron plasma frequency, and hence the electron density. This is achieved using Equation 2.9.

$$f_{UH}^2 = f_{pe}^2 + f_{ce}^2 \tag{2.9}$$

where f_{UH} is the upper hybrid frequency (which is observable in the wave observations, see Figure 1.18), f_{pe} is the electron plasma frequency and f_{ce} is the electron gyrofrequency. Determining f_{pe} is useful for understanding the effectiveness of electron acceleration by interaction with chorus waves which is dependent on the parameter, f_{pe}/f_{ce} [*Summers et al.*, 1998].

2.5.3.2 Magnetometer (MAG)

The EMFISIS fluxgate magnetometer measures the 3-components of the vector magnetic field in high time resolution (64 vectors per second). Knowledge of the magnetic field is a crucial for understanding the dynamics of particle distributions that are heavily dependent on the magnetic field and its fluctuations.

Chapter 3

Solving the Radiation Belt Riddle: A Guide to Phase Space Density

The following work is published in Astronomy and Geophysics *(Hartley, D. P. and M. H. Denton, (2014), Solving the Radiation Belt Riddle, Astronomy and Geophysics, December 2014, Volume 55, Issue 6, Pp. 6.17-6.20).*

3.1 Abstract

The radiation belts - areas around the Earth where high-energy charged particles are trapped by the planet's magnetic field - are complex regions influenced by factors such as the solar wind, particle interactions and solar activity. Understanding them is important because of the potential damage that high-energy particles can inflict. The ability to interpret satellite measurements of electron flux at a single position and time - in parallel with the variations of the geomagnetic field - is essential to advance the understanding of radiation belt dynamics. Phase space density is a calculated quantity that can account for these magnetic fluctuations because it exists in a coordinate system relating to the trajectories of radiation belt particles. We provide a step-by-step review of the techniques used to convert measured electron fluxes to phase space density, independent of satellite instrumentation and detailed analysis. In addition, we discuss examples of how specific source and loss processes might be observed in the phase space density signature. We hope that this review of phase space density calculation techniques will prove useful for newcomers to this exciting and burgeoning field.

3.2 Introduction

In 1958 the Explorer I spacecraft launched, carrying an experiment designed by James Van Allen [*Van Allen et al.*, 1959; *Van Allen and Frank*, 1959]. Intended to measure cosmic rays, the instrumentation was also sensitive to highly energetic electrons. Measurements revealed energetic electrons encompassing the Earth - something that led one of Van Allens colleagues, Ernie Ray, to state, famously, 'space is radioactive!'. This inadvertent discovery prompted research into what are now known as the Van Allen radiation belts - two toroidal regions of energetic particles constrained within the Earths magnetic field (see Figure 3.1).

The processes that fuel the belts high degree of variability are of great interest to the scientific community. While many source and loss processes have been identified (e.g. *Friedel et al.* [2002]; *Liemohn and Chan* [2007]), quantitative understanding of how these processes wax and wane between different events remains elusive. Interactions with various electromagnetic waves can pitch-angle scatter electrons and thus enhance losses to the atmosphere. In contrast, radial diffusion processes can transport electrons outwards and cause losses to the magnetopause. With observational evidence available in support of both processes, it is the quantification of the relative contribution from each mechanism that needs to be addressed. It has become clear that a complete and accurate predictive capability will be hard to achieve until these mechanisms are better understood. Energetic electron flux in the outer radiation belt can vary by up to five orders of magnitude in only a few hours (e.g. *Baker et al.* [2007]; *Horne et al.* [2009]), meaning that a high degree of spatial and temporal resolution is required in order for the mysteries behind these processes to be unravelled.

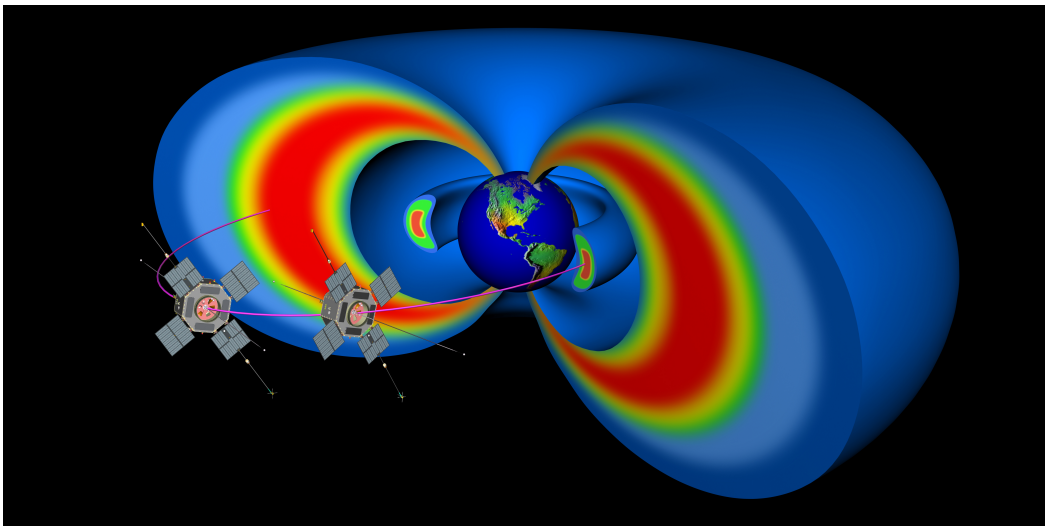

FIGURE 3.1: A representation of the Van Allen radiation belts with two spacecraft, representing the Van Allen Probes, and their orbit through the heart of the radiation belts. Credit: JHU/APL, NASA

In 2012, more than 50 years since the discovery of the radiation belts, the high-profile NASA Van Allen Probes mission was launched successfully. Onboard the two identical spacecraft are detectors designed specifically to study the particles of the radiation belts in high temporal and spatial resolution. With interest in radiation belt dynamics heightening during the Van Allen Probes mission, there has been a rapid output of new and exciting research results that implement the phase space density (PSD) calculation. This article is intended to supplement these publications by providing a thorough description of the PSD calculation that is independent from detailed analysis of any individual event.

Particle detectors typically measure the electron flux at a distinct set of parameters; energy, E, pitch angle, α, position, $\mathbf{x}$, and time, t. In turn, each of these parameters relates to one, or more, of the adiabatic invariants associated with electron motion in the geomagnetic field. The first adiabatic invariant, μ (associated with the gyro-motion of a particle about a magnetic field line), is dependent upon both the particle's pitch

angle (the angle between the particle's velocity vector and the magnetic field vector) and the particle's energy. The second adiabatic invariant, K (related to a particle's bounce motion along a magnetic field line between the magnetic mirror points), depends upon pitch angle, while the inverse of the third adiabatic invariant, L^* (related to a particle's drift motion about the Earth), depends upon both position and pitch angle. A full definition of the adiabatic invariants is given by *Schulz and Lanzerotti* [1974], *Walt* [1994], and *Green and Kivelson* [2004]. The aim of this article is to provide a step-by-step review of the techniques used to convert measured electron fluxes to PSD, independent from satellite instrumentation and detailed analysis. In order to follow the steps outlined in this article, electron flux measurements are required to be resolved in terms of both pitch-angle and energy.

PSD is used in multiple fields of physics research such as quantum mechanics, thermodynamics, astrophysics, and space science. Here, we discuss how PSD can assist in differentiating between source mechanisms, as well as being used to identify loss processes, for radiation belt dynamics.

In the context of the radiation belts, PSD is defined as the electron flux divided by the square of the momentum (e.g. *Chen et al.* [2007b]). It is therefore possible to convert measured electron fluxes to PSD and obtain the corresponding adiabatic invariants. This, however, would result in PSD values with different adiabatic invariants at each instant of time. Typically, values for the first and second adiabatic invariants are selected to remain constant for the duration of a study, thus allowing determination of the variations in PSD and L^*. Converting to PSD, which uses a coordinate system aligned with radiation belt particle trajectories, allows the geomagnetic field variations to be considered in parallel

with electron flux variations. This technique has been developed and described in detail in a number of studies using electron flux measurements from different spacecraft (e.g. *Hilmer et al.* [2000]; *Green and Kivelson* [2004]; *Chen et al.* [2006]; *Shprits et al.* [2012]). Descriptions of how signatures of different physical mechanisms might be observed in the PSD vs. L^* profile have also been produced (e.g. *Turner et al.* [2012]; *Reeves et al.* [2013a]).

3.3 Methodology

Because in situ observations of the geomagnetic field provide measurements at only one location on a magnetic field line, it is necessary to implement a magnetic field model in order to calculate the second adiabatic invariant, K, and the inverse of the third invariant, L^*. If using measurements from a spacecraft without a magnetometer onboard, it is necessary to use a magnetic field model for the calculation of all three adiabatic invariants. Calculating the PSD at chosen values of μ and K can be performed in six steps;

1. Calculate the pitch angle of chosen K
2. Calculate the energy of chosen μ and K
3. Calculate the fluxes (for each energy channel) at chosen K
4. Convert these fluxes at chosen K to PSD
5. Calculate the PSD at chosen μ and K
6. Calculate L^*

Once these steps have been carried out (as summarised in Figure 3.2), the PSD vs. L^* profile can be interpreted to provide evidence for active source and loss processes.

For step 1, to calculate the second adiabatic invariant, K, as a function of pitch angle and time, it is common to use the International Radiation Belt Environment Modeling Library [*Boscher et al.*, 2004-2008] and Equation 3.1. This relationship is shown schematically in Figure 3.2a.

$$K = \int_{s_m}^{s'_m} \left[B_m - B\left(s\right)\right]^{1/2} ds \tag{3.1}$$

The IRBEM-LIB is a set of source code dedicated to modelling the radiation belts available at: http://sourceforge.net/projects/irbem/files/. Depending upon the chosen magnetic field model, the IRBEM library requires different solar wind parameters and geomagnetic activity indices as drivers (e.g. Disturbance-storm-time index, Solar wind dynamic pressure, Interplanetary magnetic field, etc...). These can be obtained from OMNIweb [*King and Papitashvili*, 2005], a database of solar wind observations propagated to the Earth's bowshock. Various functions within the IRBEM-LIB can be utilised, with some directly providing adiabatic invariants, or related quantities, as outputs. IRBEM-LIB is used to obtain a value for quantity, I, in small increments of pitch angle, at each instance of time. This value, I, is related to the second adiabatic invariant, K, through the equation; $K = I\sqrt{(B_m)}$ where B_m is the magnetic field at the mirror point, which can also be output by the library functions. It is then possible to interpolate between the calculated $K(\alpha)$ values to obtain a pitch angle for any desired K at each instance of time (Figure 3.2a). (Common units for the second adiabatic invariant, K, are $G^{1/2}km$,

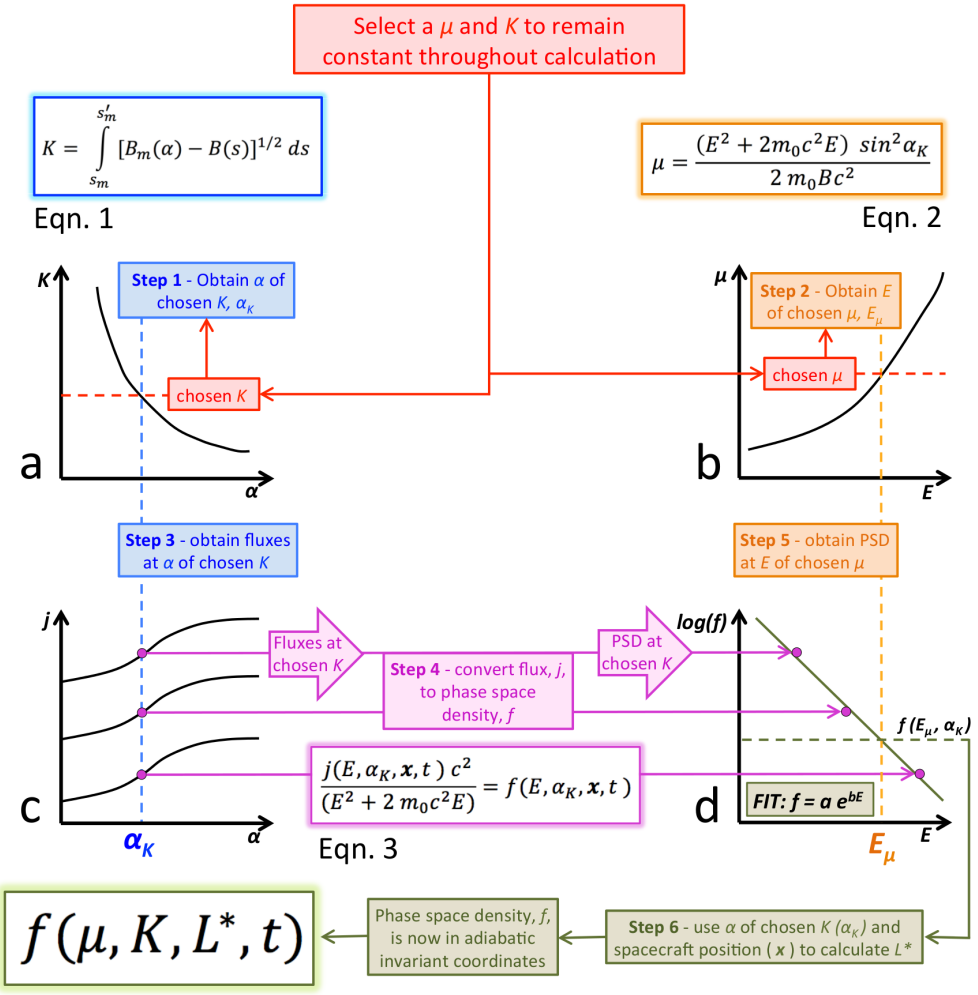

FIGURE 3.2: A schematic representation of the phase space density calculation. Initially, a value of μ and K are selected to remain constant throughout the calculation. Panel (a) shows schematically the relationship between the second adiabatic invariant, K, and pitch angle, α, for one instance of time, calculated by Eqn. 1 from the Figure. The dashed red line indicates the selected value of K, and the dashed blue line indicates the pitch angle that corresponds to the selected K, α_K. Panel (b) is a schematic representation of the relationship between μ and E, (as calculated by Eqn. 2 from the Figure) for the pitch angle obtained in panel (a), α_K. The dashed red line indicates the selected value of μ and the dashed orange line indicates the energy that corresponds to the selected value of μ, E_μ. Panel (c) represents the electron flux pitch-angle distribution for three instrument energy channels. The dashed blue line indicates the pitch angle that corresponds to the selected K, α_K, from panel (a). From these pitch-angle distributions, it is possible to 'read off' the electron flux values at the pitch angle α_K to obtain a set of flux values that vary with instrument energy channels. These flux values are then converted to PSD using Eqn. 3 from the Figure. Panel (d) displays these phase space density values as a function of the instrument energy channels. By fitting a function to these values of the form shown on panel (d), and substituting in the energy corresponding to the selected value of μ, E_μ, from panel (b), it is possible to obtain the phase space density corresponding to selected values of μ and K, $f(E_\mu, \alpha_K)$. Using α_K and the spacecraft position $\mathbf{x}$, the IRBEM library is used to calculate L^*. The electron PSD has now been calculated in adiabatic invariant coordinates for one instance of time. This process can be repeated for the required number of time intervals.

model output units are: I in Earth radii, R_E, and B_m in nT, yielding units of $nT^{1/2}R_E$.) A value of the second invariant, K, is selected to remain constant throughout the calculations. This, in turn, yields a pitch angle of fixed K, which will be referred to as α_K hereafter (see Figure 3.2a). While K is kept constant over time, the pitch angle at fixed K temporally evolves due to the varying input solar wind conditions that drive the magnetic field model. The pitch angle obtained, α_K, is also used in calculation of the first and third adiabatic invariants.

Step 2 involves calculating the energy of chosen μ and K (see Figure 3.2b) by using Equation 3.2. This relationship is shown schematically in Figure 3.2b.

$$\mu = \frac{\left(E^2 + 2m_0c^2E\right) sin^2\alpha}{2m_0c^2B} \tag{3.2}$$

If using measurements from a spacecraft with a magnetometer onboard, the measured magnetic field can be used in the calculation of μ, otherwise it is required to implement the model magnetic field. Because μ is pitch-angle dependent, the pitch-angle of chosen K, α_K, is used. Calculating μ in small intervals of energy, negates the complication of solving Equation 3.2 for E. It is thus possible to interpolate between these calculated μ values, obtaining the energy corresponding to the chosen value of μ and K, E_μ, at a single instance of time (see Figure 3.2b). Typical units for μ are MeV/G, care must be taken to avoid confusion between units of energy (m_0c^2 is in Joules whereas units for E are likely to be in eV, keV or MeV).

Step 3, calculating the flux (for each energy channel) at chosen K, requires performing a fit of the pitch angles to the measured electron flux, j (see Figure 3.2c). This is

required at each of the instrument energy channels available. There are several methods available for calculating the full pitch angle distributions, such as fitting sums of powers of trigonometric functions (e.g. *Green and Kivelson* [2004]) or to invert an accurate pitch-angle distribution using optimal estimation (e.g. *Selesnick and Blake* [2000a]; *Hartley et al.* [2013]). After obtaining the full pitch-angle distribution, it is possible to determine the flux at pitch angle, α_K, for each energy channel. This, in turn, yields a set of flux values at constant K, varying in energy.

In step 4, using Equation 3.3, the flux values obtained for the selected value of K are converted to PSD.

$$\frac{j\left(E, \alpha_K, x, t\right) c^2}{\left(E^2 + 2m_0 c^2 E\right)} = f\left(E, \alpha_K, x, t\right) \tag{3.3}$$

The energies, E, to be used in this equation are the central energies of the satellite instrument channels. Again, the user needs to be aware of different units of energy. These calculated PSD values are at the chosen value of K, varying in energy.

Through step 5 it is now possible to produce a fit of these PSD values of chosen K against energy using an equation of the form, $f = ae^{bE}$, where f is PSD, E is energy and a and b are the fit coefficients. Having obtained the energy of fixed μ (E_μ) in step 2, this can now be substituted into the fitting equation, using the calculated coefficients a and b, to obtain the PSD at the chosen values of μ and K, $f(E_\mu, \alpha_K)$ (see Figure 3.2d).

Finally, the inverse of the third adiabatic invariant, L^*, is calculated, as step 6. L^* is the radial distance in the equatorial plane where an electron would reside if all external fields were removed, leaving only the internal geomagnetic field. This makes L^* a commonly

used parameter in PSD studies. To calculate L^*, it is required to implement a magnetic field model and the IRBEM library. Since the drift path of a particle depends upon its pitch angle, the pitch angle corresponding to the desired value of K, α_K, is used as an input. L^* is a direct output from the IRBEM library. This gives L^* and PSD at fixed values of the first and second adiabatic invariants, μ and K, for one time instance. This process can then be repeated for each time interval to provide the PSD and L^* variation at constant μ and K.

3.4 Sources and Losses

Calculating the PSD vs. L^* profile can assist in differentiating between internal acceleration mechanisms (local acceleration in the inner magnetosphere radiation belt region) or external acceleration (electrons are transported and accelerated inwards from a seed population in the outer magnetosphere). Figure 3.3 is a schematic diagram showing how internal and external acceleration might look in the PSD vs. L^* profile (adapted from *Green and Kivelson* [2004]). The red lines indicate the PSD vs. L^* profile prior to acceleration (time = t_1) with the blue line showing the effect of the acceleration event (time = t_2). It is generally accepted that external acceleration alone does not lead to negative gradients inwards of the source region because they rely on radial diffusion to transport and accelerate the electron population (see Figure 3.3a). Therefore, a negative gradient in the PSD vs. L^* profile is a strong signature of internal acceleration mechanisms that violate either the first, or second, adiabatic invariant (see Figure 3.3b). However, external acceleration mechanisms, coupled with electron losses at large L-shells, may

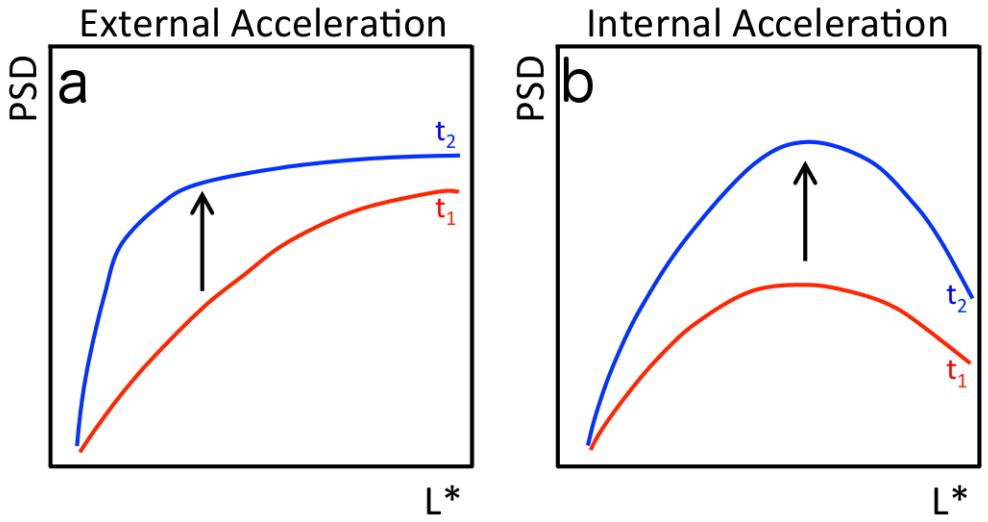

FIGURE 3.3: Schematic diagram showing how internal and external acceleration may appear in the PSD vs. L^* profile (adapted from *Green and Kivelson* [2004]). Panel (a) shows a PSD increase caused by radial diffusion from an external source mechanism, whereas panel (b) indicates a PSD increase caused by a local internal acceleration mechanism. The red lines indicate the PSD vs. L^* profile prior to acceleration (time = t_1) with the blue line showing the effect of the acceleration event (time = t_2).

also cause a negative gradient in the PSD vs. L^* profile. These two processes may be distinguished by studying the time evolution of the PSD vs. L^* profile.

Figure 3.4 is a schematic diagram of how specific loss mechanisms, particularly magnetopause shadowing (the loss of particles to the solar wind via the dayside magnetopause), might look in the PSD vs. L^* profile (adapted from *Turner et al.* [2012]). Figure 3.4a shows a PSD vs. L^* profile prior to a solar wind pressure increase; the vertical red line indicates the magnetopause location. Figure 3.4b displays the PSD vs. L^* profile during enhanced solar wind pressure. This increase in solar wind pressure causes the magnetopause to move inwards, intersecting previously closed electron drift paths, resulting in losses. Figure 3.4c shows the PSD vs. L^* profile once the solar wind pressure has relaxed and the magnetopause has returned to larger L^*. There is a steep radial gradient in the PSD due to the magnetopause shadowing process. Radial diffusion will always

act to transport particles so that PSD gradients are reduced. Such outwards transport (radial diffusion) may cause further magnetopause losses as well as an apparent loss at a fixed L^* due to the radial diffusion process. In order to study other loss processes (such as losses to the atmosphere through pitch-angle scattering) it is common to couple PSD calculations with spacecraft observations in low Earth orbit (LEO) (e.g. *Turner et al.* [2013]) or with observations from the Balloon Array for RBSP Relativistic Electron Losses (BARREL) [*Millan and the BARREL team*, 2011; *Millan et al.*, 2013].

3.5 Summary

Overall, PSD has successfully been used by numerous authors to investigate the processes that drive the electron radiation belts variability (e.g. *Hilmer et al.* [2000]; *Brautigam and Albert* [2000]; *Selesnick and Blake* [2000a]; *Green and Kivelson* [2004]; *Chen et al.* [2006, 2007b]; *Turner et al.* [2012]; *Hartley et al.* [2013]; *Reeves et al.* [2013a]; *Schiller et al.* [2014]). It is the uniqueness of considering electron measurements in parallel to the geomagnetic field variations, and in a coordinate system that follows particle trajectories, that makes PSD an essential tool in solving the radiation belt riddle.

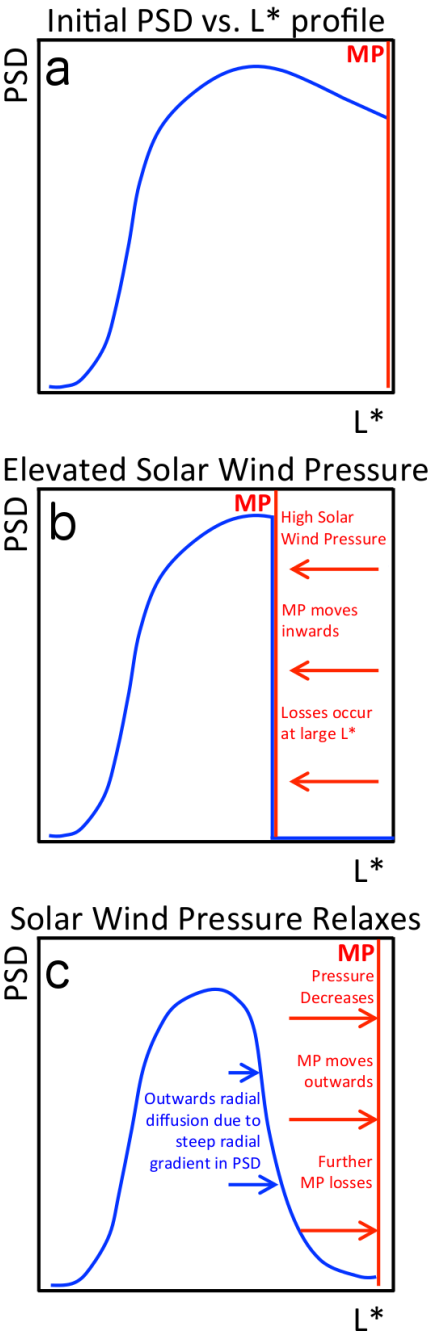

FIGURE 3.4: A schematic diagram showing how the PSD vs. L^* profile might evolve during a period of elevated solar wind pressure (adapted from *Turner et al.* [2012]). Panel (a) shows an initial peaked PSD vs. L^* profile. Panel (b) depicts the magnetopause location moving inwards, due to the increased solar wind pressure, resulting in losses to the magnetopause (magnetopause shadowing). In panel (c), the solar wind pressure relaxes, resulting in the magnetopause location moving back to larger L^*. The PSD vs. L^* profile contains a steep radial gradient at the magnetopause location from panel (b), resulting in enhanced radial diffusion (blue arrows). Outwards radial transport may result in further losses to the magnetopause.

Chapter 4

Case Studies of the Impact of High-Speed Solar Wind Streams on the Electron Radiation Belt at Geosynchronous Orbit: Flux, Magnetic Field and Phase Space Density

The following work is published in the Journal of Geophysical Research: Space Physics *(Hartley, D. P., M. H. Denton, J. C. Green, T. G. Onsager, J. V. Rodriguez, and H. J. Singer (2013), Case studies of the impact of high-speed solar wind streams on the electron radiation belt at geosynchronous orbit: Flux, magnetic field, and phase space density, J. Geophys. Res. Space Physics, 118, 6964-6979, doi:10.1002/2013JA018923).*

4.1 Abstract

Investigation of electron radiation belt dropouts has revealed the importance of a number of loss processes, yet there remains a lack of quantitative detail as to how these processes wax and wane between events. The overarching aim of this study is to address the issue of electron radiation belt dropouts. This is achieved using in situ observations at geostationary orbit from GOES-13 (pitch-angle-resolved electron data and magnetic field measurements) to examine the outer electron radiation belt during three high-speed stream-driven storms. Analysis and interpretation are aided by calculation of the phase space density (PSD) as a function of the three adiabatic invariants. Our results confirm the importance of outwards adiabatic transport as a mechanism for causing electron dropouts at GEO, however study of the pitch-angle distributions indicates that other loss mechanisms are also likely to be occurring during these HSS-driven storms. Two of the studied events exhibit similar evolutionary structure in their pitch-angle distributions, (i) highly peaked distributions immediately prior to the dropout (ii) sharp transitions between peaked and isotropic and then subsequent butterfly distributions, and (iii) isotropic distributions at minimum flux shortly afterwards (dusk). We also address the difficulty in interpreting PSD calculations by comparing the T96 model

magnetic field with that measured by GOES-13. Our results are intended as a first step in quantifying the timeline of events that occur in the radiation belts following the arrival of a HSS - particularly timely given the increase in HSS-occurrence expected in the declining phase of the current solar cycle.

4.2 Introduction

The intensity of the outer radiation belt depends on complex physics connecting the global magnetosphere including the plasma sheet, the ring current, and the ionospheric plasma. All of these systems are modified when high-speed solar-wind streams (HSSs) impact on the magnetosphere. Our goal is to unravel this coupling by analysing several HSS events and their impact on the outer radiation belt.

High-speed streams exhibit characteristic structure in the solar wind (e.g. *McPherron and Weygand* [2006]; *Tsurutani et al.* [2006] and references therein). Upon impact on the magnetosphere HSSs are known to cause dramatic changes to the Earth's plasma populations [*Borovsky and Denton*, 2006], as well as driving electromagnetic waves which may lead to losses (e.g. *Elkington et al.* [1999]; *Mann et al.* [2004]; *Thorne* [2010]; *MacDonald et al.* [2010]). HSSs cause morphological changes in the outer electron radiation belt (e.g. *Miyoshi et al.* [2007]; *Hudson et al.* [2008]; *Borovsky and Denton* [2009b]; *Morley et al.* [2010]), the plasma sheet (e.g. *Denton and Borovsky* [2009]), the ring current (e.g. *Jordanova et al.* [2012]), the ionosphere-plasmasphere (e.g. *Denton et al.* [2009]; *Sojka et al.* [2009]) and the magnetotail (e.g. *Denton and Cayton* [2011]; *Borovsky and Denton* [2011]).

In the outer radiation belt the arrival of a HSS is usually associated with a rapid decrease (*dropout*) in the measured electron flux (e.g. *Onsager et al.* [2002], *Green et al.* [2004]). The onset of this dropout usually occurs after the passage of the IMF sector reversal prior to the passage of the corotating interaction region stream interface [*Borovsky and Denton*, 2009b]. Following the dropout is a subsequent increase (*recovery*) in electron flux some hours or days later [*Freeman*, 1964; *Nagai*, 1988; *Chen et al.*, 2007b]. In many instances the electron flux may recover to a level greater than that prior to HSS-arrival [*Miyoshi and Kataoka*, 2008; *McPherron et al.*, 2009b]. *Reeves et al.* [2003b] found that about half of geomagnetic storms increased the fluxes; about one in five storms decreased the fluxes; and the remaining storms produced changes that were less than a factor of two either up or down. The precise cause of the dropout has been variously associated with a number of processes (e.g. *Friedel et al.* [2002]; *Shprits et al.* [2008a,b]) including (i) transport, both adiabatic and non-adiabatic (the electrons move away from the detector, for example via inwards or outwards radial diffusion), (ii) loss to the atmosphere (as wave-particle interactions cause electrons to temporarily populate the bounce-loss cone), (iii) loss to the magnetopause (as wave-particle interactions cause electrons to temporarily populate the drift-loss cone). Evidence for these processes, along with various combinations, has been uncovered by numerous authors although there remains a lack of quantitative detail as to how these processes wax and wane between different events. *Borovsky and Denton* [2009b] suggest electromagnetic ion-cyclotron (EMIC) waves as the primary cause of HSS-driven relativistic-electron dropouts, whereas *Turner et al.* [2012] suggests outwards radial transport with losses being primarily to the magnetopause. Additionally, *Meredith et al.* [2011] concluded that there is no evidence for enhanced precipitation of relativistic electrons during the MeV flux drop out, although

noted that precipitation of lower energy electrons did become enhanced during the passage of the high-speed stream. Although aspects of the physics involved are known, a complete and accurate physical understanding, and predictive capability, remains elusive.

In this study we first analyse the quiet day variation of the electron radiation belt in order to provide a baseline from which to compare the impact of different HSS-induced dropout events. We then present case studies of three HSS induced dropouts, focusing on measured electron flux, calculated phase space density and pitch angle distribution variations in order to investigate the loss mechanisms that drive these rapid electron reductions. Studying these parameters, in addition to the geomagnetic field, allows us to build up a picture of the different processes that drive the variation of the electron radiation belt.

4.3 Analysis Method and Instrumentation

The Magnetospheric Electron Detector (MAGED) onboard GOES-13 [GOES N Databook Revision C, CDRL PM-1-1-03] provides pitch-angle-resolved flux measurements in the 30-600 keV energy range. Consisting of nine telescopes, each with a central pitch angle, α, defined by the orientation of the magnetic field at any time instant, MAGED measures flux in five energy channels parametrized as 30-50, 50-100, 100-200, 200-350 and 350-600 keV. The fluxes are dead-time and proton-contamination corrected. Converting to differential flux gives central energies of 40, 75, 150, 275 and 475 keV. A magnetometer measures the three orthogonal components of the magnetic field within a range of $\pm$512 nT and is accurate to $\pm$ a few nT.

In this study we perform a fit of the flux-pitch angle distribution for each 1-minute interval along the orbit following the method of *Selesnick and Blake* [2000b] (for full details see Appendix A). It is then possible to extrapolate electron flux values at all pitch angles. This allows us to calculate the pitch-angle anisotropy between perpendicular ($\alpha = 90°$) and parallel ($\alpha = 15°$) orientation for each energy channel where pitch-angle anisotropy is parametrized as the electron flux at 15° divided by the electron flux at 90° ($\parallel$ / $\perp$). Additionally, we calculate the omnidirectional electron flux measurement from all nine telescopes of GOES-13 at 1-minute time intervals. This allows for a single flux measurement (hereby referred to as electron flux, unless a specific pitch-angle/orientation is stated) to be presented at each energy at each instance of time.

Trapped radiation belt electrons undergo three characteristic types of motion; gyro-motion about magnetic field lines, bounce motion along magnetic field lines between the mirror points and drift motion around the earth. Each type of motion has an associated adiabatic invariant. These invariants remain conserved so long as changes to the magnetic field occur on time-scales longer than the associated particle motion period (adiabatic). Violation of these invariants results in magnetospheric changes that are irreversible (non-adiabatic). Following the techniques used by *Green and Kivelson* [2004], we use the *Boscher et al.* [2004-2008] library, T96 magnetic field model [*Tsyganenko and Stern*, 1996] and in-situ magnetic field measurements to calculate the phase space density (PSD) as a function of the three adiabatic invariants, μ (calculated using magnetic field from GOES), K and L^* (calculated using T96 magnetic field model). The values chosen were μ=200 MeV/G (as this best represents the 350-600 keV energy channel from GOES-13) and K=2500 $G^{1/2}$km or K$\sim$ 0.4 $G^{1/2}R_E$ (equating to a pitch angle between $\sim$15° and

$\sim$35°). Permitted input values to the T96 magnetic field model include -100$\leq$ Dst (nT) $\leq$20, 0.5$\leq$ P_{SW} (nPa) $\leq$10, |By_{IMF}|(nT) $\leq$10, |Bz_{IMF}|(nT) $\leq$10. Where required input values exceed the maximum permitted, the maximum value is used (as is the case with P_{SW} at times during this study). *Huang et al.* [2008] showed that for storms where the Dst index does not go below -60 nT (as is the case in all examples presented here), the T96 magnetic field model predicts magnetic field components that lie within non-storm magnetospheric fluctuations.

Calculating the phase space density with fixed values of the first and second adiabatic invariants allows us to observe how the L^* parameter, in addition to the phase space density itself, vary over the periods of interest. Observing variations in L^* provides insight as to whether electrons are being adiabatically transported either inwards or outwards. It is noted that PSD calculations are subject to limitations in the accuracy of the implemented magnetic field model. It is also noted that the calculation of L^* returns a value regardless of double minima along dayside field lines, where radiation belt particles undergo drift orbit bifurcation and thus cannot be associated with a specified drift shell (e.g. *Ukhorskiy et al.* [2011]).

The implications of errors in the magnetic field model can be understood. Figure 4.1 displays the effect of errors in calculating L^* and K on the PSD as in *Green and Kivelson* [2004]. If the model overestimates/underestimates the magnetic field magnitude, this leads to an overestimate/underestimate of L^* which, in turn, affects the calculated PSD as shown in Figure 4.1 panel (a). An underestimate of L^* leads to an underestimate of the PSD at high L^* and an overestimate of the PSD at low L^*. An overestimate of L^* leads to an overestimate of the PSD at high L^* and an underestimate of the PSD at low L^*.

Since the second adiabatic invariant, K, depends upon the length of the magnetic field line as well as the magnetic field strength along it, any discrepancies between the model and actual magnetic field magnitude and stretching component will affect the calculation. Therefore, if the implemented model predicts an over/under stretched magnetic field then this yields an underestimate/overestimate of K and if the implemented model over/under predicts the magnetic field magnitude then this leads to an overestimate/underestimate of K. This has implications on the calculated PSD as shown in Figure 4.1 panel (b); an overestimate of K yields an overestimate of the PSD at the chosen K, whereas an underestimate of K yields an underestimate of the PSD at the chosen K.

Firstly, a quiet day is studied in order to understand the behaviour of the fluxes and PSD and to evaluate the performance of the T96 model during quiet geomagnetic conditions. Subsequently, three dropout events are examined with periods of interest shown in Table 4.1. Additionally, Table 4.1 lists specific details for each event; maximum and minimum solar wind velocities, maximum flow pressure, maximum and minimum fluxes, maximum and minimum Dst index and maximum Kp index. The selection of these HSS driven events was performed through observations of solar wind parameters, identifying the characteristic HSS structure (increase in solar wind velocity, density pulse straddling the boundary between slow and fast solar wind, shear flow).

4.4 Quiet Time Variation

In order to observe the behaviour of electron flux and calculated phase space density at geosynchronous orbit (GEO) during quiet time, a single day (January 30, 2011) was examined, where the solar and geomagnetic conditions were calm and stable. Figure

	Quiet Time	Event 1	Event 2	Event 3
Start Time	Jan 30, 2011 0UT	Jan 6, 2011 16UT	Feb 4, 2011 12 UT	Apr 11, 2011 12 UT
End Time	Jan 31, 2011 0 UT	Jan 7, 2011 10UT	Feb 5, 2011 12 UT	Apr 12, 2011 12 UT
V_{max} (km/s)	299.5	551.0	678.2	630.7
V_{min} (km/s)	270.3	327.8	360.6	312.0
P_{max} (nPa)	1.80	15.2	15.2	17.4
$log_{10}(flux_{max})$	1.697	2.268	2.820	2.945
$log_{10}(flux_{min})$	1.222	-0.361	-0.277	-0.995
Dst_{max} (nT)	7	24	21	32
Dst_{min} (nT)	-4	-38	-59	-51
Kp_{max}	3.0	5.0	5.7	5.0

TABLE 4.1: Solar wind and geophysical parameters for the events in this study; maximum/minimum solar wind velocity, maximum solar wind pressure, maximum/minimum flux observed by GOES-13 in the 475 keV electron channel, maximum/minimum Dst index and maximum Kp index.

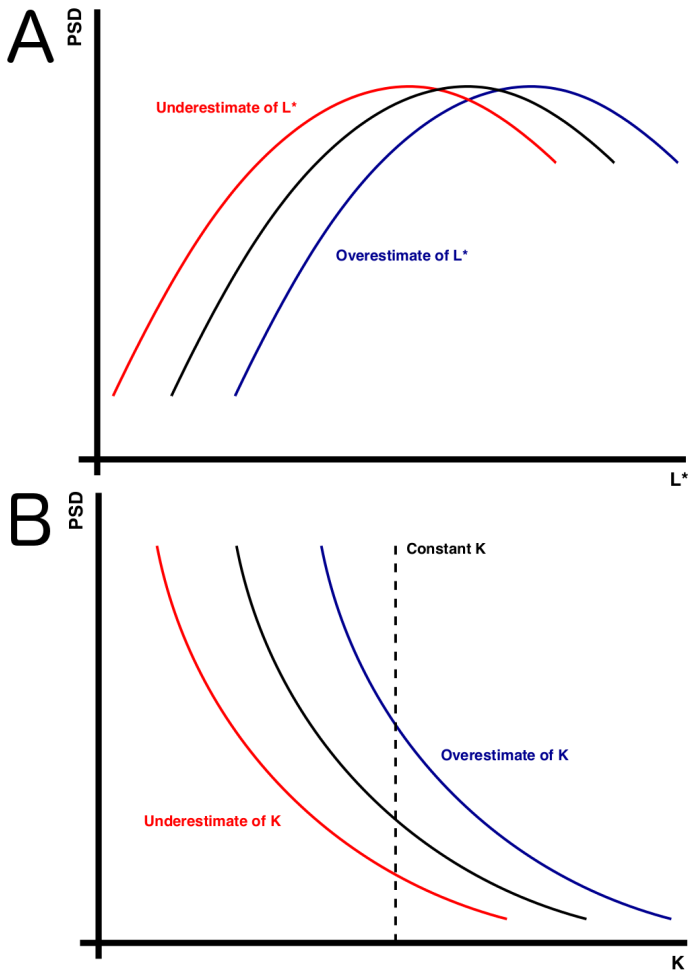

FIGURE 4.1: (a) Schematic representation of how an error in the calculation of the inverse of the third adiabatic invariant, L^*, will affect the predicted phase space density. (b) Schematic representation of how an error in the calculation of the second adiabatic invariant, K, will affect the predicted phase space density (after *Green and Kivelson* [2004]).

4.2 displays a variety of parameters for this quiet period. Panel (a) shows the solar wind velocity (V_{SW}) and solar wind flow pressure from OMNI 2 [*King and Papitashvili*, 2005]. Panel (b) displays geomagnetic indices Kp, Dst and SYM-H in addition to Dst* (the pressure corrected Dst index), calculated using the methodology of *Borovsky and Denton* [2010a]. Panel (c) shows the magnetic field magnitude as measured by GOES-13 at GEO and the predicted magnetic field magnitude from the T96 model at the location of GOES-13. In addition, an indicator of the 'goodness' of the model fit to the observed

magnetic field is displayed in color at the top of the panel; green indicates that the model is within ±15% of the measured magnetic field, yellow indicates ±30%, orange ±45% and red ± > 45%.

$$\theta_{stretch} = arctan(B_Z/({B_X}^2 + {B_Y}^2)^{1/2}) \tag{4.1}$$

Panel (d) displays the magnetic field stretching angle in centred dipole coordinates (MAG) as defined in equation 4.1 of both the measured field from GOES-13 and the predicted magnetic field from the T96 model at the GOES-13 position. This panel also displays an indication of 'goodness' of fit of the model stretching angle to the observations with the colors parameterized the same as in panel (c). Panel (e) shows the omnidirectional electron flux measurements averaged over all 9 look directions for three energy channels from GOES-13 in addition to their pitch-angle anisotropy in relation to the measured magnetic field. Panel (f) shows the calculated phase space density as a function of time and L^* with fixed values of μ and K (μ=200 MeV/G and K=2500 $G^{1/2}$km ($\sim$ 0.4 $G^{1/2}R_E$)).

The solar wind speed remains relatively constant around 300 km s^{-1} for the entire period with the solar wind flow pressure remaining less than 2 nPa. The Kp index remains very low for the duration of the quiet period with geomagnetic indices Dst, Dst* and SYM-H showing no large disturbances. The magnetic field magnitude is slightly greater on the dayside than the nightside due to the compression by the solar wind. The magnetic field stretching angle, defined in equation 4.1, describes the shape of the magnetic field lines as measured at GOES-13.

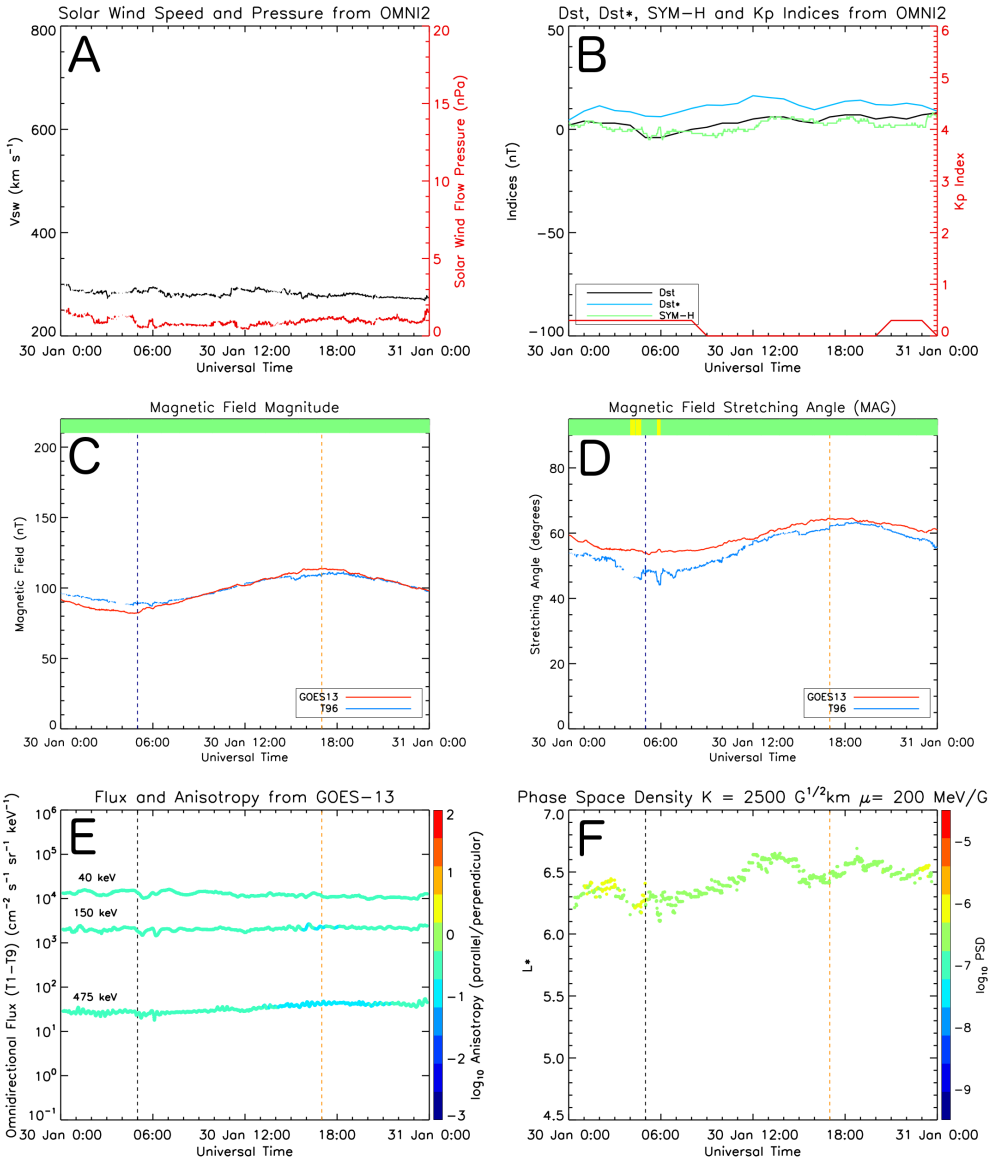

FIGURE 4.2: Quiet time variation: 0 UT January 30 to 0 UT January 31. (a) Solar wind speed (black) and solar wind flow pressure (red) from OMNI2. (b) Geomagnetic indices Dst, Dst* (calculated using methodology of *Borovsky and Denton* [2010a]), SYM-H and Kp indices. (c) The magnetic field magnitude from the T96 magnetic field model and as measured in situ by GOES-13. (d) The magnetic field stretching angle from T96 and as measured by GOES-13 (centred dipole coordinates). An indicator of the 'goodness' of the model fit to the observed magnetic field is displayed in colour at the top of the panel; green indicates that the model is within ±15% of the measured magnetic field, yellow indicates ±30%, orange ±45% and red ± > 45%. (e) Omnidirectional flux measurements for three energy channels from GOES-13 where colour coding is electron anisotropy (warm colours indicating parallel orientation and cold colours indicating perpendicular orientation). (f) The phase space density as a function of time and L^* with fixed values of μ and K (μ=200 MeV/G and K=2500 $G^{1/2}$km or K$\sim$ 0.4 $G^{1/2}R_E$). In panels (c) through (f) vertical dashed orange and black lines indicate local noon and midnight respectively.

An angle closer to 90° indicates a largely dipolar field (since GOES-13 is at approximately 11° geomagnetic latitude, the stretching angle will normally be less than 90° unless the magnetosphere is compressed) whereas a smaller angle indicates a highly stretched field. Hence, the compression on the dayside gives a more dipolar field (stretching angle close to 90°) with a more stretched field on the nightside (smaller stretching angle) as is expected during quiet conditions. In this study we display the magnetic field stretching angle in centred dipole coordinates (MAG) in order to remove any seasonal effects. The T96 magnetic field model yields results that accurately follow the measurements from GOES-13 (within ±15% in magnitude and stretching angle for the vast majority of the period). Electron flux measurements from GOES-13 remain steady during this quiet period displaying very little variation in magnitude. The pitch-angle anisotropy is as expected considering drift shell splitting; the electron pitch-angle-distribution is more perpendicularly-oriented on the dayside than the nightside and vice-versa with relatively smooth transitions between the two. This can also be seen in the complete pitch-angle-distribution (see Figure 4.6 panel (a)). Such variations are not caused by changes in the averaged electron flux, rather variations in the pitch-angle distribution around the spacecraft orbit, and must be considered when interpreting data for active periods. The L^* parameter from the PSD calculation during this time varies between around 6.1 and 6.7. The phase space density for this period remains relatively steady with only minor variations. These variations may be due to PSD gradients in L^* (since the drift shell contours are not circles, at geosynchronous orbit we sample a range of L^*) or errors introduced by the magnetic field model. This 'noise' in the PSD calculation must also be considered when analysing active periods (small scale changes in PSD may not necessarily be attributable to a physical process. For larger variations, it is more

likely that the noise is being dominated by the process driving the variations).

4.5 Event 1: January 6, 2011

Figure 4.3 contains plots of the same parameters as described for Figure 4.2 for the period of interest highlighted for Event 1 in Table 4.1.

4.5.1 Solar Wind and Geomagnetic Conditions

The solar wind structure (see Figure 4.3 panel (a)) is characteristic of a HSS with an initial calm period [*Borovsky and Steinberg*, 2006] with slow solar wind speeds. The solar wind speed then exhibits a clear increase, remaining elevated for several days. A density pulse arises due to the interaction between slow and fast solar wind, thus producing a peak in the flow pressure. The co-rotating interaction region (CIR) consists of compressed slow solar wind followed by compressed fast solar wind. At around ∼15 UT Jan 6, the Kp index increases abruptly, indicating the onset of enhanced convection, and remains elevated for around 2 days (see Figure 4.3 panel (b)). In addition, the geomagnetic disturbance due to the HSS arrival is evident in Dst, Dst* and SYM-H indices.

4.5.2 Flux

Electron flux and pitch-angle anisotropy are shown in Figure 4.3 panel (e), with the full pitch-angle distribution shown in Figure 4.6 panel (b). Between 16-21 UT Jan 6, prior to

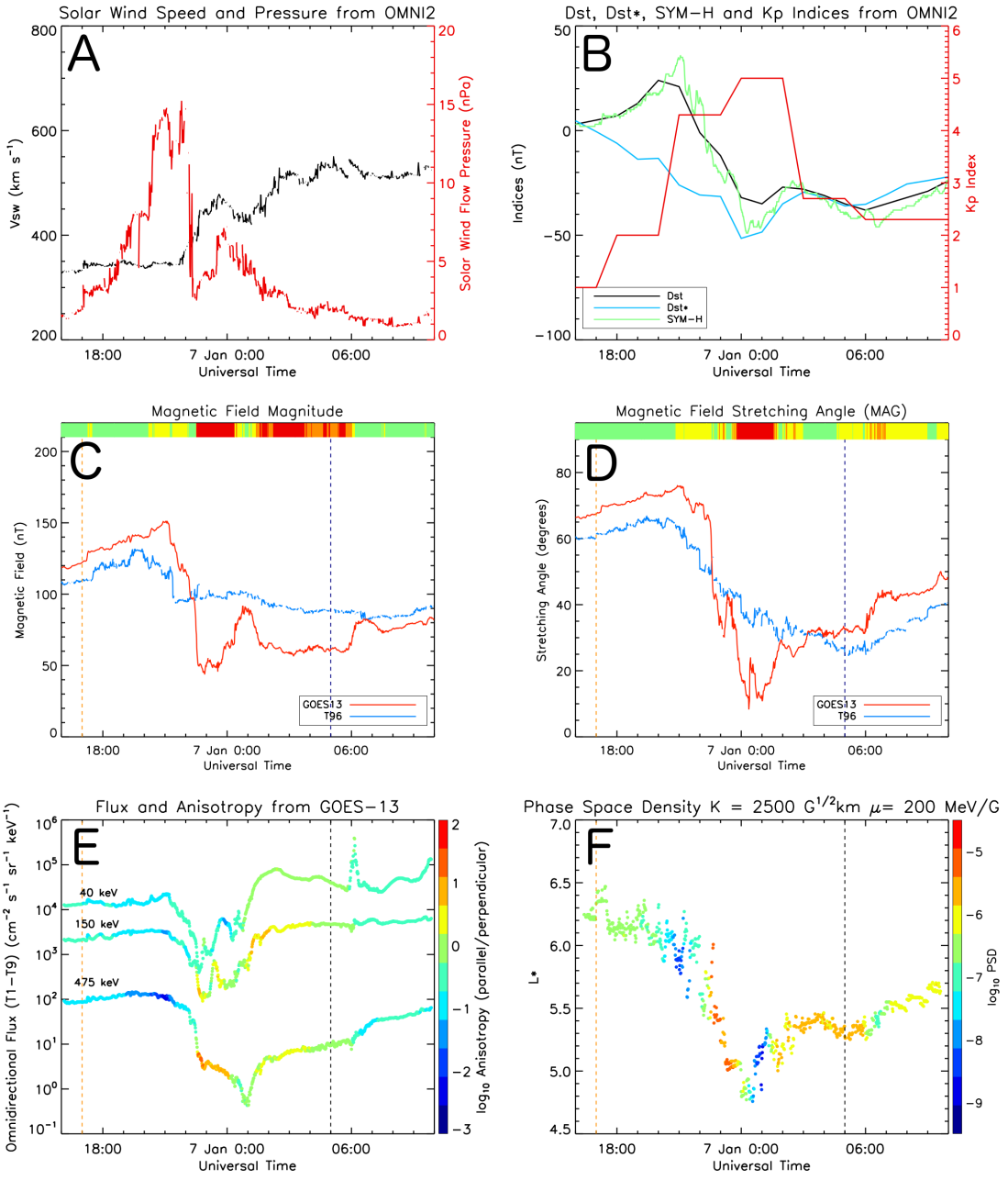

FIGURE 4.3: Event 1: 16 UT January 6 to 10 UT January 7. Displays the same parameters as described in Figure 4.2.

the dropout, the flux of 475 keV electrons increases steadily whilst the pitch-angle distribution becomes progressively more perpendicular oriented. Immediately prior to the dropout (around dusk local time) the electron distribution is extremely perpendicularly oriented. From 21 to 23 UT a large reduction in the electron flux is observed (almost two orders of magnitude), with the pitch angle distribution becoming highly parallel oriented towards 23 UT. From this point, the flux continues to reduce by a further order of magnitude reaching a minimum around 1 UT January 7. During this reduction, the pitch angle distribution becomes approximately isotropic. From 1-2 UT January 7 we observe a recovery in the electron flux by approximately one order of magnitude. From 2 UT until the end of the period of interest at 10 UT, the electron flux recovers steadily.

4.5.3 Pitch Angle Distribution

The pitch-angle-distribution (see Figure 4.6 panel (b)) is peaked (higher fluxes close to 90°, GOES-13 on the dayside) prior to the dropout, becoming increasingly peaked as the dropout approaches (21 UT Jan 6, increasing pressure). This can be seen by increasing fluxes close to 90° and decreasing fluxes around 0° and 180°. As the dropout occurs (21 UT Jan 6), the pitch-angle distribution becomes more isotropic with increasing fluxes around 0° and 180° and decreasing fluxes around 90°. At around 22:30 UT January 6, the flux around 90° suddenly reduces by several orders of magnitude whilst the flux closer to 0° and 180° also decreases, but at a much slower rate. By around 1 UT January 7, the electron flux has dropped out across the entire pitch-angle distribution. Following this time the flux begins to recover, firstly at more parallel pitch angles (butterfly distribution, GOES-13 on the nightside) with perpendicular electrons returning later. The

pitch-angle distribution follows the following sequence during this dropout event: (i) peaked distribution, (ii) increasingly peaked distribution immediately prior to dropout, (iii) reduction around 90° and increase around 0° and 180° leading to more isotropic distribution, (iv) sudden loss around 90° leading to butterfly distribution, (v) decay of butterfly distribution to become isotropic (minimum flux), (vi) recovery as butterfly distribution, (vii) recovery across all pitch angles.

4.5.4 Magnetic Field

Magnetic field magnitude and stretching angle as measured by GOES-13 are displayed in Figure 4.3 panels (c) and (d). The magnetic field strength increases steadily between 16-21 UT from 120 nT to around 150 nT. The peak magnetic field strength measured by GOES-13 does not occur when the spacecraft is located at noon local time, rather this peak is coincident with the onset of the dropout in the measured electron flux. From 21-23 UT, the magnetic field magnitude reduces from 150 nT to around 50 nT before increasing again between 23 UT January 6 and 1 UT January 7 from 50 nT to around 90 nT. The field then decreases to between 60 and 70 nT and remains at this magnitude for approximately 4 hours (2-6 UT). Around 6 UT the magnetic field magnitude increases by around 20 nT before remaining approximately constant until the end of the period of interest at 10 UT.

The magnetic field stretching angle between 18-21 UT January 6 displays a steady increase from around 65-75° indicating an increasingly dipolar field. The time of largest stretching angle (most dipolar) is coincident with the onset of the dropout in the electron flux. The stretching angle then decreases slowly at first between 21-22 UT before

rapidly decreasing from approximately 70° to 30° in the next hour (22-23 UT). At 23 UT the magnetic field stretching angle increases by approximately 10° to around 40° before decreasing further to a minimum of around 10° (very highly stretched) just after 0 UT January 7. Following this, we observe a brief spike in the stretching angle approximately 20° in magnitude between 0-1 UT January 7 before observing a steady increase in the stretching angle between 1 UT and the end of the period of interest at 10 UT.

4.5.5 Phase Space Density

Calculated phase space density as a function of time and L^* with fixed values of μ and K (μ=200 MeV/G and K=2500 $G^{1/2}$km ($\sim$ 0.4 $G^{1/2}R_E$)) is shown in Figure 4.3 panel (f). Between 16-21 UT January 6 the calculated phase space density reduces by approximately one order of magnitude with L^* slowly decreasing to around 5.8. Between 21-23 UT the decrease in L^* hastens with the phase space density values increasing by around two orders of magnitude. Between 23 UT January 6 and 0 UT January 7 we observe a plateau in L^* between 5.0-5.1 with the phase space density beginning to decrease. Around 0 UT January 7, L^* decreases once more to between 4.7-4.9 with phase space density continuing to decrease. L^* then returns to between 5.0-5.1 around 1 UT with very low phase space density values. For the remainder of the period of interest we observe L^* trend upwards barring a small reduction as the spacecraft passes around midnight local time. The calculated phase space density remains highly dynamic during this period although is generally elevated as the electron flux increases during recovery.

4.5.6 Discussion

Measurements from GOES-13 show two reductions in the electron flux that contribute to the dropout. Firstly a reduction from 21 UT to approximately 22:30 UT January 6, then a secondary reduction occurring between 22:30 UT January 6 and 1 UT January 7. During the first reduction in electron flux, the pitch-angle anisotropy becomes steadily less perpendicular oriented before abruptly becoming highly parallel oriented at around 22:30 UT January 6. This can be seen in the full pitch-angle distribution in Figure 4.6 panel (b) as a sudden loss of electrons around 90° (magnetopause losses). The lower energy electrons begin to return to GEO at this time (22:30 UT), however the 475 keV electron flux continues to decrease, albeit less abruptly. During this second reduction the pitch-angle anisotropy shifts from parallel orientation to rather more isotropic. This shift occurs much slower than the initial change to parallel orientation. Whilst the variation in L^* during the dropout indicates that radial transport, coupled with a radial gradient in the electron flux, could play a crucial role in reducing electron fluxes at GEO, it is noted that PSD calculations are very sensitive to the magnetic field and therefore any variation between the model output and the measured magnetic field could lead to errors in both PSD and L^*, thus affecting our interpretation (as described in Figure 4.1). These errors in magnitude are largest between 23:30 and 0:30 UT and 1:30 and 6:30 UT and largest in stretching angle between 23:30 and 1:30 UT indicating that the PSD results may not be accurate during these times. The first reduction in electron flux (between 21 UT and 22:30 UT) occurs when the solar wind flow pressure is reducing, causing the geomagnetic field magnitude measured by GOES-13 to decrease. It therefore follows that outwards adiabatic transport of electrons would occur shown by a reduction in L^*

from the phase space density calculation. Losses to the magnetopause may occur and are consistent with the shift in pitch-angle anisotropy. Such losses may greater affect the higher energy electron population due to their drift speed being higher than that of lower energy electrons. Therefore for a given time period on an open drift shell, more high energy electrons are likely to escape the system than those with lower energy. The secondary reduction in 475 keV electron flux (between 22:30 UT January 6 and 1 UT January 7) occurs during a period when the solar wind flow pressure is increasing, causing the geomagnetic field to increase in magnitude and become increasingly stretched. If we consider the period from 23 UT January 6 to 1 UT January 7 and only PSD values with an L^* between 5.0 and 5.1, it is apparent that the PSD decreases rapidly (two orders of magnitude in around two hours). This indicates that there is some other process, besides adiabatic transport, causing a reduction in electron flux at GEO. This could be outwards radial diffusion caused by a steep radial gradient in the PSD following losses to the magnetopause as concluded by *Turner et al.* [2012], who attributed the dropout primarily to outwards radial transport with losses being primarily to the magnetopause. In addition, given the fact that the pitch angle distribution is highly parallel oriented at this time, any pitch angle scattering from wave-particle interactions could efficiently cause concurrent losses to the atmosphere. Whilst some authors have concluded that atmospheric losses are not significant during HSS-driven dropout events [*Morley et al.*, 2010; *Meredith et al.*, 2011; *Hendry et al.*, 2012], some also suggest precipitation immediately prior to the recovery [*Hendry et al.*, 2012; *Clilverd et al.*, 2013] indicating that precipitation into the atmosphere may not be the primary driver of flux dropouts, but may certainly play a role, and even be involved in a process that triggers the recovery. RBSP/BARREL [*Millan et al.*, 2013] conjunctions may be able to clarify the importance

of atmospheric loss as a mechanism for contributing to radiation belt dropouts. Another possible contributing factor to the electron reduction between 22:30 UT January 6 and 1 UT January 7 is the inherent local time variation; electrons respond adiabatically to the extreme stretching of the magnetic field (dusk sector) resulting in flux asymmetry in local time [*Green et al.*, 2004]. It is noted however that the T96 output magnitude and the magnetic field measured in situ by GOES-13 display a large discrepancy (around 50 nT) during the time of this second reduction in electron flux which could indicate potential inaccuracies in PSD and L^* (as highlighted in Figure 4.1, overestimate of L^* causing an overestimate of PSD at high L^* and underestimate of PSD at low L^*).

It appears that outwards transport, adiabatic or otherwise, plays a key role in causing losses for this event, as concluded by *Turner et al.* [2012]. In addition, there appears to be some other mechanism, differing from adiabatic transport, causing losses to the system. This indicates a two-stage process of loss mechanisms causing the flux dropout at GEO for this event.

4.6 Event 2: February 4, 2011

Figure 4.4 displays the same parameters as described in Figure 4.2 for the period of interest highlighted for Event 2 in Table 4.1.

4.6.1 Solar Wind and Geomagnetic Conditions

The solar wind speed displays a steady increase starting around 20 UT February 4 (see Figure 4.4 panel (a)). The flow pressure becomes elevated around this increase as is

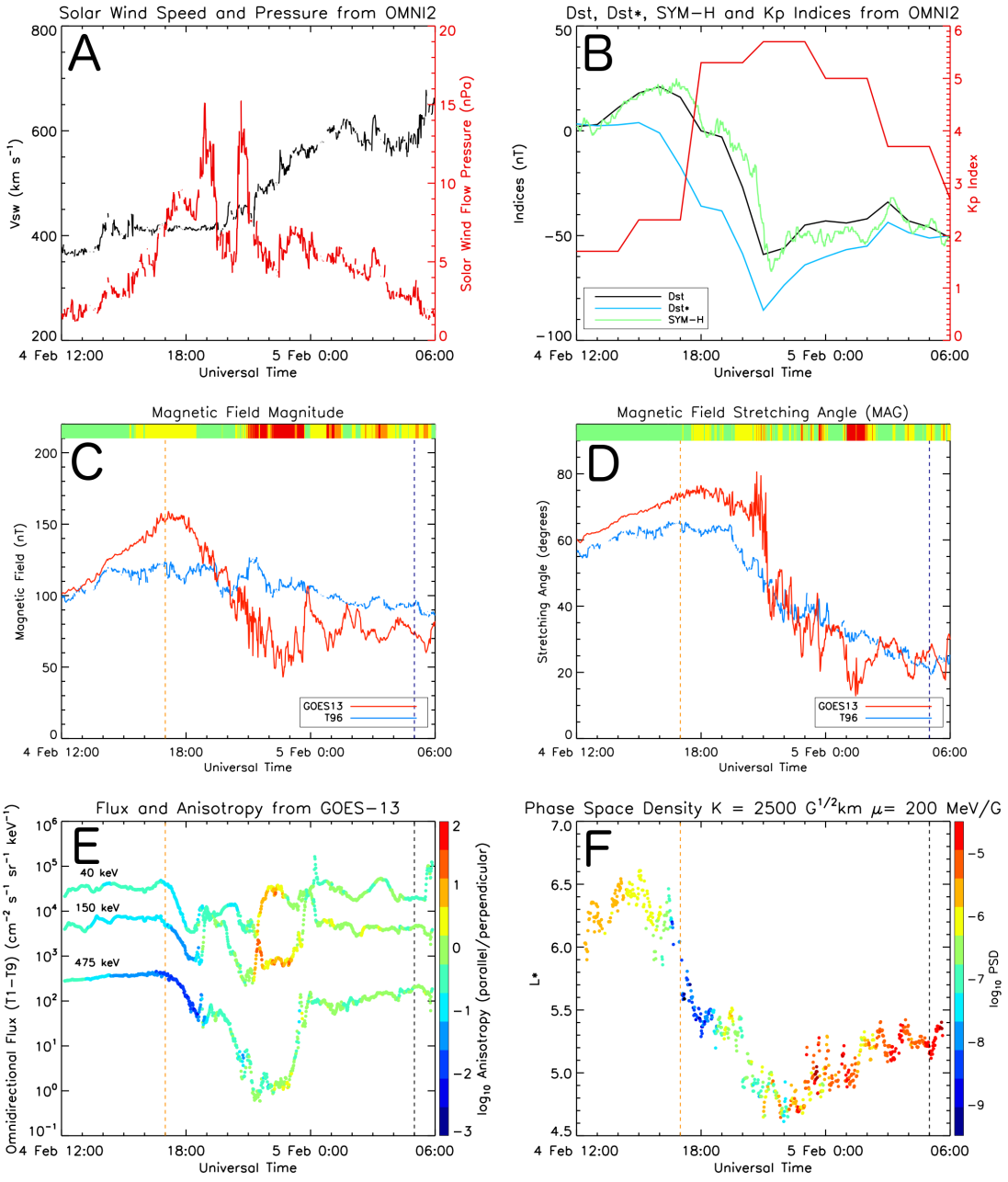

FIGURE 4.4: Event 2: 12 UT February 4 to 6 UT February 5. Displays the same parameters as described in Figure 4.2.

characteristic of high-speed solar-wind streams. The Kp index starts off relatively low before increasing sharply to above 5 at around 17 UT February 4 indicating the onset of enhanced convection and the arrival of the HSS (see 4.4 panel (b)). The geomagnetic disturbance is evident in the Dst, Dst* and SYM-H indices starting at around 13 UT February 4. Dst and SYM-H begin to become increasingly positive between 13-16 UT February 4 peaking around +20 nT before decreasing between 16-21 UT February 4 to a minimum between -60 and -70 nT.

4.6.2 Electron Flux

Electron flux and pitch-angle anisotropy are shown in Figure 4.4 panel (e), with the full pitch angle distribution shown in Figure 4.6 panel (c). From 12 UT to 17 UT on February 4, 2011, a slow steady increase in the flux of 475 keV electrons is observed. From 17 UT through 21 UT, the flux reduces by more than two orders of magnitude. From being highly perpendicularly oriented prior to this dropout, the pitch-angle anisotropy changes during the course of the event so that by the time of minimum flux, the pitch-angle distribution appears to be largely isotropic. From this time, the electron population remains extremely low for approximately 2 hours (∼21-23 UT) before abruptly increasing by around two orders of magnitude in a period of approximately 1 hour (∼23-0 UT). The measured electron flux remains approximately constant and largely isotropic for at least 6 hours following this period (0-6 UT).

4.6.3 Pitch Angle Distribution

The pitch-angle-distribution (see Figure 4.6 panel (c)) is initially isotropic with high fluxes across the entire pitch-angle-distribution. From 12-17 UT February 4, the distribution becomes increasingly peaked with elevating flues close to 90° and decreasing fluxes around 0° and 180°. Between 17-19 UT, the fluxes reduce around 90° with a sharp boundary where the distribution becomes suddenly isotropic, possibly even butterfly, around 19 UT. The fluxes across the entire distribution then fall, with the minimum occuring between 21-23 UT. Following this, the flux begins to recover as a butterfly distribution (GOES-13 on the nightside). The pitch-angle distribution follows the following sequence during this dropout event: (i) isotropic distribution, (ii) highly peaked distribution prior to dropout, (iii) reduction around 90° and increase around 0° and 180° leading to more isotropic, possibly even butterfly distribution, (iv) decay of butterfly distribution to become isotropic (minimum flux), (v) recovery as butterfly distribution (GOES-13 on nightside).

4.6.4 Magnetic Field

Magnetic field magnitude and stretching angle as measured by GOES-13 are displayed in Figure 4.4 panels (c) and (d). The magnetic field magnitude from 12 UT to 17 UT measured by GOES-13 displays a steady increase from 100 nT to 150 nT with the peak approximately coincident with when the spacecraft is located at noon local time. This is also the time that electron population begins to decrease. The magnetic field magnitude from 17-18 UT is steady at around 150 nT. Following this time, the magnetic field magnitude decreases from 150 nT to 50 nT within 4-5 hours. The magnetic field

magnitude then sharply increases to around 100 nT at 0 UT February 5 before decreasing to approximately 70 nT within the subsequent hour. After this period, the magnetic field stays within the 60-95 nT range. Between 12-18 UT, February 4, we observe a steady increase in the magnetic field stretching angle from around 60° to 75°. From 18-20 UT the magnetic field stretching angle decreases from 75° to 65° before a quick increase back up to 80°. At around 21 UT the magnetic field stretching angle decreases abruptly from 80° to around 35° within a 30 minute period. From this point, the stretching angle is highly dynamic although trends downwards reaching a minimum of about 15° between 1-2 UT February 5. It is noted that the spacecraft is situated in the dusk sector during this highly variable period.

4.6.5 Phase Space Density

Calculated phase space density as a function of time and L^* with fixed values of μ and K (μ=200 MeV/G and K=2500 $G^{1/2}$km ($\sim$ 0.4 $G^{1/2}R_E$)) is shown in Figure 4.4 panel (f). Initially, (from 12- 18 UT February 4) a decrease in phase space density is observed with L^* varying between 5.8-6.6. From 17-22 UT we see a sizeable decrease in the L^* parameter indicating that GOES-13 is now on a drift shell that was previously closer to the Earth. From 22 UT Feb 4 to around 0 UT Feb 5, a large increase in the PSD is observed whilst L^* only increases slightly, between 4.6-5.4. The PSD then remains high and L^* between 4.7-5.5 for the remainder of the period of interest (until 6 UT Feb 5).

4.6.6 Discussion

From 12-17 UT February 4 we observe a slow, steady increase in electron flux yet the calculated phase space density decreases greatly. This is attributed to a change in the pitch-angle distribution of the electrons and thus we observe a decrease in phase space density at our chosen K. The flux values support this explanation (see Figure 4.4 panel (e) and Figure 4.6 panel (c)). As the flux increases steadily, the orientation of the electrons becomes more perpendicular to the magnetic field and therefore at our chosen K value, equivalent to around 30°, we observe a decrease in electron flux, and thus phase space density. L^* during this period (12-15 UT) displays an increase from 6.0-6.5 and then a decrease back to 6.0 between 15-17 UT. Whilst from 12-15 UT, discrepancies between the measured magnetic field by GOES-13 and the output of T96 are relatively small (a maximum of around 10 nT in magnitude and 10° in stretching angle), from 15-17 UT these discrepancies increase (a maximum of around 35 nT in magnitude and almost 20° in stretching angle) indicating that the errors highlighted in Figure 4.1 must be considered and that interpretation PSD results during this period should be approached with caution.

Between 17-21 UT, the 475 keV electron flux reduces by around 3 orders of magnitude with a sharp boundary from a peaked pitch-angle-distribution to an isotropic or even butterfly distribution occurring at 19 UT (see Figure 4.6 panel (c)). During this period, we observe a large decrease in the L^* parameter (outwards radial transport of electrons). However, the magnetic field magnitude measured by GOES-13 shows discrepancies to that produced by the T96 model. Between 15-19 UT, output from T96 predicts a weaker magnetic field than that observed by GOES-13 whereas from around 20 UT February 4

to the end of the period of interest at 6 UT February 5, the output from T96 predicts a stronger magnetic field than that measured by GOES-13. Between 21-0 UT the error in magnetic field magntiude is largest, implying that the calculated L^* during this period may well be an overestimate since $|B_{T96}| >> |B_{GOES}|$. In this event, the stretching angle from T96 follows the measured stretching angle relatively closely and therefore the magnitude errors are likely to be more significant in affecting the calculated PSD and L^* (as described in Figure 4.1). Again it appears that transport, adiabatic or otherwise, contributes substantially to this dropout event. The pitch-angle-distribution displays similar structure to that observed for Event 1 (Figure 4.6 panels (b) and (c)); a highly peaked distribution immediately prior to the dropout, with a sharp boundary between a peaked distribution and an isotropic/butterfly distribution apparent, whilst the averaged electron fluxes are still decreasing. This sharp transition occurs as the solar-wind pressure decreases. It is noted however that this similarity in evolutionary structure could at least partly be due to the similar position of GOES-13 in local time during these dropout events.

4.7 Event 3: April 11, 2011

Figure 4.5 displays the same parameters as described in Figure 4.2 for the period of interest highlighted for Event 3 in Table 4.1.

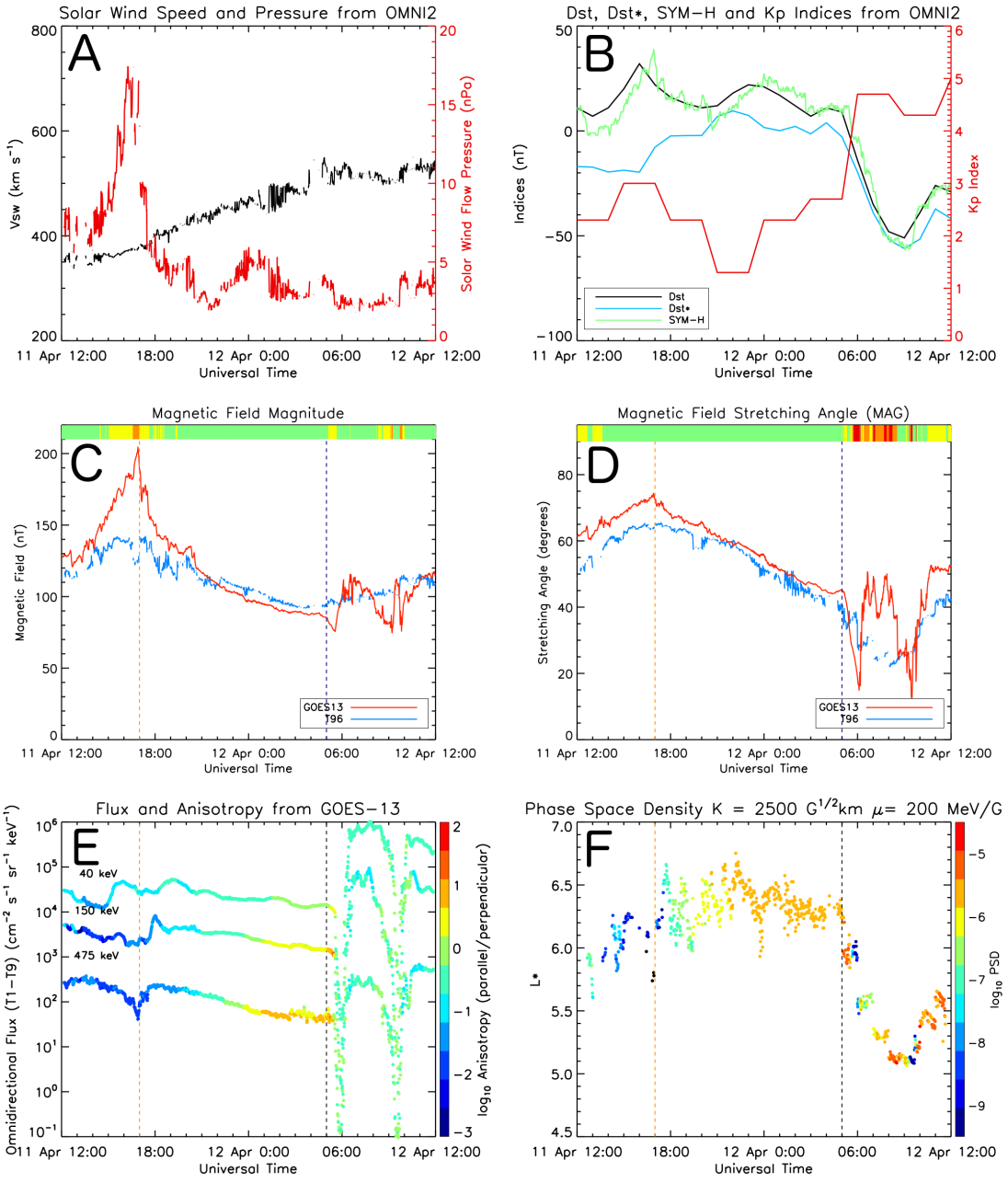

FIGURE 4.5: Event 3: 12 UT April 11 to 12 UT April 12. Displays the same parameters as described in Figure 4.2.

4.7.1 Solar Wind and Geomagnetic Conditions

The solar wind speed for this event (see Figure 4.5 panel (a)) exhibits a slow increase from around 350 km s^{-1}, at 12 UT April 11, up to around 550 km s^{-1} by 5 UT April 12. The pressure is observed to increase, as is characteristic of a high-speed solar-wind stream, peaking around 17 UT April 11. The Kp index displays a small increase coincident with the enhanced solar wind pressure before a subsequent decrease. It is not until later (around 5 UT April 12) that we see a larger increase in Kp (coincident with IMF turning abruptly southward), indicating enhanced magnetospheric convection. Geomagnetic indices Dst and SYM-H become increasingly positive between 13-17 UT in response to the increased solar wind flow pressure (see Figure 4.5 panel (b)). It is not until around 5 UT that the characteristic decrease associated with the main phase is observed.

4.7.2 Electron Flux

Electron flux and pitch-angle anisotropy are shown in Figure 4.5 panel (e), with the full pitch angle distribution shown in Figure 4.6 panel (d). From April 11, 12-14 UT, the 475 keV electron flux displays a small increase before decreasing steadily between 14-17 UT (around noon local time). This reduction is not observed in the lower energy electron channels. Subsequently, the 475 keV electron flux increases, reaching pre-reduction values within 1 hour (17-18 UT). Throughout this period, the electrons are highly perpendicularly oriented to the magnetic field. From 18 UT April 11 to 5 UT April 12, the electron fluxes at all measured energies decrease steadily, by almost an order of magnitude. During this reduction, the pitch-angle anisotropy of the 475 keV electrons shifts

from being highly perpendicularly oriented at 18 UT April 11, to being highly parallel oriented by 5 UT April 12. Between 5 and 6 UT April 12, the electron fluxes rapidly decrease by three orders of magnitude. The fluxes then recover rapidly to an elevated level between 6-7 UT. Flux measurements undergo a second rapid loss and recovery between 8 and 11 UT. This reduction is similar in magnitude to the first with fluxes reducing by approximately three orders of magnitude. During the first of these rapid losses and subsequent recoveries, the pitch-angle anisotropy of the 475 keV electrons changes from being highly parallel oriented prior to the reduction, to approximately isotropic afterwards. During the loss and recovery occurring between 8 and 11 UT, the electron orientation to the magnetic field remains approximately isotropic.

4.7.3 Pitch Angle Distribution

The pitch-angle-distribution (see Figure 4.6 panel (d)) is initially highly peaked (GOES-13 on the dayside, 12-18 UT April 11). Between 18 UT April 11 and 5 UT April 12, the distribution steadily turns butterfly with increasing fluxes more parallel oriented to the magnetic field and decreasing fluxes perpendicularly oriented to the magnetic field. Between 5-6 UT and 9-10 UT April 12, the flux across the entire distribution falls to very low values. Almost immediately after, the flux promptly becomes elevated at all pitch angles (isotropic). The pitch-angle distribution follows the following sequence during this dropout event: (i) highly peaked distribution, (ii) steady turning to butterfly distribution as GOES-13 progresses to the nightside, (iii) two rapid reductions across all pitch angles with prompt isotropic recovery to elevated levels.

4.7.4 Magnetic Field

Magnetic field magnitude and stretching angle as measured by GOES-13 are displayed in Figure 4.5 panels (c) and (d). Between 13-17 UT April 11, the measured magnetic field strength exhibits a clear increase from approximately 120-200 nT. The peak magnetic field strength is observed when the spacecraft is located around noon local time. Following this, the magnetic field strength decreases steadily for approximately 12 hours (17 UT April 11 to 5 UT April 12) from around 200-85 nT, with the minimum coincident with when the spacecraft is located at midnight local time. At 5 UT April 12 the magnetic field magnitude reduces slightly, by around 10 nT, before increasing to over 110 nT. A second reduction in magnetic field strength (to around 85 nT) is observed between 7-9 UT. Between 9 and 10 UT, GOES-13 measures a spike in the magnetic field magnitude of about 30 nT. Between 10-12 UT April 12, the magnetic field strength increases steadily, reaching around 115 nT by 12 UT. The magnetic field stretching angle from 13-17 UT April 11 displays a steady increase from approximately 60° to 75°. The peak in stretching angle (most dipolar) is coincident with when the spacecraft is positioned at noon local time. From 17 UT April 11 to 5 UT April 12, the magnetic field stretching angle decreases steadily from around 75° to 45°. Just after midnight local time (5 UT April 12) GOES-13 measures a large change in the stretching of the magnetic field from 45° to around 15° within a period of little over 1 hour. The stretching angle then rapidly increases again from 15° to 50° in the following hour (6-7 UT). The stretching angle then exhibits a second large decrease and rapid increase between 2 and 5 UT April 12 with similar magnitude to the first.

4.7.5 Phase Space Density

Calculated phase space density as a function of time and L^* with fixed values of μ and K (μ=200 MeV/G and K=2500 $G^{1/2}$km ($\sim$ 0.4 $G^{1/2}R_E$)) is shown in Figure 4.5 panel (f). The phase space density during 12-16 UT April 11 shows a small decrease whilst L^* increases slightly from around 5.7-6.3. Following this, we observe a sudden decrease and subsequent increase in L^* whilst the PSD remains low (16-18 UT). This occurs approximately coincident to the small reduction in the measured 475 keV electron flux. From 18 UT April 11 to 5 UT April 12, the phase space density increases by several orders of magnitude whilst the L^* parameter remains within the 5.9 to 6.8 range. From 5-9 UT April 12, L^* decreases from around 6.3-5.1 with the minimum L^* occurring at the same time as the second rapid reduction and subsequent increase in the measured 475 keV electron flux (8-10 UT April 12). During this reduction in L^*, the PSD is highly dynamic, reducing rapidly when the electron flux decreases and increasing when the electron fluxes are elevating. These variations of around three orders of magnitude in the PSD occur on timescales of 1-2 hrs. From 10-12 UT April 12, the PSD values are high with L^* values increasing from around 5.1 to 5.7.

4.7.6 Discussion

We consider this event in three stages; 12 UT April 11 to 18 UT April 11, 18 UT April 11 to 5 UT April 12, 5 UT April 12 to 12 UT April 12.

Firstly, the small reduction in 475 keV electron flux observed centred around noon local time (16-18 UT) occurs simultaneous to a large increase in the magnetic field magnitude

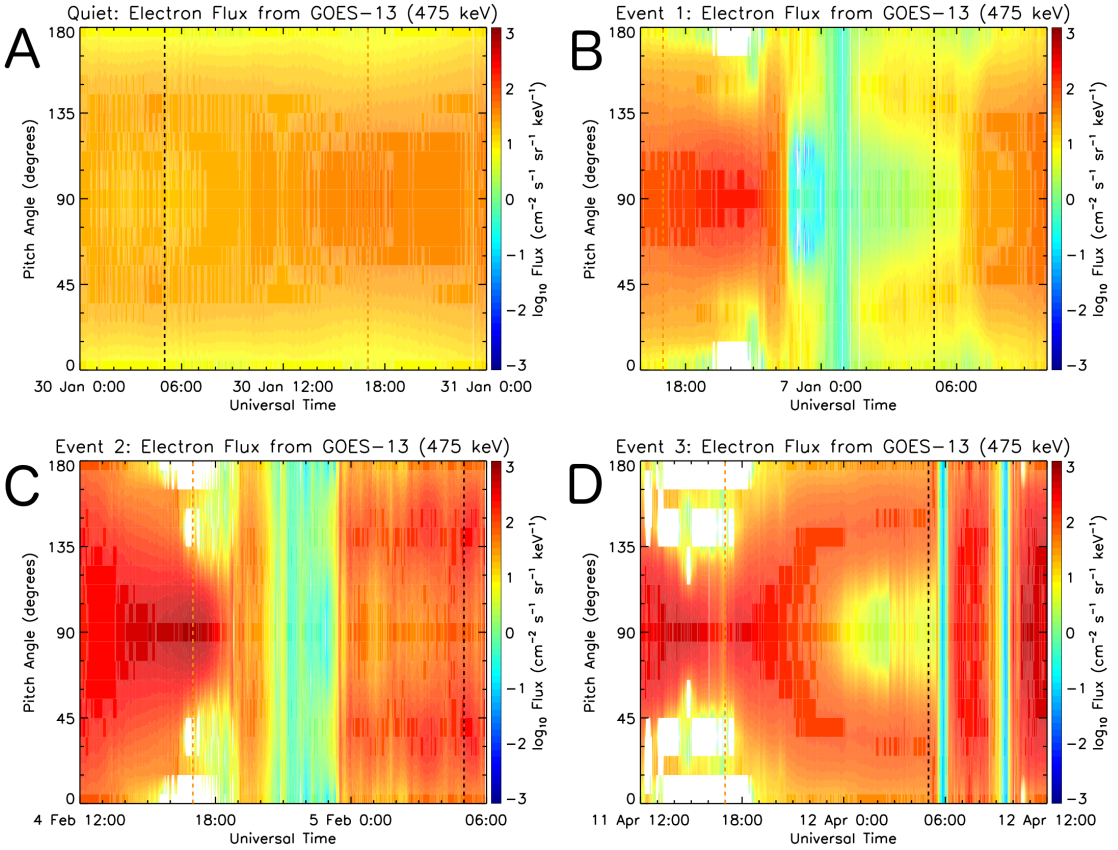

FIGURE 4.6: Pitch angle distributions for the quiet event and the three HSS events. Unfilled white areas indicate either bad/missing data or where the fit of the pitch angle distribution to the data produces unrealistically low flux values. These pitch angle distributions are used to calculate the pitch-angle anisotropy indicated in panel (e) of Figures 4.2, 4.3, 4.4 and 4.5.

measured by GOES-13. This appears to be compression of the magnetosphere, increasing the magnetic field strength and transporting electrons inwards from GEO. However the L* values calculated using the T96 magnetic field model do not support this explanation. At the time of the reduction of 475 keV electron flux, the magnetic field model suggests an L^* decrease, corresponding to outwards transport of electrons. Clearly there is some disagreement between the measurements from GOES-13 and the L* parameter from the phase space density calculation. A likely cause of this discrepancy would be a large disagreement between the T96 output and the actual geomagnetic field, causing

phase space density and L^* values to not be truly representative (larger discrepancy in magnitude coloured orange at 17 UT). Whilst from 12-15 UT April 11 we observe that the T96 model and the measured magnetic field from GOES-13 are in relative agreement, from around 15-19 UT the measured magnetic field magnitude is much larger than that predicted by T96 with the greatest difference of around 80 nT occurring just before noon local time (16-17 UT). At the time of this large difference, a small reduction in the T96 magnetic field strength can be seen (about 15 nT), when in reality the local geomagnetic field strength is increasing (see Figure 4.5 panel (c)). This is coincident with the time that we see the rapid decrease and subsequent increase in the L^* parameter. It is therefore a fair assumption to say that the inaccuracies in the T96 magnetic field model at this time/position are causing this discrepancy, and thus the phase space density and L^* at this time are unlikely to be a true representation of reality. The primary reason for the discrepancy is likely to be the input pressure limit of the T96 magnetic field model (10 nPa), given that the solar wind pressure is quite high during this time.

Secondly, the electron flux measurements from 18 UT April 11 to 5 UT April 12 display a steady reduction whilst becoming increasingly parallel oriented with respect to the magnetic field. During this time, the phase space density increases by about three orders of magnitude. This is due to our selection of constant K and the changing pitch-angle distribution to be more parallel in orientation as the spacecraft moves to the nightside.

Thirdly, between 5-12 UT April 12 we observe two rapid variations in the electron flux at all observed energies. Reductions in electron flux occur at times when the magnetic field, as measured by GOES-13, is highly stretched with the subsequent increases in electron flux occurring as the magnetic field quickly returns to a less stretched state

(dipolarisations). This appears to be due to substorm activity injecting high levels of isotropic plasma (as shown in the pitch-angle-distribution in Figure 4.6 panel (d)). The phase space density during this period displays rapid decreases when the flux decreases. Calculated L^* values begin to reduce at the time of the first decrease in electron flux, and continue to reduce until the second reduction of electron flux. The shape of this L^* variation appears to match the stretching angle output from the T96 magnetic field model. However, the measured stretching angle from GOES-13 displays large discrepancies (up to almost 30°) from the T96 model output during this time (shown in red and orange on the discrepancy indicator in Figure 4.5 panel (d)). This leads to the conclusion that the L^* variation shown between 5-12 UT April 12 in Figure 4.5 panel (e) is not accurate. It would seem more likely for L^* to decrease whilst the field is becoming stretched and for L^* to increase during the period when electron flux is returning and the field is becoming less stretched (dipolarising).

The initial loss (around 17 UT, noon LT) can be attributed to the magnetosphere compressing due to an increase in the solar wind flow pressure causing the magnetic field magnitude to increase. The two sudden variations in electron flux between 5 UT and 12 UT are likely caused due to substorm activity given the position in local time, the signatures in the measured magnetic field and the elevated electron flux that follows.

4.8 Summary and Conclusions

None of the events studied here have particularly large Dst, Dst* or SYM-H signatures, yet a substantial dropout of the electron flux is still apparent (cf. *Borovsky and Denton* [2009b]; *Morley et al.* [2010]; *Meredith et al.* [2011]; *Turner et al.* [2012]; *Hendry et al.*

[2012]). In many respects, such events are more straightforward to analyse compared to large storm events driven by coronal mass ejections.

For Event 1, it is clear that outwards adiabatic radial transport plays a key role, with loss of electrons to the magnetopause. However, given the reduction in PSD at an L^* of approximately 5, it appears that there is a loss process, differing from adiabatic transport, acting also. This could be outwards radial diffusion caused by a steep radial gradient in the PSD following magnetopause losses, and/or pitch-angle scattering leading to atmospheric losses.

For Event 2, it appears that the reduction in electron flux at GEO is largely attributable to outwards radial transport of electrons based upon the decrease in L^*. However, given the discrepancies between the output of the T96 magnetic field model and the magnetic field measured by GOES-13 during this event, it is not apparent how accurate these PSD and L^* values may be. Therefore caution must be used when interpreting data for this period due to the errors highlighted in Figure 4.1.

For Event 3, there is not a well defined dropout period observed (GOES-13 on the dayside). Instead, we observe a compression of the magnetosphere, causing a small reduction in electron flux around local noon (17 UT) before a steady reduction in electron flux and shift in pitch-angle anisotropy. This could be due to local time variations as GOES-13 progresses in orbit. The rapid variations in the electron flux at all observed energies at 5 and 12 UT April 12 are concluded to be substorm activity, based upon the position of the satellite in local time, the observed magnetic field variations and the elevated electron flux that follows.

The progression of GOES-13 through local time complicates interpretation of electron measurements somewhat, however, this is clearly not the only factor causing variability between HSS events.

The electron dropouts associated with Event 1 and Event 2 display similar structure. This is most evident when studying the full pitch-angle-distributions shown in Figure 4.6 panels (b) and (c). Immediately prior to both dropouts, the pitch-angle-distributions become highly peaked (increasing fluxes perpendicular to the magnetic field, decreasing fluxes parallel to the magnetic field). Additionally, midway through both dropout periods, whilst the 475 keV electron fluxes are still falling, a clearly defined transition from a peaked distribution to an isotropic, or even butterfly, distribution is evident as the solar wind pressure begins to decrease. The fluxes then fall to very low values at all pitch angles. These distributions compare well with the averaged pitch-angle-resolved fluxes from Los Alamos Satellites also at GEO [*Borovsky and Denton*, 2011].

Based upon our study of the impact of three high-speed stream events on electron fluxes at geosynchronous orbit we conclude that:

1. There is a high degree of variability in electron flux measurements, the magnitude and duration of the dropout, and the calculated phase space density between HSS events that appear similar based upon solar wind observations.

2. Outwards adiabatic transport plays a key role in causing radiation belt flux dropouts at GEO. This can then lead to magnetopause losses and subsequent outwards radial diffusion. Other loss processes may also play a role.

3. Whilst calculating the phase space density is an invaluable tool for interpreting variation in the radiation belts, due to discrepancies between output from magnetic field models and in situ measurements, it is necessary to consider our calculations in the broader context of additional observed parameters (electron fluxes and magnetic field measurements).

4. The pitch-angle-distributions for Events 1 and 2 display similar structure; highly peaked distribution immediately prior to the dropout with a sharp boundary between a peaked distribution and an isotropic/butterfly distribution apparent as the solar-wind pressure decreases. Following this, the electron flux steadily decreases to a minimum across the entire distribution.

Adiabatic transport of electrons, leading to magnetopause losses (since the last closed drift shell moves to lower L^*) and subsequent outwards radial diffusion plays a significant role in causing electron dropouts at GEO, however other loss mechanisms are also a factor (wave-particle interactions and loss to the atmosphere). Future work using coincident measurements of in-situ wave-phenomena from the Van Allen Probes Mission and of particle precipitation into the atmosphere (e.g. BARREL [*Millan and the BARREL team*, 2011] and *Clilverd et al.* [2012]) is certain to further our understanding of these important mechanisms.

Chapter 5

Electron number density, temperature and energy density at GEO and links to the solar wind: A simple predictive capability

The following work is published in the Journal of Geophysical Research: Space Physics *(Hartley, D. P., M. H. Denton, and J. V. Rodriguez (2014), Electron number density, temperature, and energy density at GEO and links to the solar wind: A simple predictive capability, J. Geophys. Res. Space Physics, 119, 4556-4571, doi:10.1002/2014JA019779).*

5.1 Abstract

Many authors have studied the outer radiation belts response to different solar wind drivers, with the majority investigating electron flux variations. Using partial moments (electron number density, temperature and energy density) from GOES-13 during 2011 allows for changes in the number of electrons and the temperature of the electrons to be distinguished, which is not possible with the outputs of individual instrument channels. This study aims to produce a coarse predictive capability of the partial moments from GOES-13 by determining which solar wind conditions exhibit the strongest relationship with electron variations at GEO. Investigating how the electron distribution at GEO is affected by fluctuations in this primary driver, both instantaneous and time delayed, allows for this to be achieved. These predictive functions are then tested against data from 2012. It is found that using solely the solar wind velocity as a driver results in predicted values that accurately follow the general trend of the observed moments. This study is intended to make further progress in quantifying the relationship between the solar wind and electron number density, temperature and energy density at GEO. Our results provide a coarse predictive capability of these quantities that can be expanded upon in future studies to incorporate other solar wind drivers to improve accuracy.

5.2 Introduction

Energetic electron fluxes at geosynchronous orbit (GEO) can be highly variable depending upon the state of the solar wind and its time history. Both coronal mass ejections (CMEs) and co-rotating interaction regions (CIRs) are known, upon impact with the magnetosphere, to cause variability in electron populations at GEO [*Borovsky and Denton*, 2006] from rapid decreases (*dropouts*) which can occur over a period of minutes (e.g. *Onsager et al.* [2002], *Green et al.* [2004], *Clilverd et al.* [2013], *Hartley et al.* [2013]), to subsequent increases (*recoveries*) some hours or days later [*Freeman*, 1964; *Nagai*, 1988; *Chen et al.*, 2007b; *Liemohn and Chan*, 2007; *Borovsky and Denton*, 2009b]. The relationship between solar wind velocity and electron flux at GEO has long been established [*Paulikas and Blake*, 1979]. Comparison of electron fluxes with various solar wind parameters (velocity, temperature, pressure, density, IMF etc...) has been the basis of many studies, with the primary aim being to obtain a predictive capability of radiation belt electrons for a given set of solar wind input parameters (e.g. *Nagai* [1988]; *Boynton et al.* [2013]; *Horne et al.* [2013]). However, the complexity of the relationship between the solar wind and energetic electrons in the magnetosphere means that a reliable, accurate predictive model remains elusive. There have been many studies investigating the variability of radiation belt electrons and their response to different solar wind drivers (e.g. *Baker et al.* [1986]; *Hudson et al.* [1997]; *O'Brien et al.* [2001]; *Reeves et al.* [2003b]; *Weigel et al.* [2003]; *Mann et al.* [2004]; *Li et al.* [2005]; *Borovsky and Denton* [2006]; *Liemohn and Chan* [2007]; *Millan and Thorne* [2007]; *Onsager et al.* [2007]; *Hudson et al.* [2008]; *Miyoshi and Kataoka* [2008]; *Borovsky and Denton* [2010b]; *Morley et al.* [2010]; *Hartley et al.* [2013] and references therein). In addition, there is strong evidence that

relativistic electrons are somewhat seasonally dependent [*Baker et al.*, 1999; *McPherron et al.*, 2009a].

Recently *Reeves et al.* [2011, 2013b] compared electron fluxes to solar wind drivers (primarily solar wind velocity) concluding that the electron flux distribution could not be explained by scatter about a linear relationship as previously considered, but rather a 'triangle shape' distribution was revealed, with a velocity dependent lower limit and a velocity independent upper limit.

An alternative picture to that obtained by looking solely at the electron flux is provided by considering the electron temperature and number density at GEO [*Cayton et al.*, 1989; *Borovsky et al.*, 1998; *Denton et al.*, 2010; *Borovsky and Cayton*, 2011; *Denton and Cayton*, 2011]. A density and temperature description of the electron radiation belt has advantages over the traditional flux description. Changes in the number of electrons and changes in the temperature of the electrons are distinguishable. This is crucial since small variations in the temperature of the electron distribution may appear as order-of-magnitude changes in the relativistic-electron fluxes. Examination of the density and temperature reveals how the entire population respond to different conditions, rather than the flux at a particular energy, thus providing an alternative picture of the evolution of the electron radiation belt, with the potential to reveal physical processes that may not be apparent with the traditional flux description (i.e. the measured flux at a particular energy is determined by changes in either the density or the temperature of the overall population). However, even with the density-temperature description used in this study, these are partial moments and therefore not sensitive to the entire population. It still remains unclear exactly how electrons in the outer radiation belt at GEO respond to

solar-wind velocity and density variations. By comparing partial moments (electron temperature and number density from GOES-13) with instantaneous and time-delayed solar wind conditions from the OMNI 2 database [*King and Papitashvili*, 2005], it is possible to investigate the complexity of the relationship and make further progress towards understanding the effect of solar wind conditions on electron temperature and number density at GEO.

In this study we summarise the primary solar wind drivers of electron number density and temperature at GEO as measured by GOES-13 during 2011. It appears that the 1-minute resolution electron temperature and electron number density variations at GEO display some dependency on the solar wind proton density, however the relationship with solar wind velocity is more well-defined. Additionally, we find that both electron number density and temperature at GEO exhibit solar-wind-velocity dependent lower limits (elevated temperature and number density at GEO only occur during, or some time after, fast solar wind). The electron energy density is also considered and is also found to be subject to a solar-wind-velocity dependent lower limit. By producing fits to the data, we calculate a linear function that describes these upper/lower limits within given confidence bounds. This is done using instantaneous solar wind data, as well as time-delayed solar wind parameters in intervals of 12 hours. Using time-delayed solar wind data and the calculated linear functions allows for a predictive capability of the electron number density, temperature and energy density at GEO. These predictions are then tested against GOES-13 partial moments data from 2012 in order to study the accuracy of the calculated functions.

5.3 Instrumentation

The Magnetospheric Electron Detector (MAGED) onboard GOES-13 provides pitch-angle-resolved flux measurements in the 30-600 keV energy range. Consisting of nine telescopes, each with a central pitch angle, α, defined by the orientation of the magnetic field measured by the GOES-13 magnetometer at any time, MAGED measures flux in five energy channels parametrised as 30-50, 50-100, 100-200, 200-350 and 350-600 keV. The fluxes are dead-time and proton-contamination corrected. The current NOAA real-time processing assumes a flat spectrum over each channel and mean central energies of 40, 75, 150, 275 and 475 keV. Using these electron measurements, it is possible to calculate the number density, n, and temperature, T, through the partial moments Equations 5.1, 5.2, 5.3 and 5.4, in addition to the energy density, $\mathcal{E}$, using Equation 5.5.

$$n = 2\pi \iint f_v(\alpha, v)\, v^2 \sin(\alpha)\, d\alpha\, dv \tag{5.1}$$

$$T_{perp} = \frac{\pi m}{n} \iint f_v(\alpha, v)\, v^4 \sin^3(\alpha)\, d\alpha\, dv \tag{5.2}$$

$$T_{para} = \frac{2\pi m}{n} \iint f_v(\alpha, v)\, v^4 \cos^2(\alpha) \sin(\alpha)\, d\alpha\, dv \tag{5.3}$$

$$T = \frac{2T_{perp} + T_{para}}{3} \tag{5.4}$$

$$\mathcal{E} = nT \tag{5.5}$$

Where $f_v(\alpha, v)$ is a velocity distribution converted from differential flux as a function of the central pitch angle of each telescope.

The calculation of partial moments, although based on a Maxwellian formulation, does not use a Maxwellian fit, unlike the work of *Cayton et al.* [1989]. Rather, it approximates the integrals as weighted two-dimensional sums of the velocity distribution at each measured energy and pitch angle. The velocity distribution is approximated as uniform across the energy range of each channel listed above and between pitch angle limits defined as the average of the telescope central pitch angles, with the lowest limit set to 0 deg and the highest limit set to 90 deg. Due to the sparse pitch angle sampling, fluxes with pitch angles between 90 and 180 deg are assigned to the supplement of their pitch angle, and the sum from 0 to 90 deg is doubled in calculating the integral. For the electrons, relativistic versions of equations 5.1, 5.2 and 5.3 are used, but the difference at MAGED energies is only a few percent. The electron energy density, $\mathcal{E}$, is also considered [*Gurgiolo et al.*, 1979; *Daglis et al.*, 1994]. This is calculated by removing the number density denominator in the temperature integrals (multiplying the partial number density by partial temperature). This is investigated in order to consider any artificial anti-correlation between the electron number density and temperature caused by the partial nature of the GOES-13 moments. Since theory suggests that these parameters may be anti-correlated in general [*Scudder*, 1992], it is crucial to be aware of this possible artificial behaviour.

Cayton et al. [1989] found that the electron energy distribution at geosynchronous orbit could be well described by Maxwellian distributions. (It is also noted that Pierrard and Lemaire [1996] found that the electron energy spectra away from geosynchronous orbit could also be well described by Maxwellians). Whilst the Maxwellian distribution is not be the only possible representation of radiation belt electrons (the kappa distribution is also commonly used), it has shown to be a useful representation (e.g. *Gary* [1993]; *Onsager et al.* [2004]; *MacDonald et al.* [2008]; *Denton et al.* [2010]; *Denton and Cayton* [2011]; *Clilverd et al.* [2013]). Since the Maxwellian distribution is a limiting case of the kappa distribution (e.g., *Christon et al.* [1988]; *Gkioulidou et al.* [2009]), it is important to establish the behaviour of the simpler model before investigating the more-general model. It should also be noted that the quantities of energy density and number density are model-independent.

5.4 Analysis and Results

The methodology used in this study is designed to:

1. Determine which solar wind parameter displays the strongest relationship with the electron number density, temperature and energy density at GEO (both instantaneous and time-delayed in 12 hour intervals).

2. Investigate how the distribution of electron number density, temperature and energy density at GEO vary with this driving solar wind parameter (both instantaneous and time-delayed in 12 hour intervals).

3. Calculate linear fits to these distributions (instantaneous and time-delayed) in order to obtain, given a measurement of the primary solar wind driver, a prediction of the electron number density, temperature and energy density at GEO in intervals of 12 hours in the future.

4. Test how accurate these calculated functions are at predicting the electron number density, temperature and energy density at GEO.

5.4.1 Determining the primary driver

1-minute resolution electron temperature and number density from GOES-13 at GEO during 2011 are calculated using Equations 5.1, 5.2, 5.3 and 5.4. Additionally, the electron energy density is calculated by multiplying the electron temperature by the number density (see Equation 5.5). Initially, we compare these partial moments with solar wind velocity and density in order to establish the primary driving solar wind parameter. This is done by comparing the partial moments from GOES-13 with solar wind measurements in intervals of 12 hours prior, from 48 hours to instantaneous. We also consider a negative 12 hour delay (partial moments from GOES-13 observed 12 hours prior to the solar wind measurements). While no causal relationship can exist between the GOES observations and the solar wind parameters observed 12 hours in the future, this is included in order to provide a baseline from which to compare any apparent structure that may exist with increasing time delays.

Figure 5.1a displays each 1-minute resolution electron temperature and number density measurement at GEO by GOES-13 during 2011 for all local time sectors, with the colour indicating the solar wind velocity for one time delay, 24 hours (warm colours indicate

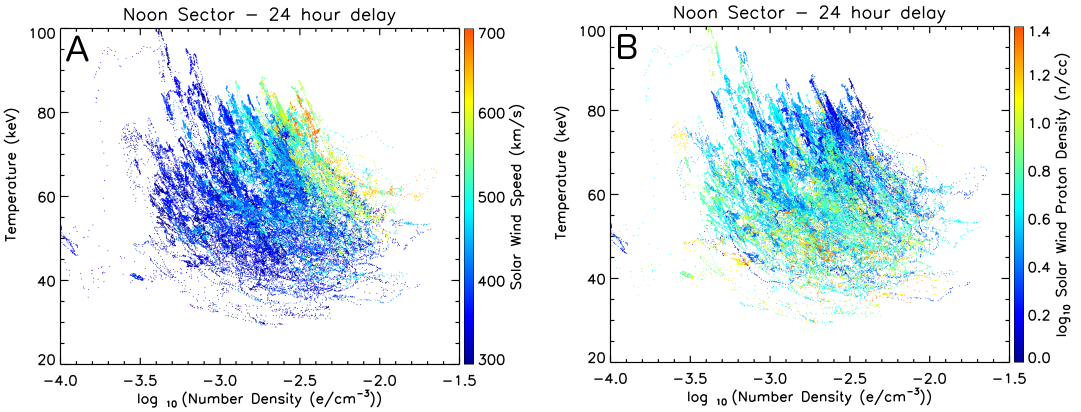

FIGURE 5.1: Variability of partial moments (electron number density and temperature) measured at GEO by GOES-13 with solar wind velocity (a) and density (b) for a 24 hour time delay in the noon sector.

elevated velocities, cool colours indicate slower velocities). Figure 5.1b displays the same parameters with the colour this time indicating the solar wind density (warm colours indicate elevated densities, cool colours indicate lower densities). These figures exhibit similarities to that displayed by *Denton et al.* [2010] for the 'soft component' of the relativistic Maxwellian fits to LANL-01a spacecraft data for the years 2001-2007. The temperatures calculated for GOES-13 are significantly higher than those from LANL-01a, since the soft component has an upper limit of 300 keV and MAGED has an additional channel (350-600 keV) above that limit. This analysis was performed for a range of time delays (-12 hour, 0 hour, 12 hour, 24 hour, 36 hour, 48 hour), with no large increase or decrease in structure apparent. To calculate the time delay, we simply take the solar wind velocity measurement from the number of delay hours prior to the GOES observation (i.e. GOES[n] corresponds to OMNI[n-(i*60)] for i hour delay and data at 1-minute time intervals).

For the solar wind velocity (Figure 5.1a), it is apparent that elevated number density and elevated temperature occur independently 24-hours following a broad range of solar

wind velocities. However, for both to be simultaneously elevated, the solar wind speed must have been elevated [*Borovsky and Denton*, 2010b; *Denton et al.*, 2010; *Borovsky and Cayton*, 2011; *Denton and Cayton*, 2011]. It is noted that there are clear inverse law striations apparent in Figure 5.1 which may be, at least partly, attributable to the number density denominator in the temperature integrals. To remove this behaviour, the electron energy density is also considered during this study.

When comparing the electron number density and temperature to the solar wind density (Figure 5.1b) there is also some structure apparent. Elevated electron temperature and number density at GEO primarily occur during periods of depleted solar wind density (note that elevated electron fluxes have also been shown to occur at low solar wind densities by *Balikhin et al.* [2011]). However, it appears that there is a more well-defined structure when considering the solar wind velocity instead of the solar wind density.

In order to further investigate this relationship, data are binned based upon the solar wind conditions 24-hours prior in 5 km s^{-1} solar wind velocity bins and 0.05 $\log_{10}$ cm^{-3} solar wind density bins. Additional binning is performed for the electron number density, temperature and energy density from GOES-13. The logarithm of the number density is binned in intervals of 0.05 $\log_{10}$ cm^{-3}, the temperature is binned in intervals of 2 keV and the logarithm of the electron energy density is binned in intervals of 0.05 $\log_{10}$ keV cm^{-3}. We then display the number of occurrences recorded in each bin in colour. These results are shown in Figure 5.2.

For the solar wind velocity, Figure 5.2a, c and e, it is apparent that as velocity increases, the minimum observed electron temperature, number density and energy density also increases (velocity dependent lower limit). This is not the case when comparing the

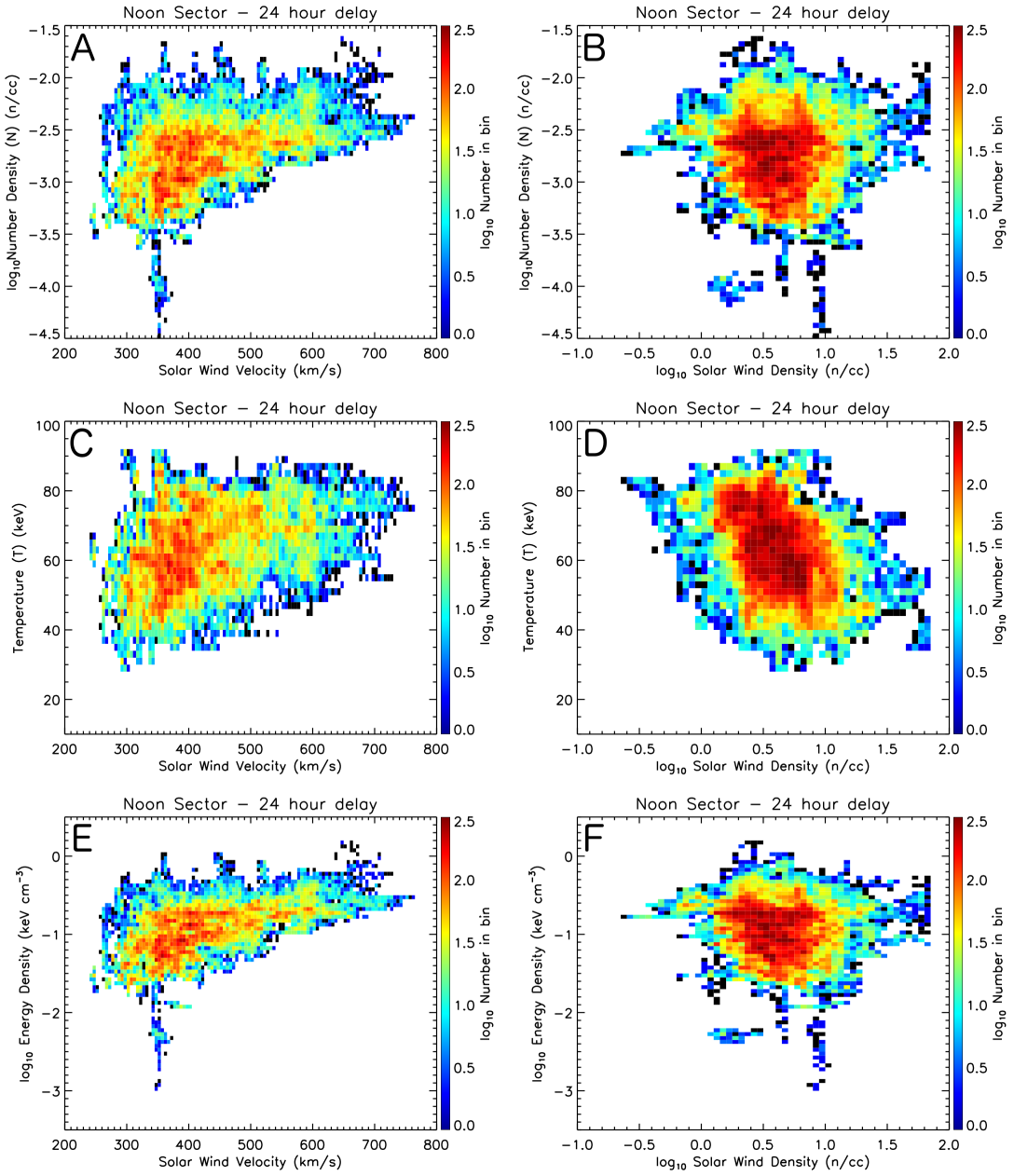

FIGURE 5.2: Density plots displaying the partial moments (electron number density, temperature and energy density) from GOES-13 at GEO for varying solar wind conditions with a time delay of 24 hours applied; solar wind velocity (a), (c) and (e), and solar wind density (b), (d) and (f).

partial moments with the solar wind density (Figure 5.2b, d and f) which does not display a clear structure.

Our results suggest that the electron temperature, electron number density and electron energy density variations at GEO display some dependency on the solar wind density, however the relationship with solar wind velocity is more well-defined.

5.4.2 Distribution of partial moments with varying primary solar wind driver

Having established that the solar wind velocity has a stronger relationship with the electron number density, temperature and energy density variations at GEO than the solar wind density, we investigate the variations of the GOES-13 moments with solar wind velocity in more detail. Due to inherent local time variations, we sort GOES-13 measurements in local time, binning data into four local time bins (Dawn 4-8 LT, Noon 10-14 LT, Dusk 16-20 LT and Midnight 22-2 LT). From this point forward we display results from the noon sector only, although the analysis is repeated for all local time sectors. Studying the number of occurrences of electron number density, temperature and energy density in small solar wind velocity intervals allows for the distribution of GOES-13 partial moments with respect to the solar wind velocity to be obtained. Figures 5.3, 5.4 and 5.5 display the results of this analysis. Data are binned in 5 km s^{-1} solar wind velocity bins. Additional binning is performed for the electron number density, temperature and energy density from GOES-13. The logarithm of the number density is binned in intervals of 0.05 $\log_{10}$ cm^{-3}, the temperature is binned in intervals of 2 keV and the logarithm of the energy density is binned in intervals of 0.05 $\log_{10}$ keV cm^{-3}. We

then display the number of occurrences recorded in each bin in colour. Displaying data in this way allows for more detail of the distributions to be shown than merely producing a scatter plot. Figure 5.3 displays the distributions of electron number density at GEO for time delays from (-12) hours to 48 hours in intervals of 12 hours. Figures 5.4 and 5.5 contain the same analysis repeated for the electron temperature and energy density at GEO respectively.

Firstly, considering the electron number density (Figure 5.3), it is apparent that elevated number densities can occur simultaneous to, or several hours following, a broad range of solar wind velocities, however there are few instances where a high solar wind velocity results in a low electron number density at GEO. This result, when observed using electron fluxes, lead to the suggestion of a velocity-dependent lower limit on the electron flux [*Reeves et al.*, 2011, 2013b]. The results in Figure 5.3 (for positive delays) show that this also appears to be the case with the electron number density as measured by GOES-13. It is noteworthy that there is little quantifiable difference between the negative 12 hour delay plot (Figure 5.3a), and the plot for zero delay (Figure 5.3b), thus indicating that the consideration of a time delay is imperative. (Note: 12 hour time delay intervals were selected as a balance between the large and small timescale variations of the electron population at GEO. It is apparent from the analysis presented in this study that whilst the distributions of the partial moments with solar wind velocity do change within the 12 hour intervals, the extent of these variations does not appear large enough to consider repeating the analysis with smaller time delay intervals.)

Secondly we study the electron temperature at GEO (Figure 5.4). With no time delay, the electron temperature appears to have little relationship to solar wind velocity, with

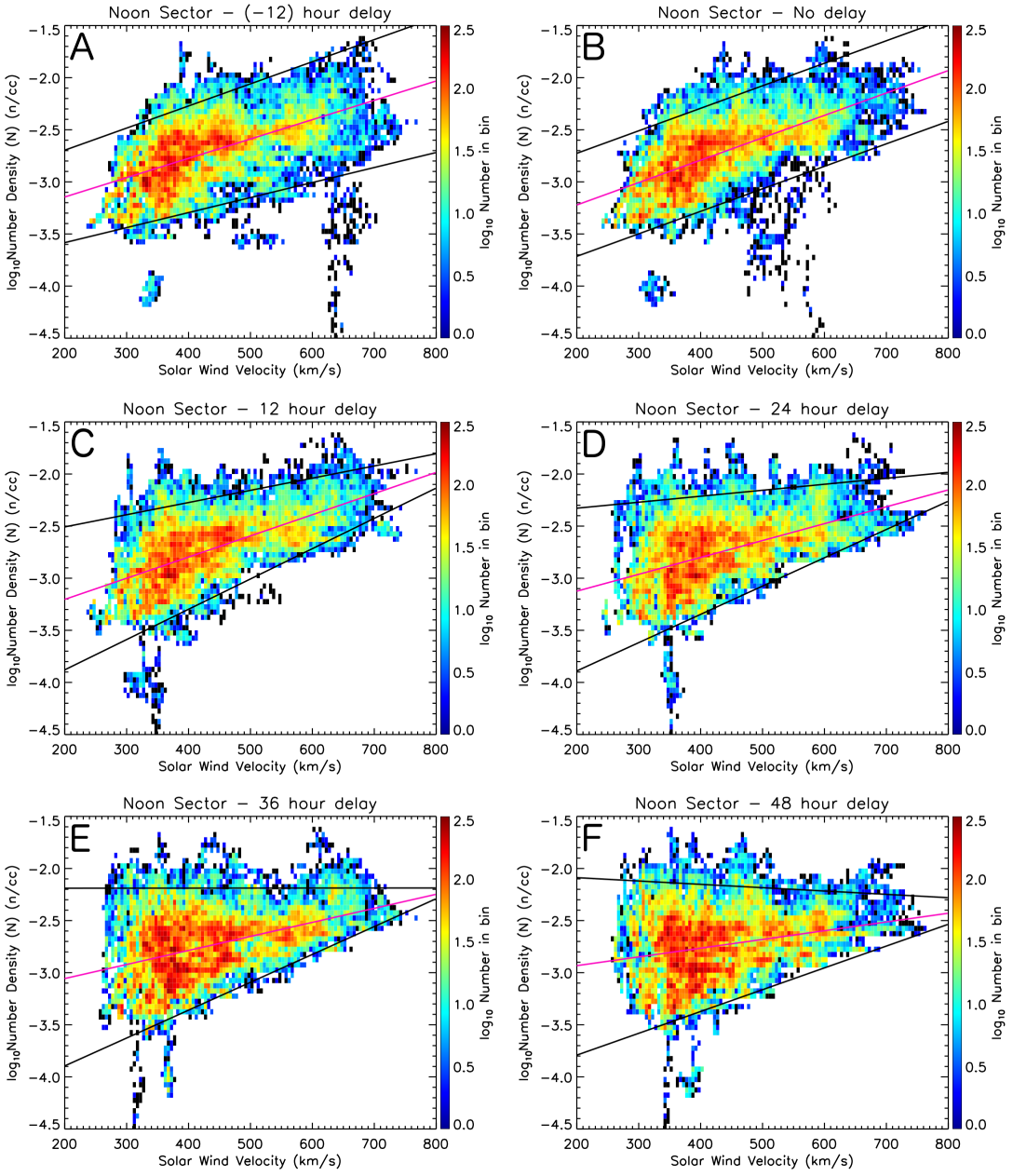

FIGURE 5.3: Density plots of solar wind velocity against electron number density at GEO in the noon sector for increasing time delay. (a) negative 12 hour delay, (b)instantaneous, (c) 12 hour delay, (d) 24 hour delay, (e) 36 hour delay and (f) 48 hour delay. The pink line indicates the median number density for each solar wind velocity bin whilst the straight black lines indicate a linear fit of the mean ± two standard deviations for each solar wind velocity bin (lower and upper bounds). Equations describing these upper and lower bounds, as well as the predicted quantity, are listed on the Equation 5.6 with coefficients listed in Table 5.1.

both elevated and low temperatures occurring across a broad range of solar wind velocities. However, as the time delay is increased, a velocity dependent lower limit of the electron temperature becomes increasingly apparent (24 hour delay, 36 hour delay and 48 hour delay). Therefore, elevated temperatures only occur some time after the arrival of fast solar wind. This is consistent with the results of *Borovsky and Denton* [2010b] who showed that the temperature of the electron distribution at GEO increases during the fast solar wind following the passing of a co-rotating interaction region. Again, it is noted that there is little difference between negative 12 hours delay and zero delay (Figure 5.4a and b).

Thirdly, we study the energy density of electrons at GEO (Figure 5.5). The energy density exhibits similar structure to the electron number density with elevated energy densities occurring over a broad range of solar wind velocities and few instances where an elevated solar wind velocity results in a low energy density of electrons at GEO (velocity dependent lower limit). Considering the energy density, thus removing the number density denominator dependence on the electron temperature, appears to increase the correlation of the second moment with solar wind velocity. This should therefore increase chances of obtaining a more accurate predictive capability for this moment.

5.4.3 Calculating prediction functions

Using the distributions presented in Figures 5.3, 5.4 and 5.5, linear functions are calculated in order to quantify the observed velocity-dependent lower limit, upper limit and average of the observed quantity for instantaneous and positive time delays only. Other data based modelling techniques are noted (e.g. ARMAX [*Johansson*, 1993; *Ljung*, 1999;

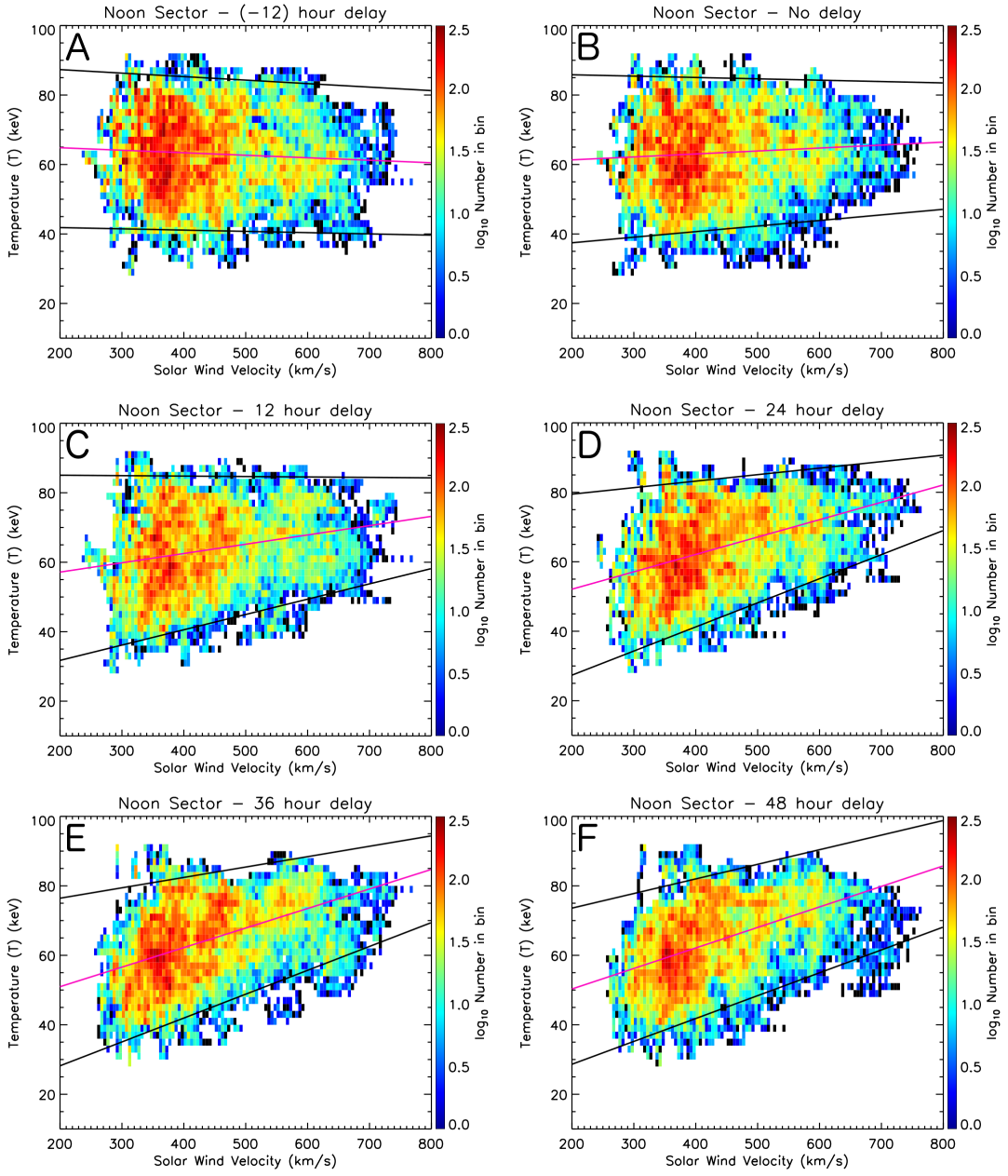

FIGURE 5.4: Density plots of solar wind velocity against electron temperature at GEO in the noon sector for increasing time delay. (a) negative 12 hour delay, (b)instantaneous, (c) 12 hour delay, (d) 24 hour delay, (e) 36 hour delay and (f) 48 hour delay. The pink line indicates the median temperature for each solar wind velocity bin whilst the straight black lines indicate a linear fit of the mean ± two standard deviations for each solar wind velocity bin (lower and upper bounds). Equations describing these upper and lower bounds, as well as the predicted quantity, are listed on the Equation 5.7 with coefficients listed in Table 5.2.

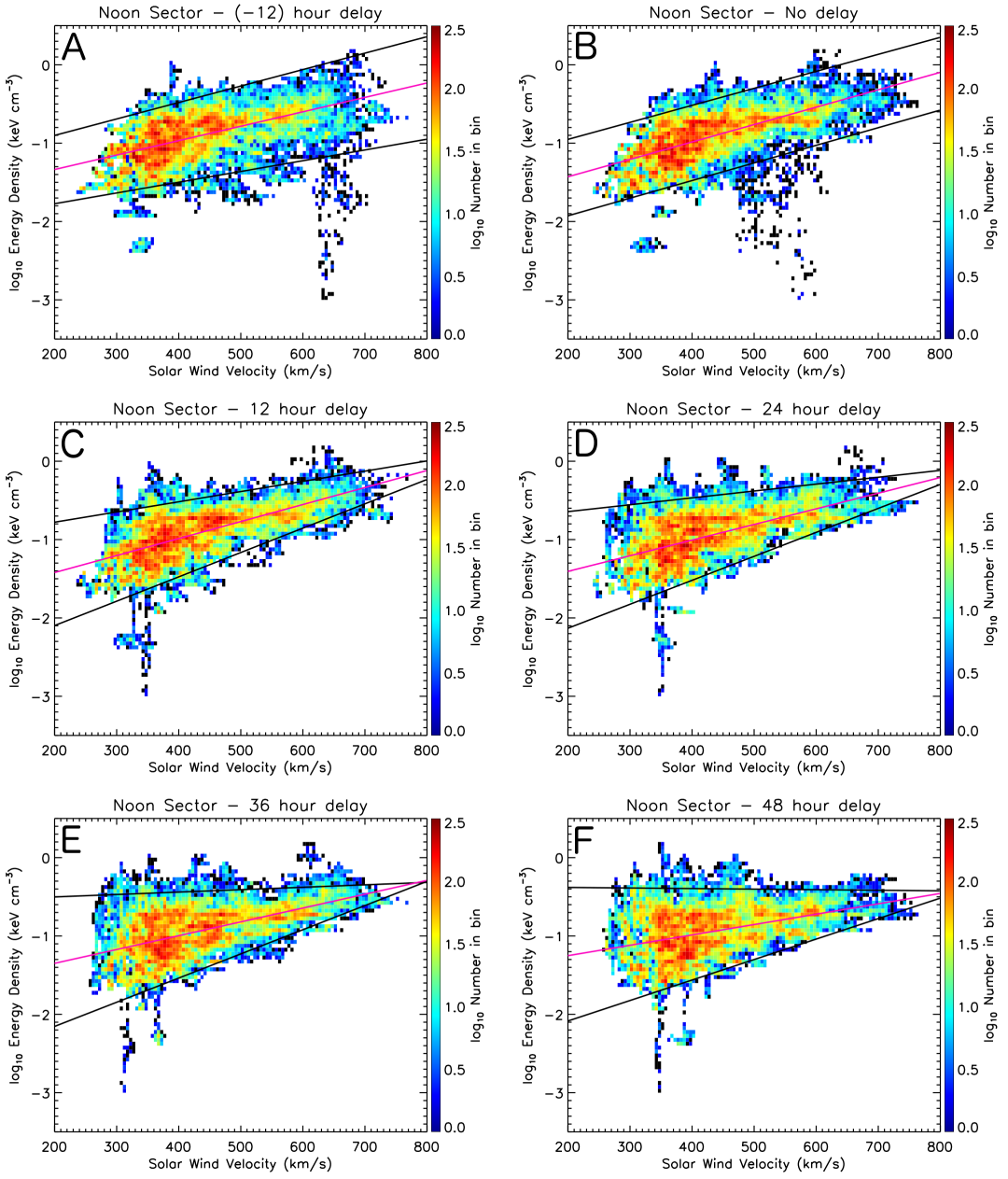

FIGURE 5.5: Density plots of solar wind velocity against electron energy density at GEO in the noon sector for increasing time delay. (a) negative 12 hour delay, (b)instantaneous, (c) 12 hour delay, (d) 24 hour delay, (e) 36 hour delay and (f) 48 hour delay. The pink line indicates the median energy density for each solar wind velocity bin whilst the straight black lines indicate a linear fit of the mean ± two standard deviations for each solar wind velocity bin (lower and upper bounds). Equations describing these upper and lower bounds, as well as the predicted quantity, are listed on the Equation 5.8 with coefficients listed in Table 5.3.

Nelles, 2001], neural networks [*Koons and Gorney*, 1991; *Fukata et al.*, 2002], NARMAX [*Balikhin et al.*, 2011; *Boynton et al.*, 2013]), however a simple single-term linear method was selected in order to easily quantify the limits (upper/lower/median) of the observed 'triangle shape' distributions and obtain a first order predictive capability. This data-driven modelling technique is purely for GEO and may be useful for other models that require the conditions at GEO as boundary conditions. These linear functions are displayed in Figures 5.3, 5.4 and 5.5; lower and upper limits in black and average observed quantity in pink. As these functions are calculated for several time delays, using them should allow for a prediction to be made in intervals of 12 hours in the future following a solar wind observation. In order to quantify the velocity-dependent lower and upper limits, the mean $\pm 2\sigma$ (where σ is the standard deviation) is calculated for each solar wind velocity bin. A linear fit through these values is then produced (black). This encapsulates $\sim 90\%$ of the data and is therefore considered to be a 90% confidence bound on the data. Additionally, the median value in each solar wind velocity bin is calculated, with a linear fit through these values produced (pink). The result is a function whereby $\sim 50\%$ of the data lies above and $\sim 50\%$ below. This is the predicted value of the electron number density/temperature/energy density at GEO. These linear functions are displayed in Figures 5.3, 5.4 and 5.5 (black lines indicating the 90% confidence bound and the pink line indicating the predicted quantity). The equations describing these functions are listed as Equations 5.6, 5.7 and 5.8 with coefficients ($c_0(N)$, $c_1(N)$, $c_0(T)$, $c_1(T)$, $c_0(\mathcal{E})$ and $c_1(\mathcal{E})$) listed in Tables 5.1, 5.2 and 5.3 for all local time sectors. These calculated functions have a validity range of solar wind velocities between 250 km s^{-1} and 750 km s^{-1}.

$$N\left(cm^{-3}\right) = 10^{\,c_0(N)V_{SW}+c_1(N)} \tag{5.6}$$

$$T\left(keV\right) = c_0(T)V_{SW} + c_1(T) \tag{5.7}$$

$$\mathcal{E}\left(keVcm^{-3}\right) = 10^{\,c_0(\mathcal{E})V_{SW}+c_1(\mathcal{E})} \tag{5.8}$$

For zero delay, the electron number density distribution in the noon sector (Figure 5.3b) can be explained by scatter about a linear trend, since the gradient of the upper and lower bound, as well as the predicted value, are approximately equal. However, with the addition of a time delay (Figure 5.3c, d, e and f), a velocity dependent lower limit becomes increasingly apparent. This leads to the conclusion that for any given time, knowing the instantaneous solar wind velocity allows for a prediction of the minimum electron number density at GEO at some time in the future. With regards to a velocity-dependent upper limit, as larger time delays are applied the calculated gradient of this limit decreases. This indicates that the upper limit is not dependent upon the solar wind velocity.

With no time delay, the electron temperature (Figure5.4b) appears to have little relationship to solar wind velocity, with both elevated and decreased temperatures occurring across a broad range of solar wind velocities. The median line (pink) is relatively flat, varying very little with solar wind velocity. As the time delay is increased (Figure5.4c,

d ,e and f), a velocity dependent lower limit of the electron temperature becomes increasingly apparent (24 hour delay, 36 hour delay and 48 hour delay). Thus, elevated temperatures only occur some time after fast solar wind. The gradient of the velocity-dependent lower bound is steepest when a time delay of 24 hours is applied, although remains relatively well defined up to 48 hour delay.

The energy density of electrons at GEO appears similar in structure to the electron number density. With zero delay the energy density distribution in the noon sector (Figure 5.5b) could be explained by scatter about a linear trend, since there is little difference between the gradient of the upper bound, lower bound and the predicted quantity. However, as with the electron number density, with the addition of a time delay, the distribution becomes more like the 'triangle distributions' observed for electron fluxes by *Reeves et al.* [2011].

This method is then repeated for the dawn, dusk and midnight local time sectors with calculated coefficients $c_0(N)$, $c_1(N)$, $c_0(T)$, $c_1(T)$, $c_0(\mathcal{E})$ and $c_1(\mathcal{E})$) listed in Tables 5.1, 5.2 and 5.3. The calculated gradient coefficients for the predicted quantities are generally larger in the noon sector than in the midnight sector for all quantities, with the intercept coefficients also larger in the noon sector than in the midnight sector for the majority of time delays. This is consistent with the results of *Borovsky and Denton* [2010b] who concluded that the outer electron radiation belt at local noon at GEO is hotter than the outer electron radiation belt at local midnight at GEO.

Number Density (cm^{-3})						
	Prediction		Lower Bound		Upper Bound	
Noon Sector						
Delay	$c_0(N)$	$c_1(N)$	$c_0(N)$	$c_1(N)$	$c_0(N)$	$c_1(N)$
0 hr	2.15×10^{-3}	-3.65	2.16×10^{-3}	-4.15	2.16×10^{-3}	-3.16
12 hr	2.03×10^{-3}	-3.61	2.91×10^{-3}	-4.46	1.17×10^{-3}	-2.74
24 hr	1.62×10^{-3}	-3.45	2.72×10^{-3}	-4.43	0.57×10^{-3}	-2.44
36 hr	1.35×10^{-3}	-3.33	2.67×10^{-3}	-4.43	0.00×10^{-3}	-2.19
48 hr	0.84×10^{-3}	-3.10	2.09×10^{-3}	-4.21	-0.32×10^{-3}	-2.02
Midnight Sector						
0 hr	1.96×10^{-3}	-3.66	0.39×10^{-3}	-3.80	3.52×10^{-3}	-3.59
12 hr	2.16×10^{-3}	-3.77	2.17×10^{-3}	-4.53	2.35×10^{-3}	-3.11
24 hr	1.87×10^{-3}	-3.66	2.40×10^{-3}	-4.64	1.60×10^{-3}	-2.78
36 hr	1.39×10^{-3}	-3.46	2.14×10^{-3}	-4.57	0.94×10^{-3}	-2.47
48 hr	1.17×10^{-3}	-3.36	2.17×10^{-3}	-4.60	0.43×10^{-3}	-2.24
Dusk Sector						
0 hr	1.84×10^{-3}	-3.62	0.97×10^{-3}	-3.857	2.32×10^{-3}	-3.28
12 hr	1.89×10^{-3}	-3.65	3.03×10^{-3}	-4.67	0.86×10^{-3}	-2.71
24 hr	1.76×10^{-3}	-3.60	3.14×10^{-3}	-4.74	0.44×10^{-3}	-2.51
36 hr	1.34×10^{-3}	-3.42	2.83×10^{-3}	-4.62	0.08×10^{-3}	-2.35
48 hr	1.13×10^{-3}	-3.34	2.81×10^{-3}	-4.64	-0.32×10^{-3}	-2.16
Dawn Sector						
0 hr	2.50×10^{-3}	-3.78	1.83×10^{-3}	-4.10	3.35×10^{-3}	-3.46
12 hr	2.30×10^{-3}	-3.71	2.29×10^{-3}	-4.34	2.49×10^{-3}	-3.07
24 hr	1.80×10^{-3}	-3.50	2.32×10^{-3}	-4.38	1.69×10^{-3}	-2.69
36 hr	1.50×10^{-3}	-3.38	2.50×10^{-3}	-4.49	0.82×10^{-3}	-2.30
48 hr	1.11×10^{-3}	-3.21	2.22×10^{-3}	-4.39	0.13×10^{-3}	-1.99

TABLE 5.1: A table showing the parameters to be used in equation 5.6 to calculate the predicted value, the lower bound and the upper bound of the electron number density at GEO for five different time delays (0 hr, 12 hr, 24 hr, 36 hr, 48 hr) for four local time sectors at GEO.

5.4.4 Testing the prediction

Having used data from GOES-13 throughout the duration of 2011 to calculate coefficients to a linear function that relates the solar wind velocity to the electron number density, temperature and energy density at GEO in four local time sectors, we now test this relationship using GOES-13 moments data from 2012 and a time delay of 24 hours. The 24hr lag was chosen since *Denton and Borovsky* [2009] showed that the time between observed solar wind velocity variations and associated variations in the plasma

Temperature (keV)						
	Prediction		Lower Bound		Upper Bound	
Noon Sector						
Delay	$c_0(T)$	$c_1(T)$	$c_0(T)$	$c_1(T)$	$c_0(T)$	$c_1(T)$
0 hr	0.85×10^{-2}	59.6	1.61×10^{-2}	34.3	-0.39×10^{-2}	86.6
12 hr	2.67×10^{-2}	51.8	4.41×10^{-2}	22.9	-0.13×10^{-2}	85.3
24 hr	5.00×10^{-2}	42.1	6.94×10^{-2}	13.5	1.87×10^{-2}	75.7
36 hr	5.63×10^{-2}	39.7	6.87×10^{-2}	14.5	2.99×10^{-2}	70.5
48 hr	5.91×10^{-2}	38.5	6.58×10^{-2}	15.5	4.21×10^{-2}	65.2
Midnight Sector						
0 hr	-0.87×10^{-2}	60.7	-1.98×10^{-2}	41.3	-0.16×10^{-2}	80.5
12 hr	2.33×10^{-2}	47.4	0.66×10^{-2}	30.3	2.48×10^{-2}	69.4
24 hr	3.81×10^{-2}	41.3	2.35×10^{-2}	24.3	3.49×10^{-2}	64.2
36 hr	5.02×10^{-2}	36.5	3.40×10^{-2}	20.1	5.24×10^{-2}	56.7
48 hr	5.35×10^{-2}	35.1	3.65×10^{-2}	19.3	5.19×10^{-2}	56.9
Dusk Sector						
0 hr	2.09×10^{-2}	53.3	1.34×10^{-2}	35.4	2.16×10^{-2}	73.7
12 hr	4.23×10^{-2}	44.3	6.03×10^{-2}	17.5	1.81×10^{-2}	73.9
24 hr	5.86×10^{-2}	37.2	7.16×10^{-2}	13.2	3.34×10^{-2}	66.6
36 hr	6.28×10^{-2}	35.8	7.59×10^{-2}	12.2	4.05×10^{-2}	63.4
48 hr	6.09×10^{-2}	36.6	7.46×10^{-2}	12.9	4.53×10^{-2}	60.8
Dawn Sector						
0 hr	-2.40×10^{-2}	67.2	-2.22×10^{-2}	43.3	-1.86×10^{-2}	88.1
12 hr	1.01×10^{-2}	53.1	0.25×10^{-2}	32.7	0.55×10^{-2}	78.2
24 hr	3.03×10^{-2}	45.2	1.67×10^{-2}	27.1	2.32×10^{-2}	70.5
36 hr	3.76×10^{-2}	42.1	2.10×10^{-2}	25.4	3.48×10^{-2}	64.9
48 hr	4.45×10^{-2}	39.3	2.20×10^{-2}	25.4	4.74×10^{-2}	59.5

TABLE 5.2: A table showing the parameters to be used in equation 5.7 to calculate the predicted value, the lower bound and the upper bound of the electron temperature at GEO for five different time delays (0 hr, 12 hr, 24 hr, 36 hr, 48 hr) for four local time sectors at GEO.

sheet density was between 8 and 18 hours (depending on LT). Given that the plasma sheet is the seed population for the electron radiation belt, it followed to use a solar wind velocity delay greater than 18 hours, hence 24 hours was selected. Figure 5.6 displays the solar wind velocity for May 2012, the electron number density, temperature and energy density as measured by GOES-13 at GEO (red) during the same period, in addition to the predicted value (dark blue) and the 90% confidence bounds (pale blue shading) for electron number density, temperature and energy density as calculated in

Energy Density (keV cm^{-3})						
	Prediction		Lower Bound		Upper Bound	
Noon Sector						
Delay	$c_0(\mathcal{E})$	$c_1(\mathcal{E})$	$c_0(\mathcal{E})$	$c_1(\mathcal{E})$	$c_0(\mathcal{E})$	$c_1(\mathcal{E})$
0 hr	2.22×10^{-3}	-1.87	2.25×10^{-3}	-2.38	2.17×10^{-3}	-1.39
12 hr	2.17×10^{-3}	-1.86	3.11×10^{-3}	-2.72	1.30×10^{-3}	-1.04
24 hr	2.00×10^{-3}	-1.81	3.06×10^{-3}	-2.74	0.88×10^{-3}	-0.82
36 hr	1.76×10^{-3}	-1.70	3.08×10^{-3}	-2.77	0.31×10^{-3}	-0.56
48 hr	1.32×10^{-3}	-1.52	2.61×10^{-3}	-2.61	-0.07×10^{-3}	-0.37
Midnight Sector						
0 hr	2.01×10^{-3}	-1.91	0.33×10^{-3}	-2.06	3.39×10^{-3}	-1.77
12 hr	2.36×10^{-3}	-2.08	2.35×10^{-3}	-2.87	2.41×10^{-3}	-1.38
24 hr	2.15×10^{-3}	-2.00	2.71×10^{-3}	-3.03	1.74×10^{-3}	-1.10
36 hr	1.87×10^{-3}	-1.90	2.54×10^{-3}	-2.99	1.21×10^{-3}	-0.84
48 hr	1.63×10^{-3}	-1.79	2.68×10^{-3}	-3.07	0.59×10^{-3}	-0.57
Dusk Sector						
0 hr	2.09×10^{-3}	-1.93	0.94×10^{-3}	-2.09	2.60×10^{-3}	-1.58
12 hr	2.19×10^{-3}	-1.98	3.38×10^{-3}	-3.05	1.09×10^{-3}	-1.00
24 hr	2.17×10^{-3}	-1.98	3.58×10^{-3}	-3.15	0.76×10^{-3}	-0.85
36 hr	1.78×10^{-3}	-1.81	3.33×10^{-3}	-3.05	0.42×10^{-3}	-0.70
48 hr	1.62×10^{-3}	-1.76	3.47×10^{-3}	-3.14	-0.12×10^{-3}	-0.44
Dawn Sector						
0 hr	2.39×10^{-3}	-1.96	1.86×10^{-3}	-2.31	2.99×10^{-3}	-1.62
12 hr	2.37×10^{-3}	-1.96	2.51×10^{-3}	-2.61	2.34×10^{-3}	-1.34
24 hr	2.04×10^{-3}	-1.83	2.70×10^{-3}	-2.70	1.63×10^{-3}	-1.01
36 hr	1.86×10^{-3}	-1.76	3.02×10^{-3}	-2.87	0.73×10^{-3}	-0.61
48 hr	1.40×10^{-3}	-1.58	2.78×10^{-3}	-2.80	-0.10×10^{-3}	-0.31

TABLE 5.3: A table showing the parameters to be used in equation 5.8 to calculate the predicted value, the lower bound and the upper bound of the electron energy density at GEO for five different time delays (0 hr, 12 hr, 24 hr, 36 hr, 48 hr) for four local time sectors at GEO.

this study (further plots are given in Appendix B for January and August 2012). Having calculated these coefficients for 4-hour local time sectors centered around dawn/noon/-dusk/midnight, these coefficients are then applied to larger, 6-hour local time sectors. Due to the method used in this study, the calculated coefficients change as the spacecraft crosses between local time sectors. This results in discontinuities or 'stepping' (apparent in Figure 5.6) of the predicted values between local time sectors. While this behaviour is not physical, and merely an artefact of binning the data, it does capture the trends of

the general local-time variations.

For the electron number density (Figure 5.6b), the calculated values appear to quite closely follow the overarching trend throughout the month. There are some large discrepancies although these do occur during highly dynamic periods in the measured number density which are likely caused by electron dropouts at GEO or substorm injections. During the most extreme of these cases (i.e. on May 9, May 20 and May 23), the measured quantity does fall outside of our shaded 90% confidence bounds, however these do not occur frequently.

Considering the electron temperature (Figure 5.6c), the predicted values again follow the general trend of the measured temperature from GOES-13. There are again periods where large discrepancies do occur, primarily between May 27 and 29. The discrepancy during this period is likely due to the passing of the two high-speed solar-wind streams resulting in elevated fluxes in the 350-600 keV energy range, thus elevating the temperature considerably. It is also noted that during this period there are few substorm injections, hence the temperature remains elevated and does not decrease around midnight. The measured temperature does occasionally fall outside of the shaded pale blue 90% confidence bounds, however not frequently. Although given the large range encapsulated by the pale blue bounds, this result is not surprising.

For the energy density, (Figure 5.6d), the predicted values closely follow the general trend of the observed quantity. Outside of the large reductions in energy density observed on May 9 and 23, the observed value rarely falls outside of the calculated pale blue limits. The variability in energy density appears to be more easily predicted than the electron temperature when using the methodology implemented in this study. This is due to the

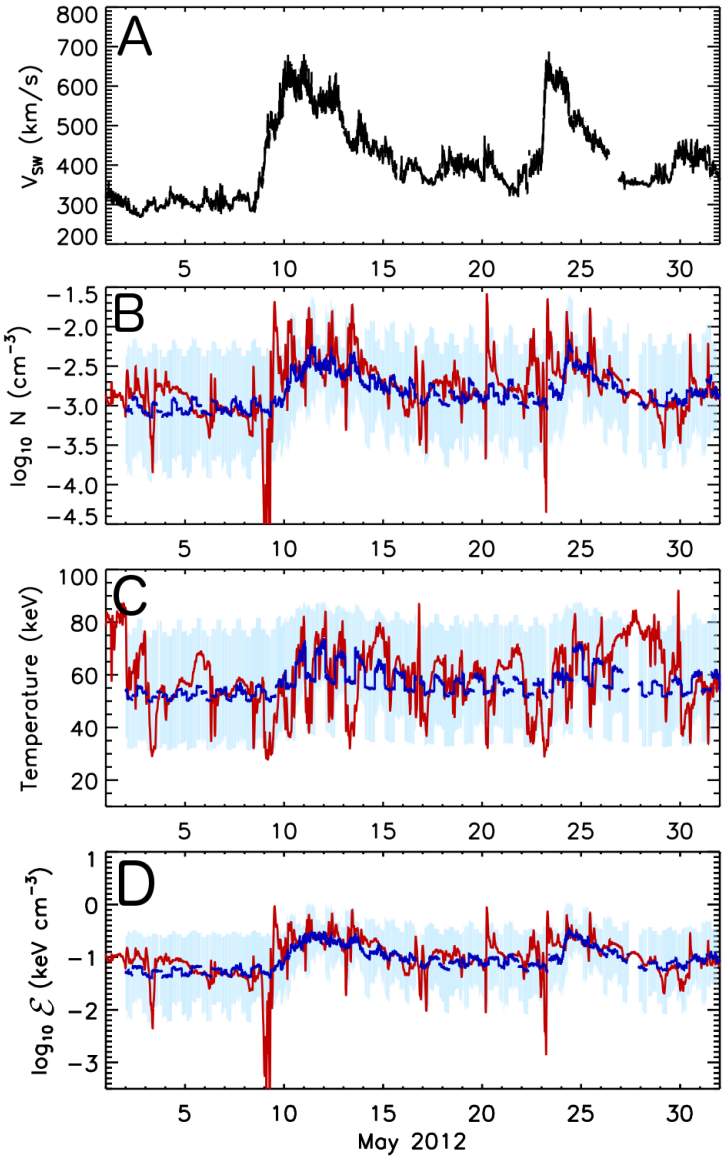

FIGURE 5.6: (a) The solar wind velocity during May 2012, (b) the electron number density at geosynchronous orbit measured by GOES-13 (red), the prediction as calculated 24 hours in advance (dark blue) and the upper and lower bounds to 90% confidence limits (blue shading), (c) the electron temperature at geosynchronous orbit measured by GOES-13 (red), the prediction as calculated 24 hours in advance (dark blue) and the upper and lower bounds to $\sim$ 90% confidence limits (blue shading), and (d) the electron energy density at geosynchronous orbit measured by GOES-13 (red), the prediction as calculated 24 hours in advance (dark blue) and the upper and lower bounds to $\sim$ 90% confidence limits (blue shading).

higher correlation of electron energy density at GEO with solar wind velocity compared to electron temperature.

Figure 5.7 displays a quantitative analysis of the residuals between the predicted (median) and observed parameters for the same time period (May 2012) and delay (24hr) as in Figure 5.6. The percentage error (magnitude of the residual divided by the observed quantity) is shown for number density (top), temperature (middle) and energy density (bottom). At the bottom of each figure panel is a colour indicator showing the magnitude of the percentage error at each time interval; less than 10% (green), between 10% and 25% (yellow), between 25% and 50% (orange) and greater than 50% (red). Also, listed next to each figure panel is the percentage of the time period whereby the percentage error falls in the defined bounds. That is, for number density (top panel), this method yields values that are accurate to within 50%, 71% of the time (sum of green yellow and orange), and accurate to within 25% (sum of green and yellow), 39% of the time. For temperature (middle panel), this method yields values that are accurate to within 50%, 95% of the time, and accurate to within 25%, 81% of the time. For energy density (bottom panel), this method yields values that are accurate to within 50%, 77% of the time, and accurate to within 25%, 41% of the time.

It is apparent that the solar wind velocity plays a large role in driving the electron number density, temperature and energy density at GEO, with a coarse predictive capability acquired using solely this quantity as input. This study provides a simple method of predicting the electron number density, temperature and energy density at GEO for different time-scales in the future that has shown to produce results that follow the general trend of observations.

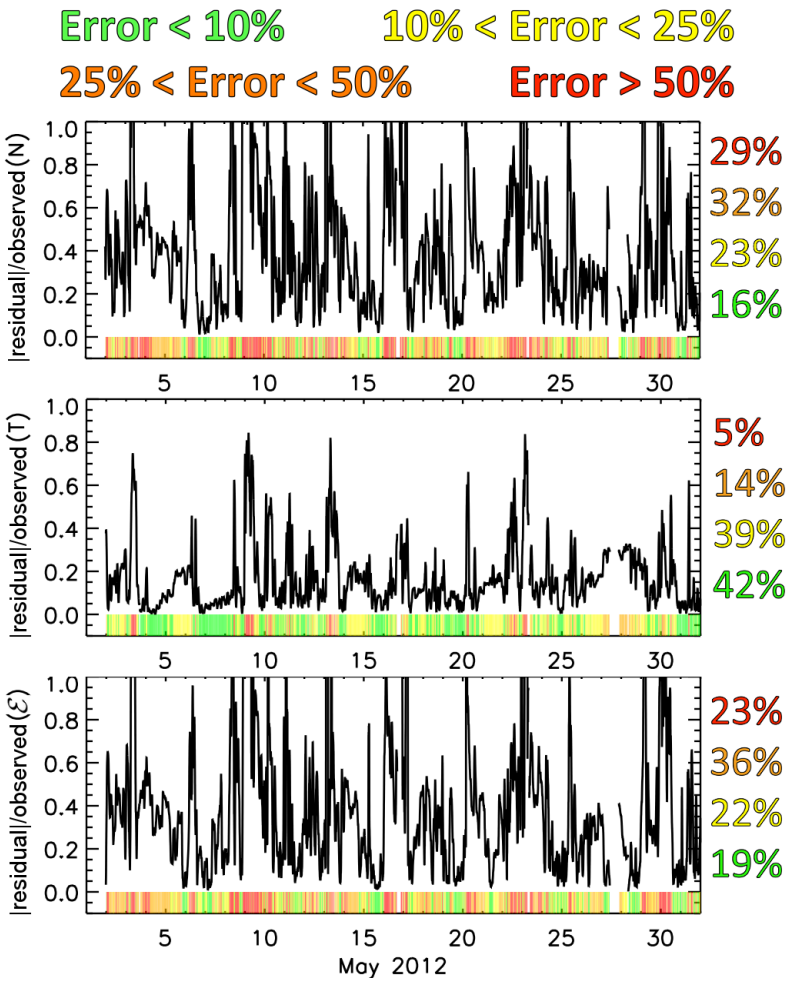

FIGURE 5.7: Figure showing the percentage error (magnitude of the residual divided by the observed quantity) for the same time period and delay shown in Figure 5.6 (May 2012, 24hr delay). The figure also contains a colour indicator at the bottom of each panel in order to show the magnitude of the percentage error; less than 10% (green), between 10% and 25% (yellow), between 25% and 50% (orange) and greater than 50% (red). Also listed on the figure is the percentage of the time period whereby the percentage error falls in the bounds defined above.

5.5 Discussion and Conclusions

This study provides insight into the driving of electron number density, temperature and energy density in four local time sectors at GEO by the solar wind. Both solar wind velocity and density exhibit a relationship with the variation of the electron number density, temperature and energy density calculated from GOES-13, with the relationship to

solar-wind velocity more well-defined than that of the solar-wind density. Elevated electron temperatures and number densities in the outer electron radiation belt can occur during slow solar wind, however for both elevated electron temperature and elevated electron number density to occur simultaneously, elevated solar wind speed is required, either instantaneous, or some time in the previous 48 hours. Solar wind velocity dependent lower limits are visible in electron temperature, number density and energy density at GEO, similar to the 'triangle shape' uncovered by *Reeves et al.* [2011] for electron flux, with the limits becoming clearer with the addition of a time delay. A function describing this velocity dependent lower limit is calculated, in addition to an upper limit and a predicted value. These functions are shown in Equations 5.6, 5.7 and 5.8 with coefficients listed in Tables 5.1, 5.2 and 5.3 for all four local time sectors. This result allows for a coarse prediction for the electron number density, temperature and energy density at GEO for intervals of 12 hours in the future (within given confidence levels), given an instantaneous solar wind velocity. These functions and corresponding coefficients are then tested on GOES-13 data from 2012 and are shown to follow the overarching trend of the observed values.

The temperature distributions, when observed over the range of time delays applied in this study, are consistent with the heating of a low energy population by elevated solar wind velocity. This is apparent in Figure 5.4 as an increasing gradient of the calculated velocity dependent lower limit once a time delay is applied (i.e. several hours following an observation of elevated solar wind velocity, it is unlikely that the temperature of electrons at GEO will be low). This is consistent with the results of *Borovsky and Denton* [2010b].

From testing the calculated prediction functions (Figure 5.6), it appears that the calculated electron number density, N, and energy density, $\mathcal{E}$, follow the general trend of observations more cleanly than the electron temperature, T, via the methodology used in this study. Given that electron number density and temperature are the fundamental physical parameters of a plasma, the result is a testable model that addresses elementary plasma properties. Hence, for a Maxwellian plasma, it is possible to infer the flux at any energy, not just energy channels tied to a particular instrument. The electron energy density at GEO is not a quantity that has been widely considered in recent publications. Perhaps with the direct relationship to solar wind velocity highlighted in this study, it is a quantity that could be further examined in research of radiation belt dynamics. Additionally, it may be beneficial for future studies to consider other candidate solar wind drivers in addition to the solar wind velocity. Whilst using solely this parameter has been shown to be capable of obtaining a coarse prediction of the partial moments from GOES-13, obviously it does not capture all of the short timescale variability.

In conclusion;

1. The electron temperature, electron number density and electron energy density variations at GEO display a dependence on the solar wind proton density, however the relationship with solar wind velocity is more well-defined.

2. Both elevated electron temperature and elevated electron number density in the outer electron radiation belt can occur over a broad range of solar wind velocities. For both elevated electron temperature and elevated electron number density to occur simultaneously, fast solar wind is usually observed approximately 24 hours previous.

3. The electron number density at GEO displays similar characteristics to the structure observed in the fluxes described by *Paulikas and Blake* [1979] and more recently by *Reeves et al.* [2011] ('triangle distribution'). The electron number density at GEO is subject to a solar wind velocity dependent lower limit.

4. The electron temperature at GEO does not display a velocity dependent lower limit when compared with the instantaneous solar wind velocity. However with increasing time lag, a velocity dependent lower limit does become more apparent (i.e. the temperature of the electron distribution at GEO increases during the fast solar wind following the passing of a co-rotating interaction region).

5. Considering the electron energy density instead of the electron temperature improves the correlation of this moment with solar wind velocity (due to the removal of the number density term in the denominator of the temperature integrals). The electron energy density is subject to a solar wind velocity dependent lower limit.

6. It is possible, given a solar wind velocity, to obtain a coarse prediction of the electron number density, temperature and energy density at GEO (within given confidence limits) at some time in the future. These predictions, and 90% confidence limits, are defined using Equations 5.6, 5.7 and 5.8 with coefficients listed in Tables 5.1, 5.2 and 5.3 for electron number density, temperature and energy density respectively for all local time sectors.

Chapter 6

Applying the cold plasma dispersion relation to whistler mode chorus waves: EMFISIS wave measurements from the Van Allen Probes

The following work is published in the Journal of Geophysical Research: Space Physics *(Hartley D. P., Y. Chen, C. A. Kletzing, M. H. Denton, and W. S. Kurth (2015), Applying the cold plasma dispersion relation to whistler mode chorus waves: EMFISIS wave measurements from the Van Allen Probes, J. Geophys. Res. Space Physics, 120, doi:10.1002/2014JA020808).*

6.1 Abstract

Most theoretical wave models require the power in the wave magnetic field in order to determine the effect of chorus waves on radiation belt electrons. However, researchers typically use the cold plasma dispersion relation to approximate the magnetic wave power when only electric field data are available. In this study, the validity of using the the cold plasma dispersion relation in this context is tested using EMFISIS observations of both the electric and magnetic spectral intensities in the chorus wave band (0.1-0.9 f_{ce}). Results from this study indicate that the calculated wave intensity is least accurate during periods of enhanced wave activity. For observed wave intensities $>10^{-3}$ nT^2, using the cold plasma dispersion relation results in an underestimate of the wave intensity by a factor of 2 or greater, 56% of the time over the full chorus wave band, 60% of the time for lower band chorus, and 59% of the time for upper band chorus. Hence during active periods, empirical chorus wave models that are reliant on the cold plasma dispersion relation will underestimate chorus wave intensities to a significant degree, thus causing questionable calculation of wave-particle resonance effects on MeV electrons.

6.2 Introduction

Relativistic electron fluxes in the outer radiation belt ($3 < L < 7$) are highly dynamic during periods with enhanced geomagnetic activity (e.g., *Onsager et al.* [2002]; *Green et al.* [2004]; *Borovsky and Denton* [2009a]; *Hartley et al.* [2014]). This variability is driven by an imbalance between source, loss and transport mechanisms, each of which may become enhanced during geomagnetic storms (e.g., *Reeves et al.* [2003a]; *Chen et al.* [2007a]; *Liemohn and Chan* [2007]; *Morley et al.* [2010]; *Turner et al.* [2012]; *Hartley et al.* [2013]).

Previous studies indicate that enhancements of energetic electrons in the outer radiation belt are driven by acceleration processes within the magnetosphere (e.g. *Li et al.* [1997]). It is well established that radial diffusion, which violates the third adiabatic invariant of particle motion, can transport electrons inwards and therefore increase their energy through betatron and Fermi acceleration processes (e.g., *Schulz and Lanzerotti* [1974]). This type of acceleration requires positive gradients in the phase space density vs. L-shell profile inwards of the source region. Recent studies have shown that persistent local maxima in the phase space density profiles exist between $4 < L < 5.5$ (e.g., *Green and Kivelson* [2004]; *Chen et al.* [2007b]; *Turner et al.* [2010]; *Shprits et al.* [2012]; *Reeves et al.* [2013a]). These studies demonstrate that local acceleration mechanisms, such as wave-particle interactions, which violate the first and second adiabatic invariants of particle motion, are also at work within the outer belt region.

Whistler-mode chorus waves are considered to be highly efficient for local acceleration of electrons up to relativistic energies [*Summers et al.*, 1998; *Thorne*, 2010]. Chorus waves

are in the VLF (Very Low Frequency) range ($\sim$ 100 Hz$-$10s of kHz), and typically occur in two bands, lower and upper, typically separated by a gap at half of the electron gyrofrequency. Modelling electron resonances with this type of wave requires the knowledge of chorus distributions, a topic that has been actively studied (e.g., *Horne and Thorne* [2003]; *Meredith et al.* [2003a]; *Li et al.* [2009a,b]; *Tu et al.* [2013]). Aside from the recently developed particle proxies (e.g., *Li et al.* [2013]; *Chen et al.* [2014]), empirical chorus models (e.g., *Meredith et al.* [2003a, 2012]) are traditionally used. However when no magnetic wave field data were available, previous studies used cold plasma theory to infer the magnetic wave power from electric field observations and thus, current empirical wave models are based on this assumption. Recently, equipped with comprehensive wave and plasma instruments, the successfully operating Van Allen Probes mission provides an opportunity to explore the validity of this assumption.

6.3 Motivation and Methodology

Previous studies often used the wave data set from the Combined Release and Radiation Effects Satellite (CRRES) to examine the role of chorus waves in radiation belt dynamics, more specifically, the acceleration of electrons to MeV energies (e.g. *Meredith et al.* [2003a,b, 2012]). The Plasma Wave Experiment (PWE) on-board the CRRES satellite measured wave electric fields with high resolution in the frequency range 5.6 Hz to 400 kHz, which fully covers the chorus frequency range [*Anderson and Gurnett*, 1992]. Given the need to investigate the energization of radiation belt electrons, and given that energy diffusion rates scale with the magnetic field intensity [*Kennel and Petschek*, 1966; *Summers and Ma*, 2000], it was necessary to convert the electric field spectral intensities

(as measured by CRRES) to magnetic field spectral intensities. This can be performed using the expression:

$$S_B = \frac{1}{c^2}\left(1 - \frac{f_{pe}^2}{f\,(f - f_{ce})}\right) S_E \tag{6.1}$$

which is derived from Maxwell's third equation (Faraday's Law), assuming a cold plasma dispersion relation for parallel propagating whistler mode waves [*Meredith et al.*, 2004] (see Appendix C). Here, S_B and S_E are the magnetic and electric field spectral intensities respectively, c is the speed of light, f is the wave frequency, f_{pe} is the electron plasma frequency and f_{ce} is the electron gyrofrequency. The applicability of the cold plasma dispersion relation in this manner was untested when employed in previous studies. Of course the cold plasma dispersion relation is applicable in a cold plasma; however when the plasma has a significant warm/hot component, implementation of the cold plasma dispersion relation may result in large uncertainties of calculated quantities. For example, the cold plasma dispersion relation is likely to yield accurate results when applied to hiss (e.g. *Meredith et al.* [2004]) inside of the plasmasphere (a relatively cold magnetospheric plasma $\sim$ 1 eV). Outside of the plasmasphere the plasma is warmer and thus the cold plasma dispersion relation may not be as applicable to chorus waves that occur in this region (e.g. *Meredith et al.* [2003a]).

With the comprehensive wave instrumentation now available aboard the Van Allen Probes mission, it is possible to test the accuracy of using the cold plasma dispersion relation to calculate the integral magnetic field intensity. The Waves Instrument, part of the Electric and Magnetic Field Instrument Suite and Integrated Science (EMFISIS)

instrument suite, onboard the Van Allen Probes [*Kletzing et al.*, 2013] measures both electric and magnetic field spectral intensities across the chorus wave frequency range. Comparing the measured magnetic field spectral intensity with the calculated magnetic field spectral intensity (using the measured electric field spectral intensity and Equation 6.1) provides a quantitative determination of the accuracy of the cold plasma assumption. The electron gyrofrequency is easily calculated using the magnetic field measured by the Van Allen Probes EMFISIS magnetometer instrument whilst the plasma frequency, f_{pe}, is inferred from the upper hybrid line (UHL). The plasma frequency dataset inferred from the UHL is not yet complete and therefore only available for those orbits processed to date.

Using the measured electric field spectral intensity and Equation 6.1, the magnetic field spectral intensity is calculated (e.g. *Meredith et al.* [2003a,b, 2004, 2012]). This quantity is then integrated across the full (0.1-0.9 f_{ce}), lower (0.1-0.5 f_{ce}) and upper (0.5-0.9 f_{ce}) band chorus frequency ranges in order to calculate the chorus wave intensities. These calculated wave intensities can then be directly compared to the observed chorus wave intensities as a test of the cold plasma assumption.

Plasmaspheric hiss can also occur in the lower band chorus frequency range at low L-shells (inside the plasmasphere). Therefore, in this study, the plasma density is required to be less than $10 \times (6.6/L)^4$ or 30 cm^{-3} (whichever is smaller) in order for a location to be defined as outside of the plasmasphere, thus excluding plasmaspheric hiss emissions (e.g. *Li et al.* [2014]).

The method described above is applied to a 20 day sample of Van Allen Probe A data where the plasma frequency, f_{pe}, inferred from the UHL, is available. This data sample

provides preliminary results that span a limited range of L-shells, MLT, solar wind conditions and geomagnetic activity indices. However, during this sample period, a broad range of wave activity levels are observed, thus allowing for the accuracy of using the cold plasma dispersion relation to calculate the magnetic field spectral intensity, and wave intensity, to be tested across a range of conditions. For data quality, two of the measured frequency bands (centred around $\sim$ 2 and 4 kHz) are removed due to increased noise levels. Since the same frequency bands are removed from both the electric and magnetic field wave observations, the calculated integral wave powers remain comparable. Also in this study, the instrument background levels are subtracted from both the electric and magnetic field spectral intensities. If the background subtraction results in either electric or magnetic spectral intensities below zero at a given frequency, the spectral intensity of both the wave electric and magnetic field is set to zero at this frequency.

6.4 Results

Firstly, the measured spectral intensity of the electric and magnetic wave field is observed for a sample case where whistler-mode chorus waves are present. Figure 6.1 shows the electric, S_E, (top) and magnetic, S_B, (bottom) wave spectral intensities observed by Van Allen Probe A during an 8-hour period on December 16, 2012. The dashed pink lines indicate 0.1 and 0.9 f_{ce} and the dashed red line indicates 0.5 f_{ce} as calculated from the onboard magnetometer measurements. Whistler mode chorus waves are evident in both the electric and magnetic field spectral intensity, occurring in two bands, lower and upper, separated by half of the electron gyrofrequency. Plasmaspheric hiss is also evident

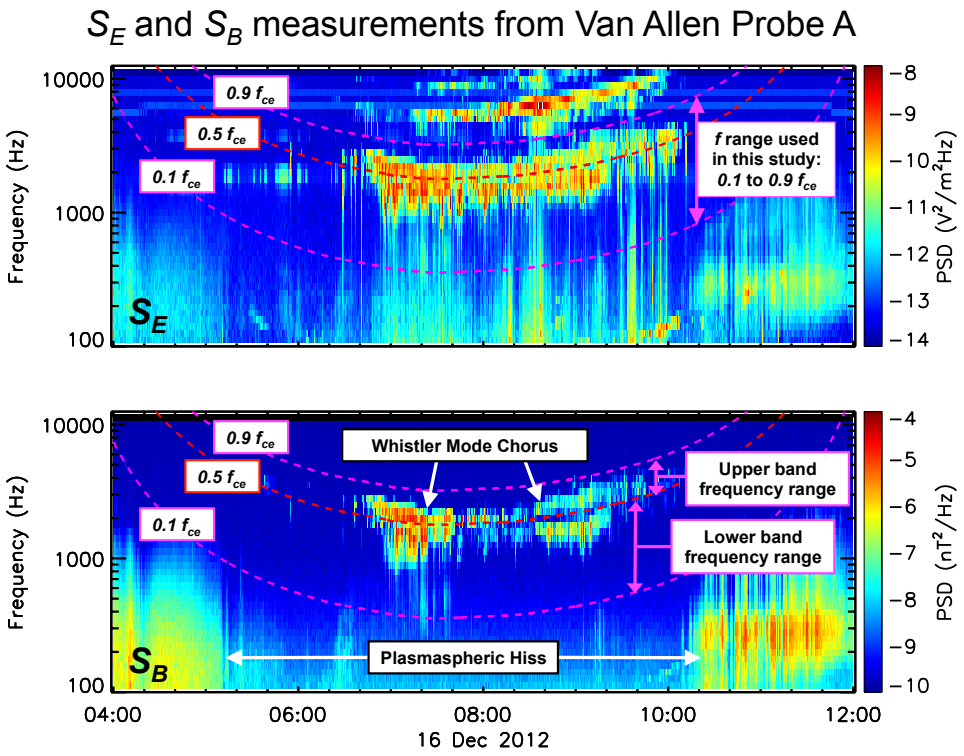

FIGURE 6.1: A survey plot of the electric, S_E, (top) and magnetic, S_B, (bottom) wave spectral intensity observed by Van Allen Probe A during an 8-hour period on December 16, 2012. The dashed pink lines indicate 0.1 and 0.9 f_{ce} and the dashed red line indicates 0.5 f_{ce} as calculated from the onboard magnetometer measurements. Whistler mode chorus waves and plasmaspheric hiss are highlighted in the spectrogram.

- an unstructured emission that is generally confined to the plasmasphere occurring at frequencies below a few thousand Hz.

As a test of the methodology described above, the measured power spectral density is compared to that calculated using the cold plasma dispersion relation. Figure 6.2 displays the power spectral density of the wave magnetic field in the chorus wave frequency range as measured by EMFISIS (blue) and as calculated using the cold plasma dispersion relation (red) for three instances of time. The normalized root-mean-square (RMS) deviations are also listed. For the first time instance, 12:01:41 on November 20, 2012, (Figure 6.2a) using the cold plasma dispersion relation allows for the magnetic field

power spectral density between 0.1 and 0.9 f_{ce} to be accurately calculated. That is, the red and blue lines shown in Figure 6.2a match extremely well. Both upper and lower band chorus waves are apparent during this period with a gap between the two at approximately half of the electron gyrofrequency. The normalized RMS error is very low for this time instance (0.111). For the second instance of time, 11:21:47 on November 20, 2012, (Figure 6.2b) using the cold plasma dispersion relation results in the calculated power spectral density being around one order of magnitude less than that observed across the entire lower band chorus wave frequency range. That is, the red line on Figure 6.2b is significantly lower than the blue line over the entire 0.1-0.5 f_{ce} frequency range. The normalized RMS error for this time instance is 0.287. For the third time instance, 12:00:11 on November 20, 2012, (Figure 6.2c) the shape of the calculated power spectral density does not quite match that observed by EMFISIS. That is, in contrast to the systematic shift in power spectral density shown in Figure 6.2b, the discrepancies in this case are frequency dependent. At some frequencies the calculated power spectral density is greater than that observed, and at other frequencies the calculated power spectral density is less than that observed. The normalized RMS error for this time instance is 0.217. Discrepancies between the observed and calculated quantities, such as those shown in Figure 6.2b and c, will certainly affect the calculated integral magnetic field wave intensity, B_w^2. Cases similar to those shown in Figure 6.2b (systematic shift) will result in significant errors in the calculated chorus wave intensity. Cases similar to those shown in Figure 6.2c (frequency dependent error) may result in errors in the calculated chorus wave intensity, however it is also possible that when integrated to calculate the wave intensity in the chorus frequency range, the discrepancies could cancel out resulting in the calculated wave intensity matching that measured by the Van Allen Probes. Despite

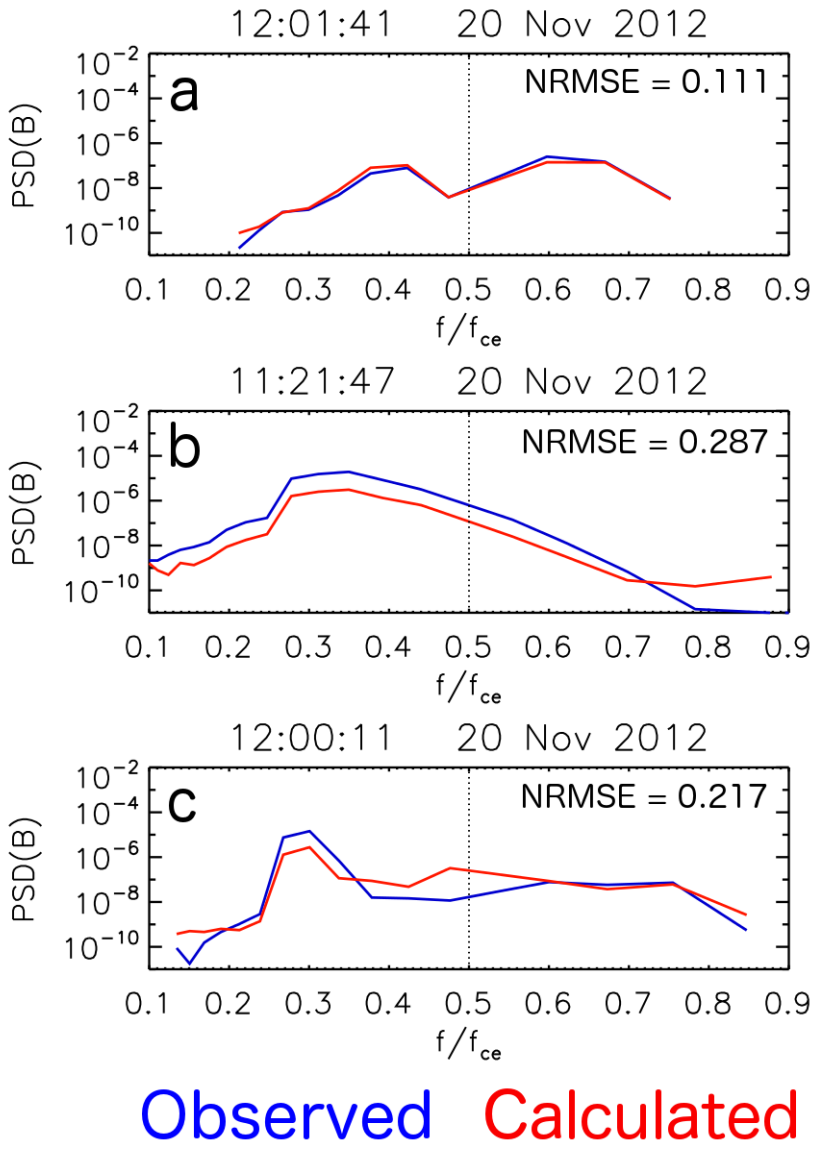

FIGURE 6.2: The magnetic field power spectral density in the chorus wave frequency band (between 0.1 and 0.9 f_{ce}) as measured by EMFISIS on-board Van Allen Probe A (blue) and as calculated using the cold plasma dispersion relation (red) at 12:01:41 (a), 11:21:47 (b) and 12:00:11 (c) on November 20, 2012. The normalized root-mean-square errors (NRMSE) are also listed.

the normalized RMS errors shown in Figures 6.2b and c being approximately equal, in cases similar to that shown in Figure 6.2c it is likely that the calculated integral wave intensity will be less affected by these deviations in comparison to cases similar to that presented in Figure 6.2b.

Applying the methodology described in Section 6.3 to a 20 day sample of Van Allen Probe A EMFISIS wave data where the plasma frequency inferred from the UHL is available allows for the accuracy of using the cold plasma dispersion relation to be considered. Figure 6.3a compares measured and calculated magnetic field chorus wave intensity, the integral of the power spectral density between 0.1 and 0.9 f_{ce}. The color indicates the number of occurrences in each bin, normalized to the maximum event number in each observed wave intensity column. In this way, distributions of calculated magnetic wave intensities for a given observed magnetic wave intensity can be clearly seen. If all calculated wave intensities were equal to those observed (i.e. the cold plasma assumption yielded perfect results), all points would lie on the diagonal equivalence line. Also shown are the number of occurrences in each observed wave intensity column, in addition to the total number of occurrences (ΣN) and the number of occurrences with high observed wave intensity (ΣN ($B_w^2 > 10^{-3} nT^2$)). It is apparent that for the vast majority of the period studied, the calculated magnetic field wave intensity is relatively close to that observed by Van Allen Probe A. During periods of low observed magnetic field wave intensity, there are a number of points that lie above the line of equivalence, with some calculated values greater than three orders of magnitude larger than those observed. At times when the observed magnetic field wave intensity is elevated (B_w^2 $>10^{-3}$ nT^2), the higher density of points appears to drift below the line of equivalence; the observed magnetic field wave intensity is greater than that calculated using the cold plasma dispersion relation.

To further investigate whether using the cold plasma dispersion relation to calculate magnetic field power spectral densities, and thus wave intensities, is more accurate for

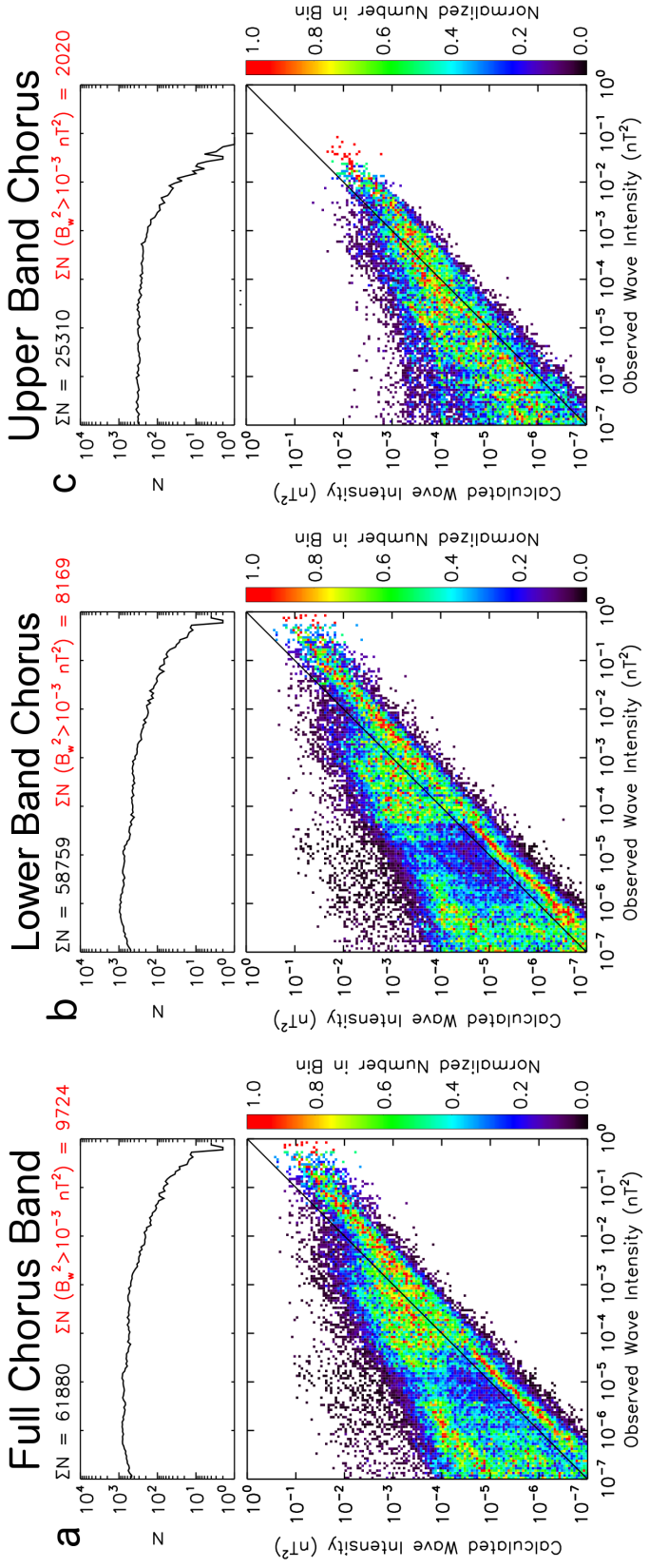

FIGURE 6.3: (a) Plot showing how the observed wave intensity from Van Allen Probe A compares with that calculated using the cold plasma dispersion relation in the 0.1 to 0.9 f_{ce} range for the 20 day sample period used in this study. The color indicates the number of occurrences in each bin, normalized to the number of occurrences in each observed wave intensity column. The line plot above each panel indicates the number of occurrences in each observed wave intensity column, in addition to listing the total number of occurrences (ΣN) and the number of occurrences with high observed wave intensity (ΣN ($B_w^2 > 10^{-3} nT^2$)). (b and c) The same quantities calculated separately for lower band (0.1 to 0.5 f_{ce}) and upper band (0.5 to 0.9 f_{ce}) chorus frequencies.

specific frequency bands, the data are sorted between lower (0.1 and 0.5 f_{ce}) and upper (0.5 and 0.9 f_{ce}) band chorus frequencies. Figure 6.3b and c display the same quantities as shown in Figure 6.3a, after this sorting in frequency band has taken place. It is apparent that wave intensities are generally higher in the lower band chorus frequency range compared to upper band chorus frequencies. The structure observed for lower band chorus wave frequencies (Figure 6.3b) is largely similar to that observed for the full chorus band (Figure 6.3a). Again, during periods of low observed magnetic field wave intensity, there are a number of points significantly above the line of equivalence with some calculated quantities over three orders of magnitude larger than those observed. At times when the observed magnetic field wave intensity is elevated ($B_w^2 > 10^{-3}$ nT^2), the higher density of points exists below the equivalence line with very few data points above the equivalence line. That is, the observed magnetic field wave intensity is generally greater than that calculated using the cold plasma dispersion relation during elevated chorus activity. For upper band chorus frequencies (Figure 6.3c), there is a substantially greater spread of data from the line of equivalence than for lower band chorus frequencies. Thus, using the cold plasma dispersion relation to calculate upper band chorus wave intensity will result in a greater number of deviations from the observed magnetic wave intensity when compared to the same technique used for lower band chorus frequencies.

In order to better understand the deviations from the line of equivalence, the ratio of calculated and observed wave intensities (observed/calculated) are considered for both low and elevated wave activity. Low wave intensity is parametrized as $B_w^2 < 10^{-3} nT^2$ and elevated wave intensity as $B_w^2 > 10^{-3} nT^2$. Figure 6.4a and b show the probability

distributions of the logarithm of the wave intensity ratio in the full chorus wave frequency band (observed/calculated) for both low and elevated observed wave intensities respectively. Also shown are the percentages of data that occur in discreet ratio bins parametrized as; calculated wave intensity is an overestimate by greater than a factor of 5 (Ratio < 0.2, dark blue), calculated wave intensity is an overestimate by greater than a factor of 2 but by less than a factor of 5 ($0.2 <$ Ratio < 0.5, light blue), calculated wave intensity is within a factor of 2 of the observed value ($0.5 <$ Ratio < 2.0, green), calculated wave intensity is an underestimate by greater than a factor of 2 but by less than a factor of 5 ($2.0 <$ Ratio < 5.0, orange), and calculated wave intensity is an underestimate by greater than a factor of 5 (Ratio > 5.0, red). For the full chorus band, the mean wave intensity ratio is 0.83 (-0.08 on logarithmic scale) during low wave activity. That is, on average using the cold plasma dispersion relation to calculate the wave intensity between 0.1-0.9 f_{ce} will yield relatively accurate results during low wave activity. However, during elevated chorus activity, the mean wave intensity ratio is 2.88 (0.46 on logarithmic axis). Therefore, on average, using the cold plasma dispersion relation will result in an underestimate of the wave intensity by a factor of $\sim$3 during periods of intense wave activity. There is a clear shift in the distribution towards underestimates of the calculated wave intensity when considering only periods of enhanced wave activity. The percentages listed in Figure 6.4a and b reveal that for elevated observed wave activity ($B_w^2 > 10^{-3} nT^2$), the calculated wave intensity is an underestimate by a factor of 2 or greater for 56% of the data (sum of percentages where $2.0 <$ Ratio < 5.0 and Ratio > 5.0).

The probability distributions for lower band chorus wave frequencies, as shown in Figure

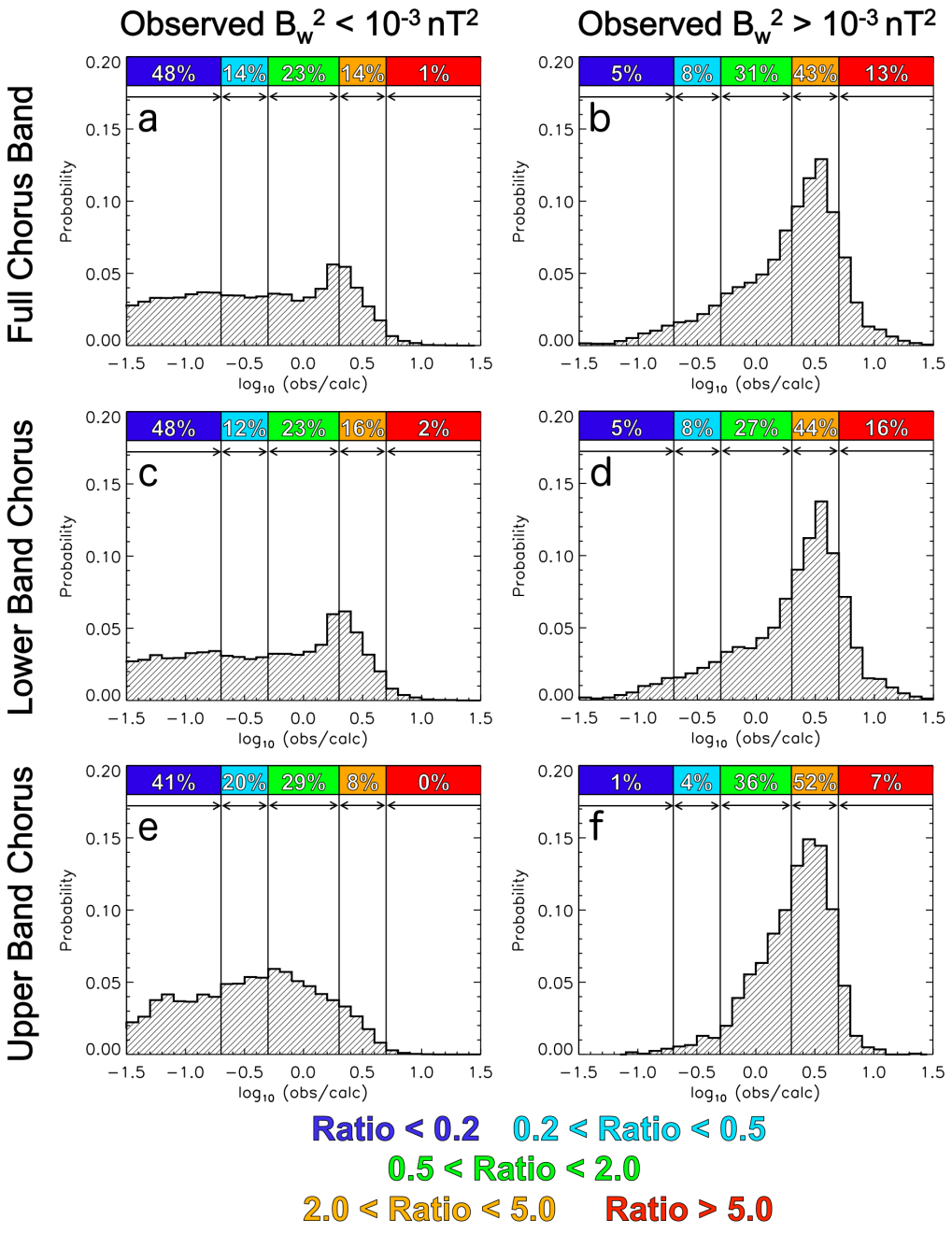

FIGURE 6.4: The probability distributions of the logarithm of the wave intensity ratio (observed/calculated) in the full chorus wave frequency band for low ($B_w^2 < 10^{-3} nT^2$, (a)) and elevated ($B_w^2 > 10^{-3} nT^2$, (b)) observed wave intensities. Also shown are the percentages of data that occur in discreet ratio bins parametrized as; Ratio < 0.2, $0.2 <$ Ratio < 0.5, $0.5 <$ Ratio < 2.0, $2.0 <$ Ratio < 5.0, and Ratio > 5.0. (c) and (d) show the same parameters for lower band chorus and (e) and (f) show the same parameters for upper band chorus.

6.4c and d, exhibit similar structure to that observed for the full chorus band. The mean wave intensity ratio is 0.92 (-0.04 on logarithmic scale) during low wave activity (Figure 6.4c). This again implies that, on average, using the cold plasma dispersion relation to calculate lower band chorus wave intensities will yield relatively accurate results during low wave activity. However, during enhanced chorus activity (Figure 6.4d) the mean wave intensity ratio is 3.15 (0.50 on logarithmic axis). This means that on average, using the cold plasma dispersion relation to calculate lower band chorus wave intensities will result in an underestimate by a factor of $\sim$3 during periods of elevated chorus wave activity. The probability distributions for upper band chorus are shown in Figure 6.4e and f. Again, during elevated wave activity (Figure 6.4f), the average upper band chorus wave intensity ratio is greater than unity (2.59, 0.42 on logarithmic scale). This implies that on average, using the cold plasma dispersion relation to calculate the upper band chorus wave intensity will result in an underestimate by a factor of $\sim$2.5 during active periods.

6.5 Discussion

This study addresses the applicability of using the cold plasma dispersion relation to calculate magnetic field spectral intensities, S_B, from electric field spectral intensities, S_E, in a plasma that may contain a significant warm/hot component (cf. *Meredith et al.* [2003a,b, 2004, 2012].

Results indicate that on average, wave intensities calculated using the cold plasma dispersion relation closely match observations during periods of low activity. However,

during elevated wave activity ($B_w^2 > 10^{-3}nT^2$), there is a clear shift in the distributions which clearly indicates that using the cold plasma dispersion relation will result in underestimates of the chorus wave intensity. That is, using the cold plasma dispersion relation to calculate the chorus wave intensity results, on average, in an underestimate by a factor of ∼3 for the full band, ∼3 for lower band and ∼2.5 for upper band on average during enhanced wave activity. For lower band chorus waves, using the cold plasma dispersion relation to calculate the wave intensity results in an underestimate by a factor of 2, or greater, 60% of the time. For waves in the upper chorus frequency band, this number is 59%, although the number of larger underestimates is significantly lower. These discrepancy percentages, particularly for lower band chorus waves, highlight the need for new empirical wave models based on direct observations.

Some possible explanations for the discrepancies that arise from implementing the cold plasma dispersion relation are considered. Firstly, implementation of the cold plasma dispersion relation in a plasma that has a significant warm/hot component may explain the observed deviations of ratios away from unity. Secondly, large amplitude chorus waves may propagate highly obliquely in a quasi-electrostatic mode (e.g. *Agapitov et al.* [2013]). Given that the wave propagation angle is not identified in this study, this may be a factor that contributes towards the observed discrepancies in calculated wave intensity. The uncertainty in the inferred plasma frequency is between 10-20% which would lead to a maximum error factor of ~ 1.44 in the spectral intensities. Hence errors in the determined f_{pe} cannot fully explain the observed factor of 2 or greater deviations.

6.6 Conclusions

In this study, EMFISIS observations of chorus wave magnetic spectral intensities have been directly compared to spectral intensities calculated using the cold plasma dispersion relation and the wave electric field. The direct comparison between observed and calculated wave intensities reveals that for observed wave intensities $>10^{-3}$ nT^2, using the cold plasma dispersion relation results in an underestimate of the wave intensity by a factor of 2 or greater, 56% of the time over the full chorus wave band, 60% of the time for lower band chorus, and 59% of the time for upper band chorus. The impact of this is that empirical wave models that are based on CRRES data may tend to underestimate the chorus wave intensity during active periods, thus wave-particle resonance effects (i.e. energy diffusion rates which scale with the magnetic field wave intensity [*Kennel and Petschek*, 1966; *Summers and Ma*, 2000]) on MeV electrons may be underestimated. Therefore, improved empirical wave models based upon direct measurements from the Van Allen Probes are highly desirable.

Chapter 7

Summary and Further Research

The research presented in the preceding chapters explores the spatial and temporal variability of the outer electron radiation belt. Previous research studies have identified many different source, loss and acceleration mechanisms that drive the dynamics of the outer radiation belt (e.g. *Shprits et al.* [2008a,b] and references therein) yet a complete understanding of the relative contribution of each processes, and how these contributions vary over time, is yet to be determined. Radiation belt dropouts are driven by a sudden enhancement of loss mechanisms and are therefore an area of active research. The evolution of the electron radiation belt through three HSS induced dropouts is the focus of the work presented in Chapter 4. Exactly how radiation belt electrons are accelerated to relativistic energies is also a topic of intense research. Persistent phase space density peaks existing between $4 < \mathrm{L} < 5.5$ have been highlighted by numerous authors (e.g., *Green and Kivelson* [2004]; *Chen et al.* [2007b]; *Turner et al.* [2010]; *Shprits et al.* [2012]; *Reeves et al.* [2013a] and references therein), thus showing that local acceleration mechanisms are at work within the outer belt region. Electron interactions with whistler-mode chorus

waves are considered to be highly efficient for local acceleration [*Summers et al.*, 1998; *Thorne*, 2010] and are a crucial component of current wave models. However, due to the limitations of past in-situ wave measurements, empirical wave models may be based on inferred parameters that assume a cold plasma dispersion relation (e.g. *Meredith et al.* [2003a,b, 2004, 2012]). With the NASA Van Allen Probes mission housing instrumentation that allows for this assumption to be tested [*Kletzing et al.*, 2013], Chapter 6 presents results that provide the first step towards quantifying the limitations of this assumption. Understanding not only the variability of the electron radiation belt, but also the variability in the mechanisms that drive it, is a crucial component of building an accurate physical model. Another approach is to build an empirical model based on observations and statistics. Comparing radiation belt and solar wind observations allows for correlative studies to take place (e.g. [*Reeves et al.*, 2011]), with the addition of a time delay allowing for a predictive model to be obtained. This is the approach taken for the research presented in Chapter 5.

A brief summary of the research results presented in Chapters 4, 5 and 6 is given below.

7.1 Case Studies of the Impact of High-Speed Solar Wind Streams on the Electron Radiation Belt at Geosynchronous Orbit: Flux, Magnetic Field and Phase Space Density

Radiation belt dropouts are known to occur during the passing of high-speed solar wind streams (HSSs). Three HSS induced radiation belt dropouts are studied using pitch-angle-resolved electron data, in addition to magnetic field observations, from the GOES-13 satellite at geosynchronous orbit. The phase space density (PSD) is calculated at fixed values of the first and second adiabatic invariants whilst studying the evolution of PSD and the third invariant (L^*) over time. The results of this study highlight the importance of outwards adiabatic transport as a contributing mechanism for driving the observed reductions in electron flux at GEO. In addition, the pitch-angle distributions observed during the passing of the HSS interface show signatures of other loss mechanisms (magnetopause shaddowing, outwards radial diffusion). The pitch-angle distributions during two of the studied HSS events exhibit similar evolutionary structure. That is, (i) highly peaked distributions (centred around 90°) immediately prior to the dropout (ii) sharp transitions between peaked and isotropic and then subsequent butterfly distributions, and (iii) isotropic distributions at minimum flux shortly afterwards (dusk sector). The similarity between these events is likely to be due to the comparable position of GOES-13 in local time. The issue of interpreting PSD calculations (that are reliant on magnetic field models) is addressed through comparisons of the T96 model magnetic field and

that measured in-situ by GOES-13. The results of this study provide a first step towards quantifying the timeline of events that occur in the outer radiation belt following during the passing of a HSS. This is particularly timely given the expected increase in the occurrence of HSS during the declining phase of the current solar cycle.

7.2 Electron number density, temperature and energy density at GEO and links to the solar wind: A simple predictive capability

The response of electron flux in the outer radiation belt to different solar wind parameters has been uncovered by numerous authors. This study investigates the response of the partial moments (electron number density, temperature and energy density) from GOES-13. This allows for changes in the number of electrons and the temperature of the electrons to be distinguished, which is not possible with the outputs of individual instrument channels. Investigating how the electron distribution at GEO is affected by fluctuations in different solar wind drivers, both instantaneous and time delayed, allows for the primary driver to be determined. This, in turn, allows for a coarse predictive capability of the partial moments from GOES-13 to be developed. By testing the calculated prediction functions against data from 2012, it is found that using solely the solar wind velocity as a driver results in predicted values that accurately follow the general trend of the observed moments. Given that the number density and temperature are the fundamental physical parameters of a plasma distribution, the result of this study is a testable model that addresses elementary plasma properties. Hence, for a Maxwellian

plasma, it is possible to infer the flux at any energy, not just energy channels tied to a particular instrument. The electron energy density is not a parameter that has been widely considered in recent publications. Perhaps, with the direct relationship to solar wind velocity uncovered by this study, future research into the dynamics of the radiation belts may consider the electron energy density as an important parameter.

7.3 Applying the cold plasma dispersion relation to whistler-mode chorus waves: EMFISIS wave measurements from the Van Allen Probes

The energy diffusion rates of electrons in the outer radiation belt scale with the magnetic field wave intensity. However when no magnetic wave field data were available, as in previous studies, cold plasma theory was used to infer the magnetic wave power from electric field observations. Therefore, current empirical wave models are based on this assumption. With the comprehensive wave and plasma instruments now available onboard the Van Allen Probes mission, the validity of this assumption can be explored. EMFISIS measurements of chorus wave magnetic spectral intensities have been compared to spectral intensities calculated using the cold plasma dispersion relation and the wave electric field. The comparison between calculated and observed wave intensities reveals that during elevated observed wave intensity (B_w^2 $>10^{-3}$ nT^2), using the cold plasma dispersion relation results in an underestimate of the wave intensity by a factor of 2 or greater, 56% of the time over the full chorus wave band, 60% of the time for

lower band chorus, and 59% of the time for upper band chorus. Since the error in the inferred plasma frequency is between 10-20%, the observed discrepancies between observed and calculated wave intensities are unlikely to be caused by errors in the f_{pe} inferred from the upper hybrid line. Implementation of the cold plasma dispersion relation in a plasma that has a significant warm/hot component may explain the observed deviations of ratios away from unity. Given that the wave propagation angle is not identified in this study, this may also be a factor that contributes towards the observed discrepancies in calculated wave intensity. The impact of this study is that empirical wave models that are based on CRRES data may tend to underestimate the chorus wave intensity during active periods, therefore wave-particle resonance effects on MeV electrons may be underestimated. This identifies the need for improved empirical wave models based upon direct measurements from the Van Allen Probes.

7.4 Further Research

The conclusions presented in Chapters, 4, 5 and 6 highlight the need for additional research in radiation belt dynamics. Listed below are several additional studies that could be conducted either through the continuation, or expansion, of the research studies presented in the preceding chapters.

7.4.1 Testing the validity of the cold plasma dispersion relation for different wave modes

The discrepancies between observed and calculated wave intensities for chorus waves is highlighted in Chapter 6, however the same cold plasma dispersion relation has also been used to infer the wave amplitude of plasmaspheric hiss (e.g. [*Meredith et al.*, 2004]). The applicability of the cold plasma dispersion relation for plasmaspheric hiss can be tested by using the same criteria for identifying plasmaspheric hiss as used in *Meredith et al.* [2004], and using EMFISIS wave observations. As more Van Allen Probes data becomes available, the magnetic local time, L-shell, and substorm dependence of the applicability of the cold plasma dispersion relation can also be explored for different wave modes. Using the temperature from the Helium Oxygen Proton Electron (HOPE) instrument onboard the Van Allen Probes may reveal a threshold for when implementing the cold plasma dispersion relation is a valid assumption. This research study allows for the improvement of empirical wave models, and will therefore contribute towards an improved predictive capability of the radiation belts.

7.4.2 Evidence of acceleration by whistler-mode chorus waves at geosynchronous orbit

Kennel and Petschek [1966] established a connection between low-energy electrons and chorus wave activity. During geomagnetic storms and substorms, low-energy electrons are injected from the plasma sheet into the inner magnetosphere, and due to adiabatic effects, their pitch angle distributions can become anisotropic. These anisotropies may then excite instabilities that, in turn, generate chorus waves. Through the study of the

low-energy pitch angle distributions observed by the Van Allen Probes HOPE instrumentation, in parallel to the EMFISIS chorus wave intensities, it is possible to explore the threshold anisotropy required to generate chorus waves. This allows for the pitch angle distributions to be used as a proxy for chorus wave activity. The proxy obtained using Van Allen Probes data can then be applied to the pitch angle distributions observed by the Magnetospheric Electron Detector (MAGED) onboard the GOES satellites at geosynchronous orbit. Given that whistler-mode chorus waves are considered to be highly efficient for local acceleration of electrons up to relativistic energies [*Summers et al.*, 1998; *Thorne*, 2010], the effect of chorus waves will be observable in the GOES MAGED and Energetic Proton Electron and Alpha Detector (EPEAD) as an increase in relativistic electron fluxes, in addition to an increase in the gradient of the distribution function vs. energy spectrum (increasing temperature).

7.4.3 Predictive model using Van Allen Probes data

Paulikas and Blake [1979], and more recently *Reeves et al.* [2011], investigated the relationship between radiation belt electron fluxes and solar wind velocity and revealed that plotting the electron fluxes at GEO against solar wind velocity produced a 'triangular' distribution. Therefore, a model that uses solar wind velocity as the sole input will only be able to provide a broad range of predicted flux values during slow solar wind speeds. In order to address this issue, meaningful physical parameters can be generated, and their correlations with relativistic electron fluxes studied. For example, *Burin des Roziers et al.* [2009] showed that a strong correlation exists between 10s of keV plasma sheet electrons and >2 MeV electrons observed at geosynchronous orbit 2 days later.

Thus, using the flux of 10s of keV electrons, would be a meaningful quantity to use in a model that is designed to determine the relativistic electron fluxes at GEO 2 days later. From the 'triangle' distributions presented in *Reeves et al.* [2011], it can be concluded that for a given solar wind velocity, the radiation belts respond differently depending upon the time history of the solar wind. A simple way of including this response in correlative studies would be to calculate parameters such as; 'sign of solar wind velocity gradient' (positive or negative), and 'time since gradient change in the solar wind velocity'. The relationship between these generated parameters and the relativistic electron fluxes at GEO can then be investigated. In addition to using measured solar wind parameters, these physically-meaningful calculated parameters can be compared with Van Allen Probes relativistic electron observations in order to develop a highly-desirable, L-shell and local time dependent, radiation belt model.

Appendix A

Pitch-Angle Distribution Retrievals from GOES 13-15 Magnetospheric Electron Detector (MAGED) Observations

The following technique for inferring pitch angle distributions from GOES MAGED data is provided by J. V. Rodriguez.

The purpose of the method outlined here is to invert an accurate pitch angle distribution (PAD), with self-consistent error bars, from multiple telescope measurements that have broad fields-of-view. This approach was motivated in part by the authors' experience that sums of powers of trigonometric functions are very frequently inadequate for fitting MAGED PADs. Moreover, an algorithm that treats the measurements as points in pitch

angle space is likely to introduce biases in the fitted PADs. This problem was solved for the Polar High Sensitivity Telescope (HIST) by *Selesnick and Blake* [2000b] using optimal estimation [*Rodgers*, 1976; *Tarantola and Valette*, 1982]. In this development we have followed *Selesnick and Blake* [2000b] closely, using the familiar matrix notation of *Rodgers* [1976], with the necessary changes to account for the three-axis stabilized GOES spacecraft and the MAGED instrument characteristics.

The basic problem is the inversion of the measurement integral. The observed quantity is the number of counts R_{ik} measured during the accumulation period for each energy channel i at each look direction (telescope) k, and we wish to estimate the differential flux $j(E, \theta, \phi)$ on a regular pitch-angle grid. The count rate is related to the differential flux by the measurement integral:

$$R_{ik} = \iint j(E, \theta, \phi)\, A_{ik}(E, \theta, \phi) d\Omega\, dE \tag{A.1}$$

where $A_{ik}(E, \theta, \phi)$ is the effective area (cm^2) of channel i from telescope k at particle kinetic energy E and direction (θ, ϕ). We identify the polar angle θ with pitch angle α and the azimuth ϕ with the gyroangle β. The cylindrically-symmetric and energy-independent modelled MAGED A_{ik} is a good approximation of the measured response [*Hanser*, 2011]. Therefore, we treat A_{ik} as a function only of θ_t (the polar angle from the telescope axis). Its energy independence allows us to treat the energy spectrum estimate separately and therefore to replace the energy integral at this step with the product of the flux at average energy $\overline{E}_i$ and the channel energy bandwidth δE_i [*Hanser*, 2011].

The telescope axis angle is related to the pitch angles and gyroangle as follows:

$$\cos\theta_t = \cos\alpha_o \cos\alpha + \sin\alpha_o \sin\alpha \cos\beta \tag{A.2}$$

where α_o is the central pitch angle of a given telescope. Using this transformation and the energy-independence of A_{ik}, the integral is rewritten as follows:

$$R_{ik} = \delta E_i \int j(\overline{E}_i, \alpha)\ G_k(\alpha) d\alpha \tag{A.3}$$

$$G_k(\alpha) = \sin\alpha \int_0^{2\pi} A_k[\overline{E}_i \theta_t(\alpha, \beta)] d\beta \tag{A.4}$$

The quantity G_k, the response function of telescope k, has units cm^2 rad and is defined from 0 to 180° pitch angle. It is identically zero at 0 and 180°, due to the $\sin\alpha$ factor, and is positive in between.

Setting vector $\mathbf{y}$ equal to the set of measured count rates and vector $\mathbf{x}$ equal to the desired differential fluxes, these integrals are expressed approximately in terms of a matrix multiplication with the weighting function matrix $\mathbf{K}$ relating $\mathbf{y}$ and $\mathbf{x}$:

$$\mathbf{y} = \mathbf{K}\ \mathbf{x} \tag{A.5}$$

The weighting function $\mathbf{K}$ is a discrete function given by the product $G_k(\alpha)\ \Delta\alpha\ \delta E_i$ and has units cm^2 sr keV. The value of the weighting function depends on the angular sampling of the telescope response function used in the retrieval, and therefore the intervals on which the fluxes are retrieved: the coarser the sampling, the larger the value of the weighting function. The integral for calculating G_k on the equally-spaced

α output grid is evaluated by calculating A_k for θ_t at each α, stepping β from 0 to 2π. Since the telescope central pitch angles vary with time, G_k must be recalculated at each time step.

The desired differential fluxes $\mathbf{x}$ and their covariances $\mathbf{S}$ are estimated as follows [*Rodgers*, 1976]:

$$\mathbf{x} = \mathbf{x_o} + \mathbf{S_x}\ \mathbf{K^T}\left(\mathbf{K}\ \mathbf{S_x}\ \mathbf{K^T} + \mathbf{S_e}\right)^{-1}(\mathbf{y} - \mathbf{K}\ \mathbf{x_o}) \tag{A.6}$$

$$\mathbf{S} = \mathbf{S_x} - \mathbf{S_x}\ \mathbf{K^T}\left(\mathbf{K}\ \mathbf{S_x}\ \mathbf{K^T} + \mathbf{S_e}\right)^{-1}\mathbf{K}\ \mathbf{S_x} \tag{A.7}$$

$\mathbf{S_e}$ is the covariance matrix of the measurements $\mathbf{y}$. Following *Selesnick and Blake* [2000b], we define $\mathbf{S_e}$ as a diagonal matrix whose elements (corresponding to each channel) are the sums of the error variances due to counting statistics and other sources of error such as on-orbit lossy compression.

The quantities $\mathbf{x_o}$ and $\mathbf{S_x}$ are the *a priori* estimate and its covariance matrix, which are required constraints for this underdetermined problem. Much of the challenge lies in selecting appropriate *a priori* constraints. We set $\mathbf{x_o}$ equal to the omnidirectional average of the measured fluxes, although there is little difference in the results from setting it to zero, as *Selesnick and Blake* [2000b] do. Following *Tarantola and Valette* [1982], we define the elements of the *a priori* covariance matrix as follows:

$$S_x(\alpha, \alpha_o) = \sigma^2 \exp\left[-\frac{1}{2}\frac{(\alpha - \alpha_o)^2}{\Delta^2}\right] \tag{A.8}$$

The correlation length Δ is set to the full-width at half-maximum (FWHM) of the telescope field-of-view [*Selesnick and Blake*, 2000b]. The coefficient σ^2 is set equal to the variance in the measurements (at a given energy) about the omni-directional average

$\mathbf{x_o}$. The covariance matrices represent absolute errors, in differential flux units squared. The reported uncertainties on each of the retrieved PAD points are the square roots of the diagonal elements of the covariance matrix $\mathbf{S}$.

The pitch angle α is defined only from 0 to 180°. Because of the sparse angular sampling of MAGED, fluxes measured at center pitch angles greater than 90° are assigned to the supplementary angles $(180° - \alpha)$; the 90-180° variation is set to the 90-0° variation to define the full input PAD from 0 to 180°. In order to constrain the solution at the 0 and 180° end points, we extend the input vector $\mathbf{y}$ cyclically to −90° and +270°. Only flux values for pitch angles between 0 and 180° are reported. In the present work, the output $\mathbf{x}$ is defined on a 10° grid starting at 5°.

A benefit of optimal estimation is that the output covariance matrix $\mathbf{S}$ represents the propagation of the measurement errors and *a priori* assumptions through the inversion, enabling a self-consistent estimate of the retrieval error at each point on the output grid. The advantage of this linear inversion is its relative simplicity, requiring only one matrix inversion (per energy channel) and no iterations. The drawback is that, due to the lack of a positivity constraint, one or more negative fluxes are reported occasionally in a PAD, often when one measured point in the PAD is very low. In the current work, negative fluxes are rejected. A non-linear, iterative retrieval involving a positivity constraint, which is planned, would be more generally valid but also much slower than the present method.

Figure A.1 displays examples of the results from this PAD retrieval method for both peaked and butterfly PADs.

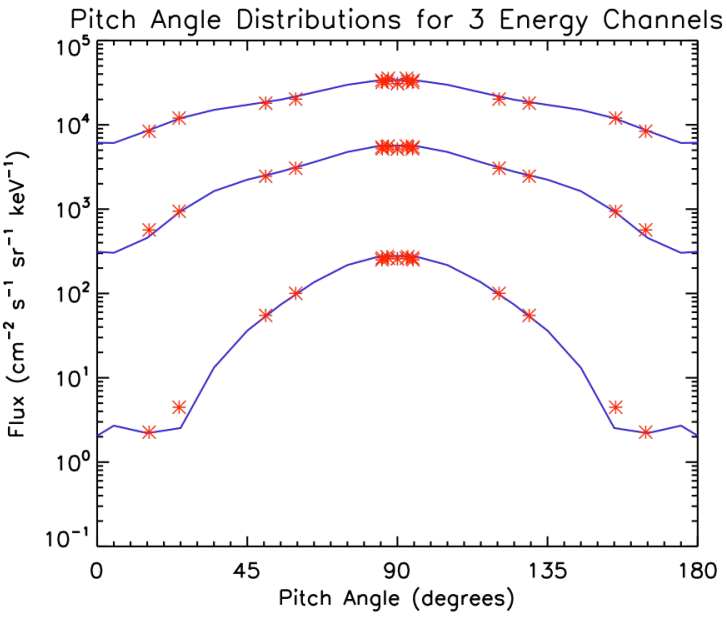

(a)

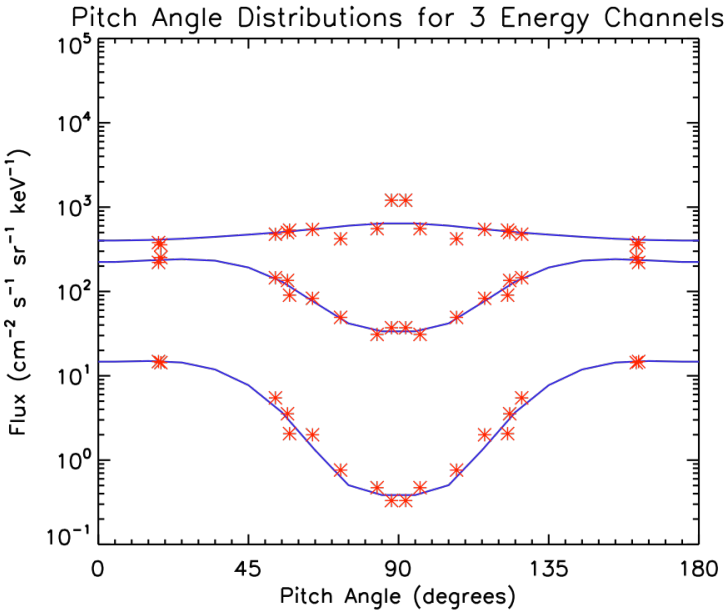

(b)

FIGURE A.1: Examples of PADs (peaked and butterfly) obtained using the retrieval code as described in the appendix for energy channels; 40 keV, 150 keV and 475 keV. The blue line indicates the retrieved PAD with red stars indicating the measurements from GOES-13.

Appendix B

Further examples of testing the prediction functions calculated in Chapter 5

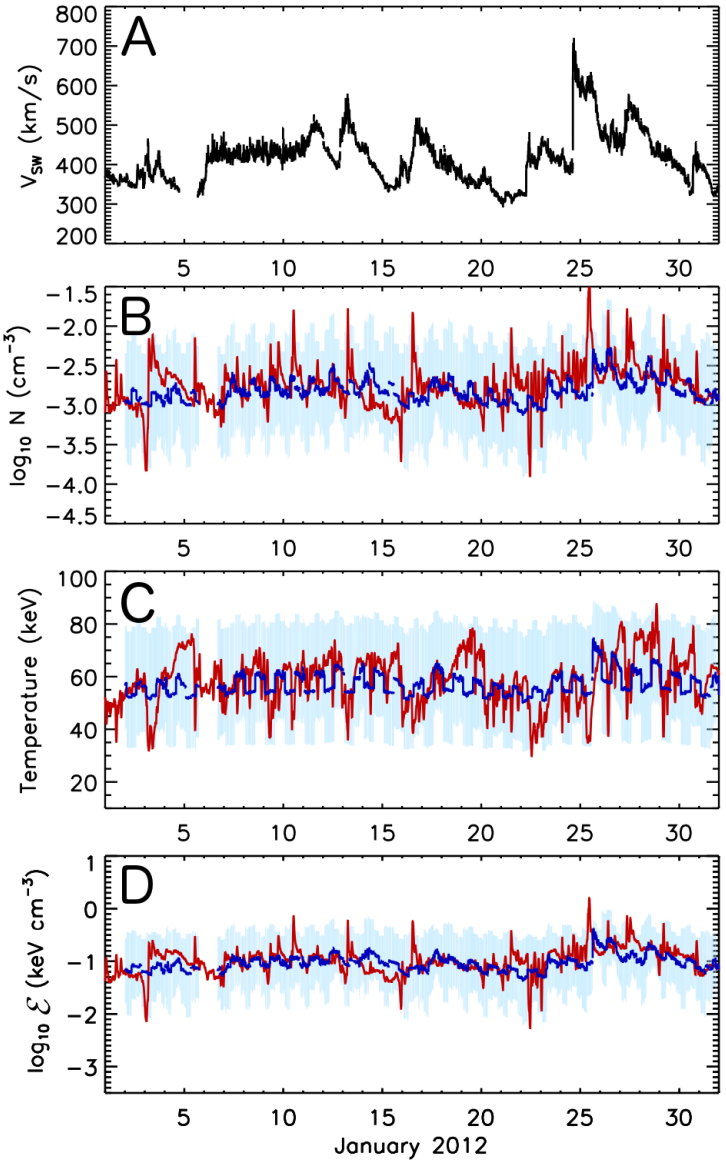

FIGURE B.1: The same parameters as shown in Figure 5.6 for January 2012.

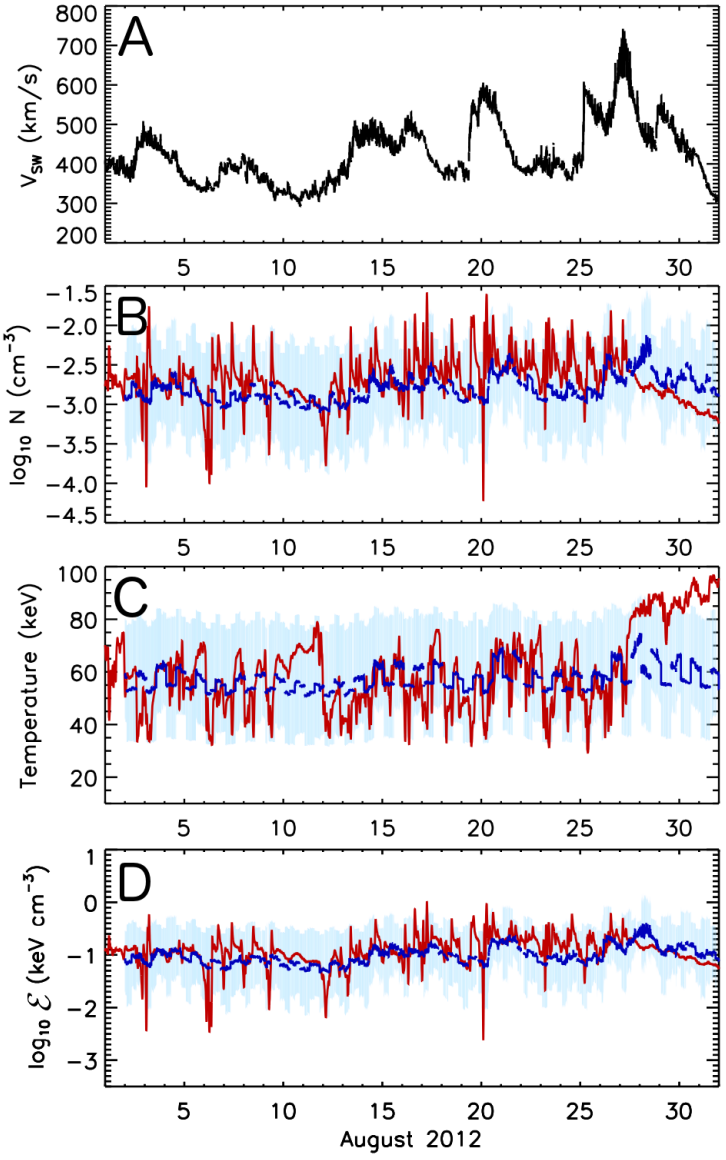

FIGURE B.2: The same parameters as shown in Figure 5.6 for August 2012.

Appendix C

The Cold Plasma Dispersion Relation ($k \parallel B_0$)

Maxwell's third equation (Faraday's Law) is given as:

$$\nabla \times E = -\frac{\partial B}{\partial t} \tag{C.1}$$

Perturbation quantities vary according to $e^{i(\omega t - kr)}$. Therefore, $\nabla \equiv ik$ and $\partial/\partial t \equiv -i\omega$. Consider waves propagating parallel to the background magnetic field ($k \parallel B_0$) with $\mathbf{B}_0 = B_0\hat{z}$ and $\mathbf{k} = k\hat{z}$ (this configuration is shown in Figure C.1).

Maxwell's third equation therefore becomes:

$$\mathbf{k} \times \mathbf{E} = \omega B_1 \tag{C.2}$$

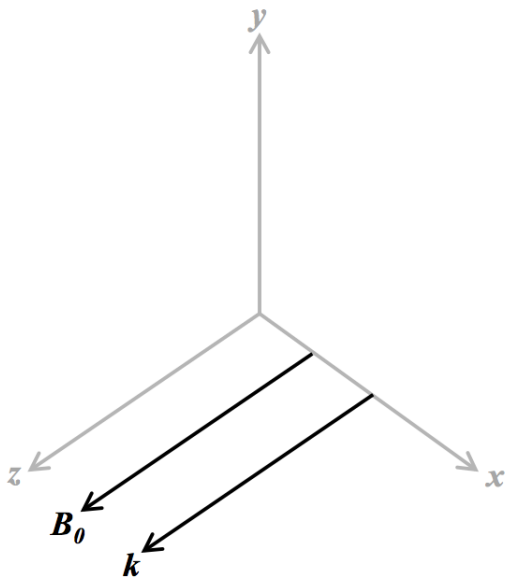

FIGURE C.1: The geometry used for waves propagating parallel to the background magnetic field, $k \parallel B_0$. Both the background magnetic field and wave vector are oriented in the z direction, $\mathbf{B}_0 = B_0\hat{z}$ and $\mathbf{k} = k\hat{z}$.

where B_1 is the time-dependent wave field superposed on the static background field, B_0. That is, $B = B_0 + B_1$. In vector form, Maxwell's third equation may be written as:

$$\begin{vmatrix} \hat{x} & \hat{y} & \hat{z} \\ E_x & E_y & E_z \\ 0 & 0 & k \end{vmatrix} = \omega \begin{vmatrix} B_x \\ B_y \\ B_z \end{vmatrix} \tag{C.3}$$

and therefore:

$$\begin{vmatrix} kE_y \\ -kE_x \\ 0 \end{vmatrix} = \omega \begin{vmatrix} B_x \\ B_y \\ B_z \end{vmatrix} \tag{C.4}$$

Squaring both sides yields:

$$\begin{vmatrix} kE_y \\ -kE_x \\ 0 \end{vmatrix} \cdot \begin{vmatrix} kE_y \\ -kE_x \\ 0 \end{vmatrix} = \omega^2 \begin{vmatrix} B_x \\ B_y \\ B_z \end{vmatrix} \cdot \begin{vmatrix} B_x \\ B_y \\ B_z \end{vmatrix} \tag{C.5}$$

and thus:

$$k^2 \left(E_x^2 + E_y^2\right) = \omega^2 \left(B_x^2 + B_y^2 + B_z^2\right) \tag{C.6}$$

The Appleton-Hartree equation for a collisionless plasma assuming parallel wave propagation is given as:

$$n^2 = \frac{k^2 c^2}{\omega^2} = 1 - \frac{\omega_{pe}^2}{\omega\left(\omega - \omega_{ce}\right)} \tag{C.7}$$

Substituting in the E and B terms from Equation C.6 yields:

$$\left(B_x^2 + B_y^2 + B_z^2\right) = \frac{1}{c^2}\left(1 - \frac{\omega_{pe}^2}{\omega\left(\omega - \omega_{ce}\right)}\right)\left(E_x^2 + E_y^2\right) \tag{C.8}$$

defining $S_B = \left(B_x^2 + B_y^2 + B_z^2\right)$ and $S_E = \left(E_x^2 + E_y^2\right)$ yields:

$$S_B = \frac{1}{c^2}\left(1 - \frac{\omega_{pe}^2}{\omega\left(\omega - \omega_{ce}\right)}\right) S_E = \frac{1}{c^2}\left(1 - \frac{f_{pe}^2}{f\left(f - f_{ce}\right)}\right) S_E \tag{C.9}$$

Bibliography

Agapitov, O., A. Artemyev, V. Krasnoselskikh, Y. V. Khotyaintsev, D. Mourenas, H. Breuillard, M. Balikhin, and G. Rolland (2013), Statistics of whistler mode waves in the outer radiation belt: Cluster STAFF-SA measurements, *Journal of Geophysical Research: Space Physics*, *118*(6), 3407–3420, doi:10.1002/jgra.50312.

Alfvén, H. (1942), Existence of electromagnetichydrodynamic waves, *Nature*, *150*, 405406.

Anderson, R., and D. Gurnett (1992), The development of static and dynamic models of the earths radiation belt environment through the study of plasma waves, wave-particle interactions and plasma number densities from in situ observations in the earths magnetosphere with the crres spacerad instruments, philips Lab., Hanscom AFB, MA.

Baker, D., S. Kanekal, T. Pulkkinen, and J. Blake (1999), Equinoctial and solstitial averages of magnetospheric relativistic electrons: A strong semiannual modulation, *Geophys. Res. Lett.*, *26*(No. 20), 3193.

Baker, D., X. Li, J. Blake, and S. Kanekal (1998), Strong electron acceleration in the Earth's magnetosphere, in *PARTICLE ACCELERATION IN SPACE PLASMAS*, *ADVANCES IN SPACE RESEARCH*, vol. 21, edited by Blake, JB and Slavin, JA, pp. 609–613, Comm Space Res; Sci Comm Solar Terr Phys; European Space Agcy, doi:{10.1016/S0273-1177(97)00970-8}, D0 3 Symposium of COSPAR Scientific-Commission-D on Particle Acceleration in Space Plasmas at the 31st COSPAR Scientific Assembly, UNIV BIRMINGHAM, BIRMINGHAM, ENGLAND, JUL 14-21, 1996.

Baker, D. N., R. W. Klebesadel, P. R. Higbie, and J. B. Blake (1986), Highly relativistic electrons in the earths outer magnetosphere: 1. lifetimes and temporal history 1979-1984, *J. Geophys. Res.*, *91*, 4265–4276.

Baker, D. N., S. G. Kanekal, R. B. Horne, N. P. Meredith, and S. A. Glauert (2007), Low-altitude measurements of 26 MeV electron trapping lifetimes at 1.5 l 2.5, *Geophysical Research Letters*, *34*(20), n/a–n/a, doi:10.1029/2007GL031007.

Balikhin, M. A., R. J. Boynton, S. N. Walker, J. E. Borovsky, S. A. Billings, and H. L. Wei (2011), Using the narmax approach to model the evolution of energetic electrons fluxes at geostationary orbit, *Geophys. Res. Lett.*, *38*(L18105), doi:10.1029/2011GL048980.

Bartels, J., N. H. Heck, and H. F. Johnston (1939), The three-hour-range index measuring geomagnetic activity, *J. Geophys. Res.*, *44*(411).

Baumjohann, W., and R. A. Treumann (1997), *Basic Space Plasma Physics*, Imperial College Press, ISBN: 1-86094-079-X (pbk).

Birn, J., and E. R. Priest (2007), *Reconnection of Magnetic Fields: Magnetohydrodynamics and Collisionless Theory and Observations*, Cambridge University Press.

Borovsky, J. E., and T. E. Cayton (2011), Entropy mapping of the outer electron radiation belt between the magnetotail and geosynchronous orbit, *J. Geophys. Res.*, *116*(A06216), doi:10.1029/2011JA016470.

Borovsky, J. E., and M. H. Denton (2006), Differences between CME-driven storms and CIR-driven storms, *J. Geophys. Res.*

Borovsky, J. E., and M. H. Denton (2009a), Electron loss rates from the outer radiation belt caused by the filling of the outer plasmasphere: The calm before the storm, *J. Geophys. Res.*, *114*(A11203), doi:10.1029/2009JA014063.

Borovsky, J. E., and M. H. Denton (2009b), Relativistic-electron dropouts and recovery: A superposed epoch study of the magnetosphere and the solar wind, *J. Geophys. Res.*, *114*(A02201), doi:10.1029/2008JA013128.

Borovsky, J. E., and M. H. Denton (2010a), Magnetic field at geosynchronous orbit during high-speed stream-driven storms: Connections to the solar wind, the plasma sheet, and the outer electron radiation belt, *J. Gephys. Res.*

Borovsky, J. E., and M. H. Denton (2010b), On the heating of the outer radiation belt to produce high fluxes of relativistic electrons: Measured heating rates at geosynchronous orbit for highspeed streamdriven storms, *J. Gephys. Res.*

Borovsky, J. E., and M. H. Denton (2011), A survey of the anisotropy of the outer electron radiation belt during high-speed-stream-driven storms, *J. Gephys. Res.*

Borovsky, J. E., and J. T. Steinberg (2006), The calm before the storm in CIR/magnetosphere interactions: Occurrence statistics, solar-wind statistics, and magnetospheric preconditioning, *J. Geophys. Res.*

Borovsky, J. E., M. F. Thomsen, D. J. McComas, T. E. Cayton, and D. J. Knipp (1998), Magnetospheric dynamics and mass flow during the November 1993 storm, *J. Geophys. Res.*

Bortnik, J., and R. M. Thorne (2007), The dual role of elf/vlf chorus waves in the acceleration and precipitation of radiation belt electrons, *Journal of Atmospheric and Solar-Terrestrial Physics*, *69*(3), 378–386, http://dx.doi.org/10.1016/j.jastp.2006.05.030.

Boscher, D., S. Bourdarie, P. O'Brien, and T. Guild (2004-2008), Onera-desp irbem library, oNERA-DESP, Toulouse France; Aerospace Corporation, Washington DC, USA.

Boyd, A. J., H. E. Spence, S. G. Claudepierre, J. F. Fennell, J. B. Blake, D. N. Baker, G. D. Reeves, and D. L. Turner (2014), Quantifying the radiation belt seed population in the 17 march 2013 electron acceleration event, *Geophysical Research Letters*, *41*(7), 2275–2281, doi:10.1002/2014GL059626.

Boynton, R. J., M. A. Balikhin, S. A. Billings, G. D. Reeves, N. Ganushkina, M. Gedalin, O. A. Amariutei, J. E. Borovsky, and S. N. Walker (2013), The analysis of electron fluxes at geosynchronous orbit employing a narmax approach, *J. Geophys. Res. Space Physics*, *118*, 15001513, doi:10.1002/jgra.50192.

Brautigam, D. H., and J. M. Albert (2000), Radial diffusion analysis of outer radiation belt electrons during the october 9, 1990, magnetic storm, *Journal of Geophysical Research: Space Physics*, *105*(A1), 291–309, doi:10.1029/1999JA900344.

Bryant, D. (1999), , IOP Publishing, CRC Press, ISBN 0 7503 0533 9.

Burin des Roziers, E., X. Li, D. N. Baker, T. A. Fritz, R. Friedel, T. G. Onsager, and I. Dandouras (2009), Energetic plasma sheet electrons and their relationship with the solar wind: A cluster and geotail study, *Journal of Geophysical Research: Space Physics*, *114*(A2), n/a–n/a, doi:10.1029/2008JA013696.

Cayton, T. E., R. D. Belian, S. P. Gary, T. A. Fritz, and D. N. Baker (1989), Energetic electron components at geosynchronous orbit, *Geophys. Res. Lett.*, *16*(147), doi:10.1029/GL016i002p00147.

Chen, Y., R. H. W. Friedel, and G. D. Reeves (2006), Phase space density distributions of energetic electrons in the outer radiation belt during two geospace environment modeling inner magnetosphere/storms selected storms, *Journal of Geophysical Research: Space Physics*, *111*(A11), n/a–n/a, doi:10.1029/2006JA011703.

Chen, Y., R. H. W. Friedel, G. D. Reeves, T. E. Cayton, and R. Christensen (2007a), Multisatellite determination of the relativistic electron phase space density at geosynchronous orbit: An integrated investigation during geomagnetic storm times, *J. Geophys. Res.*, *112*(A11214), doi:10.1029/2007JA012314.

Chen, Y., G. D. Reeves, and R. H. Friedel (2007b), The energization of relativistic electrons in the outer van allen radiation belt, *Nature Physics.*, *3*(614), doi:10.1038/nphys655.

Chen, Y., G. D. Reeves, R. H. Friedel, and G. S. Cunningham (2014), Global time-dependent chorus maps from low-earth-orbit electron precipitation and van allen probes data, *Geophys. Res. Lett.*, doi: 10.1002/2013GL059181.

Christon, S. P., D. G. Mitchell, D. J. Williams, L. A. Frank, C. Y. Huang, and T. E. Eastman (1988), Energy spectra of plasma sheet ions and electrons from ∼50 ev/e to ∼1 MeV during plasma temperature transitions, *J. Geophys. Res.*, *93(A4)*, 25622572, doi:10.1029/JA093iA04p02562.

Claudepierre, S. G., S. R. Elkington, and M. Wiltberger (2008), Solar wind driving of magnetospheric ulf waves: Pulsations driven by velocity shear at the magnetopause, *J. Geophys. Res.*, *113*(A05218), doi:10.1029/2007JA012890.

Clilverd, M. A., C. J. Rodger, D. Danskin, M. E. Usanova, T. Raita, T. Ulich, and E. L. Spanswick (2012), Energetic particle injection, acceleration, and loss during the geomagnetic disturbances which upset galaxy 15, *J. Geophys. Res.*, *117*(A12213), doi:10.1029/2012JA018175.

Clilverd, M. A., N. Cobbett, C. J. Rodger, J. Brundell, M. H. Denton, D. P. Hartley, J. V. Rodriguez, D. Danskin, T. Raita, and E. L. Spanswick (2013), Energetic electron precipitation characteristics observed from antarctica during a flux dropout event, *J. Geophys. Res.*, *118*, 69216935, doi:10.1002/2013JA019067.

Daglis, I. A., S. Livi, E. T. Sarris, and B. Wilken (1994), Energy density of ionospheric and solar wind origin ions in the near-Earth magnetotail during substorms, *J. Geophys. Res.*, *99(A4)*, 56915703, doi:10.1029/93JA02772.

Daglis, I. A., R. M. Thorne, W. Baumjohann, and S. Orsini (1999), The terrestrial ring current: Origin, formation, and decay, *Reviews of Geophysics*, *37*(4), 407–438, doi:10.1029/1999RG900009.

Davis, T. N., and M. Sugiura (1966), Auroral electrojet activity index ae and its universal time variations, *Journal of Geophysical Research*, *71*(3), 785–801, doi:10.1029/JZ071i003p00785.

Denton, M. H., and J. E. Borovsky (2009), The superdense plasma sheet in the magnetosphere during highspeedsteamdriven storms: Plasma transport time scales, *J. Atmos. Sol. Terr. Phys.*, *71*, 10451058.

Denton, M. H., and T. E. Cayton (2011), Density and temperature of energetic electrons in the Earth's magnetotail derived from high-latitude GPS observations during the declining phase of the solar cycle, *Annales Geophysicae*, *29*(10), 1755–1763.

Denton, M. H., T. Ulich, and E. Turunen (2009), Modification of midlatitude ionospheric parameters in the F2 layer by persistent highspeed solar wind streams, *Space Weather*, *7*(S04006), doi:10.1029/2008SW000443.

Denton, M. H., J. E. Borovsky, and T. E. Cayton (2010), A density-temperature description of the outer electron radiation belt during geomagnetic storms, *J. Geophys. Res.*, *115*(A01208), doi:10.1029/2009JA014183.

Dungey, J. W. (1961), Interplanetary magnetic field and the auroral zones, *Phys. Rev. Lett.*, *6*, 47–48, doi:10.1103/PhysRevLett.6.47.

Dyer, S. A. (Ed.) (2001), *Wiley Survey of Instrumentation and Measurement*, John Wiley and Sons, ISBN 0-471-39484-X.

Elkington, S. R., M. K. Hudson, and A. A. Chan (1999), Acceleration of relativistic electrons via driftresonant interaction with toroidalmode PC5 ULF oscillations, *Geophys. Res. Lett.*, *26*(3273), doi:10.1029/1999GL003659.

Fairfield, D. H. (1968), Average magnetic field configuration of the outer magnetosphere, *J. Geophys. Res. Space Physics*, *73*(23).

Fiorillo, F. (2004), *Measurement and Characterization of Magnetic Materials*, vol. A Volume in the Elsevier Series in Electromagnetism, Elsevier Academic Press, ISBN-13: 978-0-12-257251-7, ISBN-10: 0-12-257251-3, ISSN: 1567-2131.

Fitzpatrick, R. (2014), *Plasma Physics: An Introduction*, CRC Press, ISBN-13: 978-1-4665-9426-5.

Fox, N., and J. L. Burch (Eds.) (2014), *The Van Allen Probes Mission*, Springer Science and Business Media, doi:10.1007/978-1-4899-7433-4.

Freeman, J. W. (1964), The morphology of the electron distribution in the outer radiation zone and near the magnetospheric boundary as observed by Explorer 12, *J. Geophys. Res.*, *69*(1691).

Friedel, R. H. W., G. D. Reeves, and T. Obara (2002), Relativistic electron dynamics in the inner magnetosphere a review, *J. Atmos. Sol. Terr. Phys.*, *64*(265), doi:10.1016/S1364-6826(01)00088-8.

Fukata, M., S. Taguchi, T. Okuzawa, and T. Obara (2002), Neural network prediction of relativistic electrons at geosynchronous orbit during the storm recovery phase: effects of recurring substorms, *Ann. Geophys.*, *20*, 947–951, doi:10.5194/angeo-20-947-2002.

Gary, S. P. (1993), Theory of space plasma microinstabilities, *New York, NY: Cambridge University Press.*

Gkioulidou, M., C.-P. Wang, L. R. Lyons, and R. A. Wolf (2009), Formation of the harang reversal and its dependence on plasma sheet conditions: Rice convection model simulations, *J. Geophys. Res.*, *114*(A07204), doi:10.1029/2008JA013955.

GOES N Databook Revision C, CDRL PM-1-1-03 (2009), *GOES N Databook*, prepared for National Aeronautics and Space Administration Goddard Space Flight Center Greenbelt, Maryland 20771 Pursuant to Contract NAS5-98069.

Green, J. C., and M. G. Kivelson (2004), Relativistic electrons in the outer radiation belt: Differentiating between acceleration mechanisms, *J. Geophys. Res.*, *109*(A03213), doi:10.1029/2003JA010153.

Green, J. C., T. G. Onsager, T. P. O'Brien, and D. N. Baker (2004), Testing loss mechanisms capable of rapidly depleting relativistic electron flux in the Earths outer radiation belt, *J. Geophys. Res.*, *109*(A12211), doi:10.1029/2004JA010579.

Gubbins, D., and E. Herrero-Bervera (Eds.) (2007), *Encyclopedia od Geomagnetism*, Springer, ISBN-13: 978-1-4020-3992-8.

Gurgiolo, C., C. Lin, B. Mauk, G. K. Parks, and C. McIlwain (1979), Plasma injection and diamagnetism, *J. Geophys. Res.*, *84(A5)*, 20492056, doi:10.1029/JA084iA05p02049.

Haigh, J. D., I. Rüedi, M. Lockwood, M. Güdel, M. S. Giampapa, and W. Schmutz (2006), *The Sun, Solar Analogs and the Climate*, Springer Science and Business Media.

Hanser, F. A. (2011), EPS/HEPAD calibration and data handbook, *Tech. Rep. GOESN-ENG-048D*, Assurance Technology Corporation, Carlisle, Mass.

Hartley, D. P., M. H. Denton, J. C. Green, T. G. Onsager, J. V. Rodriguez, and H. J. Singer (2013), Case studies of the impact of high-speed solar wind streams on the electron radiation belt at geosynchronous orbit: Flux, magnetic field, and phase space density, *J. Geophys. Res. Space Physics*, *118*, doi:10.1002/2013JA018923.

Hartley, D. P., M. H. Denton, and J. V. Rodriguez (2014), Electron number density, temperature, and energy density at geo and links to the solar wind: A simple predictive capability, *J. Geophys. Res. Space Physics*, *119*, 4556–4571, doi:10.1002/2014JA019779.

Hendry, A. T., C. J. Rodger, M. A. Clilverd, N. R. Thomson, S. K. Morley, and T. Raita (2012), Rapid radiation belt losses occurring during high-speed solar wind streamdriven storms: Importance of energetic electron precipitation in dynamics of the Earth's Radiation Belts and Inner Magnetosphere, *Geophys. Monogr. Ser.*, *199*(213223), edited by D. Summers et al.,.

Hilmer, R. V., G. P. Ginet, and T. E. Cayton (2000), Enhancement of equatorial energetic electron fluxes near l = 4.2 as a result of high speed solar wind streams, *Journal of Geophysical Research: Space Physics*, *105*(A10), 23,311–23,322, doi:10.1029/1999JA000380.

Horne, R. B., and R. M. Thorne (2003), Relativistic electron acceleration and precipitation during resonant interactions with whistler-mode chorus, *Geophys. Res. Lett.*, *30(10)*, 1527, doi:10.1029/2003GL016973.

Horne, R. B., G. V. Wheeler, and H. S. C. K. Alleyne (2000), Proton and electron heating by radially propagating fast magnetosonic waves, *Journal of Geophysical Research: Space Physics*, *105*(A12), 27,597–27,610, doi:10.1029/2000JA000018.

Horne, R. B., R. M. Thorne, S. A. Glauert, N. P. Meredith, D. Pokhotelov, and O. Santolk (2007), Electron acceleration in the van allen radiation belts by fast magnetosonic waves, *Geophysical Research Letters*, *34*(17), doi:10.1029/2007GL030267.

Horne, R. B., M. M. Lam, and J. C. Green (2009), Energetic electron precipitation from the outer radiation belt during geomagnetic storms, *Geophysical Research Letters*, *36*(19), n/a–n/a, doi:10.1029/2009GL040236.

Horne, R. B., S. A. Glauert, N. P. Meredith, D. Boscher, V. Maget, D. Heynderickx, and D. Pitchford (2013), Space weather impacts on satellites and forecasting the earths electron radiation belts with spacecast, *Space Weather*, *11*, doi:10.1002/swe.20023.

Huang, C.-L., H. E. Spence, H. J. Singer, and N. A. Tsyganenko (2008), A quantitative assessment of empirical magnetic field models at geosynchronous orbit during magnetic storms, *J. Geophys. Res.*, *113*(A04208), doi:10.1029/2007JA012623.

Hudson, M. K., S. R. Elkington, J. G. Lyon, V. A. Marchenko, I. Roth, M. Temerin, J. B. Blake, M. S. Gussenhoven, and J. R. Wygant (1997), Simulations of radiation belt formation during storm sudden commencements, *J. Geophys. Res.*, *102(A7)*, 14,08714,102, doi:10.1029/97JA03995.

Hudson, M. K., B. T. Kress, H.-R. Müller, J. A. Zastrow, and J. B. Blake (2008), Relationship of the van allen radiation belts to solar wind drivers, *Journal of Atmospheric and Solar-Terrestrial Physics*, *70/5*, 708–729, doi:10.1016/j.jastp.2007.11.003.

Hwang, J. A., D.-Y. Lee, L. R. Lyons, A. J. Smith, S. Zou, K. W. Min, K.-H. Kim, Y.-J. Moon, and Y. D. Park (2007), Statistical significance of association between whistler-mode chorus enhancements and enhanced convection periods during high-speed streams, *J. Geophys. Res.*, *112*(A09213), doi:10.1029/2007JA012388.

Jacobs, J. A., Y. Kato, S. Matsushita, and V. A. Troitskaya (1964), Classification of geomagnetic micropulsations, *Journal of Geophysical Research*, *69*(1), 180–181, doi:10.1029/JZ069i001p00180.

Johansson, R. (1993), System modeling and identification, *Prentice-Hall, Old Tappan, N. J.*

Jordanova, V. K., D. T. Welling, S. G. Zaharia, L. Chen, and R. M. Thorne (2012), Modeling ring current ion and electron dynamics and plasma instabilities during a high-speed stream driven storm, *J. Geophys. Res.*, *117*(A00L08), doi:10.1029/2011JA017433.

Kasahara, Y., H. Kenmochi, and I. Kimura (1994), Propagation characteristics of the elf emissions observed by the satellite akebono in the magnetic equatorial region, *Radio Science*, *29*(4), 751–767, doi:10.1029/94RS00445.

Kennel, C. F., and H. E. Petschek (1966), Limit on stably trapped particle fluxes, *J. Geophys. Res.*, *71(1)*, 128, doi:10.1029/JZ071i001p00001.

King, J. H., and N. E. Papitashvili (2005), Solar wind spatial scales in and comparisons of hourly Wind and ACE plasma and magnetic field data, *J. Geophys. Res.*, *110*(A02104), doi:10.1029/2004JA010649.

Kivelson, M. G., and C. T. Russell (1995), *Introduction to Space Physics*, Cambridge University Press, ISBN: 0-521-45104-3.

Kletzing, C., W. Kurth, M. Acuna, R. MacDowall, R. Torbert, T. Averkamp, D. Bodet, S. Bounds, M. Chutter, J. Connerney, D. Crawford, J. Dolan, R. Dvorsky, G. Hospodarsky, J. Howard, V. Jordanova, R. Johnson, D. Kirchner, B. Mokrzycki, G. Needell, J. Odom, D. Mark, R. P. Jr., J. Phillips, C. Piker, S. Remington, D. Rowland, O. Santolik, R. Schnurr, D. Sheppard, C. Smith, R. Thorne, and J. Tyler (2013), The electric and magnetic field instrument suite and integrated science (EMFISIS) on RBSP, *Space Science Reviews*, doi:10.1007/s11214-013-9993-6.

Knipp, D. J. (2011), *Understanding Space Weather and the Physics Behind It*, The McGraw-Hill Companies, Space Technology Series, ISBN: 978-0-07-340890-3, 0-07-340890-5.

Koons, H. C., and D. J. Gorney (1991), A neural network model of the relativistic electron flux at geosynchronous orbit, *J. Geophys. Res.*, *96*, 5549.

Li, W., R. M. Thorne, V. Angelopoulos, J. Bortnik, C. M. Cully, B. Ni, O. LeContel, A. Roux, U. Auster, and W. Magnes (2009a), Global distribution of whistlermode chorus waves observed on the themis spacecraft, *Geophys. Res. Lett.*, *36*(L09104), doi:10.1029/2009GL037595.

Li, W., R. M. Thorne, V. Angelopoulos, J. W. Bonnell, J. P. McFadden, C. W. Carlson, O. LeContel, A. Roux, K. H. Glassmeier, and H. U. Auster (2009b), Evaluation of whistlermode chorus intensification on the nightside during an injection event observed on the themis spacecraft, *J. Geophys. Res.*, *114*(A00C14), doi:10.1029/2008JA013554.

Li, W., R. M. Thorne, J. Bortnik, Y. Nishimura, and V. Angelopoulos (2011), Modulation of whistler mode chorus waves: 1. role of compressional pc45 pulsations, *J. Geophys. Res.*, *116*(A06205), doi:10.1029/2010JA016312.

Li, W., B. Ni, R. M. Thorne, J. Bortnik, J. C. Green, C. A. Kletzing, W. S. Kurth, and G. B. Hospodarsky (2013), Constructing the global distribution of chorus wave intensity using measurements of electrons by the poes satellites and waves by the van allen probes, *Geophys. Res. Lett.*, *40*, 45264532, doi:10.1002/grl.50920.

Li, W., D. Mourenas, A. V. Artemyev, O. V. Agapitov, J. Bortnik, J. M. Albert, R. M. Thorne, B. Ni, C. A. Kletzing, W. S. Kurth, and G. B. Hospodarsky (2014), Evidence of stronger pitch angle scattering loss caused by oblique whistler-mode waves as compared with quasi-parallel waves, *Geophysical Research Letters*, *41*(17), 6063–6070, doi:10.1002/2014GL061260.

Li, X., D. N. Baker, M. Temerin, D. Larson, R. P. Lin, G. D. Reeves, M. Looper, S. G. Kanekal, and R. A. Mewaldt (1997), Are energetic electrons in the solar wind the source of the outer radiation belt?, *Geophys. Res. Lett.*, *24(8)*, 923.

Li, X., D. N. Baker, M. Temerin, G. Reeves, and R. Friedel (2005), Energetic electrons, 50 kev to 6 MeV, at geosynchronous orbit: Their responses to solar wind variations, *Space Weather*, *3*(S04001), doi:10.1029/2004SW000105.

Liemohn, M. W., and A. A. Chan (2007), Unravelling the causes of radiation belt enhancements, *Eos Trans. AGU*, *88(42)*, doi:10.1029/2007EO420001.

Ljung, L. (1999), System identification: Theory for the user, *2nd ed., Prentice Hall PTF, Upper Saddle River, N. J.*

Lui, A. T. Y., R. E. Lopez, B. J. Anderson, K. Takahashi, L. J. Zanetti, R. W. McEntire, T. A. Potemra, D. M. Klumpar, E. M. Greene, and R. Strangeway (1992), Current disruptions in the near-earth neutral sheet region, *Journal of Geophysical Research: Space Physics*, *97*(A2), 1461–1480, doi:10.1029/91JA02401.

Lyons, L. R., and R. M. Thorne (1973), Equilibrium structure of radiation belt electrons, *J. Geophys. Res.*, *78(13)*, 21422149, doi:10.1029/JA078i013p02142.

MacDonald, E. A., M. Denton, M. Thomsen, and S. Gary (2008), Superposed epoch analysis of a whistler instability criterion at geosynchronous orbit during geomagnetic storms, *Journal of Atmospheric and Solar-Terrestrial Physics*, *70*, 1789–1796, doi:/10.1016/j.jastp.2008.03.021.

MacDonald, E. A., L. W. Blum, S. P. Gary, M. F. Thomsen, and M. H. Denton (2010), High-speed stream driven interfaces of global wave distributions at geosynchronous orbit: relevance to radiation-belt dynamics, *Proc. R. Soc.*, *A 2010*, 466, doi: 10.1098/rspa.2010.0076 first published online 16 June 2010.

Mann, I. R., T. P. OBrien, and D. K. Milling (2004), Correlations between ulf wave power, solar wind speed, and relativistic electron flux in the magnetosphere: Solar cycle dependence, *J. Atmos. Sol. Terr. Phys.*, *66*(187), doi:10.1016/j.jastp.2003.10.002.

Mazur, J., L. Friesen, A. Lin, D. Mabry, N. Katz, Y. Dotan, J. George, J. Blake, M. Looper, M. Redding, T. OBrien, J. Cha, A. Birkitt, P. Carranza, M. Lalic, F. Fuentes, R. Galvan, and M. McNab (2013), The relativistic proton spectrometer (rps) for the radiation belt storm probes mission, *Space Science Reviews*, *179*(1-4), 221–261, doi:10.1007/s11214-012-9926-9.

McPherron, R., D. Baker, and N. Crooker (2009a), Role of the russellmcpherron effect in the acceleration of relativistic electrons, *Journal of Atmospheric and Solar-Terrestrial Physics*, *Volume 71*(Issues 1011), Pages 1032–1044, http://dx.doi.org/10.1016/j.jastp.2008.11.002.

McPherron, R. L., and J. Weygand (2006), The solar wind and geomagnetic activity as a function of time relative to corotating interaction regions, in recurrent geomagnetic storms: Corotating solar wind streams, p. 125, edited by B. T. Tsurutani et al.

McPherron, R. L., D. N. Baker, and N. U. Crooker (2009b), Role of the russellmcpherron effect in the acceleration of relativistic electrons, *Journal of Atmospheric and Solar-Terrestrial Physics*, *71*(10-11), 10321044.

Meredith, N., R. Thorne, A. Sicard-Piet, D. Boscher, K. Yearby, W. Li, and R. Thorne (2012), Global model of lower band and upper band chorus from multiple satellite observations, *J. Geophys. Res.*, *117*(A10225), 10.1029/2012JA017978.

Meredith, N. P., R. B. Horne, R. M. Thorne, and R. R. Anderson (2003a), Favored regions for chorus-driven electron acceleration to relativistic energies in the earths outer radiation belt, *Geophys. Res. Lett.*, *30(16)*, 1871, doi:10.1029/2003GL017698.

Meredith, N. P., M. Cain, R. B. Horne, R. M. Thorne, D. Summers, and R. R. Anderson (2003b), Evidence for chorus-driven electron acceleration to relativistic energies from a survey of geomagnetically disturbed periods, *J. Geophys. Res.*

Meredith, N. P., R. M. Thorne, R. B. Horne, D. Summers, B. J. Fraser, and R. R. Anderson (2003c), Statistical analysis of relativistic electron energies for cyclotron

resonance with emic waves observed on crres, *Journal of Geophysical Research: Space Physics*, *108*(A6), doi:10.1029/2002JA009700.

Meredith, N. P., D. S. R. B. Horne, R. M. Thorne, and R. R. Anderson (2004), Substorm dependence of plasmaspheric hiss, *J. Geophys. Res.*, *109*(A06209), doi:10.1029/2004JA010387.

Meredith, N. P., R. B. Horne, M. A. Clilverd, D. Horsfall, R. M. Thorne, and R. R. Anderson (2006a), Origins of plasmaspheric hiss, *J. Geophys. Res.*, *111*(A09217), doi:10.1029/2006JA011707.

Meredith, N. P., R. B. Horne, S. A. Glauert, R. M. Thorne, D. Summers, J. M. Albert, and R. R. Anderson (2006b), Energetic outer zone electron loss timescales during low geomagnetic activity, *J. Geophys. Res.*, *111*(A05212), doi:10.1029/2005JA011516.

Meredith, N. P., R. B. Horne, M. M. Lam, M. H. Denton, J. E. Borovsky, and J. C. Green (2011), Energetic electron precipitation during high-speed solar wind stream driven storms, *J. Geophys. Res.*, *116*(A05223), doi:10.1029/2010JA016293.

Millan, R., and the BARREL team (2011), Understanding relativistic electron losses with BARREL, *Journal of Atmospheric and Solar-Terrestrial Physics*, doi:10.1016/j.jastp.2011.01.006.

Millan, R., M. McCarthy, J. Sample, D. Smith, L. Thompson, D. McGaw, L. Woodger, J. Hewitt, M. Comess, K. Yando, A. Liang, B. Anderson, N. Knezek, W. Rexroad, J. Scheiman, G. Bowers, A. Halford, A. Collier, M. Clilverd, R. Lin, and M. Hudson (2013), The Balloon Array for RBSP Relativistic Electron Losses (BARREL), *Space Sci Rev.*

Millan, R. M., and R. M. Thorne (2007), Review of radiation belt relativistic electron losses, *J. Atmos. Sol. Terr. Phys.*, *69*, 362 377, doi:10.1016/j.jastp.2006.06.019.

Mitchell, D., L. Lanzerotti, C. Kim, M. Stokes, G. Ho, S. Cooper, A. Ukhorskiy, J. Manweiler, S. Jaskulek, D. Haggerty, P. Brandt, M. Sitnov, K. Keika, J. Hayes, L. Brown, R. Gurnee, J. Hutcheson, K. Nelson, N. Paschalidis, E. Rossano, and S. Kerem (2013), Radiation belt storm probes ion composition experiment (rbspice), *Space Science Reviews*, *179*(1-4), 263–308, doi:10.1007/s11214-013-9965-x.

Miyoshi, Y., and R. Kataoka (2008), Flux enhancement of the outer radiation belt electrons after the arrival of stream interaction regions, *J. Geophys. Res.*, *113*(A03S09), doi: 10.1029/2007JA012506.

Miyoshi, Y., A. Morioka, R. Kataoka, Y. Kasahara, and T. Mukai (2007), Evolution of the outer radiation belt during the november 1993 storms driven by corotating interaction regions, *J. Geophys. Res.*, *112*(A05210), doi:10.1029/2006JA012148.

Miyoshi, Y., K. Sakaguchi, K. Shiokawa, D. Evans, J. Albert, M. Connors, and V. Jordanova (2008), Precipitation of radiation belt electrons by EMIC waves observed from ground and space, *Geophys. Res. Lett.*, *35*(L23101), doi:10.1029/2008GL035727.

Morley, S. K., R. H. W. Friedel, E. L. Spanswick, G. D. Reeves, J. T. Steinberg, J. Koller, T. Cayton, and E. Noveroske (2010), Dropouts of the outer electron radiation belt in response to solar wind stream interfaces: global positioning system observations, *Proc. R. Soc., A 2010 466*, doi: 10.1098/rspa.2010.0078 first published online 6 May 2010.

Mozer, F. S. (1973), Electric fields and plasma convection in the plasmasphere, *Reviews of Geophysics and Space Physics*, *11*(3), 755–765.

Nagai, T. (1988), space weather forecast prediction of relativistic electron intensity at synchronous orbit, *Geophys. Res. Lett.*, *15*(425).

Nelles, O. (2001), Nonlinear system identification, *Springer-Verlag, New York*.

O'Brien, T. P., R. L. McPherron, D. Sornette, G. D. Reeves, R. Friedel, and H. J. Singer (2001), Which magnetic storms produce relativistic electrons at geosynchronous orbit?, *J. Geophys. Res.*, *106*(15), 53315,544.

Onsager, T. G., G. Rostoker, H.-J. Kim, G. D. Reeves, T. Obara, H. J. Singer, and C. Smithtro (2002), Radiation belt electron flux dropouts: Local time, radial, and particle-energy dependence, *J. Geophys. Res.*, *107(A11)*(1382), doi:10.1029/2001JA000187.

Onsager, T. G., A. A. Chan, Y. Fei, S. R. Elkington, J. C. Green, and H. J. Singer (2004), The radial gradient of relativistic electrons at geosynchronous orbit, *J. Geophys. Res.*, *109*(A05221), doi:10.1029/2003JA010368.

Onsager, T. G., J. C. Green, G. D. Reeves, and H. J. Singer (2007), Solar wind and magnetospheric conditions leading to the abrupt loss of outer radiation belt electrons, *J. Geophys. Res.*, *112*(A01202), doi:10.1029/2006JA011708.

Parker, E. N. (1958), Dynamics of the interplanetary gas and magnetic fields, *Astrophysical Journal*, *128*, 664, doi:10.1086/146579.

Paulikas, G. A., and J. B. Blake (1979), Effects of the solar wind on magnetospheric dynamics: Energetic electrons at the synchronous orbit, in Quantitative Modeling of Magnetospheric Processes, *Geophys. Monogr. Ser.*, *vol. 21*, pp. 180202, AGU, Washington, D. C.

Pizzo, V. (1978), A three-dimensional model of corotating streams in the solar wind, 1. theoretical foundations, *J. Geophys. Res.*, *83(A12)*, 55635572, doi:10.1029/JA083iA12p05563.

Reeves, G. D., K. L. McAdams, R. H. W. Friedel, and T. P. OBrien (2003a), Acceleration and loss of relativistic electrons during geomagnetic storms, *Geophys. Res. Lett.*, *30(10)*(1529), doi:10.1029/2002GL016513.

Reeves, G. D., K. L. McAdams, R. H. W. Friedel, and T. P. OBrien (2003b), Acceleration and loss of relativistic electrons during geomagnetic storms, *Geophys. Res. Lett.*, *30(10)*(1529), doi:10.1029/2002GL016513.

Reeves, G. D., S. K. Morley, R. H. W. Friedel, M. G. Henderson, T. E. Cayton, G. Cunningham, J. B. Blake, R. A. Christensen, and D. Thomsen (2011), On the relationship between relativistic electron flux and solar wind velocity: Paulikas and Blake revisited, *J. Geophys. Res.*, *116*(A02213), doi:10.1029/2010JA015735.

Reeves, G. D., H. E. Spence, M. G. Henderson, S. K. Morley, R. H. W. Friedel, H. O. Funsten, D. N. Baker, S. G. Kanekal, J. B. Blake, J. F. Fennell, S. G. Claudepierre, R. M. Thorne, D. L. Turner, C. A. Kletzing, W. S. Kurth, B. A. Larsen, and J. T. Niehof (2013a), Electron acceleration in the heart of the van allen radiation belts, *Science*, *341*(6149), 991–994, doi:10.1126/science.1237743.

Reeves, G. D., S. K. Morley, and G. Cunningham (2013b), Long-term variations in solar wind velocity and radiation belt electrons, *J. Geophys. Res.*, *118*, 1040–1048, doi:10.1002/jgra.50126.

Rodgers, C. D. (1976), Retrieval of atmospheric temperature and composition from remote measurements of thermal radiation, *Rev. Geophys.*, *14*, 609–624.

Rodriguez, J. V. (2014), GOES 13-15 MAGE/PD Pitch Angles Algorithm Theoretical Basis Document Version 1.0, *Tech. rep.*, NOAA/NESDIS/NGDC.

Santolík, O., F. Němec, K. Gereová, E. Macúšová, Y. de Conchy, and N. Cornilleau-Wehrlin (2004), Systematic analysis of equatorial noise below the lower hybrid frequency, *Ann. Geophys.*, *22*, 2587–2595, doi:10.5194/angeo-22-2587-2004.

Schiller, Q., X. Li, L. Blum, W. Tu, D. L. Turner, and J. B. Blake (2014), A nonstorm time enhancement of relativistic electrons in the outer radiation belt, *Geophysical Research Letters*, *41*(1), 7–12, doi:10.1002/2013GL058485.

Schrijver, C. J., and G. L. Siscoe (2010), *Heliophysics: Space Storms and Radiation: Causes and Effects*, Cambridge University Press, ISBN 978-0-521-76051-5.

Schrijver, C. J., and C. Zwaan (2000), *Solar and Stellar Magnetic Activity*, Cambridge University Press, ISBN: 0-521-58286-5.

Schulz, M., and L. J. Lanzerotti (1974), *Particle Diffusion in the Radiation Belts*, Springer-Verlag, New York.

Scudder, J. D. (1992), On the causes of temperature change in inhomogeneous low-density astrophysical plasmas, *The Astrophysical Journal*, *398*(299).

Selesnick, R. S., and J. B. Blake (2000a), On the source location of radiation belt relativistic electrons, *J. Geophys. Res.*, *105*, 2607–2624.

Selesnick, R. S., and J. B. Blake (2000b), On the source location of radiation belt relativistic electrons, *J. Geophys. Res.*, *105(A2)*, 26072624, doi:10.1029/1999JA900445.

Shprits, Y., M. Daae, and B. Ni (2012), Statistical analysis of phase space density buildups and dropouts, *J. Geophys. Res.*, *117*(A01219), doi:10.1029/2011JA016939.

Shprits, Y. Y., S. R. Elkington, N. P. Meredith, and D. A. Subbotin (2008a), Review of modeling of losses and sources of relativistic electrons in the outer radiation belt I: Radial transport, *J. Atmos. Sol. Terr. Phys.*, *70*(1679), doi:10.1016/j.jastp.2008.06.008.

Shprits, Y. Y., D. A. Subbotin, N. P. Meredith, and S. R. Elkington (2008b), Review of modeling of losses and sources of relativistic electrons in the outer radiation belt II: Local acceleration and losses, *J. Atmos. Sol. Terr. Phys.*, *70*(1694), doi:10.1016/j.jastp.2008.06.014.

Sojka, J. J., R. L. McPherron, A. P. van Eyken, M. J. Nicholls, C. J. Heinselman, and J. D. Kelley (2009), Observations of ionospheric heating during the passage of solar coronal hole fast streams, *Geophys. Res. Lett.*, *36(19)*(L19105), doi:10.1029/2009GL039064.

Somov, B. V. (2013), *Plasma Astrophysics, Part I, Fundamentals and Practice*, second edition ed., Springer Science, ISBN: 978-1-4614-4282-0, DOI: 10.1007/978-1-4614-4283-7.

Spence, H., G. Reeves, D. Baker, J. Blake, M. Bolton, S. Bourdarie, A. Chan, S. Claudepierre, J. Clemmons, J. Cravens, S. Elkington, J. Fennell, R. Friedel, H. Funsten, J. Goldstein, J. Green, A. Guthrie, M. Henderson, R. Horne, M. Hudson, J.-M. Jahn, V. Jordanova, S. Kanekal, B. Klatt, B. Larsen, X. Li, E. MacDonald, I. Mann,

J. Niehof, T. OBrien, T. Onsager, D. Salvaggio, R. Skoug, S. Smith, L. Suther, M. Thomsen, and R. Thorne (2013), Science Goals and Overview of the Radiation Belt Storm Probes (RBSP) Energetic Particle, Composition, and Thermal Plasma (ECT) Suite on NASAs Van Allen Probes Mission, *Space Science Reviews*, *179*(1-4), 311–336, doi:10.1007/s11214-013-0007-5.

Sugiura, M. (1964), Hourly values of equatorial Dst for the IGY, *Ann. Int. Geophys.*, 35, 945.

Summers, D., and C. Ma (2000), A model for generating relativistic electrons in the earths inner magnetosphere based on gyroresonant wave-particle interactions, *J. Geophys. Res.*, *105(A2)*(2625).

Summers, D., R. M. Thorne, and F. Xiao (1998), Relativistic theory of wave-particle resonant diffusion with application to electron acceleration in the magnetosphere, *J. Geophys. Res.*

Tarantola, A., and B. Valette (1982), Generalized nonlinear inverse problems solved using the least squares criterion, *Rev. Geophys.*, *20*, 219–232.

Thomsen, M. F. (2004), Why Kp is such a good measure of magnetospheric convection, *Space Weather*, *2*(S11004), doi:10.1029/2004SW000089.

Thorne, R. M. (2010), Radiation belt dynamics: The importance of wave-particle interactions, *Geophys. Res. Lett.*, doi:10.1029/2010GL044990.

Tsurutani, B. T., W. D. Gonzalez, A. L. C. Gonzalez, F. L. Guarnieri, N. Gopalswamy, M. Grande, Y. Kamide, Y. Kasahara, G. Lu, I. Mann, R. McPherron, F. Soraas, and V. Vasyliunas (2006), Corotating solar wind streams and recurrent geomagnetic

activity: A review, *Journal of Geophysical Research: Space Physics*, *111*(A7), doi: 10.1029/2005JA011273.

Tsyganenko, N. A., and D. P. Stern (1996), Modeling the global magnetic field of the large scale birkeland current systems, *J. Geophys. Res.*, *101*(187).

Tu, W., G. S. Cunningham, Y. Chen, M. G. Henderson, E. Camporeale, and G. D. Reeves (2013), Modeling radiation belt electron dynamics during GEM challenge intervals with the DREAM3D diffusion model, *J. Geophys. Res. Space Physics*, *118*, 61976211, doi:10.1002/jgra.50560.

Turner, D. L., X. Li, G. D. Reeves, and H. J. Singer (2010), On phase space density radial gradients of earths outer-belt electrons prior to sudden solar wind pressure enhancements: Results from distinctive events and a superposed epoch analysis, *J. Geophys. Res.*, *115*(A01205), doi:10.1029/2009JA014423.

Turner, D. L., Y. Shprits, M. Hartinger, and V. Angelopoulos (2012), Explaining sudden losses of outer radiation belt electrons during geomagnetic storms, *Nature Physics*.

Turner, D. L., V. Angelopoulos, W. Li, M. D. Hartinger, M. Usanova, I. R. Mann, J. Bortnik, and Y. Shprits (2013), On the storm-time evolution of relativistic electron phase space density in earth's outer radiation belt, *Journal of Geophysical Research: Space Physics*, *118*(5), 2196–2212, doi:10.1002/jgra.50151.

Ukhorskiy, A. Y., B. J. Anderson, K. Takahashi, and N. A. Tsyganenko (2006), Impact of ulf oscillations in solar wind dynamic pressure on the outer radiation belt electrons, *Geophys. Res. Lett.*, *33*(L06111), doi:10.1029/2005GL024380.

Ukhorskiy, A. Y., M. I. Sitnov, R. M. Millan, and B. T. Kress (2011), The role of drift orbit bifurcations in energization and loss of electrons in the outer radiation belt, *J. Geophys. Res.*, *116*(A09208), doi:10.1029/2011JA016623.

Van Allen, J. A. (1959), The geomagnetically trapped corpuscular radiation, *J. Geophys. Res.*, *64*(11), 1683–1689.

Van Allen, J. A., and L. A. Frank (1959), Radiation around the earth to a radial distance of 107,400 km., *Nature*, *183*(4659), 430–434, 10.1038/183430a0.

Van Allen, J. A., C. E. McIlwain, and G. H. Ludwig (1959), Radiation observations with satellite 1958 ϵ, *J. Geophys. Res.*, *64*, 271–286.

Walt, M. (1994), *Introduction to Geomagnetically Trapped Radiation*, Cambridge University Press 2005, Cambridge Atmospheric and Space Science Series.

Weigel, R. S., A. J. Klimas, and D. Vassiliadis (2003), Precursor analysis and prediction of large-amplitude relativistic electron fluxes, *Space Weather*, *1(3)*, 1014, doi:10.1029/2003SW000023.

Weimer, D. R., D. M. Ober, N. C. Maynard, W. J. Burke, M. R. Collier, D. J. McComas, N. F. Ness, and C. W. Smith (2002), Variable time delays in the propagation of the interplanetary magnetic field, *Journal of Geophysical Research: Space Physics*, *107*(A8), SMP 29–1–SMP 29–15, doi:10.1029/2001JA009102.

Wilson, J. S. (Ed.) (2005), *Sensor Technology Handbook*, Elsevier, ISBN: 0-7506-7729-5.

Wygant, J., J. Bonnell, K. Goetz, R. Ergun, F. Mozer, S. Bale, M. Ludlam, P. Turin, P. Harvey, R. Hochmann, K. Harps, G. Dalton, J. McCauley, W. Rachelson, D. Gordon, B. Donakowski, C. Shultz, C. Smith, M. Diaz-Aguado, J. Fischer, S. Heavner,

P. Berg, D. Malsapina, M. Bolton, M. Hudson, R. Strangeway, D. Baker, X. Li, J. Albert, J. Foster, C. Chaston, I. Mann, E. Donovan, C. Cully, C. Cattell, V. Krasnoselskikh, K. Kersten, A. Brenneman, and J. Tao (2013), The electric field and waves instruments on the radiation belt storm probes mission, *Space Science Reviews*, *179*(1-4), 183–220, doi:10.1007/s11214-013-0013-7.